The Dissertation Committee for Todd Christopher Soesbe

certifies that this is the approved version of the following dissertation:

Development and Evaluation of an EMCCD based Gamma Camera for Preclinical SPECT Imaging

Committee:

Peter P. Antich, Ph.D., Supervisor

Ralph P. Mason, Ph.D., CSci, CChem

Orhan K. Öz, M.D., Ph.D.

Frederick J. Bonte, M.D.

Development and Evaluation of an EMCCD based Gamma Camera for Preclinical SPECT Imaging

by

Todd Christopher Soesbe, M.S.

Dissertation

Presented to the Faculty of the Graduate School of Biomedical Sciences

The University of Texas Southwestern Medical Center At Dallas

in Partial Fulfillment

of the Requirements

for the Degree of

Doctor of Philosophy

The University of Texas Southwestern Medical Center At Dallas

August 2007

Dedicated to my wife Sinead
and our children Finnley and Lenna

Acknowledgments

I would like to acknowledge the many sources that have made this work possible.

I would first like to thank my advisor Dr. Peter Antich and my other Ph.D. committee members Dr. Ralph Mason, Dr. Orhan K. Öz, and Dr. Frederick Bonte for their thoughtful discussions, guidance, and insightful critiques on my dissertation research.

I would also like to thank Dr. Matthew Lewis, Dr. Edmond Richer, Billy Smith, Trung Nguyen, Dr. Nikolai Slavine, Dr. Padmakar Kulkarni, Dr. Veera Arora, Dr. Anca Constantinescu, Dr. Edward Tsyganov, and Serguei Seliounine. I worked with these colleagues very closely on a daily basis, and with their much appreciated assistance and help I was able to achieve my research goals in a timely manner. I also thank Dr. Vikram Kodibagkar, Dr. Dawen Zhao, Dr. Wei-Na Cui, Dr. Jang-Xin Yu, and Dr. Li Liu who I had the pleasure of working with during my first year lab rotation with Dr. Ralph Mason's research group.

I also thank Dr. Freek Beekman and his graduate student Jan Heemskerk at the University of Utrecht in the Netherlands for their technical assistance in applying EMCCD photodetectors to preclinical SPECT, and for inviting me to come and work with them for an amazing week in Holland.

Many thanks go to Kay Emerson, Irma Dobbins, and Jocelyn Chafouleas of the Advanced Radiological Sciences staff for their unparalleled administrative assistance with school matters and grant writing. I would also like to thank my

fellow students Dr. Celeste Roney, Dr. Bob Bollinger, Mai Lin, and Peiying Liu, who I wish the best of luck in their future research.

Finally, I would like to thank my grandmother Catherine Scheutzel for her financial support with my tuition and research trip to Utrecht, and special thanks go to my wife Sinead Soesbe and our children Finnley and Lenna whose love and support made the goal of receiving my Ph.D. possible.

TODD CHRISTOPHER SOESBE

The University of Texas Southwestern Medical Center At Dallas

August 2007

Development and Evaluation of an EMCCD based Gamma Camera for Preclinical SPECT Imaging

Publication No. _____

Todd Christopher Soesbe, Ph.D.

The University of Texas Southwestern Medical Center At Dallas, 2007

Supervisor: Peter P. Antich, Ph.D.

ABSTRACT

Pinhole collimation is extremely well suited for imaging radiopharmaceuticals in murine models of human disease. With pinhole collimation, SPECT systems are able to achieve sub-millimeter spatial resolutions. Data from such detailed images are extremely useful for preclinical studies in biomedical research including mapping *in vivo* gene expression, infectious disease modeling, drug development, and cancer diagnosis and therapy. Although high spatial resolutions can be reached with pinhole collimation, the sensitivity (cps/μCi) is still low when compared to clinical SPECT systems. An increase in pinhole SPECT sensitivity would allow for shorter scan times, higher animal throughput, and reduced dose levels.

Both the sensitivity and resolution of preclinical SPECT systems can be improved using an electron-multiplying charge-coupled device (EMCCD). The EMCCD offers improved quantum efficiencies (35 to 95%) over a broader range of wavelengths (400 to 900 nm) and a higher intrinsic resolution (< 100 μm using photon counting) when compared to photomultiplier tubes. The electron gain achieved in the multiplication register of an EMCCD effectively reduces the readout noise to less than 1 electron/pixel (e/p), making them sensitive to single photoelectrons. Both homemade and commercial systems were used to investigate the application of EMCCDs to preclinical SPECT.

The homemade prototype system used the Texas Instruments Impactron$^{\text{TM}}$ EMCCD model TC253SPD-B0 (7.4 μm square pixels) which was cooled under vacuum to -50 °C using a four stage Peltier and liquid heat exchanger. Shuttered lens-coupling was used to image the optical light from a 3 mm thick monolithic CsI(Tl) crystal. Precise clocking for the EMCCD was provided by a National Instruments FPGA controller (PCI-7811R) and LabVIEW FPGA module (version 8.0). A custom built electronics box contained the clock driver circuitry and 16-bit video board for digital conversion of the video signal. TC253 characterization tests measured a maximum gain just over 1000×, dark current rate of 0.14 e/p/s, read noise of 18.2 e/p, and spurious charge generation of 4 e/p. A light integration intrinsic resolution of 110 μm FWHM was measured. Light integration images of a line phantom using a single pinhole collimator were used for SPECT reconstruction. We found the relatively high spurious charge generation and low quantum efficiency (35% at 560 nm) of the inexpensive TC253 made it incapable of photon counting for low energy sources using lens coupling. Photon counting with the TC253 was demonstrated using fiber optic coupling.

The commercially available PhotonMAX 512B system used the e2v CCD97 EMCCD (16 μm square pixels). The improved quantum efficiency (95% at 560 nm)

and low spurious charge generation (< 0.01 e/p) made photon counting with lens coupling possible for both ^{99m}Tc and ^{125}I sources. A photon counting algorithm written with LabVIEW software was used with the PhotonMAX system to take list-mode data. A photon counting intrinsic resolution of 56 μm FWHM was measured. An energy resolution of 50% was measured for ^{57}Co. Photon counting images of ^{99m}Tc-MDP uptake within a mouse using single pinhole collimation showed an improved SNR over integration images.

This optical coupling method differs from other EMCCD SPECT systems by using lenses rather than fiber optic bundles for transfer. Although the optical coupling efficiency for lens coupling is lower than fiber coupling, it has been shown that photon counting can still be achieved provided a high quality EMCCD is used.

Contents

Chapter 1

Introduction

1.1 Definition of SPECT

Single photon emission computed tomography (SPECT) is a method used in diagnostic nuclear medicine to image the three-dimensional spatial distribution of a radioactive drug (radiopharmaceutical) that has been administered to a living organism. SPECT differs from other medical imaging methods that offer mainly anatomical information, such as radiography, x-ray CT, magnetic resonance imaging (MRI), and ultrasound, in that it is able to assess the physiological function of specific organs by measuring the location, amount, and rate of radiopharmaceutical uptake by the target organ.

SPECT answers three basic questions about the radiopharmaceutical: 1) Where has it gone within the body (spatial information), 2) How much activity is present per volume (quantitative information), and 3) How does the distribution change over time (temporal information). The basic algorithm for SPECT is as follows: After the administration of the radiopharmaceutical, a certain amount of time is allowed for the drug to reach the target. After this uptake time, a two-dimensional

projection image of the radioactive isotope distribution is taken with some type of gamma camera. A gamma camera is analogous to a conventional camera except that it measures gamma ray photons instead of optical photons. Several different projections are then taken while rotating the camera around the source. This set of two-dimensional projections are then used to reconstruct the three-dimensional radiopharmaceutical distribution based on the mathematical principles of the Radon transform [1].

1.2 Development of Clinical SPECT

"From the medical point of view, probably the most important physical question in relation to the use of radioactive isotopes is finding their distribution in the body. It would, in these instances, be a great convenience if we could obtain a visual image of the distribution of material."

W. V. Mayneord, Nature (1951)

As seen in the above quote, the problem of finding exactly where a radiopharmaceutical went within a living body was of great interest to early researchers in nuclear medicine. Not only would this information be required for accurate diagnosis, but would likewise be valuable for therapy since the spatial distribution of the radiopharmaceutical is also the basis of the radiation dosimetry [2]. This section briefly describes historical developments in nuclear medical imaging ranging from the early rectilinear scanners of the 1950s and 1960s to the first clinical tomographic machines of the 1970s.

1.2.1 Directional Geiger-Müller Counters

Early attempts at visualizing the radioactive isotope distribution used Geiger-Müller (G-M) tubes as the gamma ray detector [3]. The G-M tubes were collimated such that they only counted the radioactivity emerging from a small field of view [2, 4, 5]. These detectors would then mechanically scan a larger field of view in a linear fashion, measuring the counts at each location to form an intensity image of the radioisotopes distribution. Figure 1.1 shows images from N. Veall's 1950 paper in which a collimated G-M tube was used to map the *in vivo* isoresponse curve of ^{131}I uptake in the human thyroid gland [4]. Figure 1.2 shows images from W. V. Mayneord's 1951 paper in which a similarly collimated G-M tube was used to create scanning images of ^{198}Au line phantoms [2]. A significant drawback of these early imaging systems was that the G-M tubes were very inefficient at detecting gamma rays, which meant the need for very long scan times or high doses. For example ^{131}I (364 keV), one of the most commonly used medical isotopes in early nuclear medicine, had only a 1% detection efficiency in G-M tubes [6]. This efficiency was even lower for other commonly used radioisotopes of higher energy (*e.g.* ^{198}Au (412 keV) and ^{60}Co ($\approx$ 1200 keV)).

1.2.2 The Scintillation Counter

In 1950 Benedict Cassen replaced the G-M tube gamma ray detector with a clear calcium tungstate crystal that was coupled to a photomultiplier tube (PMT) [7, 8, 9]. The high density scintillating crystal (6.06 g/cm^3) was able to stop a much larger fraction of the incident gamma rays compared to a G-M tube, while the low light level scintillation flashes were easily amplified by the PMT for counting. This scintillation counter increased the ^{131}I detection efficiency from 1% to 26% [6]. By 1951 Cassen

had mounted his scintillation counter on an automated scanner and recorder that was used to perform *in vivo* rectilinear scanning of the human thyroid gland (see Figure 1.3). Cassen's scintillation scanner had a total resolution of 6.4 mm and could accurately map the thyroid gland with only a 150 μCi dose of radioiodine given to the patient. The highly efficient scintillation counter quickly found other additional in nuclear medicine [5, 10, 11, 12].

1.2.3 The Gamma Camera

Along with rectilinear scanning techniques, early nuclear medical imaging research was also conducted with the gamma ray camera, which could measure the radiopharmaceutical distribution in a large field of view simultaneously. The gamma camera had a lower efficiency per area compared to a rectilinear scanner due to the low sensitivity of the pinhole collimator lens. An early version of the gamma camera used a pinhole collimator and ordinary radiography film (see Figure 1.4) and had long exposure times (1 to 3 days) mainly due to the inefficiencies of the film [14]. In 1952 Hal Anger placed a thallium-activated sodium iodide crystal (NaI(Tl)) in front of the radiographic film to serve as an intensifying screen as shown in Figure 1.5 [15]. This system was used to image 20 mCi of ^{131}I uptake (therapeutic dose) in a thyroid carcinoma metastasis in a one hour exposure using a 3.2 mm pinhole. Although not as sensitive per area as the scintillation scanner, the gamma camera had the advantage of no moving parts.

In 1957 Hal Anger replaced the radiographic film with an array of photomultiplier tubes to measure the position and intensity of individual scintillation flashes within the NaI(Tl) crystal [16]. This "scintillation camera" eventually became the archetype for modern radioisotope imaging. A schematic of the original camera is

shown in Figure 1.6. The camera consisted of a single pinhole collimator made of either Lead or Platinum, a 6.4 mm thick Thallium-doped Sodium Iodine scintillating crystal (NaI(Tl)) and seven photomultiplier tubes (PMTs). Gamma rays that emerge from the source and pass through the pinhole aperture can interact within the crystal to produce isotropic bursts of optical photons. These optical photons are then measured by the seven PMTs to determine the two-dimensional position of the gamma ray interaction within the crystal. The resulting image is a planar projection of the radiopharmaceutical's three-dimensional distribution. Figure 1.6 also shows sample *in vivo* images of the human thyroid gland taken with a 6.4 mm Platinum pinhole. Each gland contained 7.5 to 12.5 μCi (0.28 to 0.46 MBq) of ^{131}I with exposure times varying from 12 to 15 minutes. Although Anger's scintillation camera was able to take *in vivo* images over a small field of view, the pinhole collimation resulted in low sensitivity for objects that were far from the pinhole aperture. This meant that in order to take an image with a large field of view, either high amounts of activity or long exposure times had to be used.

1.2.4 The Origin of Single Photon Emission CT

In 1963 David E. Kuhl and Roy Q. Edwards used a single scintillation counter to perform transverse section scanning of an ^{131}I phantom [17]. Transverse section scanning produced a two-dimensional image representing a planar slice of the radioisotopes three-dimensional distribution. A year later Kuhl and Edwards developed a clinical system based on this technique which used two opposed scintillation counters to improve the sensitivity [18]. By backprojecting the data received from several equiangular transverse scans, they were able to produce transaxial tomograms which were much more detailed than rectilinear scans (see Figure 1.7).

Kuhl and Edwards continued to improve upon their emission scanning techniques over the next decade [19, 20, 21, 22] until in 1976 when they developed the Mark IV system [23]. The Mark IV was the first SPECT system, then known as radionuclide computed tomography (RCT), in which the only motion was rotation. A schematic of the Mark IV system is shown in Figure 1.8. The Mark IV acquired simultaneous transverse section scans of the source by using a four head detector. Each head contained eight individual PMTs, with each PMT having its own 2.5 cm thick NaI(Tl) crystal and multi-channel focused lead collimator. By rotating the detector heads about the subject axis, data from several different angles could quickly be taken. These scans were then used to reconstruct the two-dimensional distribution of the radiopharmaceutical source using the cumulative additive tangent correction (CATC) iterative reconstruction algorithm. A schematic and sample images from the Mark IV system are shown in Figure 1.8.

Even after 30 years, modern clinical SPECT systems are still very similar to the Mark IV system in both overall form and detector design. While the Mark IV system had a spatial resolution of about 18 mm and a sensitivity of about 1000 cps/(μCi) over a field of view of 20 cm x 20 cm, modern clinical SPECT systems have resolutions of about 4 mm and sensitivities of about 200 cps/μCi for a field of view of 50 cm x 40 cm.
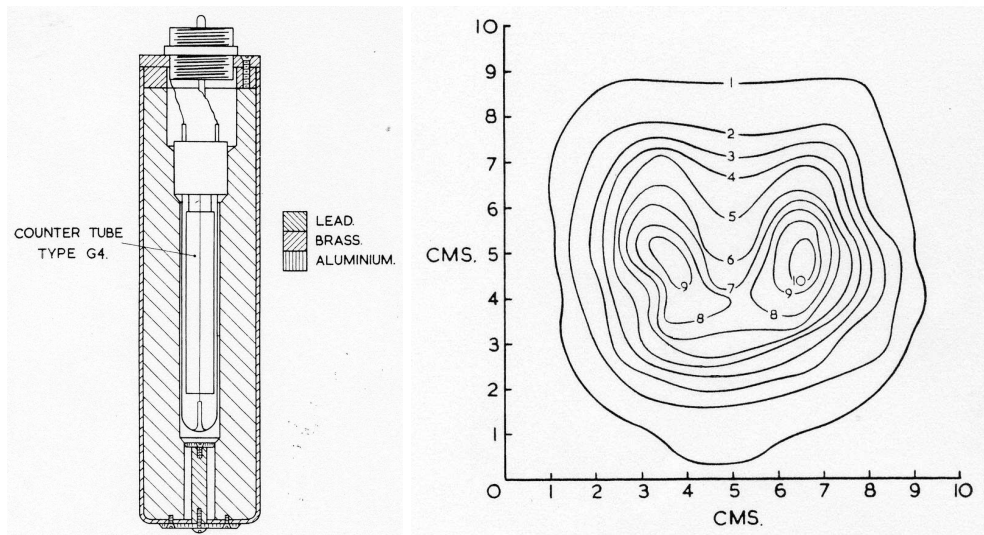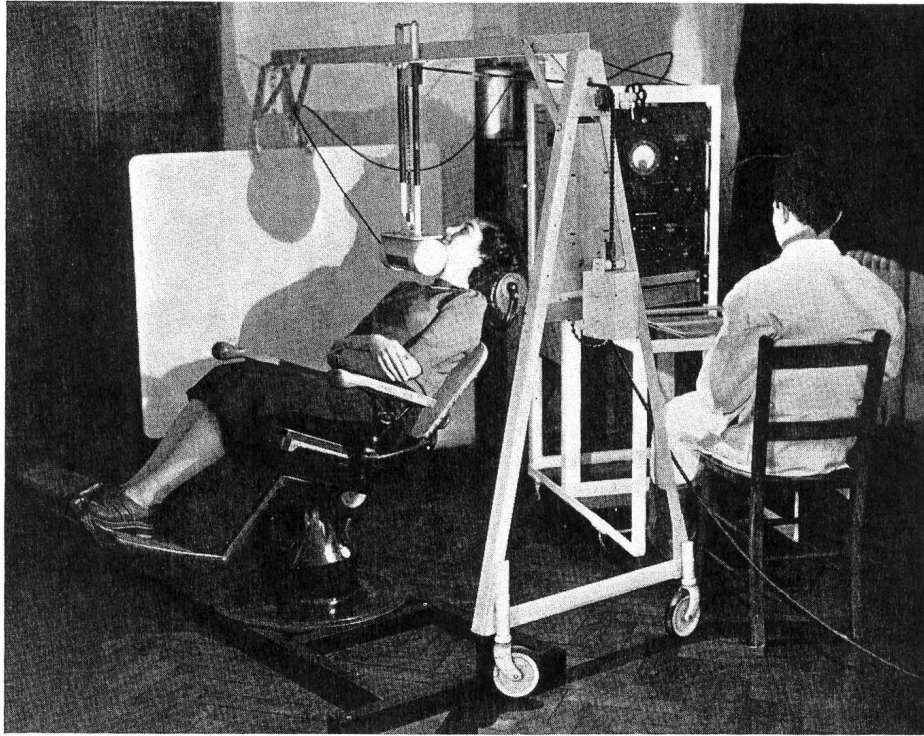
Figure 1.1: Images from N. Veall's 1950 *British Journal of Radiology* paper [4] showing the experimental set up (top), collimated G-M tube (lower left), and an *in vivo* isoresponse curve of the human thyroid gland with ≈ 1 mCi of ^{131}I uptake (lower right).
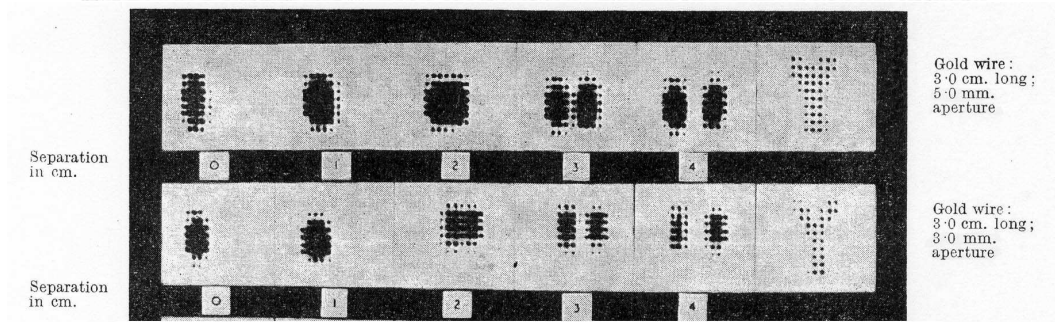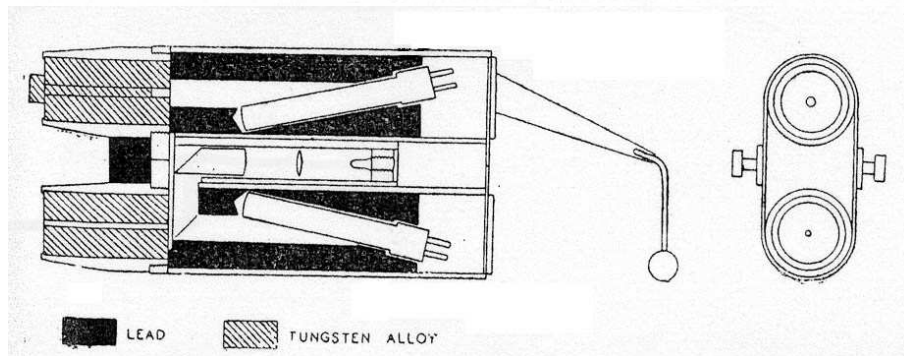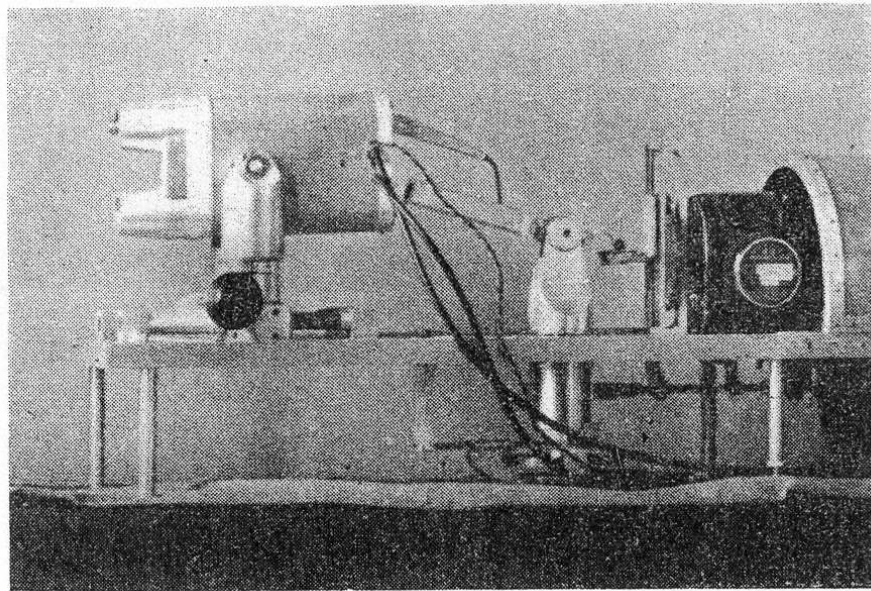
Figure 1.2: Images from W. V. Mayneord's 1951 *Nature* paper [2] showing the experimental setup (top), the collimated G-M tube arrangement (middle), and scanned images of ^{198}Au line phantoms from two different aperture diameters.
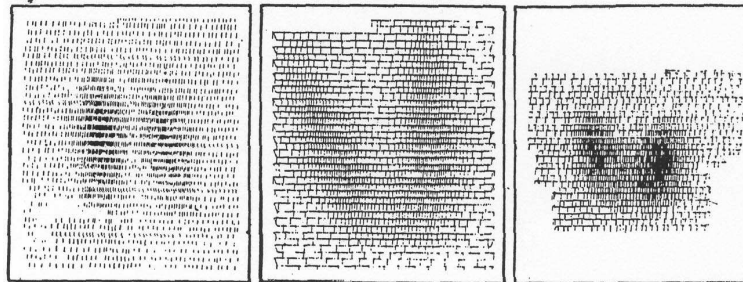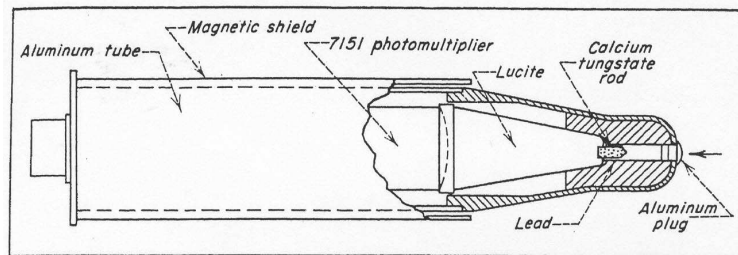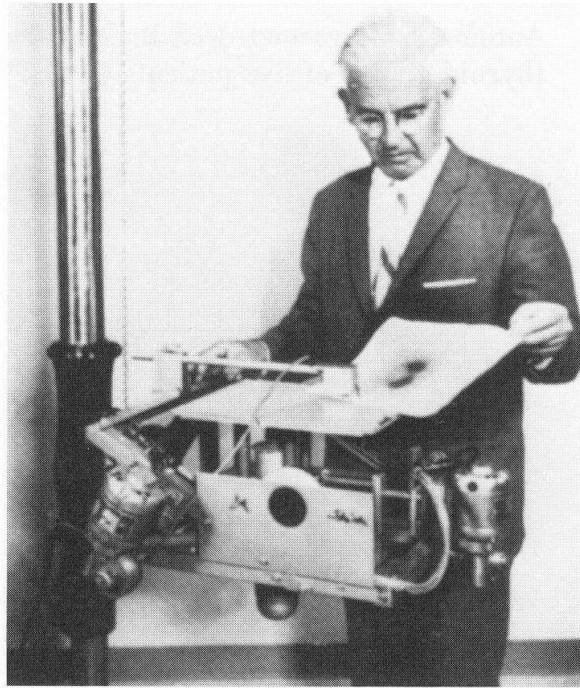
Figure 1.3: A photograph of Ben Cassen with his first rectilinear scintillation scanner (top). Images from Ben Cassen's 1951 *Nucleonics* paper [13] showing a schematic of the scintillation counter with calcium tungstate crystal and photomultiplier tube (middle), and sample *in vivo* rectilinear scans of the human thyroid gland with ≈ 150 μCi of ^{131}I uptake (bottom).
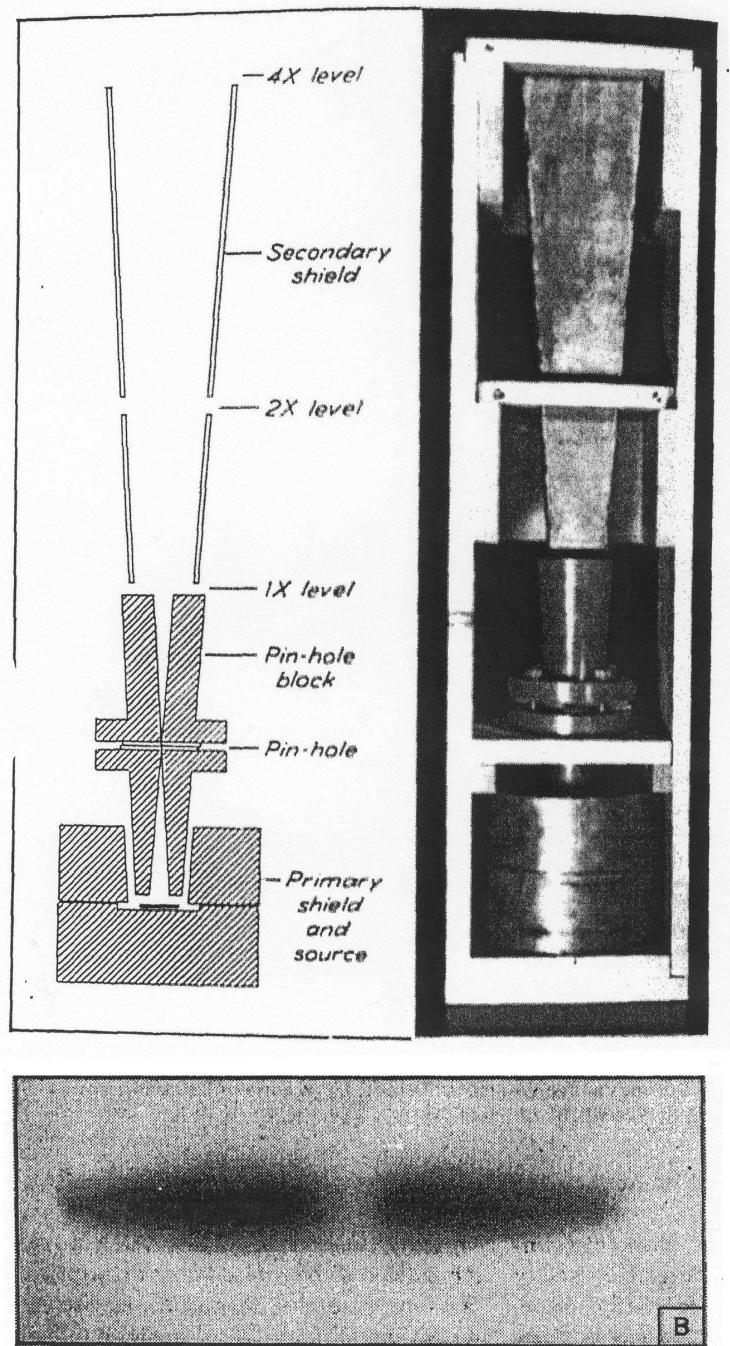
Figure 1.4: Images from D. E. Copeland's 1949 *Nucleonics* paper [14] showing an initial version of the pinhole gamma camera (top) and a radiographic film image of a 6 mg radium chloride needle measuring ≈ 3 cm in length (bottom).
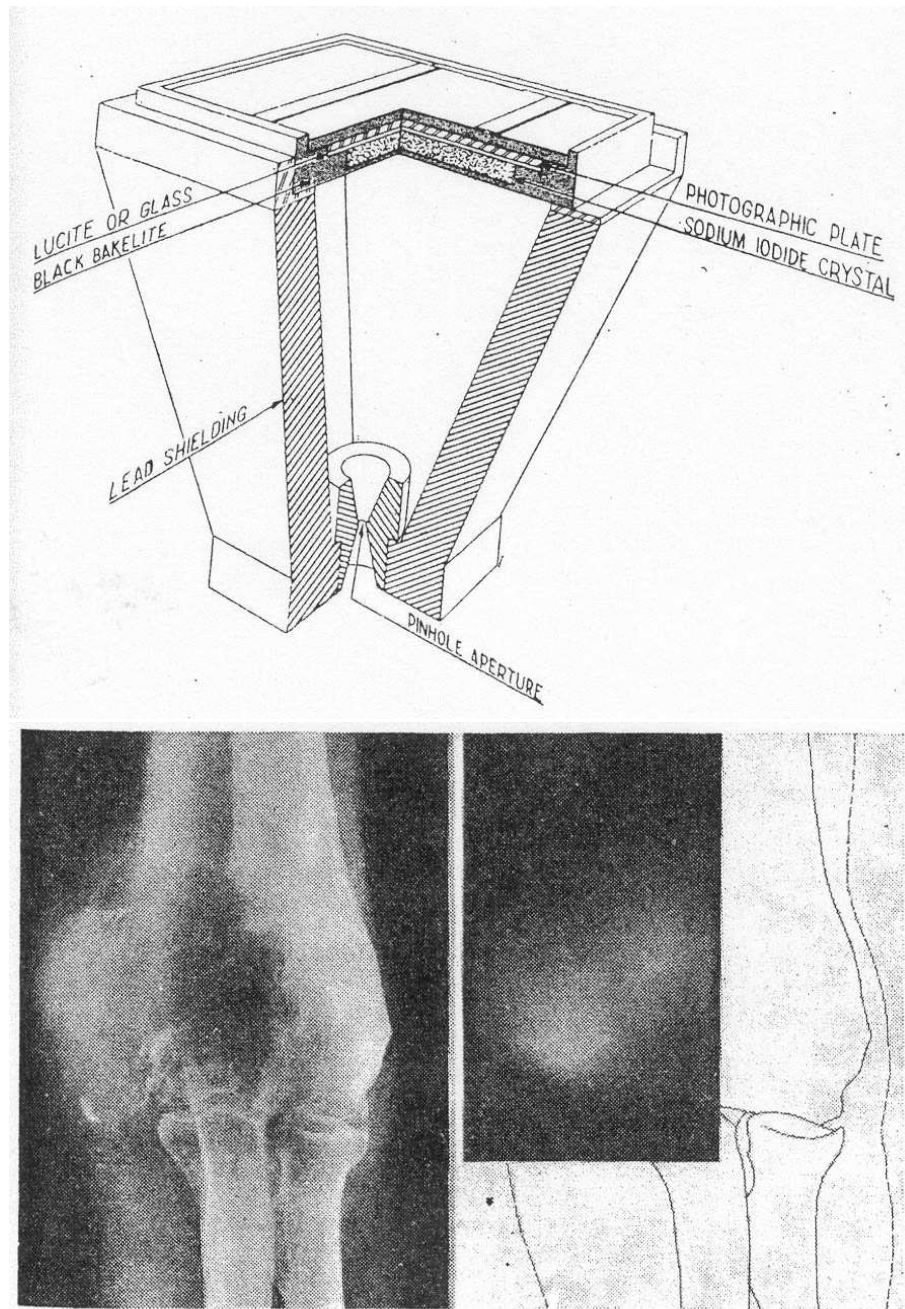
Figure 1.5: Images from Hal Anger's 1952 *Nature* paper [15] showing a schematic of his gamma camera (top), an x-ray radiograph of a thyroid carcinoma metastasis (bottom left), and a pinhole gamma camera image of the same area showing the uptake of $\approx$ 20 mCi of ^{131}I within the tumor (bottom right).

11
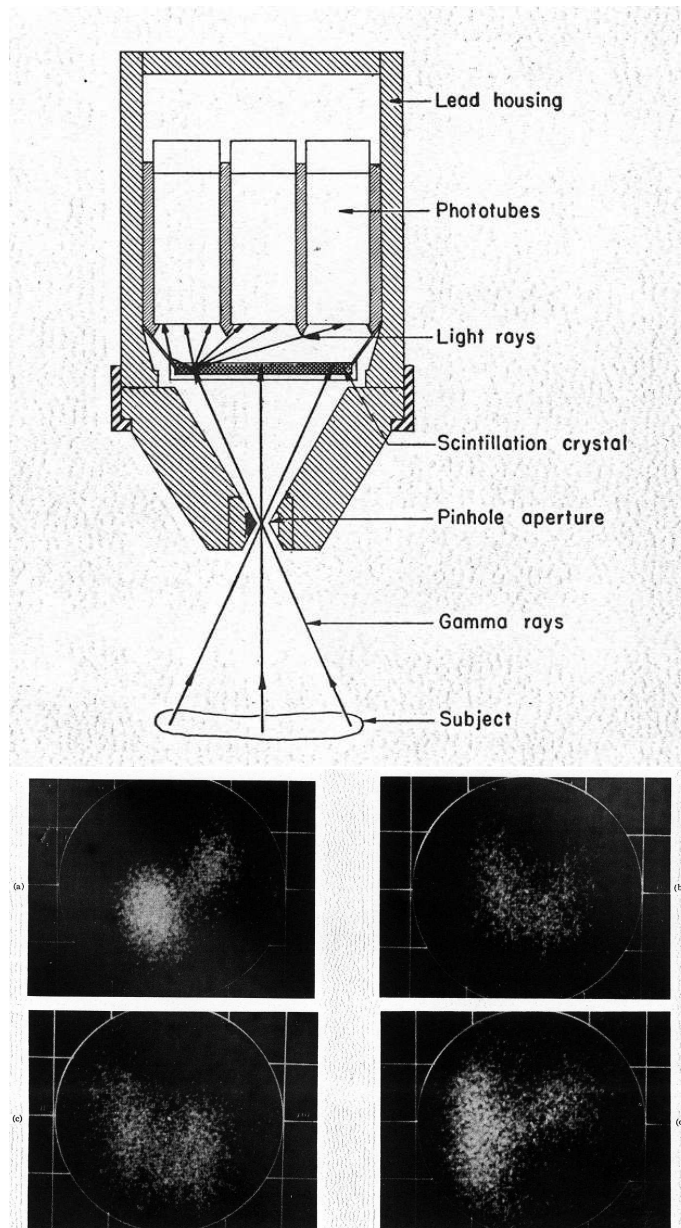
Figure 1.6: Images from Hal Anger's 1957 *Review of Scientific Instruments* paper [16] showing a schematic of his scintillation camera (top) and *in vivo* images of the human thyroid gland with ≈ 10 μCi of ^{131}I uptake (bottom). The subject to pinhole distance was ≈ 12.7 cm.
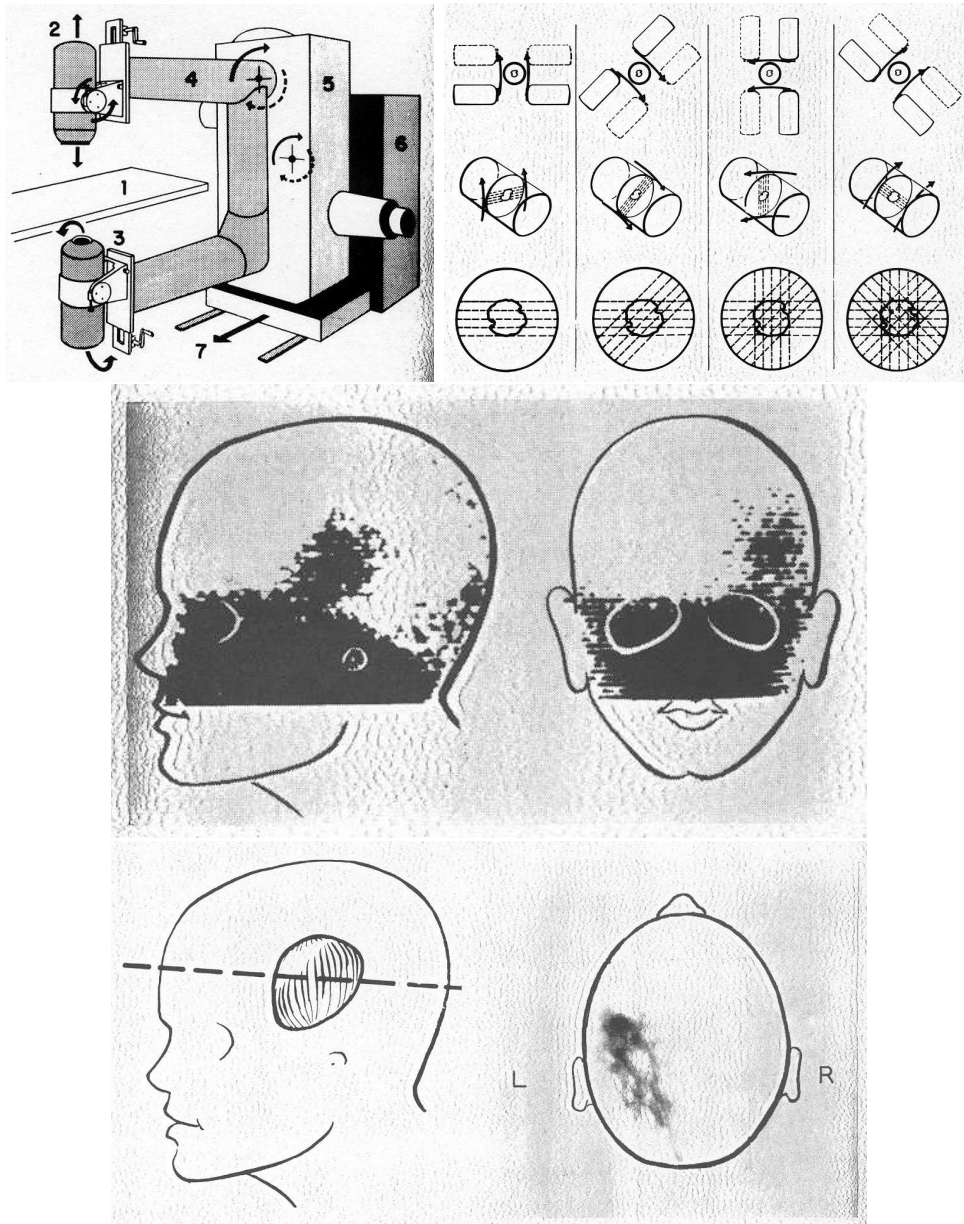
Figure 1.7: Images from Kuhl and Edwards 1964 *Radiology* paper [18] showing a schematic of the clinical scanner (top left), the transverse section scanning method (top right), and a comparison between a rectilinear (middle) and transverse section scan (bottom) of the same patient. The posterior extent of the malignant astrocytoma in the left parietal lobe was more accurately represented by the transverse section scan which was acquired in 12 minutes. These scans used 1.4 mCi of chlormerodrin ^{197}Hg ($\approx$ 70 keV).
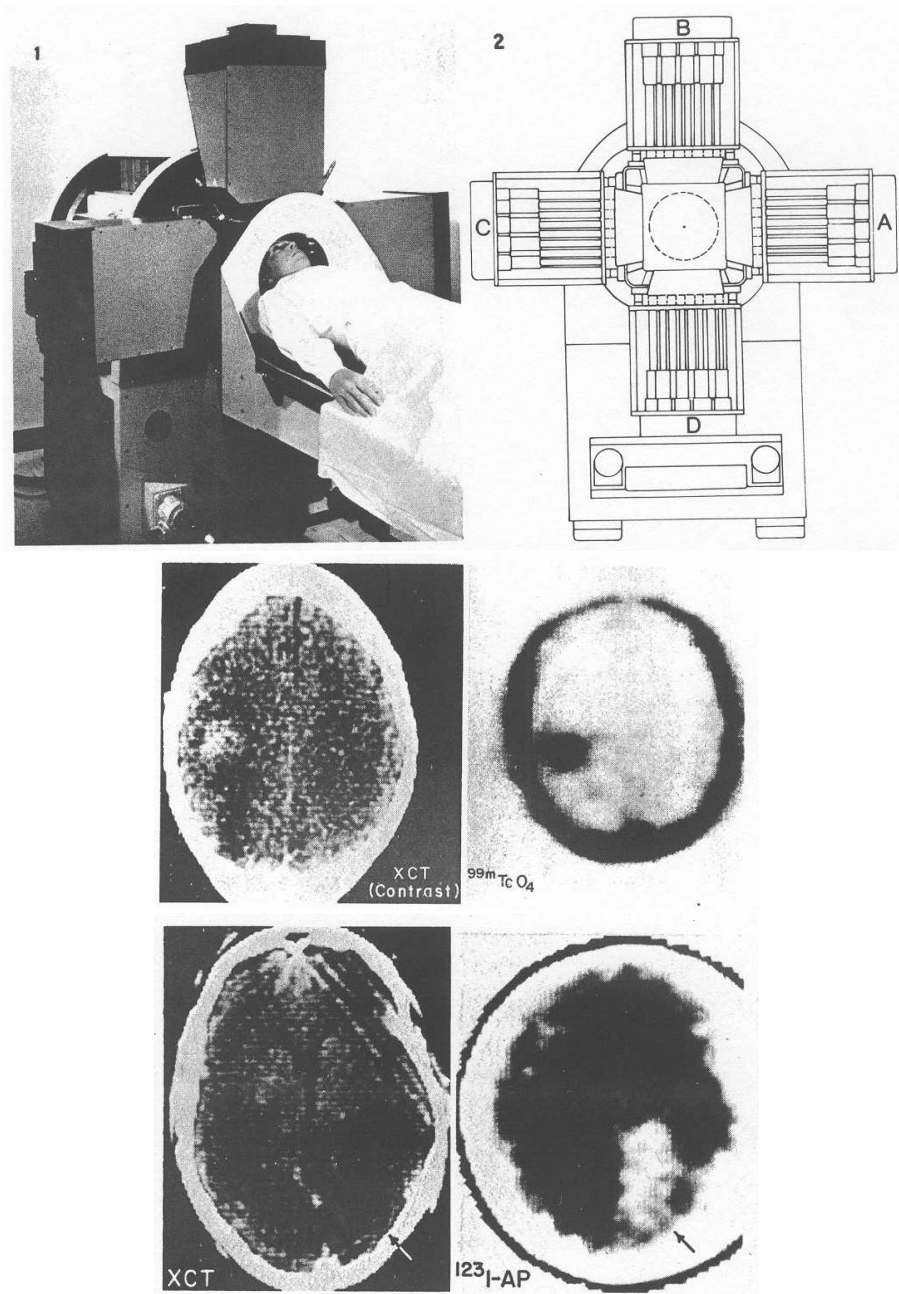
Figure 1.8: Images from Kuhl and Edwards 1976 *Nuclear Medicine* paper [23] showing a photo and schematic of the Mark IV (top), and XCT and RCT images of a brain metastasis (^{99m}TcO$_4$, 140 keV) (middle) and cerebral infarction (^{123}I-iodoantipyrine, 159 keV) (bottom).

1.3 Requirements of Preclinical SPECT

Over the past decade the demand for high-resolution preclinical (small animal) SPECT imaging has greatly increased. This increase is due to the development of new radiolabeled antibodies, receptor ligands, and other radiopharmaceuticals for both imaging and therapy [24]. The availability of genetically modified mice and *in vivo* molecular imaging for studying gene expression and regulation in human disease has also increased the demand for high-resolution SPECT [25, 26, 27, 28]. Prior to the development of preclinical SPECT, the most common method used to study radiopharmaceuticals in small animals was autoradiography. Autoradiography involves the sacrifice of several animals at different time intervals after the administration of a radiopharmaceutical. After sacrifice, the organs of interest are harvested and histological slides are created and placed on film for exposure. One drawback of the autoradiography method of analysis is that it requires several animals for a single study, since each animal can only be measured once, and several studies to achieve significant statistics due to the natural physiological differences between animals [28]. With the development of high-resolution small animal SPECT, an animal can be measured several times throughout a study, thereby allowing each animal to act as its own control. This leads to fewer animals needed per study, which helps to reduce the overall cost of the experiment.

The small field of view needed to image animals such as mice and rats ($\approx$ 10 cm x 10 cm) allows for the use of pinhole collimation to achieve sub-millimeter resolution ($<$ 1 mm FWHM). Yet, the pinhole diameter required for this resolution severely limits the sensitivity of the device. Several methods for increasing the sensitivity of small animal SPECT systems are currently being pursued. These methods include using multiple single pinhole detectors [29, 30, 31, 32, 33], multiplexing sev-

eral pinholes onto a single detector with either minimal [34, 35] or extensive [36, 37] image overlap on the crystal surface, and even using coded apertures commonly found in gamma ray astronomy [38, 39]. Existing clinical SPECT systems can be fitted with pinhole collimators to achieve adequate resolutions for small animal imaging [29, 36, 40, 41], but compact dedicated preclinical SPECT systems can offer higher resolutions and are small enough to fit on a desktop [30].

Another method to improve the sensitivity is to use a charge-coupled device (CCD) for the gamma camera photodetector. The application of CCDs to preclinical SPECT imaging has been previously shown by our group [42]. This research has been greatly accelerated by the recent availability of the electron-multiplying CCD (EMCCD) which was first technically described in 1992 [43] and made commercially available in 2001 [44, 45]. EMCCDs combine the positive aspects of photomultiplier tubes (high-gain leading to a high signal-to-noise ratio, photon counting, and energy discrimination) with the positive aspects of CCDs (high quantum efficiencies over a broad spectral range, high intrinsic resolution, and small form factor) making them well suited for preclinical SPECT applications.

1.4   Research Objectives

The objective of this research is the development and evaluation of an EMCCD based small animal SPECT device for murine model studies of human disease. Previous applications of EMCCDs to preclinical SPECT imaging mainly use fiber optic bundles to transfer the light from a micro-columnar CsI(Tl) crystal to the imaging area of the EMCCD [46, 47, 48, 49]. This requires the bundle to be placed very close to, if not touching, the EMCCD surface which creates mechanical, cooling, and vacuum complications. The method described here differs by using lens coupling

for light transfer with monolithic as well as micro-columnar CsI(Tl) crystal. With lens coupling, physical contact with the EMCCD is eliminated, although the optical coupling efficiency is lower compared to fiber coupling [50]. This method also differs by using the very low cost Texas Instruments TC253 EMCCD in our custom built camera.

This paper first describes the technical requirements for preclinical SPECT including pinhole collimator theory, scintillating material options, and photodetector requirements (Chapter 2). Initial SPECT results from a PSPMT system (Chapter 3) and a CCD system (Chapter 4) are then described. The construction, characterization, and SPECT reconstruction results from the custom built TC253 EMCCD system are described in detail (Chapter 5). This is then followed by results from the photon counting experiments using the PhotonMAX CCD97 EMCCD system (Chapter 6). Experimental summaries, conclusions, and further work are then discussed (Chapter 7).

Chapter 2

Materials and Methods

2.1 System Variables

The four major components of a preclinical SPECT system are shown in Figure 2.1 and include the source object to be imaged, collimator, scintillating crystal, and photodetector. A gamma ray that emerges from the source object and passes through the collimator aperture can interact within the scintillating crystal. This interaction can produce an isotropic burst of optical wavelength photons (400 to 900 nm). The optical photons that escape the crystal are then measured by the photodetector to determine the two-dimensional position of the gamma ray interaction within the crystal. Several gamma ray interactions are then measured to create a two-dimensional projection of the radioisotope distribution in the source object. Common choices for each system component are also shown in Figure 2.1. A brief discussion of these choices follows, with detailed discussions given in the next sections.

The two major variables for the source object include the choice of radioactive isotope (which corresponds to gamma ray energy) and subject orientation (horizon-

source_object	pinhole_collimator	scintillating_crystal	photodetector
Tc-99m (140 keV)	single	NaI(Tl)	PMT
I-125 (27 keV)	multiple (no overlap)	CsI(Tl)	PSPMT
vertical (rotate)	multiple (with overlap)	micro-columnar CsI(Tl)	CCD
horizontal (fixed)	coded aperture	LSO	EMCCD
		LPO	APD
			PSAPD
			PSD
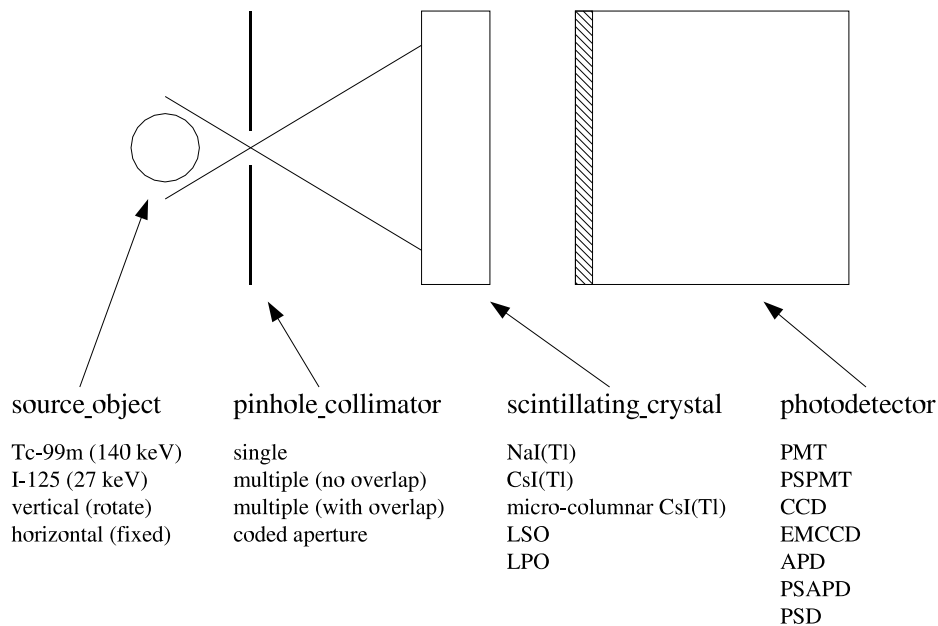
Figure 2.1: A schematic showing the four main components of a preclinical SPECT system and common choices for each component.

tal or vertical). It is desirable for the detector to be sensitive over a range of commonly used radioisotopes and their associated gamma ray energies. ^{125}I (≈ 27 keV) and ^{99m}Tc (140 keV) are frequently taken as the lowest and highest gamma ray energies respectively, although higher energy sources are sometimes used. The choice of subject orientation depends greatly upon the detector design. For a vertical orientation, the detector remains fixed while the subject is made to rotate about a vertical axis. For a horizontal orientation, the subject remains fixed while the detector rotates about the subject. In general, a horizontal orientation is preferred, for the anesthetized subject is less likely to move while acquiring data when in the natural prone position.

As discussed in the previous chapter, the choices for the pinhole collimator include a single pinhole, multiple pinholes with no image overlap on the crystal surface, multiple pinholes with image overlap on the crystal surface, and a coded aperture. These choices are shown schematically in Figure 2.2, where the first row is the number of pinholes per collimator, the second row is the pinhole configuration, and the third row represents the projected image onto the crystal surface when imaging a uniform planar source. Although the sensitivity increases when moving from left to right in Figure 2.2, it is not fully understood how the resolution changes as the image overlap increases and the tomographic reconstruction becomes more complicated.
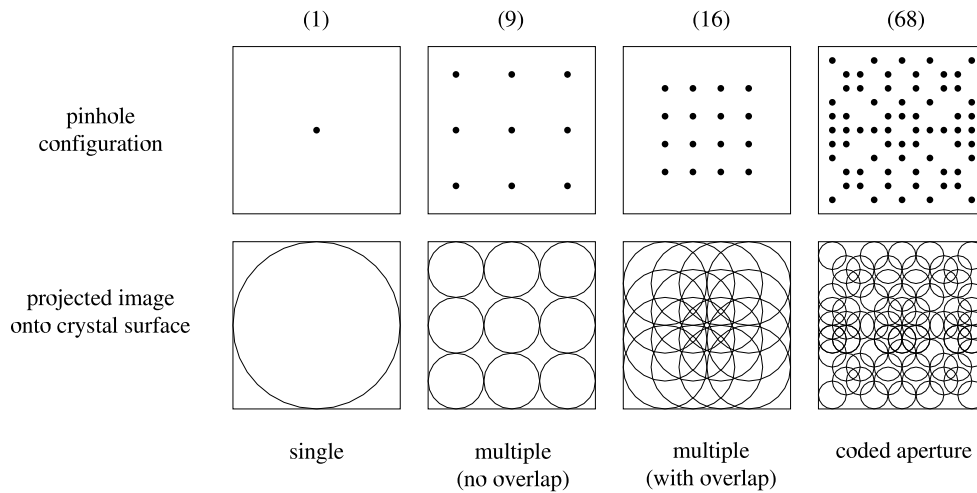
Figure 2.2: A schematic showing the four main configurations for multiple pinhole collimation. The sensitivity per collimator increases when moving from left to right.

The two most commonly used inorganic scintillating crystals are Thallium-doped Sodium Iodide (NaI(Tl)) and Thallium-doped Cesium Iodide (CsI(Tl)). NaI(Tl) has a peak emission wavelength of 410 nm and is best suited for the bi-alkali photo-

cathodes of photomultiplier tubes (PMTs). CsI(Tl) has a peak emission wavelength of 560 nm and is best suited for semiconductor detectors such as charge coupled devices (CCDs) and avalanche photodiodes (APDs). One option for the scintillating crystal is to use micro-columnar CsI(Tl), which are CsI(Tl) crystals grown in close packed needle like structures where the diameter of each needle is $< 10~\mu$m. This allows for thicker crystals to be used (which increases the stopping power and thus sensitivity) without degrading the spatial resolution caused by the varying light spot size on the crystal surface viewed by the photodetector. Other crystal options include $Lu_2(SiO_2)O$ (LSO) and $LuPO_4$ (LPO) with each having their own positive and negative characteristics as discussed in the next section.

The function of the photodetector is to measure the optical wavelength photons emerging from the scintillating crystal and use them to determine the two-dimensional position of the scintillation event within the crystal. Options include photomultiplier tubes (PMT), position sensitive photomultiplier tubes (PSPMT), charge coupled devices (CCD), electron multiplied charge couple devices (EMCCD), avalanche photodiodes (APD), position sensitive avalanche photodiodes (PSAPD), and position sensitive devices (PSD, Hamamatsu). The photodetector choices are discussed in detail in the next section.

A fifth small animal SPECT component not shown in Figure 2.1 is the optical coupler between the scintillating crystal to the photodetector. Options include direct coupling (with optical grease), fiber optic coupling (1:1 or tapered), and lens coupling (single or dual). The choice of coupling greatly effects the optical coupling efficiency and total sensitivity of the detector [50].

The above SPECT components must be chosen to meet the design requirements of the system, which are high-resolution and high-sensitivity over a small field

of view. This task can be broken up into two smaller tasks which are 1) maximizing the scintillator and photodetector coupling and 2) understanding how the multiple pinholes will image the field of view.

2.2 Scintillator and Photodetector Matching

In order to help maximize the sensitivity of the SPECT system, every gamma ray that manages to pass through the collimator should interact within the scintillating crystal and be measured by the photodetector. This depends on the intrinsic properties of the crystal and photodetector which are discussed in this section.

2.2.1 The Scintillating Crystal

As mentioned previously, the scintillating crystal converts the incident high-energy gamma ray into an isotropic burst of lower-energy optical photons, with the number of optical photons being proportional to the gamma ray energy. The photodetector then converts these optical photons into an electric signal, where the amount of charge in the electric signal is proportional to the number of optical photons measured. Therefore, the number of electrons measured per gamma ray interaction is proportional to the energy of the initial gamma ray. The digitization and analysis of the electric signals from the photodetector can give both the position of the gamma ray interaction within the crystal, and the energy spectrum of the radioisotope observed. In order to increase the system sensitivity, the electric signal from the photodetector must be maximized for each gamma ray interaction. This can be achieved by properly matching the output characteristics of the crystal to the input characteristics of the photodetector. The most important characteristics to consider when choosing a scintillating crystal are the percent absorption for a given gamma

ray energy, the luminosity, and the peak output wavelength.

Gamma Ray Stopping Power

The attenuation for a beam of photons passing through a material is given by:

$$I_f = I_o e^{-\mu x} \tag{2.1}$$

where I_o is the initial photon beam intensity, I_f is the final photon beam intensity, x is the material thickness (cm) and μ is the total linear attenuation coefficient (cm^{-1}). The total linear attenuation coefficient is the summation of the scattering and absorption coefficients that arise from the different ways a photon can interact with matter. This depends on both the photon energy and the type of material it interacts with. For a low energy gamma ray (≈ 100 keV) passing through a solid inorganic scintillating crystal ($\rho = 3$ to 5 g/cm^3), the most probable interactions are photoelectric absorption, incoherent (Compton) scattering, and coherent (Raleigh) scattering. The percent contribution to the total linear attenuation coefficient from the individual interaction coefficients is shown in Table 2.1 [51]. This table shows examples for both 140 keV and 35 keV gamma rays interacting in CsI(Tl). It can be seen that photoelectric absorption is the dominant process in both cases.

Coefficient (1/cm)	140 keV in CsI(Tl)	35 keV in CsI(Tl)
μ	0.729	19.1
photoelectric	0.573 (79%)	18.4 (96%)
inelastic (Compton)	0.103 (14%)	0.102 (0.5%)
elastic (Raleigh)	0.054 (7%)	0.619 (3%)

Table 2.1: A table showing values for the total linear attenuation coefficient for both 140 keV and 35 keV gamma rays in CsI(Tl). Also shown are the values and percent contribution of the individual interaction coefficients.

The total linear attenuation coefficient can be used with Equation 2.1 to create a plot of the percent attenuation versus crystal thickness as shown in Figure 2.3. Only the photoelectric absorption and incoherent scattering coefficients have been used in the figure since only these two processes transfer energy to electrons within the crystal (for gamma ray energies < 1,022 keV). It can be seen that it takes only 0.5 mm of either NaI(Tl) or CsI(Tl) to achieve 100% attenuation of 35 keV gamma rays (^{125}I), yet it takes > 10 mm to achieve 100% attenuation for 140 keV gamma rays (^{99m}Tc). In order to maximize sensitivity, every gamma ray that passes through the pinhole aperture should interact within the crystal and be measured. This would lead to using thicker crystals for higher energy gamma rays. Unfortunately, thicker crystals lead to a degradation of the spatial resolution by increasing the spot size of the emerging optical photons on the crystal surface viewed by the photodetector.

Crystal Luminosity

The number of optical photons created for a given gamma ray interaction within the scintillating crystal is known as the luminosity (number of photons/MeV). A list of the luminosity values for the most commonly used scintillators is given in Table 2.2 [52, 53]. For example, if a 100 keV gamma ray deposits all of its energy within the crystal through photoelectric absorption, this would produce 3800 photons in NaI(Tl) and 5200 photons in CsI(Tl). Although the luminosity of LuPO$_4$(Eu) is more than twice that for CsI(Tl), the LuPO$_4$(Eu) was measured in powder-crystalline form which could lead to artificially high values. A higher crystal luminosity means an increased number of optical photons striking the photodetector per gamma ray interaction. This can then lead to a larger electric signal output from the photodetector, and thus improved sensitivity, but this depends on the quantum

efficiency of the photodetector.

Crystal	Density (g/cm^3)	Luminosity (photons/MeV)	peak wavelength (λ_{max}) (nm)
NaI(Tl)	3.67	38,000	410
CsI(Tl)	4.51	52,000	560
Lu$_2$(SiO$_4$)O(Ce)	7.40	26,000	420
LuPO$_4$(Eu)	6.53	123,000	750

Table 2.2: A table showing density, luminosity, and the wavelength of peak output intensity (λ_{max}) of four common scintillating crystals.

Peak Output Wavelength and Quantum Efficiency

The optical photons emitted by the gamma ray absorption within the scintillating crystal are not monochromatic, but rather are dispersed throughout an emission spectrum. The emission spectrum is different for each crystal structure and is characterized by the wavelength of peak intensity (λ_{max}). It is very important to consider λ_{max} when selecting a scintillating crystal. This is because each photodetector type is more sensitive to certain wavelengths than others. The sensitivity of the photodetector is expressed as the quantum efficiency (QE) for a given wavelength.

When an optical photon strikes the surface of the photodetector, the energy of the photon is transferred to electron kinetic energy through photoelectric absorption and incoherent scattering. This photoelectron is then used to generate the electronic signal from the photodetector. The photosensitive material for a PMT is the photocathode, which is typically a thin layer of bi-alkali metal that has been vapor deposited onto glass. For a semiconductor device, the photosensitive material is usually a metal-oxide-silicon (MOS) type capacitor that creates electron-hole pairs when an optical photon is absorbed.

The quantum efficiencies for a PSPMT (Hamamatsu R2486) and a CCD (SITe SI-032 AB) are plotted versus wavelength in Figure 2.4(a) and Figure 2.4(b) respectively. It can be seen in Figure 2.4(a) that the λ_{max} for NaI(Tl) (410 nm) occurs at the maximum QE for a PSPMT ($\approx 20\%$), while the QE corresponding to the λ_{max} of CsI(Tl) (560 nm) is almost an order of magnitude lower ($\approx 2\%$). This means a much smaller electrical signal would be measured for 560 nm optical photons striking the photocathode than for the same number of 410 nm photons. Although the luminosity of CsI(Tl) is about 40% larger that of NaI(Tl), this does not compensate for the difference in QE between the two λ_{max} when measured by a PMT photodetector. In Figure 2.4(b) it can be seen that for a back illuminated CCD the QE corresponding to λ_{max} is now at 73% for NaI(Tl) (410 nm) and at 80% for CsI(Tl) (560 nm). This explains why NaI(Tl) and CsI(Tl) crystals are best suited for PMTs and semiconductor devices respectively.
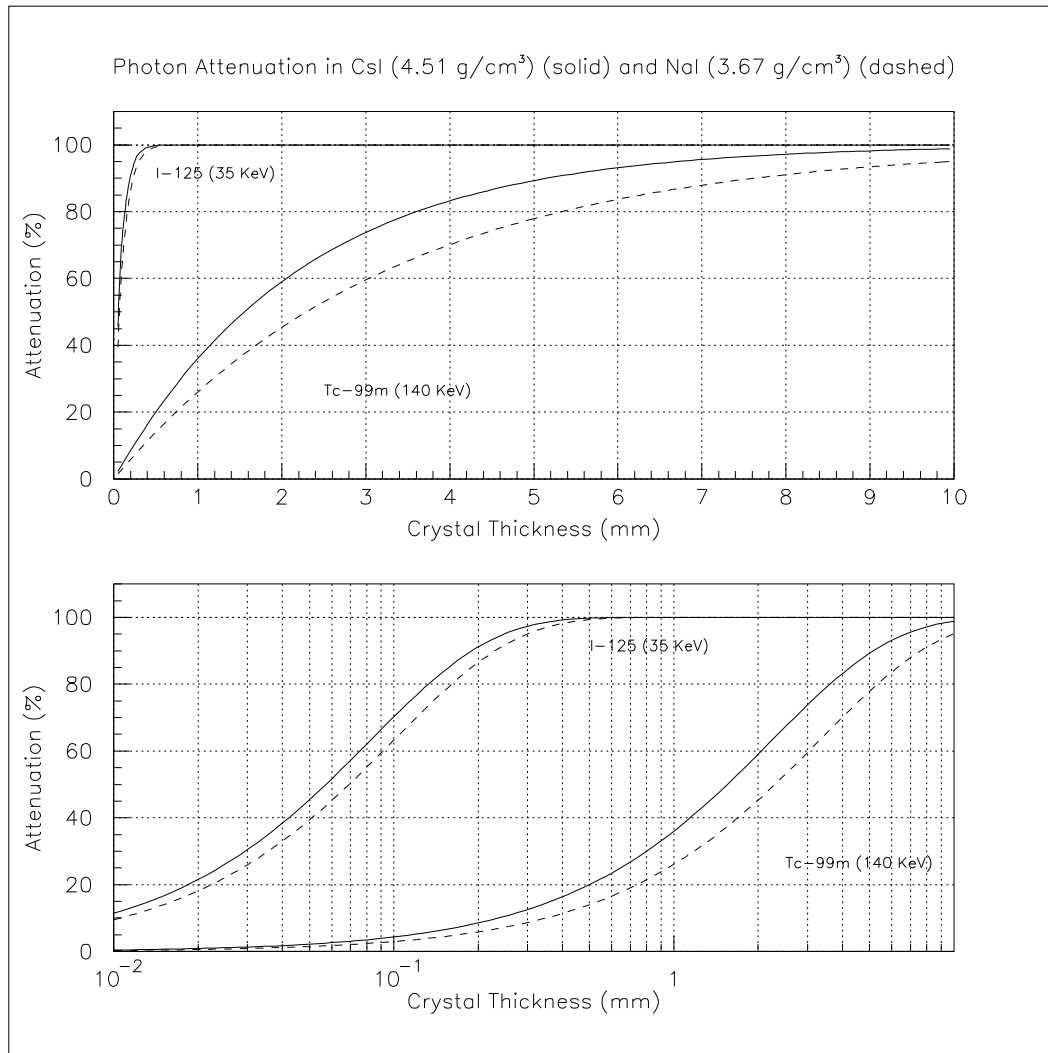
Figure 2.3: A plot of percent attenuation (photoelectric absorption and incoherent scattering) versus crystal thickness for both 35 keV and 140 keV gamma rays in CsI(Tl) and NaI(Tl). Shown in both linear (top) and log (bottom) scale.

27
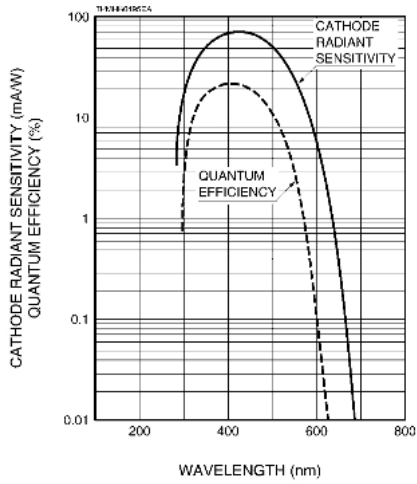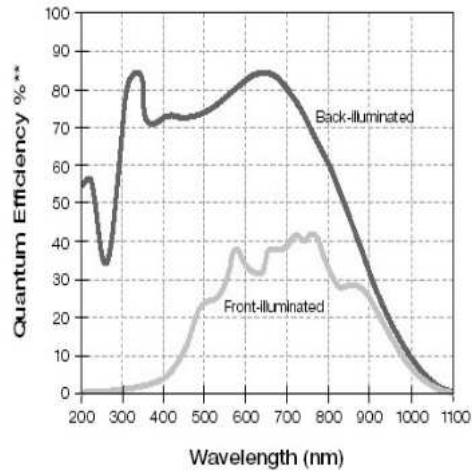
(a)   (b)

Figure 2.4: A figure showing the quantum efficiencies for a Hamamatsu R2486 PSPMT (a) and a SITe SI-032AB back-illuminated CCD (b). Figures courtesy of Hamamatsu and SITe.

2.2.2 The Photomultiplier Tube

A schematic of a photomultiplier tube (PMT) is shown in Figure 2.5. When an optical photon strikes the photocathode it has a certain probability, given by the quantum efficiency (QE), of being absorbed and causing a photoelectron to be ejected. The electric field inside the evacuated chamber of the PMT then guides the photoelectron towards the dynode chain. When the photoelectron strikes the first dynode it knocks off several more electrons which are then accelerated to the next dynode under an electric potential. When these electrons then strike the next dynode, even more electrons are ejected. By repeating this process several times, the dynode chain is able to amplify the original photoelectron signal on the order of 10^6 times before the signal reaches the anode. This gain is able to boost the initial electric signal well above the electronic noise of the PMT, enabling the counting of individual events. The amount of charge contained within the electric pulse output of the PMT is proportional to the energy of the initial gamma ray. By sending the PMT output signal to a multi-channel analyzer (MCA), a histogram of the different pulse sizes can be made. This histogram then represents the energy spectrum of the radioactive isotope being observed.

A PSPMT works in a similar manner to a PMT, but instead of having a single anode, a PSPMT has multiple anode wires (see Figure 2.6). For example, the Hamamatsu R2486 PSPMT has 16 X and 16 Y wires aligned orthogonal to each other. As the initial photoelectron enters the dynode region, it is amplified and emerges as a shower of electrons. This shower has a spatial distribution such that each anode wire collects a different amount of charge. The amount of charge collected by each wire can be digitized and used to create a pair of wire profiles (X and Y) for a single event. Each profile is then fitted with a Gaussian distribution
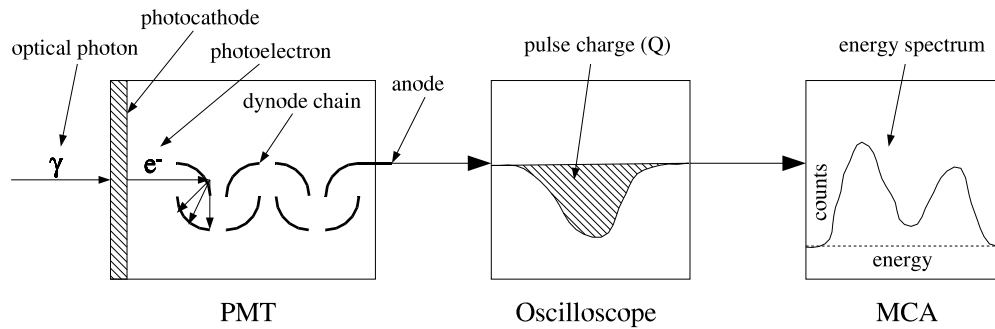
Figure 2.5: A schematic of a PMT. The pulse charge from the PMT is proportional to the initial gamma ray energy and can be used to create an energy spectrum of the source.

to find the mean X and Y values. The X and Y values correspond to the two-dimensional position of the incident gamma ray interaction within the scintillation crystal, while the total charge collected is proportional to the gamma ray energy.

Positive aspects of PMT photodetectors include a high signal gain ($\approx 10^6$) and ability to rapidly count single gamma ray events and thus acquire an energy spectrum. Also, they do not require cooling, and the crystal can be directly coupled to the photocathode surface of the PMT which increases optical coupling efficiency. Negative aspects include a low QE ($< 20\%$), fragility, and a large volume requiring extensive shielding. Also, they are only compatible with NaI(Tl) crystals, and have a low intrinsic spatial resolution (≥ 1.5 mm).
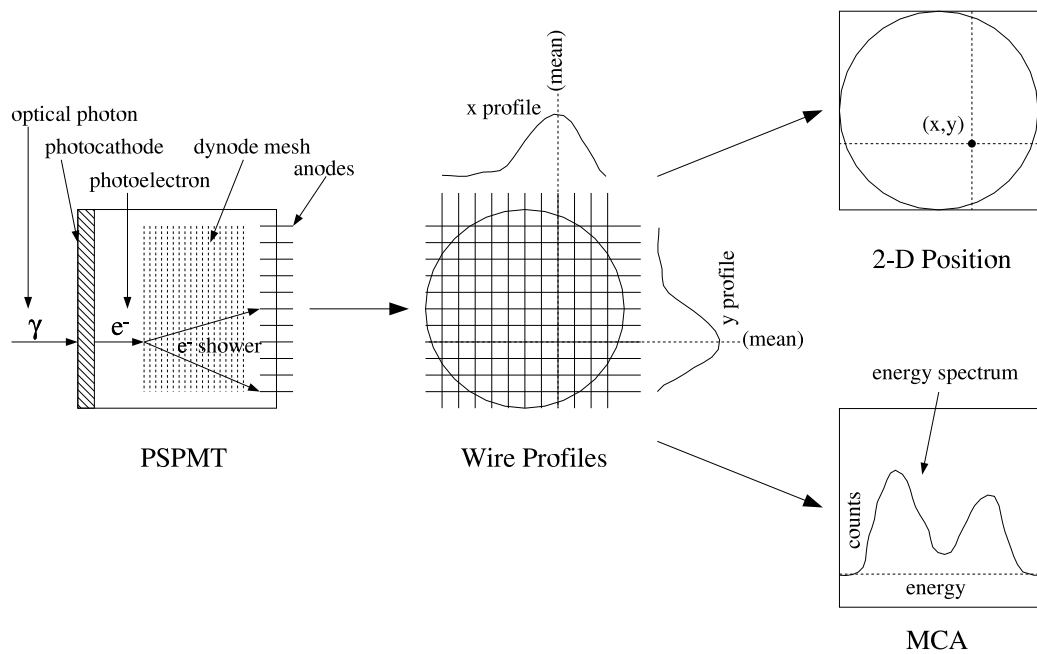
Figure 2.6: A schematic of a PSPMT, which uses multiple anode wires to measure both the interaction position and energy of the initial gamma ray.

2.2.3 The Charge Coupled Device

History and Description

The charge coupled device (CCD) was invented by Willard Boyle and George Smith at Bell Labs in 1970 [54, 55]. It was originally intended as a semiconductor memory device but soon found use in the first solid state camera. A CCD is made from a two-dimensional array of metal-oxide-silicon (MOS) capacitors with each capacitor representing a pixel on the output image. A schematic of a CCD is shown in Figure 2.7. When an optical photon strikes the surface of the CCD it has a certain probability of creating an electron-hole pair in the semiconductor layer of a MOS capacitor. In this way, each MOS capacitor acts as a sensor that converts the incoming optical photon into a photoelectron. The photoelectrons are then stored in the charge wells of the individual MOS capacitors. Once data acquisition has ended, the charge packets from the array of MOS capacitors are then parallel transferred one row at a time to the shift register. The shift register has a parallel input and a serial output. Once loaded, the shift register then serially moves the charge packets to a charge-to-voltage amplifier. An analog-to-digital converter (ADC) then converts this voltage to a digital value that is proportional to the amount of light incident on the pixel during exposure.

Noise Characteristics

The two main sources of electronic noise when measuring low light levels with a CCD are dark current noise and readout noise. Dark current is a result of spontaneous thermal electron generation within the silicon lattice of the CCD and is measured in electrons per pixel (e/p). These electrons are captured by the pixel potential wells and contribute to the non-photon related signal noise. The dark current accumula-
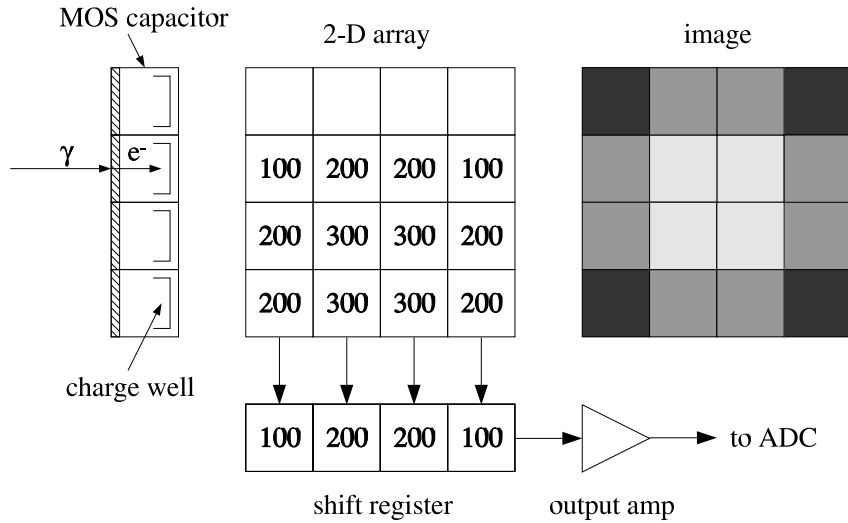
Figure 2.7: A schematic of a CCD. The number of photoelectrons collected in each charge well is transferred to the shift register then output amplifier. This information is then used to construct a light intensity image.

tion rate is expressed as electrons per pixel per second (e/p/s). Since dark current accumulation follows Poisson statistics, the root mean square (RMS) dark current noise (N_{DC}) is given by the square root of the dark current for a given exposure time:

$$N_{DC} = \sqrt{Dark\ Current} \tag{2.2}$$

The dark current accumulation rate, and thus the dark current noise, can be significantly reduced by cooling the CCD [56]. For example, the SITe SI-032AB CCD has a typical dark current specification of 360 e/p/s at 293 K (20 °C) and only 2 e/p/s at 243 K (-30 °C). Since cooling the CCD reduces the dark current noise to negligible levels, the true limiting factor for the sensitivity of a CCD is the readout noise

33

(N_R). The readout noise, expressed as electrons/pixel (e/p), arises from the charge-to-voltage output amplifier and is independent of temperature and proportional to the readout rate. For example, the SITe SI-032AB CCD has a typical readout noise of 7 e/p. Some CCDs have a readout noise as low as 2 e/p (Roper Scientific), but this is only for slow readout speeds and thus low frame rates. The total noise for a CCD is then given by:

$$N_T = \sqrt{N_R{}^2 + N_{DC}{}^2} \tag{2.3}$$

Plots showing the relation of N_T, N_R, and N_{DC} are given in Figure 2.8 for two different temperatures. These plots use the data from the SITe SI-032AB CCD. It can be seen that at high temperatures (Figure 2.8(a)) the dark current noise quickly becomes the dominant term in the total noise equation, while at lower temperatures (Figure 2.8(b)) the readout noise is the dominant term for exposure times less than 5 seconds. If a signal-to-noise ratio of 2 were required to measure a signal from the CCD, this would require over 30 e/p for a 10 second exposure at 243 K. It is this "noise floor" caused by the read noise which severely limits the low light level sensitivity of a CCD, where the signal might result in only a few electrons per pixel.

The Electron-Multiplying CCD

The sensitivity of a gamma camera system can be further improved by using an EMCCD to detect the optical photons emerging from the scintillation crystal. EMCCDs have higher quantum efficiencies (up to 95% with back-illumination) and broader spectral responses (400 to 900 nm) when compared to PMTs. Also, intrinsic resolutions less than 100 μm have been shown for EMCCD based gamma cameras [46, 47]. The most important characteristic of an EMCCD is the improved

low light level signal-to-noise ratio (SNR) when compared to conventional CCDs. This is achieved by the addition of a second serial register, known as the gain or multiplication register, to the CCD architecture as shown in Figure 2.9. Electrons are first captured within the pixel potential wells of the image area, then the entire frame (for example 680×500 pixels) is parallel-transferred to the storage area. A single pixel row is then parallel-transferred from the storage area to the serial register. The pixel row in the serial register is then serial-transferred through the multiplication register to the charge-to-voltage output amplifier of the EMCCD. This is done for each row until the entire storage area has been read. The multiplication register differs from the normal serial register by the addition of a third gate known as the charge multiplication gate (CMG) [57]. By making the voltage of the CMG very high (up to 15 Volts DC) the electrons undergo impact ionization as they move through the multiplication register, which amplifies the electric signal. Although the gain per pixel step is very low (1.01 to 1.018) a multiplication register of 400 pixels in length can allow gains of over 1000× to be reached [58]. Multiplication of the signal in the charge domain before charge-to-voltage conversion effectively reduces the readout noise of the output amplifier to less than 1 electron/pixel. This eliminates the noise floor found in conventional CCDs making EMCCDs sensitive to single electrons.

The total signal noise of an EMCCD is given by:

$$\sigma_t = \sqrt{G^2 F^2 (P + D + S) + \sigma_r^2} \tag{2.4}$$

where G is the gain, F is the excess noise (Fano) factor due to the gain process in the multiplication register, and P, D, S, and σ_r are the mean signals (electron/pixel) due to the photon (shot), dark current, spurious charge, and read noises respectively [58,

35

59]. The dark current noise (D) and the spurious charge noise (S) can be reduced to negligible levels with cooling and proper clocking respectively [60]. Also, for a gain greater than $\approx 10\times$, F approaches $\sqrt{2}$ [61]. Under these conditions the SNR for a EMCCD reduces to:

$$SNR_{EMCCD} = \frac{GP}{\sigma_t} = \sqrt{\frac{P}{2}} \tag{2.5}$$

when $G \gg \sigma_r$. This can be compared to the SNR of a conventional CCD under similar condition given by:

$$SNR_{CCD} = \frac{P}{\sqrt{P + \sigma_r^2}} \tag{2.6}$$

A plot of SNR_{EMCCD} and SNR_{CCD} versus P is shown in Figure 2.10 for a typical read noise ($\sigma_r = 25$ electrons/pixel). It can be seen that while the CCD has a SNR of 1 at 25 electrons/pixel, the EMCCD has a SNR that is 3.5 times higher.

Characteristics Summary

Positive aspects of CCD and EMCCD photodetectors include a high quantum efficiency ($> 80\%$) with back-illumination, a high intrinsic spatial resolution ($< 200~\mu$m), and a small form factor compared to PMTs. Negative aspects are that they must be cooled (-30 °C to -90 °C) to reduce thermal noise, they have no or low gain ($< 10^3$), and they can not be placed directly on the surface of the crystal to maximize optical coupling. Also, in integration mode they are unable to exclude scattered and background events in order to improve the SPECT reconstruction.
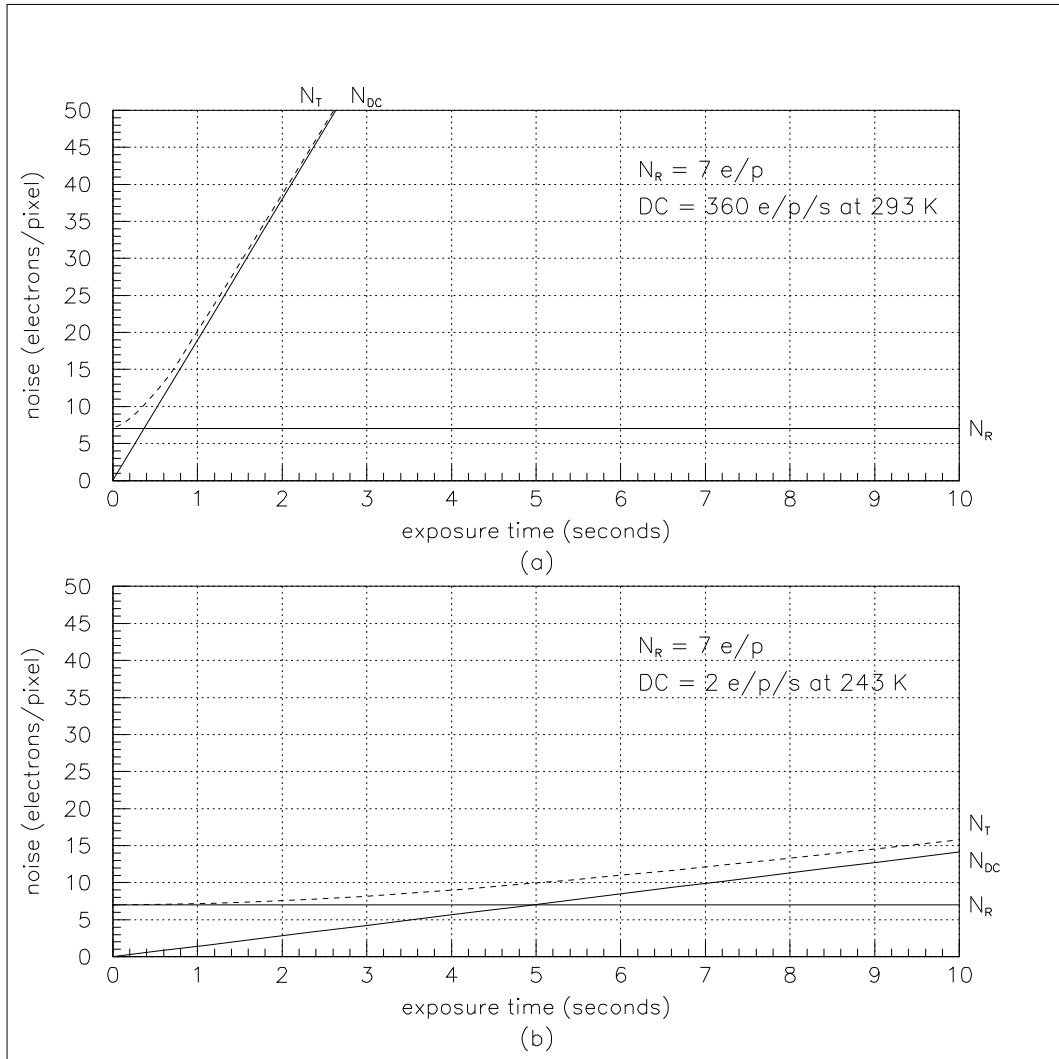
Figure 2.8: Plots showing the relationship between N_T, N_R, and N_{DC} for the SITe SI-032AB CCD. Data are shown for a CCD temperature of 293 K (a) and 243 K (b).

680 pixels

image area

500 pixels

storage area

serial register

multiplication register

400 pixels
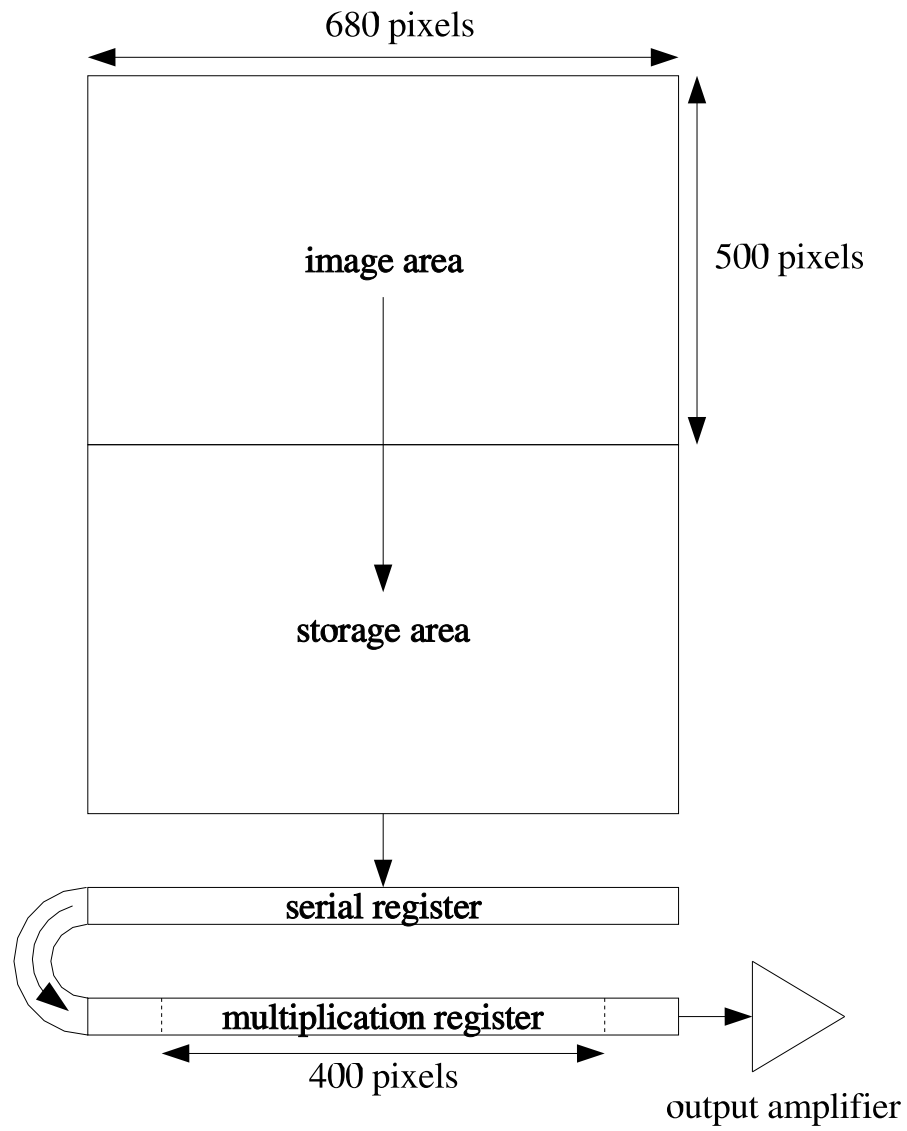
output amplifier

Figure 2.9: A schematic showing the architecture of an EMCCD. The electrons are multiplied by impact ionization as they move through the multiplication register before charge-to-voltage conversion in the output amplifier.
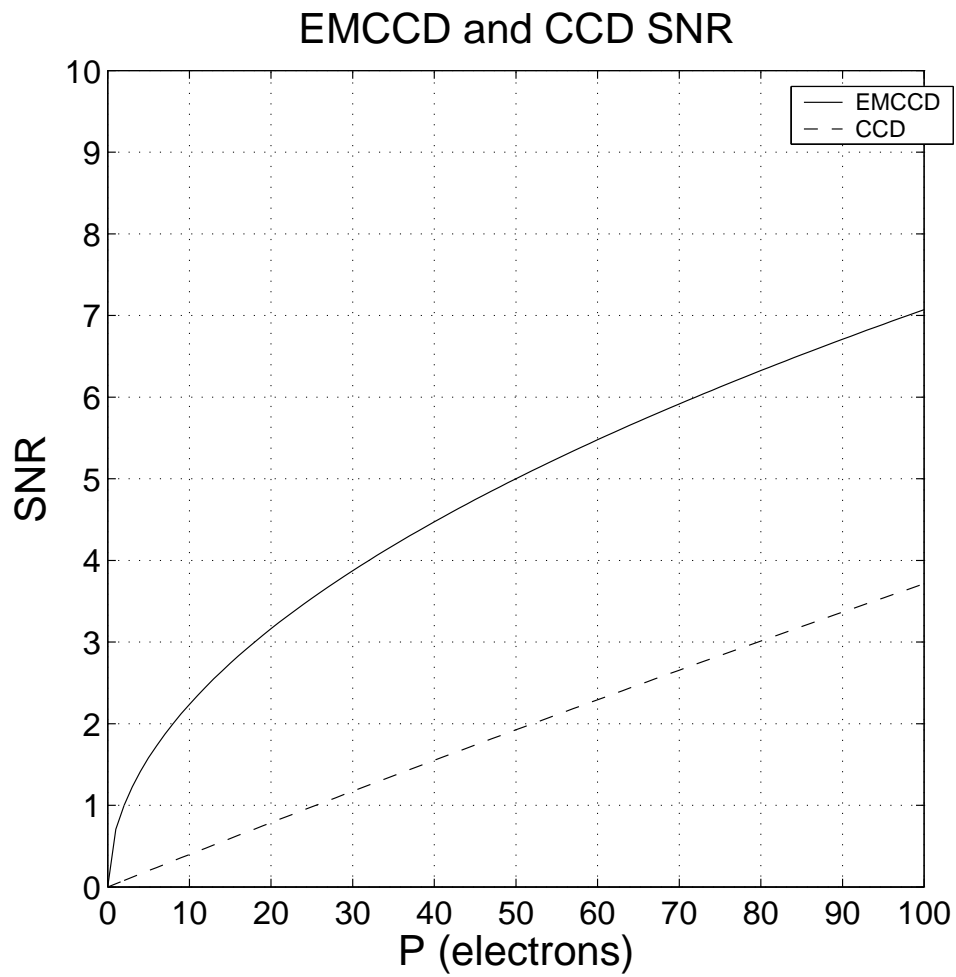
Figure 2.10: A plot showing the EMCCD and CCD SNR as a function of electrons/pixel. The EMCCD SNR is much higher for low light level imaging.

2.3 Imaging with Pinhole Collimation

"Pinhole collimators provide the best combination of sensitivity and resolution for small subjects that are positioned a short distance from the aperture."

Hal O. Anger, Instrumentation in Nuclear Medicine (1967)

As seen in the above quote, the advantages of using pinhole collimators to image small source objects that are placed close to the aperture have been known for some 40 years [62]. The use of pinhole collimators in clinical settings has declined in favor of parallel-hole collimators that offer adequate resolution and sensitivity over a much larger field of view. Recently, pinhole collimators have experienced a resurgence in preclinical applications as a means of obtaining high resolutions over small field of views not possible with parallel-hole collimators. In this section the equations governing pinhole collimator resolution and sensitivity are derived. Also, an example of using multiple pinhole imaging to improve sensitivity is shown.

2.3.1 Pinhole Resolution

Geometric Resolution

The geometric resolution (R_g) represents the closest distance two point sources can be from each other (in the source plane) and still be resolved by the pinhole. A schematic showing the calculation of R_g is given in Figure 2.11, where b is the distance from the point source plane to the pinhole plane, a is the distance from the pinhole plane to the crystal (or detector) plane, and d_e is the effective diameter of the pinhole aperture. Due to the ability of gamma rays from the source to penetrate the pinhole edges where it is thinner (see Figure 2.12), the effective diameter of the

pinhole is slightly larger than the true diameter and is given by [62]:

$$d_e = \sqrt{d\left(d + \frac{2}{\mu}\tan\left(\frac{\alpha}{2}\right)\right)} \tag{2.7}$$

Where μ is the total linear attenuation coefficient of the pinhole material for the given gamma ray energy, and α is the aperture angle of the pinhole.
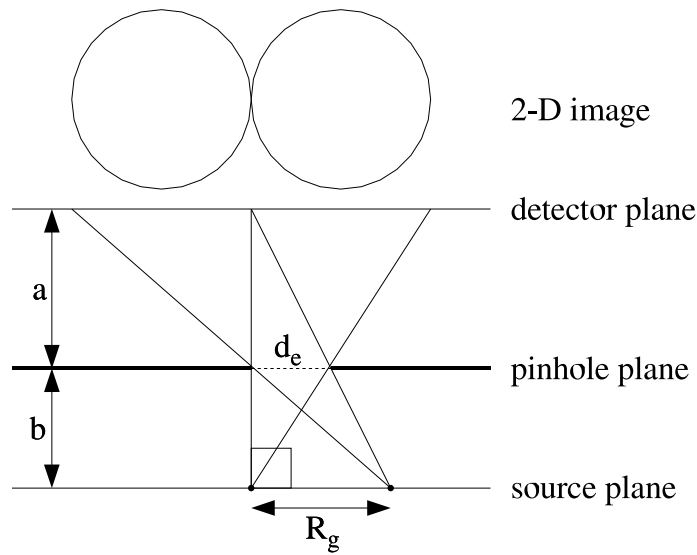
Figure 2.11: A schematic showing the calculation of R_g. Each point source projects a circular image onto the detector plane.

R_g can be calculated by placing one point source such that it is coincident with one edge of d_e, and the other point source such that their circular projections onto the detector plane are tangent. Using the geometric principle of similar triangles gives:

$$R_g = d_e\left(1 + \frac{b}{a}\right) \tag{2.8}$$
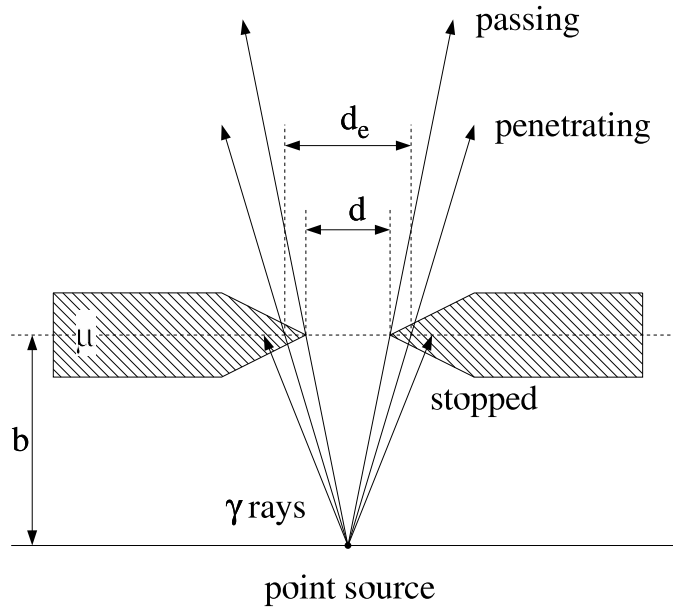
Figure 2.12: A schematic showing how gamma ray penetration at the thinner parts of a "knife edge" pinhole aperture increases d to d_e.

For $a \gg b$, it can be seen that R_g approaches d_e (Figure 2.13(a)), when $a = b$, R_g is twice as large as d_e (Figure 2.13(b)), and for $a \ll b$, R_g is much greater than d_e (Figure 2.13(c)).

Total Resolution

The overall resolution (R_t) is the quadrature addition of the geometric resolution (R_g) and the effective detector resolution $(\frac{b}{a}R_i)$ and is given by:

$$R_t = \sqrt{R_g^2 + \left(\frac{b}{a}R_i\right)^2} = \sqrt{\left(d_e\left(1 + \frac{b}{a}\right)\right)^2 + \left(\frac{b}{a}R_i\right)^2} \qquad (2.9)$$

Where R_i is the intrinsic resolution of the detector. The effective intrinsic resolution
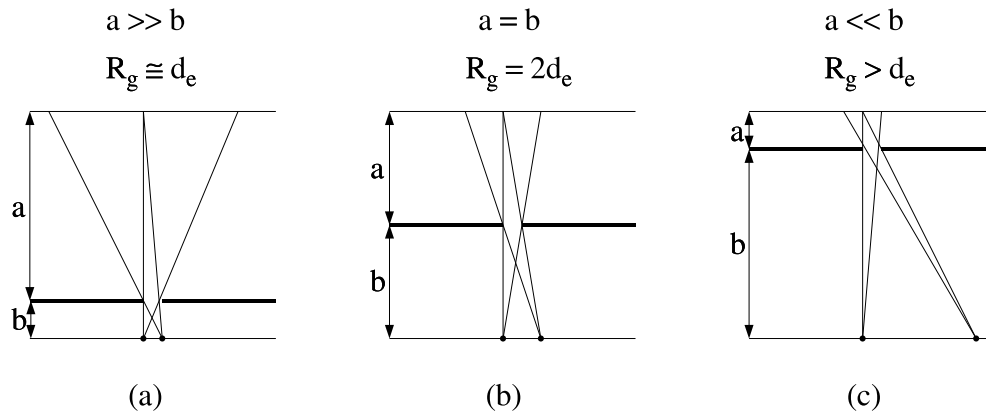
Figure 2.13: A schematic showing how R_g increases as $\frac{b}{a}$ increases.

$(\frac{b}{a}R_i)$ arises from magnification of the source object image onto the detector plane, as illustrated in Figure 2.14. Using the geometric principle of similar triangles shows how the effective intrinsic resolution can be much smaller than the intrinsic resolution if magnification of the source image $(a > b)$ is applied.

Resolution Plots

The relationship between R_t, R_g, and $\frac{b}{a}R_i$ versus $\frac{b}{a}$ is plotted in Figure 2.15. In this figure $d_e = 1.0$ mm and $R_i = 5$ mm, which correspond to the typical pinhole size used in small animal imaging and the typical intrinsic resolution of a clinical SPECT gamma camera respectively. For these conditions, it can be seen that $\frac{b}{a}R_i$ quickly becomes the limiting term for the total resolution as $\frac{b}{a}$ increases. In order to achieve an overall resolution of 1.5 mm, a magnification of 5x $(\frac{b}{a} = 0.2)$ must be used, leading to large detector surface areas and volumes. This explains why small animal SPECT systems that use existing clinical SPECT detectors, or other

43

object   pinhole   detector

R_i

$(b/a)R_i$

b   a
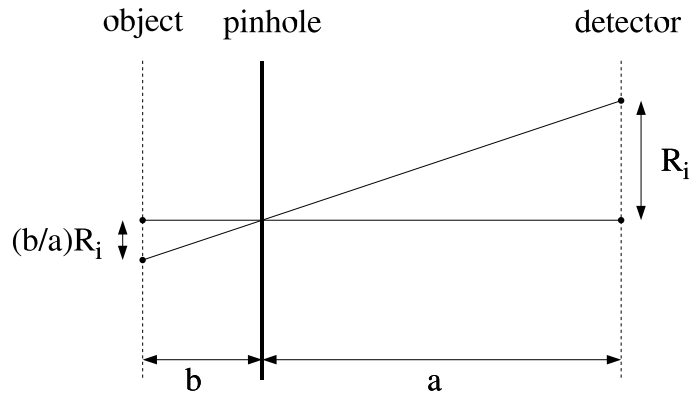
Figure 2.14: A schematic showing how $\frac{b}{a}R_i$ is less than R_i when image magnification $(a > b)$ is used.

detectors which have a low intrinsic resolution like PSPMTs, must rely on high magnification factors in order to approach spatial resolutions of 1 mm.

In Figure 2.16 d_e is again 1.0 mm but R_i has been reduced by an order of magnitude to 0.5 mm. It can be seen that R_g is now the limiting term for R_t and that a magnification of only 2x ($\frac{b}{a} = 0.5$) is needed to achieve a total resolution of 1.5 mm.

With a very low intrinsic resolution as in Figure 2.16, the total resolution of the system can be further improved by reducing d_e. In Figure 2.17 both d_e and R_i are now 0.5 mm. It can be seen that R_g is still the limiting term for the total resolution, but now a magnification of 2x ($\frac{b}{a} = 0.5$) gives a total resolution of < 1 mm. The overall resolution can be improved even further by making d_e smaller, but this would severely reduce the sensitivity (counts per second/source activity) of the system as described in the next section.

44
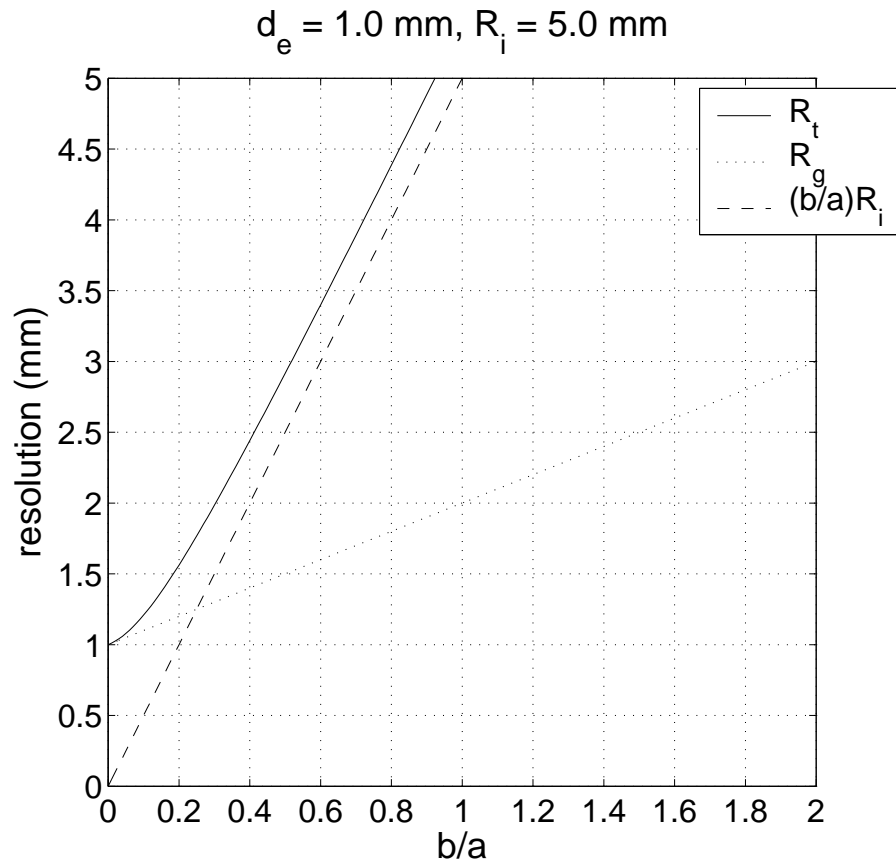
Figure 2.15: A plot showing the relation between R_t, R_g, and $\frac{b}{a}R_i$ for $d_e = 1.0$ mm and $R_i = 5.0$ mm.
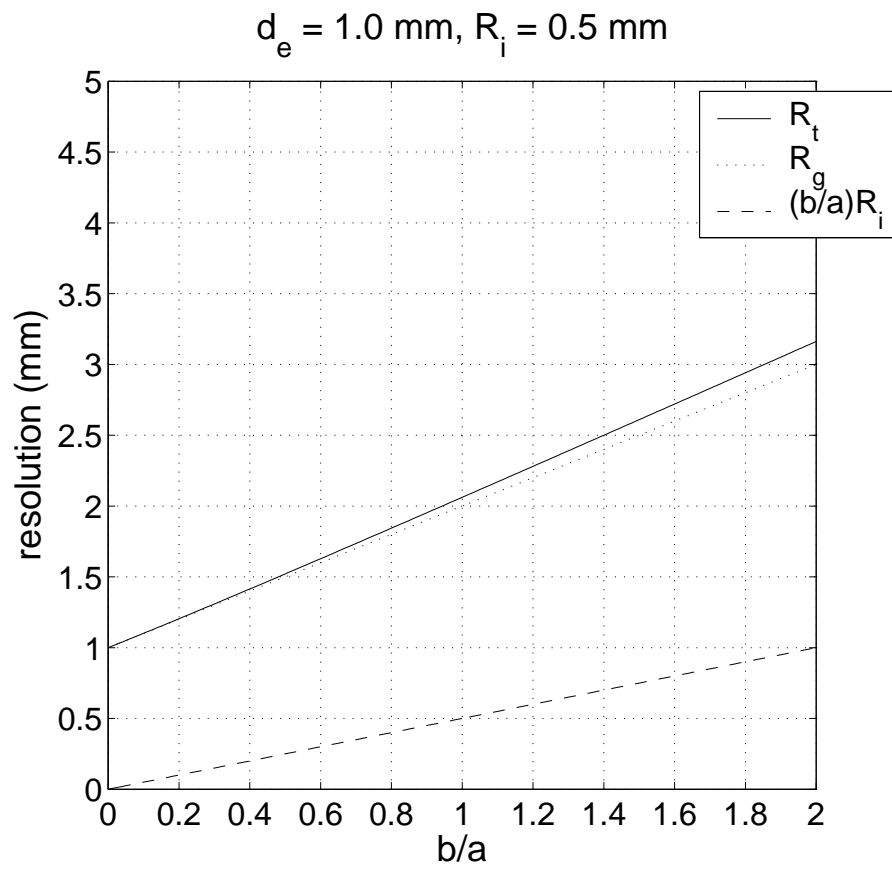
Figure 2.16: A plot showing the relation between R_t, R_g, and $\frac{b}{a}R_i$ for $d_e = 1.0$ mm and $R_i = 0.5$ mm.
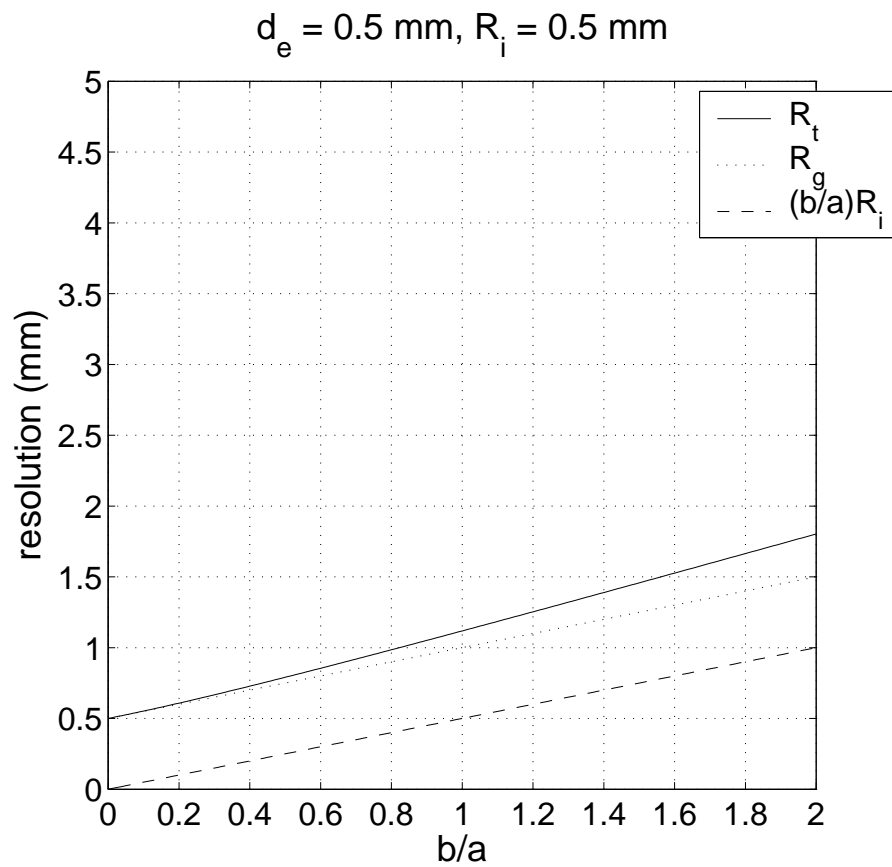
Figure 2.17: A plot showing the relation between R_t, R_g, and $\frac{b}{a}R_i$ for $d_e = 0.5$ mm and $R_i = 0.5$ mm.

2.3.2 Pinhole Sensitivity

On-Axis Geometric Efficiency

The on-axis geometric efficiency (g) of a pinhole collimator is defined as the ratio of the number of gamma rays that pass through the pinhole over the total number of gamma rays emitted from a isotropic point source. This is illustrated in Figure 2.18 where b is the distance from the point source to the pinhole and d_e is the effective diameter of the pinhole. For an isotropic point source, g is given by the ratio of the spherical cap area subtended by d_e over the total spherical area defined by the radius b. For $b \gg d_e$ the spherical cap area can be approximated by the pinhole area so that g is given by:

$$g = \frac{spherical\ cap\ area}{total\ spherical\ area} \approx \frac{\pi \left(\frac{d_e}{2}\right)^2}{4\pi b^2} = \frac{d_e{}^2}{16b^2} \tag{2.10}$$

which is the expression for g most found in the literature [30, 40, 62].

From Equation 2.10 it can be seen that for a d_e of 1.0 mm and a b of 10 mm, g is only 0.0625%. This means that 99.9% of the gamma rays emitted by the isotropic point source are not being observed. The geometric efficiency can be increased by moving the point source closer to the pinhole, with the maximum value of 50% when the source is in the plane of the pinhole ($b = 0$).

It should be noted that as b goes to zero, the expression for g given by Equation 2.10 goes to infinity. This is because the spherical cap area has been approximated by the pinhole area. The formula for the spherical cap area is given by:

$$A_{spherical\ cap} = 2\pi Rh \tag{2.11}$$
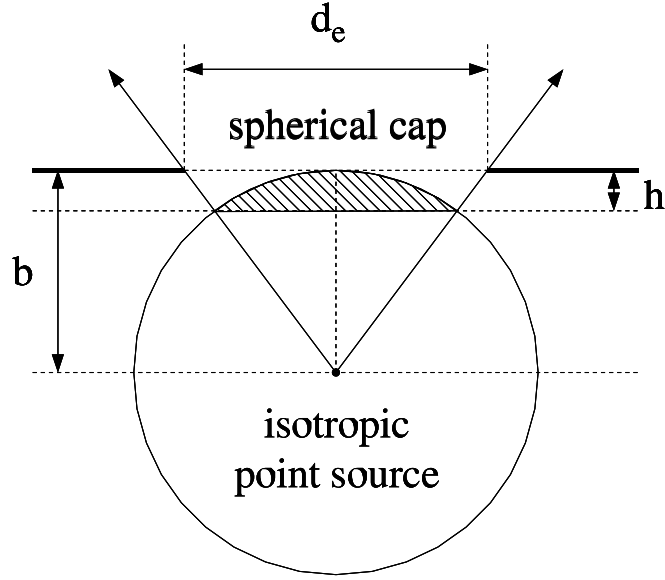
Figure 2.18: A schematic showing the calculation of the on-axis geometric efficiency (g). The hatched area represents the spherical cap.

where R is the radius of the sphere and h is the height of the spherical cap as shown in Figure 2.18. Using $R = b$, the true expression for g becomes:

$$g_{true} = \frac{2\pi bh}{4\pi b^2} = \frac{h}{2b} \tag{2.12}$$

Solving for h gives (see Appendix A):

$$g_{true} = \frac{1}{2}\left(1 - \frac{1}{\sqrt{1 + \left(\frac{d_e}{2b}\right)^2}}\right) \tag{2.13}$$

For $b \gg d_e$ the square root term in Equation 2.13 can be binomially expanded to give the approximate expression in Equation 2.10. A plot of g_{approx} and g_{true} versus

b is shown in Figure 2.19 for $d_e = 1.0$ mm. It can be seen that as b goes to zero, g_{approx} goes to infinity while g_{true} goes to 50% as it should. It can also be seen that g_{approx} and g_{true} do not truly diverge until $b \approx d_e$, which justifies the use of Equation 2.10 when $b \gg d_e$.
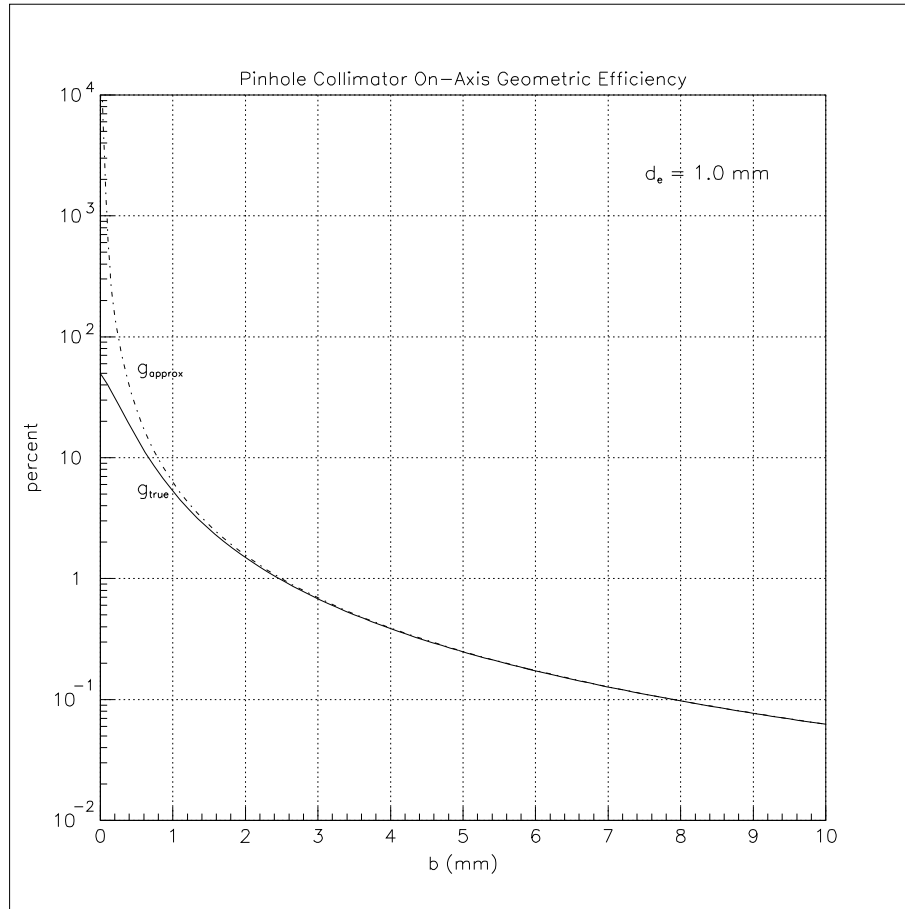
Figure 2.19: A plot of g_{approx} (dashed) and g_{true} (solid) versus b for $d_e = 1.0$ mm.

Figure 2.20 plots g_{true} versus b for two different values of d_e (1.0 and 0.5 mm). It can be seen that for $b = 8$ mm, the geometric resolution is reduced by almost an order of magnitude when going from $d_e = 1.0$ to 0.5 mm (0.1% to 0.02% respectively).

50

This explains why improving the spatial resolution by reducing the size of d_e would severely limit the sensitivity.
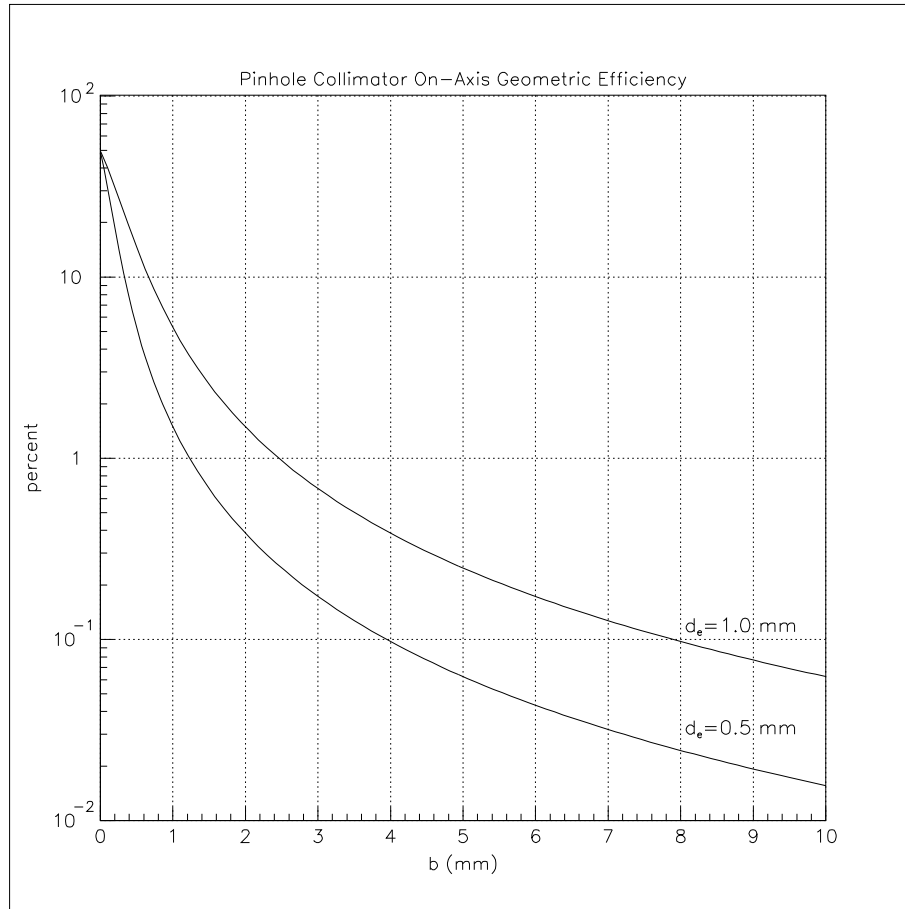
Figure 2.20: A plot of g_{true} versus b for $d_e = 1.0$ and 0.5 mm.

Off-Axis Geometric Efficiency

When the point source is not coincident with the center axis of the pinhole, the geometric efficiency given by Equation 2.10 is even further reduced. This is because as the point source moves off-axis, the pinhole no longer looks like a circle, but instead looks like an ellipse from the point of view of the point source. This effectively reduces the pinhole area, which reduces the number of gamma rays that pass through. Figure 2.21 shows a schematic for the calculation of the off-axis geometric efficiency, where b is the distance from the point source plane to the pinhole plane, d_e is the effective diameter of the pinhole, θ is the angle from the point source to the center of the pinhole, and r is the distance from the point source to the center of the pinhole. The area of the spherical cap (of radius r) subtended by d_e can be approximated using the area of the pinhole as viewed from the point source. The off-axis area of the pinhole is the area of an ellipse with the major axis given by $\frac{d_e}{2}$ and the minor axis given by $\frac{d_e}{2}\sin\theta$:

$$A_{ellipse} = \pi(major\ axis)(minor\ axis) = \pi\left(\frac{d_e}{2}\right)^2 \sin\theta \tag{2.14}$$

The off axis geometric efficiency then becomes:

$$g = \frac{spherical\ cap\ area}{total\ spherical\ area} \approx \frac{\pi\left(\frac{d_e}{2}\right)^2 \sin\theta}{4\pi\left(\frac{b}{\sin\theta}\right)^2} \tag{2.15}$$

which reduces to:

$$g = \frac{d_e^2}{16b^2}\sin^3\theta \tag{2.16}$$

where the first term in Equation 2.16 is the on-axis geometric efficiency given in

Equation 2.10 and the second term is the off-axis reduction. It can be seen that the off-axis g reduces to the on-axis g when $\theta = 90°$.
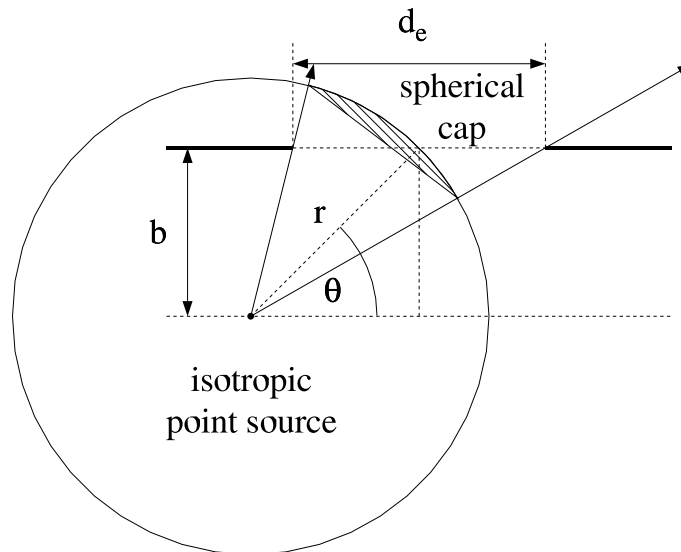
Figure 2.21: A schematic showing the calculation of the off-axis geometric efficiency.

A plot of off-axis g versus θ is shown in Figure 2.22 where the ordinate is expressed as the percent of the on-axis value (maximum at $\theta = 90°$). It can be seen that at $\theta = 45°$, the off-axis g reduces to $< 40\%$ of its on-axis value. The on-axis and off-axis geometric efficiencies explain why pinhole collimators are best suited for objects that are close to the pinhole (to maximize the on-axis g) with a small field of view (to minimize the off-axis reduction in g).
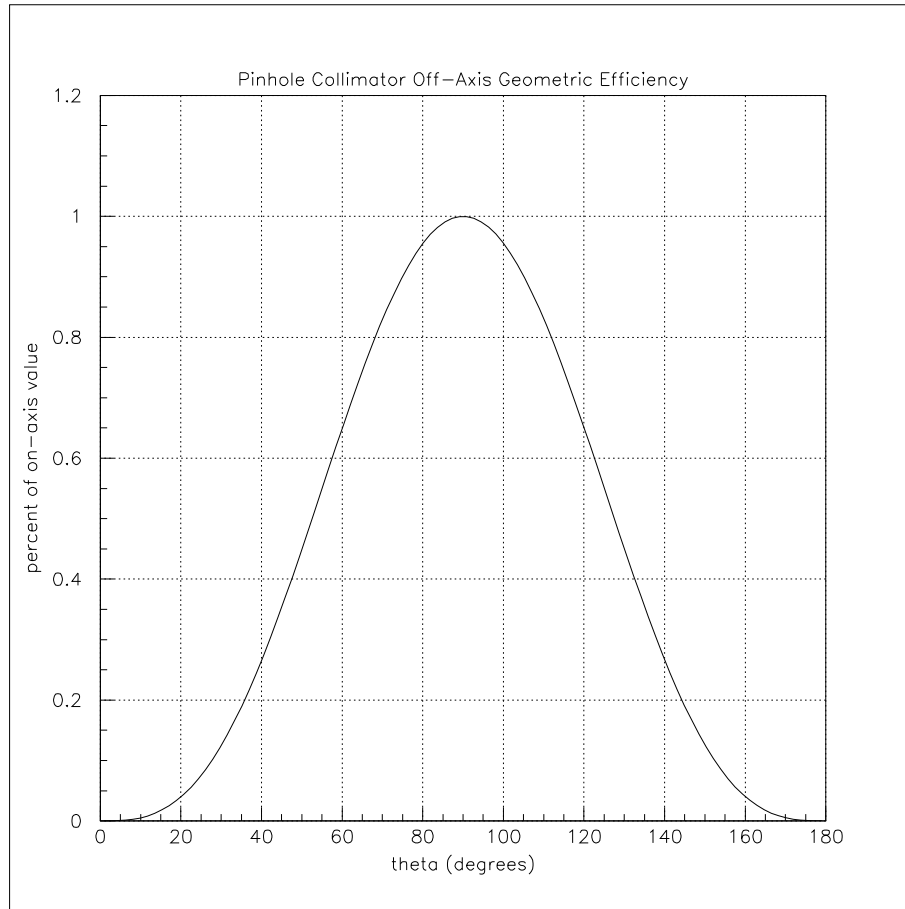
Figure 2.22: A plot of off-axis g versus θ. The ordinate is expressed as the percent of the on-axis value ($\theta = 90°$).

System Sensitivity

The overall sensitivity of a radiation measuring system is defined as the number of counts measured per second per source activity and is expressed as cps/μCi or cps/MBq (100 μCi = 3.7 MBq). The geometric efficiency can be used to calculate the expected number of counts measured per second for a given source activity, pinhole geometry, scintillating crystal, and photodetector. An example is shown in Figure 2.23. For this setup, $b = 10$ mm, $d_e = 1$ mm, and the crystal thickness is 2 mm (not drawn to scale).
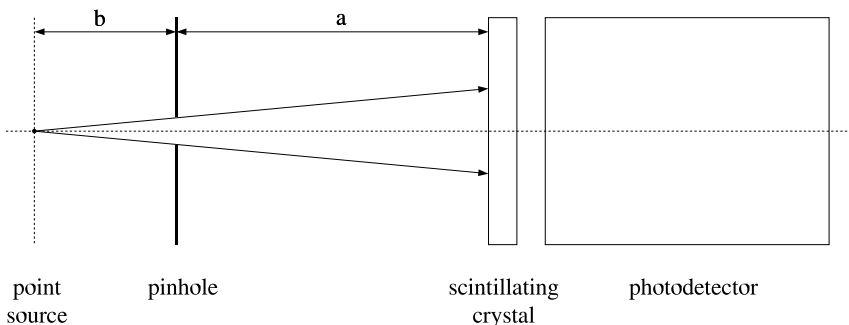
Figure 2.23: A schematic of the setup used to calculate the sensitivity of a SPECT system.

Calculating the counts measured per second can be divided into two tasks: 1) finding the number of gamma rays striking the crystal per second, and 2) finding the fraction of these gamma rays that are measured by the detector. Here the detector is defined and the scintillating crystal and photodetector combined.

The number of gamma rays striking the crystal per second can be found as follows. The intensity fraction for a 140 keV gamma ray emitted by ^{99m}Tc is 89%. This means that out of 100 decays, 89 of them will (on average) produce a 140 keV gamma ray. Therefore a 1 Ci (37 GBq) point source of ^{99m}Tc, which is undergoing

3.7x10^{10} disintegrations per second, will isotropically emit 3.3x10^{10} 140 kev gamma rays per second. Multiplying this number by the geometric efficiency for the setup ($g = 0.0625$ %) gives 2.1x10^7 140 keV gamma rays per second passing through the pinhole and striking the crystal.

The percent of these gamma rays measured by the detector depends on the crystal type and thickness and the type of photodetector used as discussed previously. The absorption factor for 140 keV gamma rays passing through a 2 mm thick CsI(Tl) crystal is 56.2%. Therefore, 1.2x10^7 gamma rays per second will interact within the crystal. Therefore, the maximum sensitivity for 140 keV gamma rays emitted by a 1 Ci point source of ^{99m}Tc would be 1.2x10^7 cps/Ci or 12 cps/μCi (324 cps/MBq). This assumes the photodetector is able to measure 100% of the interactions within the crystal. This efficiency depends on the type of photodetector used and how it is coupled to the crystal as described previously. The low sensitivity when using pinhole collimation stresses the need for improvement by multiplexing several pinholes onto a single collimator as discussed in the next section.

2.3.3 Multiple Pinhole Collimator Requirements

The preceding sections showed that spatial resolutions approaching 1 mm can be achieved with a CCD based photodetector ($R_i = 0.5$ mm) using a pinhole collimator ($d_e = 0.5$ mm) and a $\frac{b}{a}$ ratio of 1 (see Figure 2.17). This high resolution comes at a cost of lowered sensitivity. Assuming that the coupling between the scintillating crystal and photodetector has been maximized, the sensitivity of the SPECT system can be increased further by using multiple pinholes to image the source object. This can be accomplished by simply multiplexing several pinholes onto a single detector collimator. The total number of pinholes used, their geometric parameters, how they will image the source object, and what the projected images will look like on the scintillating crystal surface are discussed in this section.

Calculating the multiple pinhole parameters begins with the size of the source object to be imaged. For ease of scalability, arbitrary units will be used with the source object being a sphere of unit radius ($r = 1$). Two assumed design requirements are 1) the distance from the pinhole plane to the crystal plane (a) must be chosen such that there is no overlap of the multiple pinhole images on the crystal surface, and 2) the pinhole aperture angle (α) must subtend the entire volume of the source object. A schematic of this setup for a single pinhole is shown in Figure 2.24. Given that r is unity, the distance from the center of the source object to the center of the pinhole (b) is given by:

$$b = \frac{r}{\sin\left(\frac{\alpha}{2}\right)} \tag{2.17}$$

For example, a pinhole aperture angle of 60° gives a b of two units as shown in Figure 2.24.

Using a $\frac{b}{a}$ ratio of 1, two additional pinholes (one above and one below the
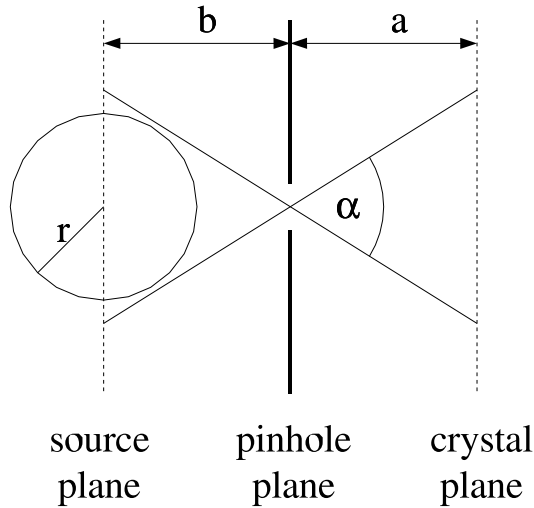
Figure 2.24: A schematic a single pinhole collimator setup. The source object volume is subtended by the pinhole aperture angle α. For $\alpha = 60°$, $b = 2r$.

central pinhole) can then be included such that their images do not overlap on the crystal surface with the existing central pinhole image, and that their aperture angle subtends the source volume as shown in Figure 2.25.

It can be seen that the new pinhole axes must be tilted by angle θ. Also, the aperture angle for the new pinholes is less than the aperture angle for the central pinhole ($\alpha' < \alpha$) since the distance from the center of the field of view area to the center of the new pinholes is larger ($b' > b$). It can also be seen that the angled pinholes have a slightly larger image area on the crystal surface than the central pinhole ($i' > i$). This is because the conic section formed by the intersection of the pinhole image cone and the crystal surface plane forms an ellipse rather than a circle. Therefore, if a 3 x 3 grid of pinholes were constructed based on these parameters, it would lead to an asymmetric division of the crystal surface area as
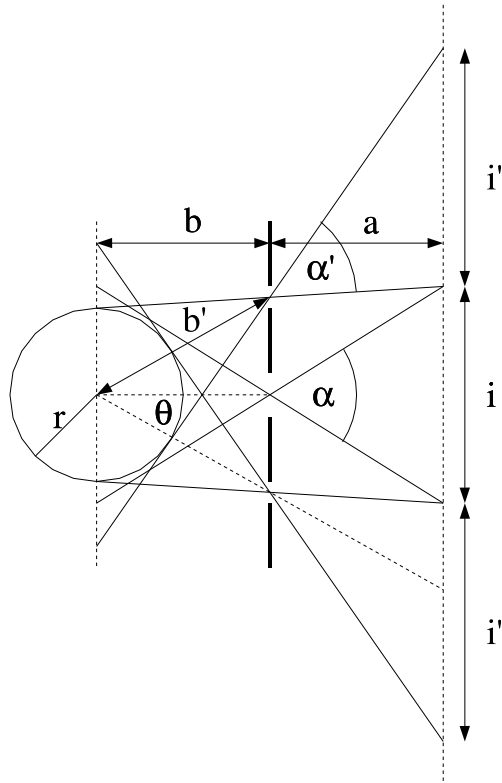
Figure 2.25: A schematic of a multiple pinhole collimator setup. All three pinholes image the same source volume to increase the sensitivity.

seen in Figure 2.26. The area of the crystal surface is given by $s^2 = (i + 2i')^2$.

One drawback of this particular design is that as b goes to r, which would help in maximizing the sensitivity, the crystal area (s^2) goes to infinity. Advantages of this design are that each pinhole images the entire field of view (which helps to increase sensitivity) and that there is no image overlap on the crystal surface (which simplifies SPECT reconstruction). With the 9 pinholes in a 3 x 3 grid, the sensitivity over the entire field of view would be increased by almost an order of magnitude. Given the high pixel resolution of a typical research grade CCD (512 x 512 pixels),
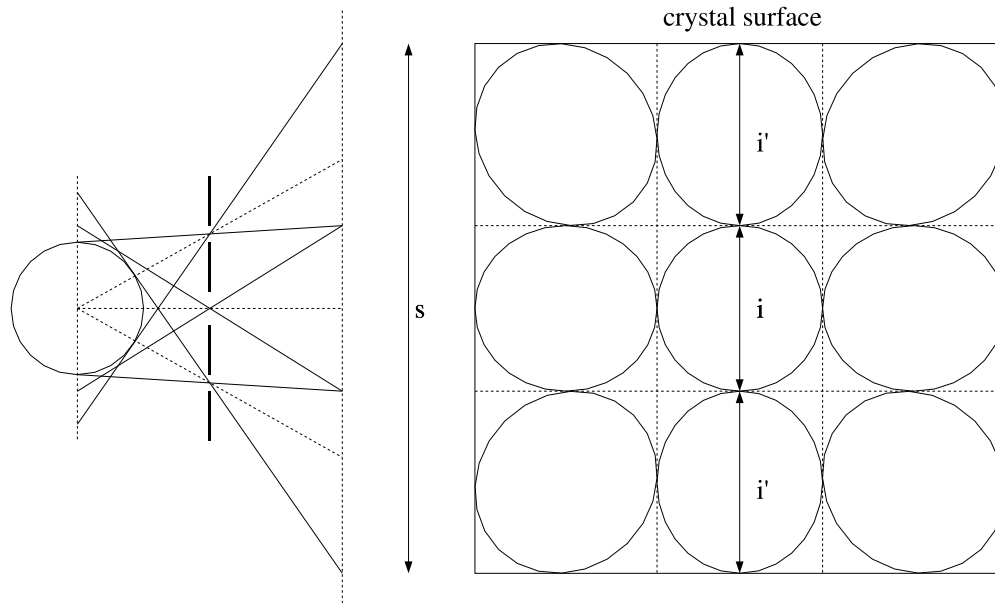
Figure 2.26: A schematic showing the asymmetric division of the crystal surface that results from using both tilted and non-tilted pinholes to image the same source volume.

the number of pinholes could be increased to 16 (4 x 4 pinholes, $\approx$ 128 x 128 pixels per pinhole) which would further increase the sensitivity.

Chapter 3

R2486 PSPMT SPECT

3.1 Overview

Before experiments with the CCD photodetectors began, a functional preclinical SPECT system was designed and constructed using a single Hamamatsu R2486 PSPMT, monolithic NaI(Tl) crystal, and pinhole collimator. A data acquisition system (DAQ) for the R2486 was already in place, therefore only the SPECT hardware needed to be designed and fabricated. The DAQ system used standard high energy physics NIM (Nuclear Instrumentation Module) and CAMAC (Computer Automated Measurement And Control) components for triggering and digitization of the anode pulses from the R2486. These data were then sent across a GPIB (General Purpose Interface Bus) for storage on a PC running LabVIEW software. Along with constructing the SPECT hardware, the LabVIEW software was upgraded and the code was rewritten in order to achieve a faster data acquisition rate. Also, code for off-line analysis of the data was written using the PAW (Physics Analysis Workstation) software from CERN. Details of this work and initial *in vivo* SPECT images are described in this chapter.

3.2 SPECT Hardware Setup

The Hamamatsu R2486 PSPMT has an active photocathode area measuring 50 mm in diameter. This area is spanned by 32 anode wires with 16 in the X direction, 16 in the Y direction, and a 3.75 mm step as shown in Figure 3.1(a). The initial photoelectrons are amplified through a 12-stage course mesh dynode structure resulting in a total gain of 5.0 x 10^5. The amplified signal for each event is then collected by the 32 anode wires, with the X and Y wire profiles giving the position, and the signal sum giving the energy. The quantum efficiency (QE) of the R2486 is 20% at 410 nm (the λ_{max} for NaI(Tl)) as shown in Figure 2.4. With direct optical coupling, approximately 20% of the scintillation photons will escape from the crystal [50]. This gives (140 keV) x (38 photons/keV) x (20% escape) x (20% QE) $\approx$ 200 photoelectrons/event for ^{99m}Tc. This then gives an intrinsic resolution (R_i) of about 1.5 mm as shown in Figure 3.1(b).
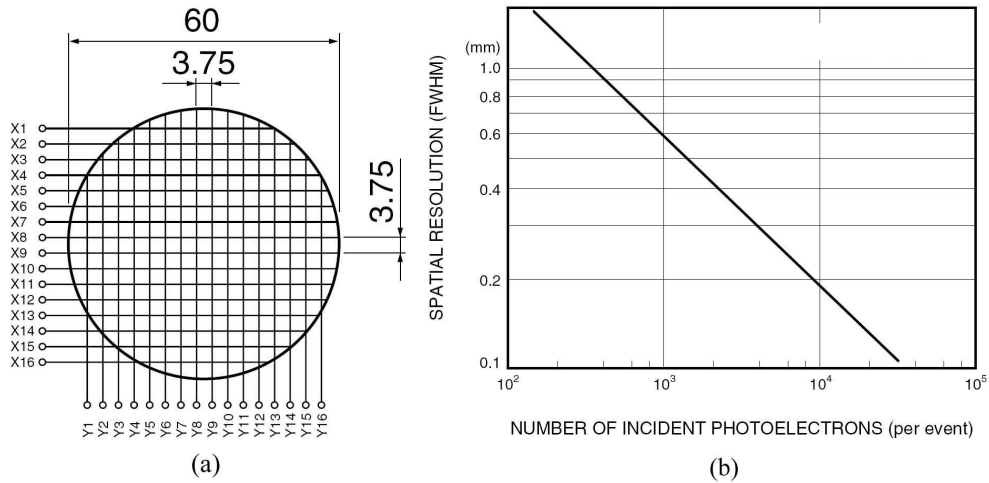
Figure 3.1: (a) A schematic of the R2486 X and Y anode wire alignment (dimensions are in mm). (b) A plot of intrinsic resolution versus photoelectrons/event for the R2486. Figures courtesy of Hamamatsu.

Since only one PSPMT was used in this system, the most logical design was to keep the detector in a fixed horizontal position and rotate the source object in a vertical position. This would save space and simplify the mechanics for taking several equiangular projections required for tomographic reconstruction. The anesthetized mouse was held vertically in a clear acrylic tube similar to the A-SPECT system [30]. A jig was then constructed from aluminum and acrylic to support the mouse tube. This jig allowed gaseous anesthesia to flow over the mouse while being rotated about the vertical axis by a hand driven turntable. The acrylic tube could also be moved up or down within the jig in order to scan different axial sections of the mouse. A photograph of the experimental setup is shown in Figure 3.2. The R2486 was placed in a magnetic shield and directly coupled to a sealed 6 mm thick, 60 mm diameter monolithic NaI(Tl) crystal using Dow Corning Q2-3067 optical couplant. This sub-assembly was then inserted into a lead cylinder that shielded the crystal from stray radiation and held the pinhole collimator insert. Several different lead pinhole inserts were made with varying pinhole diameters (2.0, 1.0, and 0.8 mm) as shown in Figure 3.3. This allowed for different levels of sensitivity and resolution to be achieved. Each single pinhole insert was 3.5 mm thick and had an aperture angle of 90 degrees.

With a 50 mm diameter active surface area, the maximum distance the scintillating crystal could be from the pinhole was 25 mm. At this distance the 90 degree pinhole angle subtends the 50 mm diameter area of the R2486. The geometry for this setup is shown in Figure 3.4. The inner diameter of the acrylic mouse tube was 25.4 mm. If the mouse tube is placed such that the 90 degree pinhole angle subtends the inner diameter, then the distance from the pinhole to the center of the tube is 18 mm. This geometry defines the distances a (25 mm) and b (18 mm) from
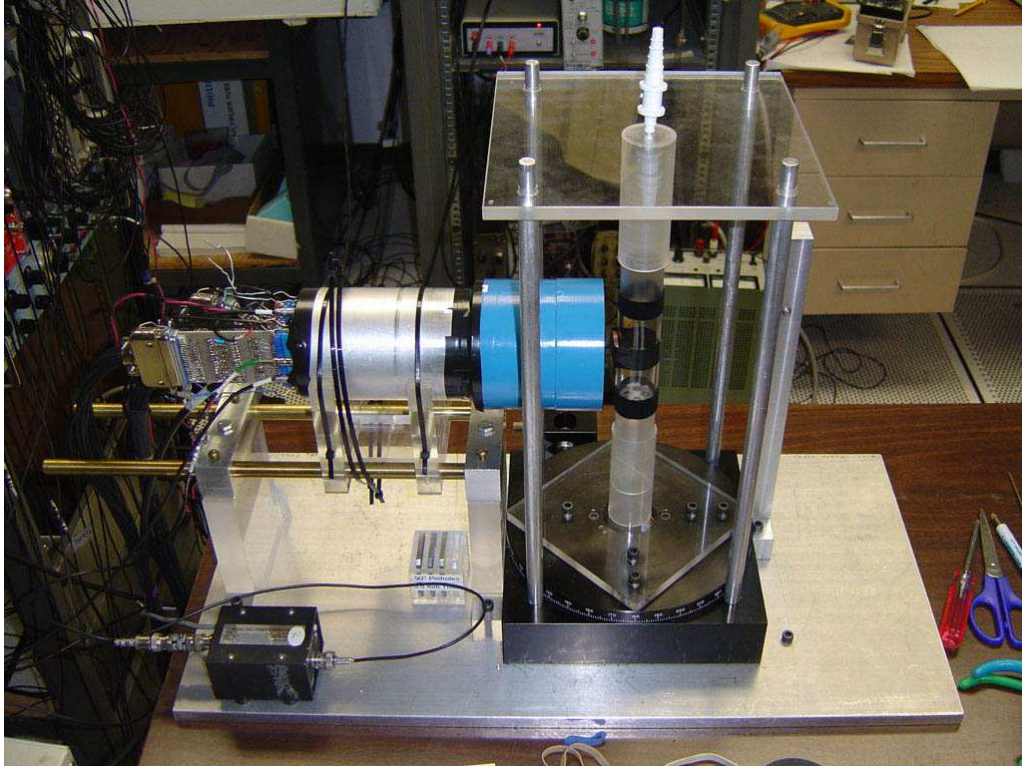
Figure 3.2: A picture of the PSPMT SPECT setup. The R2486 and NaI(Tl) crystal are located inside the lead shielding (blue), while the vertical acrylic mouse tube rotates on a hand driven turntable (black). The inlet for gaseous anesthesia (white) can be seen at the top of the mouse tube.

Equation 2.9. The image magnification for an object at the center of the mouse tube is therefore 1.4x ($\frac{b}{a} = 0.72$). A resolution plot (see Equation 2.9) using and intrinsic resolution (R_i) of 1.5 mm and an effective pinhole diameter (d_e) of 1.0 mm is shown in Figure 3.5. It can be seen that for $\frac{b}{a} = 0.72$, a total resolution (R_t) of about 2 mm is achieved. This non-submillimeter resolution is mainly due to the dominant geometric resolution term R_g (see Equation 2.10) which is limited by the effective pinhole diameter and low image magnification ($\frac{a}{b} = 1.4$). The total resolution could be improved by using a smaller pinhole size to reduce R_g, or by using an
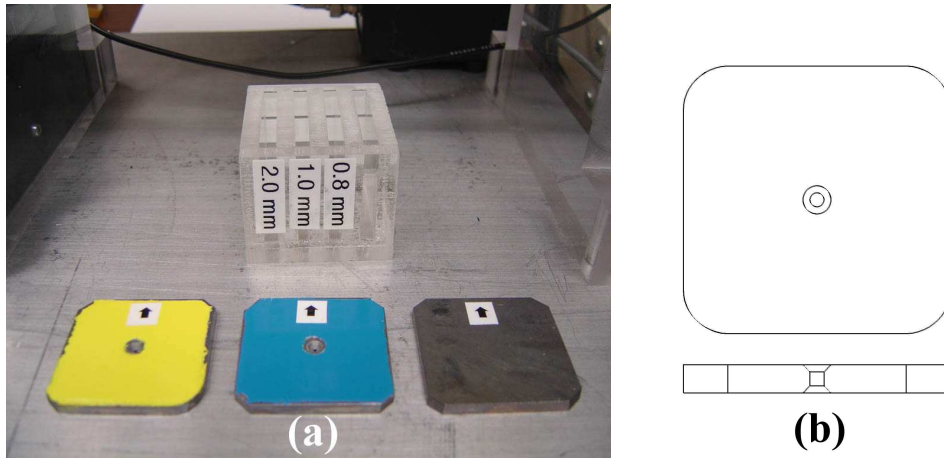
Figure 3.3: (a) A picture of the pinhole collimator inserts. Several different diameters were made (2.0, 1.0, and 0.8 mm). (b) A schematic of a pinhole insert showing the 90 degree aperture design.

acute pinhole aperture angle to increase the magnification, but both changes would reduce the sensitivity of the single pinhole.
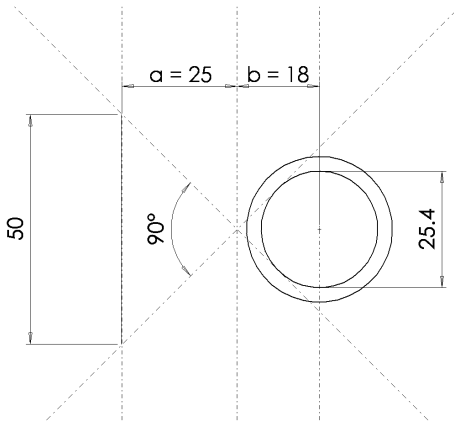
Figure 3.4: A schematic of the pinhole geometry (distances are in mm). The 90 degree pinhole angle subtends both the active area of the R2486 (50 mm) and the inner diameter of the mouse tube (25.4 mm). This defines distances a (25 mm) and b (18 mm) giving an image magnification of 1.4x
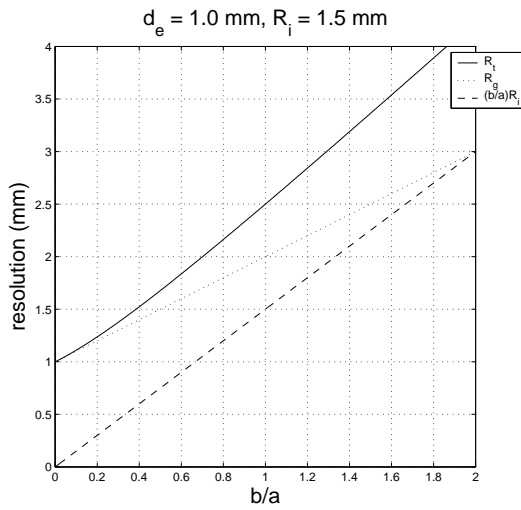
Figure 3.5: A resolution plot for $d_e = 1.0$ mm and $R_i = 1.5$ mm. For a magnification of 1.4x ($\frac{b}{a} = 0.72$) the total resolution is ≈ 2 mm.

3.3 DAQ Software Modifications

3.3.1 DAQ Setup

The 32 channels (16 X-direction, 16 Y-direction) from the Hamamatsu R2486 PSPMT
were first sent through a preamp and then digitized by three LeCroy 2249A ADCs
(see Figure 3.6). Each ADC had 12 channels (labeled 0 through 11) and a single
gate input. Due to the need for a larger integration gate width, a fourth 2249A
ADC was used to digitize the dynode signal from the PSPMT and the pulse signal
from the pulser. A LeCroy 8901A CAMAC-TO-GPIB interface was used to con-
trol the CAMAC crate. The 8901A was connected to a PC containing a National
Instruments AT-GPIB/TNT Plug-and-Play (ISA) adapter. The PC had a 90 MHz
Pentium processor with 48 MB of RAM and was running Windows 98. LabVIEW
4.1 was originally used for data acquisition. After acquisition, the data were then
transferred to different computer for off-line analysis.
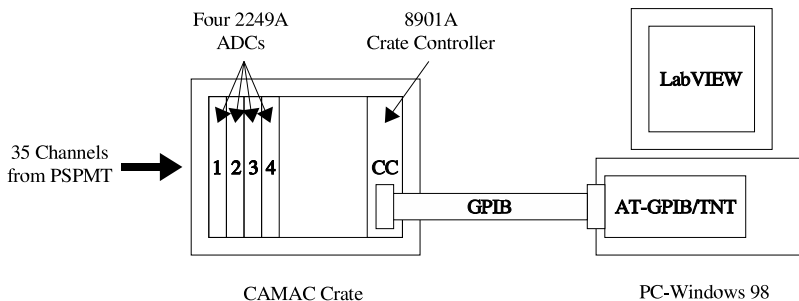
Figure 3.6: A schematic of the R2486 DAQ setup.

This existing data acquisition system, based on LabVIEW 4.1, could only
read about one event per second. This required acquisition times of 10 hours or

more to achieve adequate statistics for analysis. A reduced acquisition time was necessary to make the system capable of *in vivo* small animal studies. In an effort to maximize the readout speed, modifications were made to the LabVIEW software, code, and drivers. A list of methods used for speeding up the data acquisition is presented below, with each item being described in the following sections.

SOFTWARE MODIFICATIONS:

- Upgrade from LabVIEW 4.1 to LabVIEW 5.1

- Use latest LabVIEW CAMAC instrument drivers

- Use latest driver for the AT-GPIB/TNT (ISA) adapter

CODE MODIFICATIONS:

- Only read the ADC channels used

- Create a "null" array for the data to conserve system memory

- Minimize screen output and loop calculations

- Read block of data from the CAMAC controller

HARDWARE MODIFICATIONS:

- Upgrade to a faster computer

- Use faster crate controller

- Use different GPIB interface adapter

3.3.2 Software Modifications

The first step for modification was to upgrade the software from LabVIEW 4.1 to LabVIEW 5.1. Version 5.1 supports multi-threading which should help to speed up the data acquisition. The upgrade was done by simply removing the 4.1 version before installing the 5.1 version. Also, the driver for the AT-GPIB/TNT (ISA) adapter was upgraded to the latest version (1.70), and the latest LabVIEW instrument drivers for the LeCroy 8901A CAMAC module were used.

3.3.3 Code Modifications

The old LabVIEW code (*spect32s.vi*) read all 48 ADC channels in series, saved the data as an array, and then wrote the array to a file. This process was repeated for each event. The problem with this method is that each time the code created an array, it used a new section of memory and did not reclaim the old section from the previous array. This could lead to possible memory leak issues and system slowdown. Also, the old code wrote the data by opening, writing to, and closing the output file for each event. This created unnecessary file open/close calls in the acquisition loop.

The first modification was to allow the user to select which ADC channels were to be read. Since only 34 of the 48 ADC channels were used, a 30 % increase in speed could be achieved simply by not reading the unused channels. This was done by creating an array of Boolean (true or false) variables, where each Boolean represented a single ADC channel. By selecting which ADC channels to read using a Yes or No button (green or red respectively), the code will ignore the unused channels during the acquisition loop (see Figure 3.7). This is implemented using the *get_adc_info.vi* and '*adc_info* sub-vis (Figures 3.8 and 3.9 respectfully).
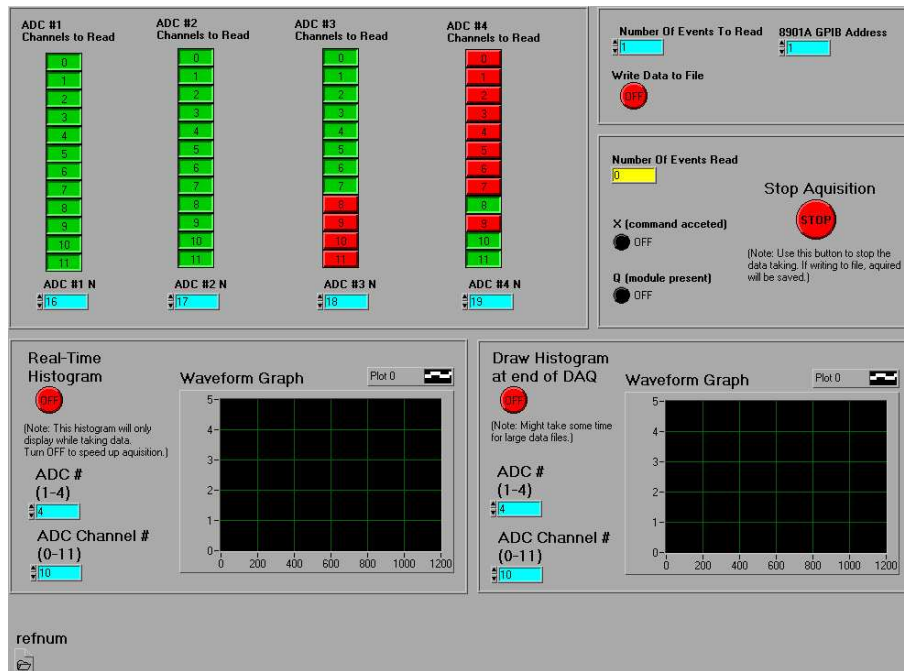
Figure 3.7: A picture of the LabVIEW 5.1 front panel for the *4adc_daq.vi* program. The ADC channels to be read are selected in the upper-left section. Inputs for the number of events to be read, 8901A GPIB address, and output file option are in the upper-right section.

In order to use the limited system memory more efficiently, the data were acquired in a slightly different manner. Using the total number of events to be read, a 12 x N array of zeroes (a null array) is created at start of the acquisition, where N = (number of events) x (number of ADCs). Thus, each event is represented by a 12 x 4 array. As the individual ADC channels are read, the zeros from the appropriate columns and rows of the null array are replaced element by element. In this way, the amount of memory required is established at the start of the program, with no memory being wasted. The ADC channels that are not used are left as zeroes in the final data array. The array of zeroes is initialized by the *make_null_array* sub-vi (see Figure 3.10). A sample data output file for 10 events is shown in Figure 3.11.

70
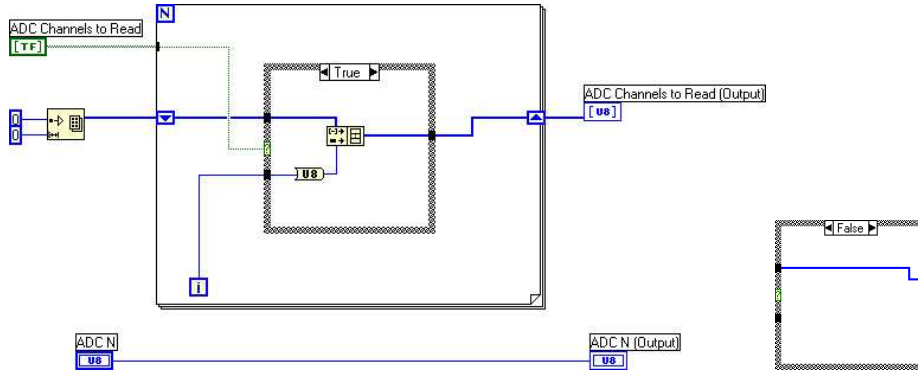
Figure 3.8: The diagram for *get_adc_info.vi*. This vi uses a Boolean array to create a numerical array of ADC channels to be read. It also passes the ADC CAMAC slot number N.
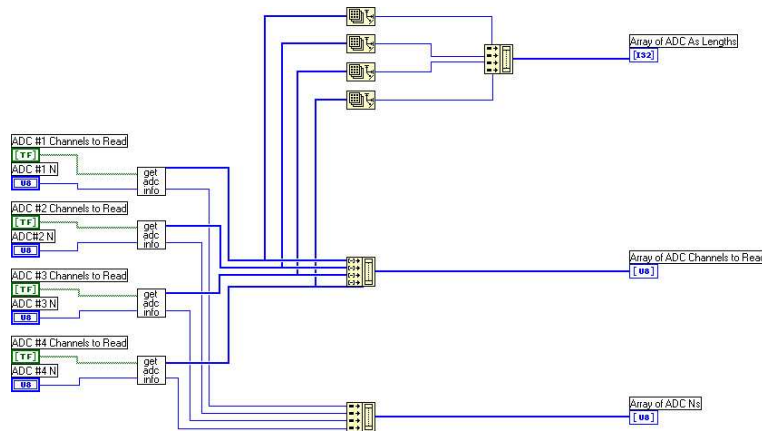
Figure 3.9: The diagram for *adc_info.vi*. This vi uses the Boolean array and CAMAC slot number N from each ADC to create an array of all ADC channels to be read, an array of all ADC CAMAC slot numbers, and an array describing the length of each ADC channel array.
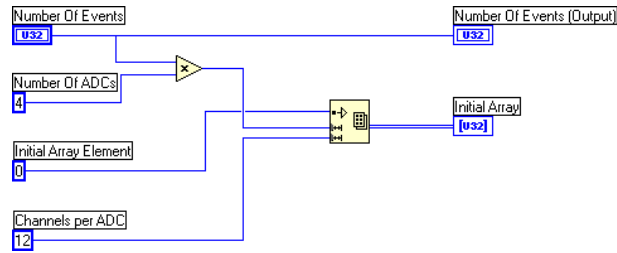
Figure 3.10: The diagram for *make_null_array.vi*. This vi takes the number of events to be read and creates a 12 x N array of zeroes, where N = (number of events)x(number of ADCs). For 100 events, the output will be a 12 x 400 array of zeroes.

```
997   1123  1123  1123  875   865   500   496   342   283   276
207   171   207   233   280   498   874   1069  1069  1069  998
437   328   323   274   267   300   250   0     0     0     0
0     0     0     0     0     0     0     38    0     500   57
330   407   539   929   648   966   1035  1124  750   437   359
203   160   196   179   179   198   211   228   260   344   594
1085  789   782   535   316   311   238   0     0     0     0
0     0     0     0     0     0     0     38    0     365   57
267   279   276   312   305   374   365   622   793   1123  1123
1067  1067  735   534   1068  1068  1068  1069  1068  630   468
323   314   315   304   301   336   294   0     0     0     0
0     0     0     0     0     0     0     39    0     958   58
262   274   254   270   273   295   267   293   257   251   254
185   152   201   178   176   192   189   202   191   163   187
187   199   209   195   204   257   195   0     0     0     0
0     0     0     0     0     0     0     39    0     56    1134
254   264   252   271   278   349   378   715   1015  1123  1123
603   253   224   239   319   674   1021  994   862   706   453
247   234   229   216   218   263   210   0     0     0     0
0     0     0     0     0     0     0     38    0     360   57
79    82    65    53    28    30    29    24    1     11    11
15    8     10    13    8     12    8     9     9     5     9
65    43    46    20    16    20    10    0     0     0     0
0     0     0     0     0     0     0     39    0     362   57
264   273   255   270   271   292   268   292   258   251   257
184   151   200   179   174   192   190   200   192   163   188
187   198   207   196   203   255   196   0     0     0     0
0     0     0     0     0     0     0     39    0     56    1134
276   285   260   279   274   294   262   285   254   251   260
189   159   210   188   182   201   204   209   199   167   195
192   201   203   191   196   255   198   0     0     0     0
0     0     0     0     0     0     0     39    0     39    1134
256   265   254   270   274   296   275   370   412   514   832
1067  1067  1067  180   180   198   212   234   281   466   808
1085  1085  1001  538   327   327   266   0     0     0     0
0     0     0     0     0     0     0     39    0     479   57
347   549   727   1123  1030  1123  886   549   337   266   250
179   147   189   259   308   643   1069  1036  896   706   493
225   206   214   201   198   241   191   0     0     0     0
0     0     0     0     0     0     0     38    0     393   57
```

Figure 3.11: A sample data output file for 10 events. Each row represents the 12 channels (0 though 11) from a single ADC. A single event is represented by 4 consecutive rows (4 ADCs per event). The zeroes in the data represent ADC channels that are not being read.

To improve the file input/output speed, the output data file is opened and closed outside the acquisition loop. Therefore, these commands only need to be called once for each data run and not for each event. Writing data to an output file can be turned ON or OFF using the Boolean button (see Figure 3.7).

In order to minimize the screen output, which can significantly reduce the program execution speed, two separate histograms were created. The first histogram is used to monitor the individual ADC channels during acquisition (*Real-Time Histogram*), while the second is used to plot a specific ADC channel at the end of the acquisition (*Draw Histogram at end of DAQ*). Each of these histograms can be turned ON or OFF using the appropriate button (see Figure 3.7). When the *Real-Time Histogram* is turned ON during acquisition, it takes the given ADC number (1 through 4) and channel number (0 through 11) and scans the entire array of acquired data to create an N x 1 dimensional array, where N is the number of events. This array is then passed to the *General Histogram* sub-vi, which plots the histogram. The only draw back of the *Real-Time Histogram* is that, in order to conserve system memory, it scans the acquired data array, and passes a N x 1 array, for each new event. This can significantly reduce the acquisition speed for large data sets. The *Real-Time Histogram* should be turned ON to monitor a few events then turned OFF to resume normal acquisition speed. The *Draw Histogram at end of DAQ* uses the same routine as the *Real-Time Histogram*, but only draws the selected ADC channel at the end of the data acquisition. This histogram is useful for calibrating single ADC channels with small sets of acquired data, but it can take some time to execute for larger sets.

Along with *Single Transfer* mode, the *LC8901A VISA Open.vi* sub-vi has the option for *Block Read* and *High Speed Block Read* data transfer mode. Although the

latter two modes could greatly increase the data acquisition speed by allowing an entire block of data from the 8901A to be read at once (instead of reading channel by channel), neither mode could be successfully implemented. One problem might be that the current CAMAC configuration does not support Block transfer mode.

Finally, the number of calculations and actions within the data acquisition loop were minimized to help improve acquisition speed.

All of these code changes are implemented in the new *4adc_daq.vi* (see Figure 3.12). This vi requires the *make_null_array.vi*, *get_adc_info.vi*, and *adc_info.vi* sub-vis in order to run. In order to halt the acquisition during a run, it is best to use the "Stop Acquisition" button (see Figure 3.7). This will prevent errors occurring from partially executed sub-vis.
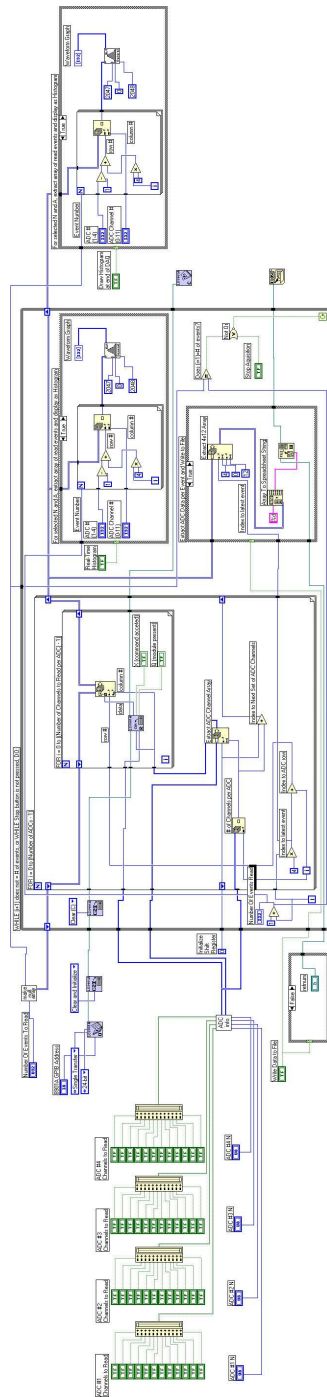
Figure 3.12: The diagram for *4adc_daq.vi*. The initializing statements are on the left, the acquisition loop is in the center, and the closing statements are on the right.

3.3.4 DAQ Modification Results

A comparison of the data acquisition speeds for the old program (*spect32s.vi*) and the new program (*4adc_daq.vi*) is shown in Table 1. Since the LabVIEW profile window was causing the computer clock to run erratically, an external stopwatch was used to take the measurements. For the *spect32s.vi* program, the stopwatch and data acquisition program were started simultaneously. As the desired number of events were reached, the lap button was pressed on the stopwatch, the time was recorded, then the stopwatch and program were left to run until the next data point. For the *4adc_daq.vi* program, the number of desired events was entered into the program, and then the stopwatch and program were started simultaneously. When the program ended, the stopwatch was immediately halted. It can be seen that the new program improves the speed by a factor of almost 7. It is important to note that the old program is reading all 48 ADC channels, while the new program is reading only 34 channels. If the number of channels read by the new program were further reduced, the number of events read per second would increase accordingly. Also, note that both the new and old programs were run under LabVIEW 5.1 for these tests.

	spect32s.vi (old)		4adc_daq.vi (new)	
events read	time (sec)	events/second	time (sec)	events/second
10	11.23	0.890	2.06	4.854
100	101.16	0.989	16.33	6.124
500	501.07	0.998	76.77	6.513
1000	1001.03	0.999	152.93	6.539
5000	5002.00	1.000	760.50	6.575
10000	9999.00	1.000	1518.67	6.585

Table 3.1: A comparison of the acquisition times for the old and new DAQ programs. The acquisition speed has been improved by a factor of almost 7. The pulser used for the trigger was set to 5 kHz for each program.

The next most significant factor that could increase the data acquisition speed even further would be to use a faster computer with more memory. Acquisition speed could also be improved by using a faster crate controller or a newer GPIB PC interface adapter. A crate controller with a faster throughput, such as the SCSI based Jorway, or a PCI or PCIX based GPIB PC interface adapter could achieve this. A different crate controller might also allow the use of the CAMAC *High Speed Block Read* for faster data transfer.

3.4 Data Analysis Algorithm

Once the list-mode data were recorded, the file was then transferred to a different computer for off-line analysis. The CERN program library packages HBOOK (Statistical Analysis and Histogramming) and PAW (Physics Analysis Workstation) were used for this purpose. The raw data file (.txt) was first read into and saved as a *Row-Wise-Ntuple* (.dat) using the HBOOK software. The *Row-Wise-Ntuple* was then used by PAW to calculate the means of the histogram pedestals for each of the 32 PSPMT wire signals. The value for each pedestal was then subtracted from the corresponding wire signal values. The X and Y wire profiles for a single event were each plotted and fitted with a Gaussian distribution. Wire profile events with zeroes in the data (read error from CAMAC crate), values of 1024 or greater (ADC overflow), or pedestal events (no scintillation light) were vetoed and not analyzed. The event number and fit data for each event were then stored in a second list-mode file (.txt). This second list-mode file was then used to create a second *Row-Wise-Ntuple* file (.dat). The second *Row-Wise-Ntuple* was used to create the two-dimensional projection data for a given rotation angle which was used for SPECT reconstruction.

3.5 Results

3.5.1 ^{57}Co Point Source

The first imaging experiments with the PSPMT SPECT system used an 0.8 mm diameter pinhole and a ^{57}Co point source (≈ 10 μCi). The point source measured ≈ 1 mm in diameter and was taped to the inside wall of the acrylic mouse tube. Figure 3.13 shows two sample projections with the point source ≈ 6 mm from the pinhole (a) and after rotating $22.5°$ (b). Sixteen equiangular projections of the ^{57}Co point source were taken by rotating the turntable in $22.5°$ steps. These data were taken without optical grease between the NaI(Tl) crystal and PSPMT photocathode. As a result, certain areas of the PSPMT were more sensitive than others as shown in the two images of Figure 3.13. In order to test the effectiveness of optical grease coupling, the pinhole collimator was removed and a flood image was created by placing the ^{57}Co point source at a close distance to the crystal surface. Figure 3.14 shows the PSPMT response without (a) and with (b) the optical grease. It can be seen that using optical grease gives a much more uniform response over the PSPMT photocathode.
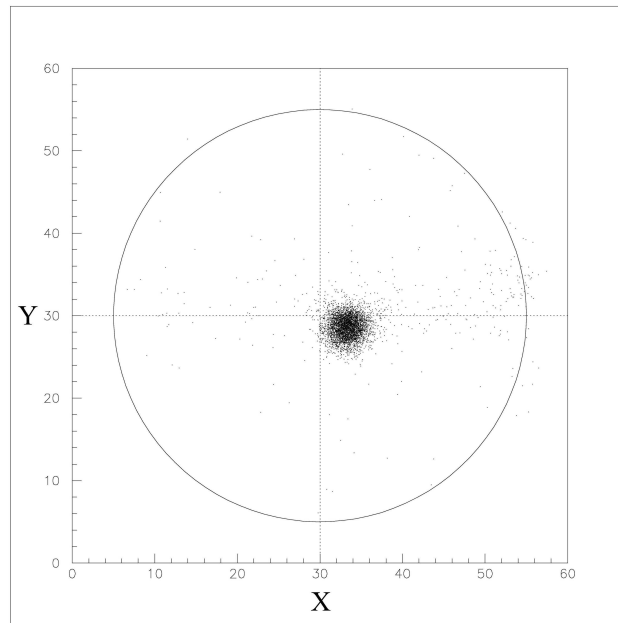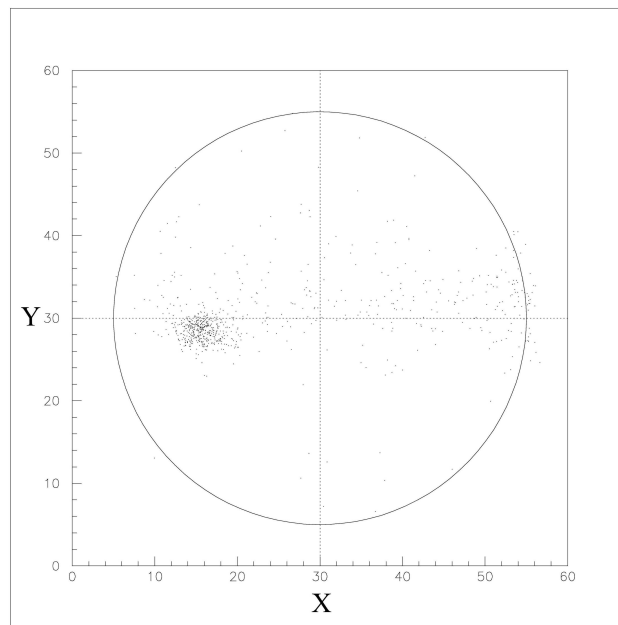
Figure 3.13: Pinhole projection images of a ^{57}Co point source ≈ 6 mm from the pinhole (a) and after rotating 22.5° (b). The circle represents the 50 mm diameter active photocathode area of the R2486 (dimensions are is mm).
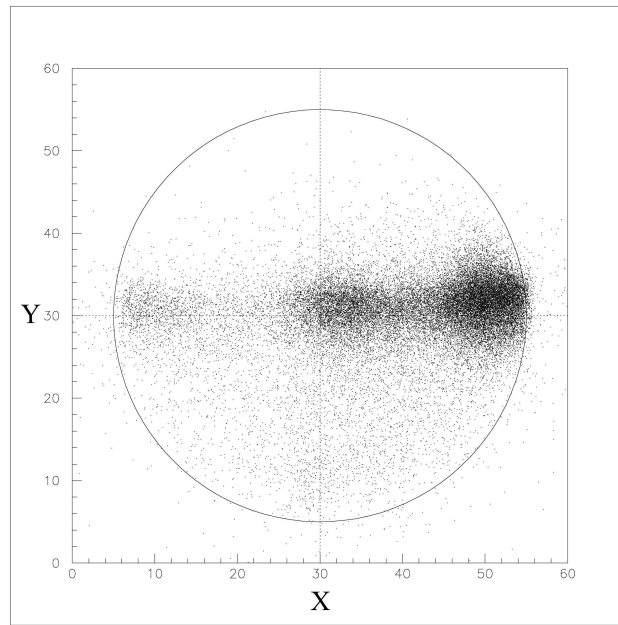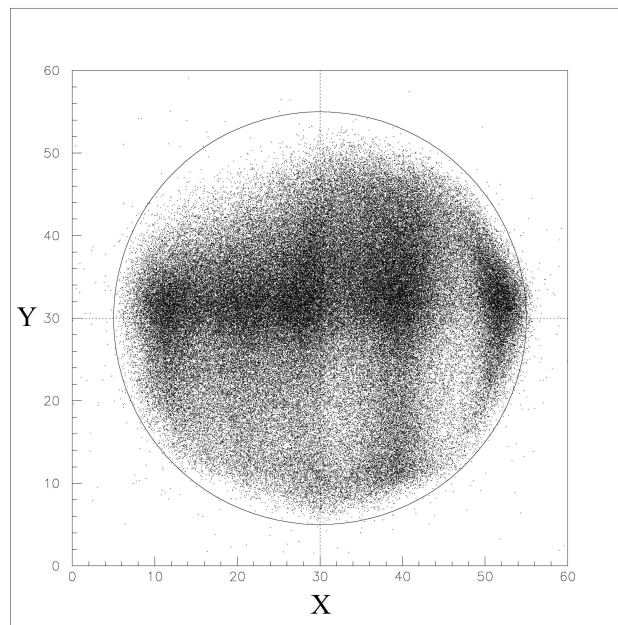
Figure 3.14: ^{57}Co point source flood images showing the R2486 response without (a) and with (b) optical grease between the scintillating crystal and photocathode (dimensions are in mm).

3.5.2 ^{99m}Tc-MDP Mouse

In vivo images for SPECT reconstruction were taken with the PSPMT system using the 0.8 mm diameter pinhole and a mouse injected with 10 mCi of ^{99m}Tc-MDP (Methyl Diphosphonate). The ^{99m}Tc-MDP uptake time was 2 hours and the exposure time per projection was < 5 minutes with an average of $\approx$ 30k events per projection. Eighteen equiangular projections ($20°$ step) were taken per axial section, with two sections needed to scan the entire mouse. The 36 total projections were acquired in about one hour. These data were then used for SPECT reconstruction to show the three-dimensional distribution of the radioisotope [63]. An image of the reconstruction is shown in Figure 3.15. This figure shows the maximum intensity voxel projections from the MLEM reconstruction algorithm. With a total resolution of approximately 2 mm, details of the mouse skeletal structure can clearly be seen. The reconstructed image was courtesy of Dr. Edward Tsyganov.

3.6 Conclusions

The 50 mm diameter active photocathode area of the R2486 PSPMT allows for an image magnification of 1.4x when viewing a 25.4 mm diameter field of view with a $90°$ pinhole. This field of view is large enough to image specific organs of interest within a mouse (*e.g.* the kidneys, brain, or lungs) in a single scan, or the whole mouse can be imaged in just two or three axial scans. The R2486 can also use thick monolithic crystals that are able to stop a high percentage of the incident radiation. For example, the 6 mm thick NaI(Tl) crystal used in these experiments stops approximately 90% of the 140 keV gamma rays from ^{99m}Tc. A high crystal stopping power helps to improve the overall sensitivity of the system as discussed in Chapter 2. Although the 20% quantum efficiency of the R2486 is typical for a
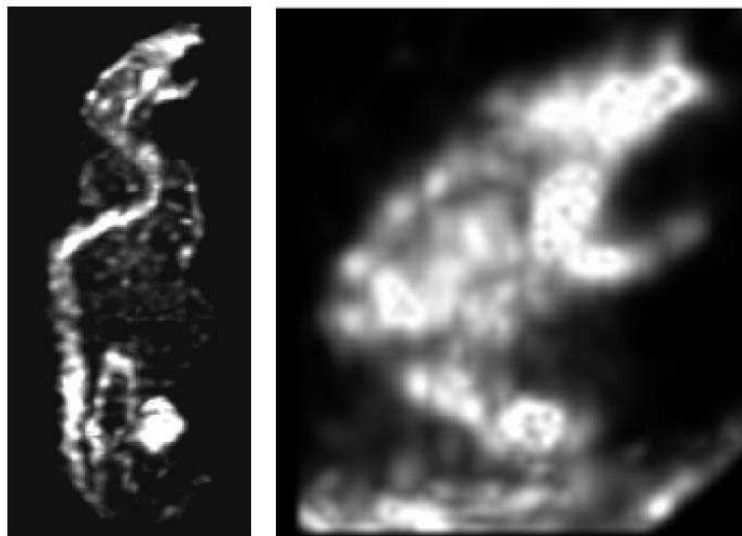
Figure 3.15: *In vivo* maximum intensity voxel projections from the MLEM reconstruction of a mouse that was administered ^{99m}Tc-MDP. The skeletal system uptake and bladder can clearly be seen. Image courtesy of Dr. E. Tsyganov.

photomultiplier tube, it is low when compared to back-illuminated CCDs that have $> 80\%$ quantum efficiency. The low quantum efficiency of the R2486 is partially offset by the direct optical coupling of the crystal and the high gain of the mesh dynode. Direct optical coupling allows for high optical transfer efficiencies to be reached ($> 50\%$) [50], while the high gain (5.0×10^5) greatly improves the signal to noise ratio. Also, the fast counting mode of the R2486 allows for a high number of events per second to be measured with list-mode data. The list-mode data can then be used for energy windowing to exclude scattered events and improve the SPECT reconstruction.

Along with the low quantum efficiency, another drawback of the R2486 PSPMT is that the DAQ system is currently very hardware intensive. Several NIM bin components, four CAMAC ADCs, a pulse generator, and many power supplies

are all needed to analyze the 32 anode wire signals from a single R2486. Also, the intrinsic resolution of the R2486 ($R_i = 1.5$ mm) is the limiting term for the total resolution. As shown in Figure 3.5, even with large image magnification the system would not be able to achieve sub-millimeter total resolution. Having sub-millimeter resolution would greatly improve the quality of images and level of information obtained from small animals such as mice. Finally, the off-line analysis of the list-mode data using PAW is very time consuming and would not be practical for a high or even moderate throughput small animal system. These factors reduce the feasibility of using PSPMTs for a multiple camera small animal SPECT system.

Chapter 4

SI-502A CCD SPECT

4.1 Overview

The first CCD SPECT tests used an existing setup that was initially built for bio-luminescence imaging (BLI) studies. The custom made setup used a conventional (non-electron multiplying) CCD camera with single lens coupling to integrate the optical light emerging from the source. The hardware setup, low light level phantom tests, and initial SPECT projection results are described in this chapter.

4.2 Hardware

4.2.1 CCD Camera

A schematic of the CCD setup is shown in Figure 4.1. An SITe model SI-502A scientific grade CCD was used for the camera photodetector [64]. The 1/2 inch format, back-illuminated SI-502A had 24 μm^2 pixels in a 512 x 512 array with a quantum efficiency of 80% at 560 nm (λ_{max} of CsI(Tl)). This quantum efficiency is four times higher than the R2486 PSPMT quantum efficiency of 20% at 410 nm

(λ_{max} of NaI(Tl)). The SI-502A was mounted to an aluminum cold-finger that was in contact with a 2-stage thermal-electric cooler (TEC, or Peltier). A liquid-based heat exchanger was used to remove the heat from the Peltier output surface. This cooling method brought the CCD temperature down to -25 °C, as measured by a sensor in the aluminum cold-finger just below the CCD. The CCD clock drivers, LC network, and preamp were located inside the camera housing which was under vacuum to reduce condensation from cooling. Shuttered lens coupling was used to focus the scintillation light onto the CCD surface. Both the camera housing and source were placed in a light tight box.
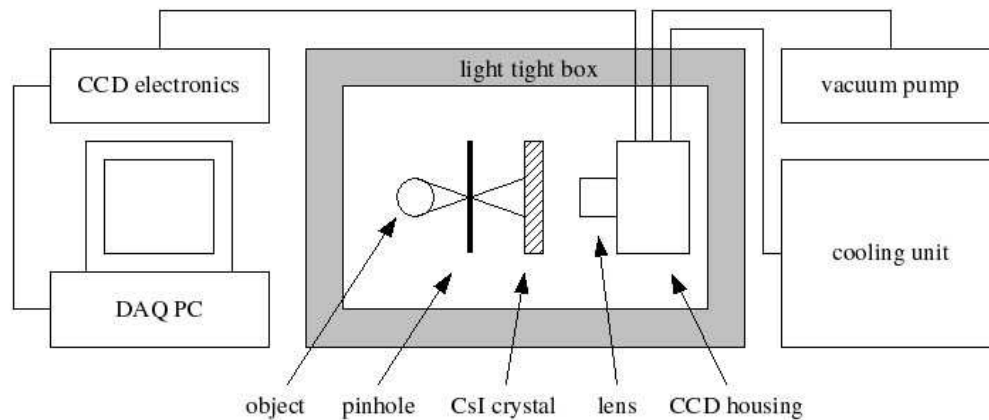
Figure 4.1: A schematic of the SI-502A CCD setup. Shuttered lens coupling was used to focus the scintillation light onto the cooled back-illuminated CCD. The CCD had a quantum efficiency of 80% at 560 nm (λ_{max} of CsI(Tl)).

4.2.2   CCD Electronics

The camera was connected to an external electronics box that contained the CCD parallel and serial clocking circuitry, power supplies, and video board for 16-bit

86

analog-to-digital conversion of the video signal from the SI-502A. The digitized signal was then sent to a PC, via a PCI digital input/output (DIO) board, that was running Igor software for display, storage, and analysis. The CCD clocking frequency for this setup was only 80 kHz. Therefore, it took several seconds to readout the 512 x 512 array of pixels, making this CCD camera only useful for integration studies and not video rate studies.

4.2.3 SPECT Setup

The setup for the initial SPECT tests is shown in Figure 4.2. A 50 mm x 50 mm area, 2 mm thick CsI(Tl) crystal was placed 80 mm from the camera housing. At this distance the crystal area just filled the field of view seen by the lens. The single C-Mount lens (Computar TV Lens, 12.5 mm, 1:1.3) was focused on the crystal surface closest to the lens. The crystal was sealed in a holder that had a 0.5 mm thick glass window on one side (facing the lens) and reflective tape with aluminum foil on the other (facing the source). Optical coupling oil was used between the crystal, glass, and tape surfaces to improve optical transfer. The crystal holder was placed in a light tight coupler that was mounted to the camera housing. The collimator and source were then placed in front of the crystal.

4.3 Results

4.3.1 Low Light Level Phantom

In order for the lens coupled CCD camera to function as a SPECT photodetector it must integrate the faint scintillation light emerging from the crystal with enough sensitivity to achieve an adequate signal to noise ratio (SNR). It must also do this in a reasonable exposure time ($\approx$ 5 minutes/projection). A phantom was constructed
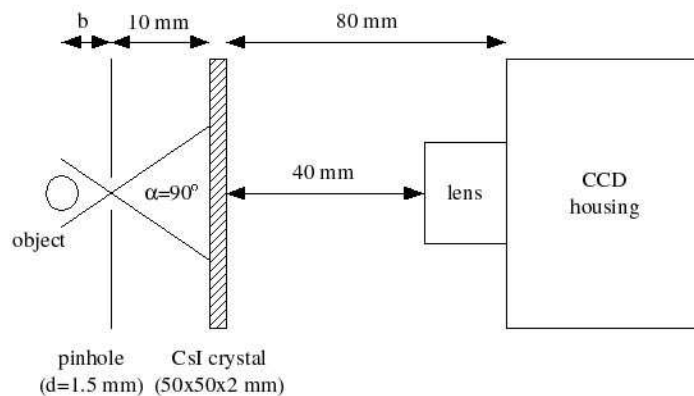
Figure 4.2: A schematic of the CCD SPECT setup. The 50 mm x 50 mm x 2 mm CsI(Tl) crystal was placed such that the area filled the field of view seen by the lens. Pinhole collimation was used to image the radioisotope distribution.

to evaluate the performance of the CCD camera at low light levels. The phantom consisted of a 3 mm diameter green LED ($\approx$ 510 nm wavelength) that was placed at the center of a 1/2 inch diameter Teflon sphere. The Teflon sphere diffused the LED light to approximate a uniform spherical source. The amount of diffuse light emerging from the Teflon sphere was controlled by limiting the current to the LED (50 mA max) with a 10 turn potentiometer. The low light levels emerging from the scintillation crystal were then simulated by adjusting the current to the LED. A photo of the LED phantom and variable current power supply is shown in Figure 4.3. The LED power supply was courtesy of Billy Smith.

The spherical phantom was placed 80 mm from the camera housing and focused on with the lens f-stop at 1.3 (open full). A 5 minute exposure of the phantom was taken with the LED potentiometer at 3.25 turns. A 5 minute dark exposure (shutter closed) was also taken then subtracted from the light image in order to reduce the background signal. A low light level image of the phantom and
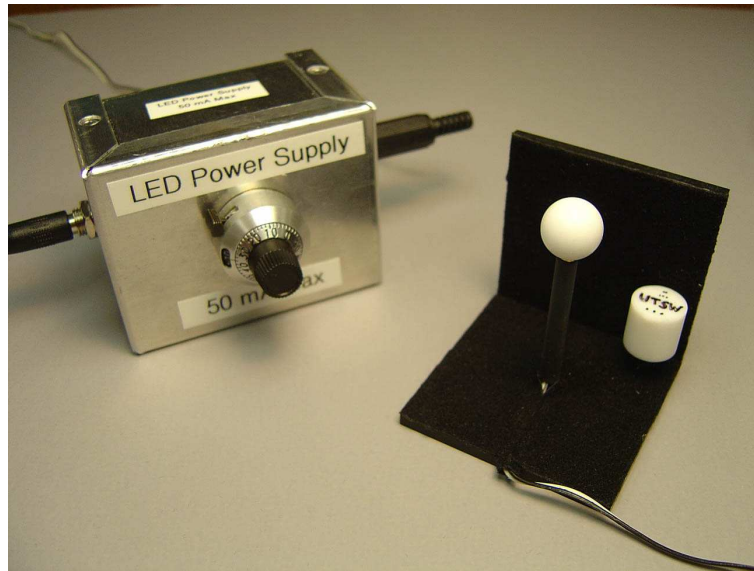
Figure 4.3: A picture of the low light level phantom and LED power supply. The 3 mm LED is mounted to the top of the long pin. Different Teflon shapes (spherical or cylindrical) can be placed on top of the LED to create diffuse sources.

accompanying horizontal line profile (through the center of the sphere) are shown in Figure 4.4(a) and Figure 4.4(b) respectively. The initial image (Figure 4.4(a)) showed there was electronic noise affecting the video signal at low light levels resulting in a SNR of only 2:1. It was determined that the noise was due to the 60 Hz frequency of a switching power supply located inside the electronics box. After replacing this power supply with a linear power supply, the noise was removed as seen in Figure 4.4(c). The new line profile shown in Figure 4.4(d) gives a signal to noise ratio of about 5:1. With the low light level performance of the CCD camera being properly tuned, the system was then evaluated for use in preclinical SPECT imaging.
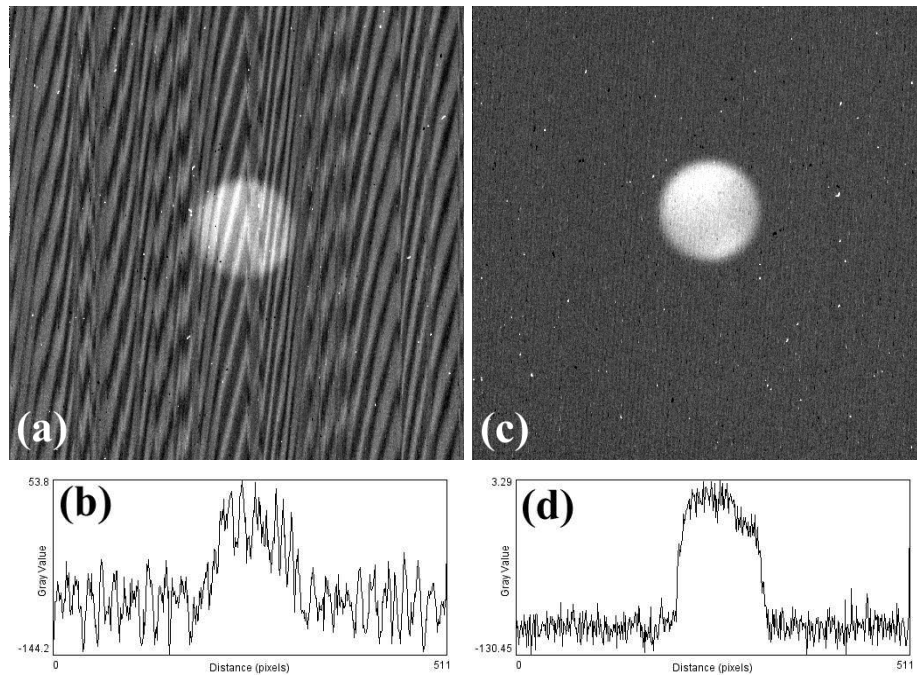
Figure 4.4: (a) A 5 minute exposure dark subtracted image of the LED Teflon phantom with the potentiometer at 3.25 turns. (b) The interference from the switching power supply noise can be clearly seen. (c and d) The noise was removed by using a linear power supply, which improved the SNR.

4.3.2 Cadaveric ^{99m}Tc-MDP Mouse

The feasibility of using a regular CCD camera with single lens coupling to perform integration based preclinical SPECT was first tested using a single pinhole collimator and cadaveric mouse injected with ^{99m}Tc-MDP. The 0.8 mm diameter lead pinhole insert previously used in the PSPMT setup was placed 10 mm from the scintillating crystal (distance a) with the mouse placed as close as possible to the pinhole (distance b). The mouse had been injected IV with approximately 6 mCi of ^{99m}Tc-MDP and sacrificed 1.5 hours later using CO_2. The total activity of the cadaveric mouse was measured with a well counter to be 640 μCi. A 5 minute

90

dark subtracted exposure of the mouse skull did not produce an image except for the slight glow of the CsI(Tl) crystal as seen in Figure 4.5. The pinhole collimator was then removed and the mouse was placed directly next to the crystal. Another 5 minute dark subtracted exposure produced the "flood-image" shown in Figure 4.6. This figure shows the overall crystal glow plus a bright area at the right corresponding to the upper body of the mouse. This figure also shows the inhomogeneous response of the CsI(Tl) crystal which could indicate hygroscopic damage or poor optical coupling between the glass and crystal. In an effort to allow more gamma rays to reach the crystal, a parallel hole collimator (1 mm hexagonal holes, 25 mm in length) was placed between the crystal and mouse. A 15 minute dark subtracted exposure produced a very faint image of the mouses lower body as seen in Figure 4.7. The signal from the knees, spine, and tail can just be seen above the background glow of the crystal. As a comparison, the same mouse and collimator were placed on top of a storage phosphor plate for a 30 minute exposure. The resulting scanned image is shown in Figure 4.8. Regions of ^{99m}Tc-MDP uptake in the mouse skeletal system can clearly be seen including the IV injection site in the tail vein. The storage phosphor image was courtesy of Dr. Matthew Lewis.
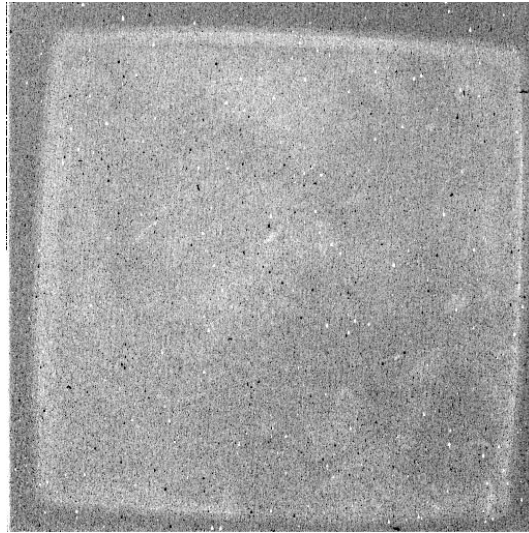
Figure 4.5: A 5 minute dark subtracted pinhole collimator image of the cadaveric ^{99m}Tc-MDP mouse. Only a slight crystal glow could be seen.
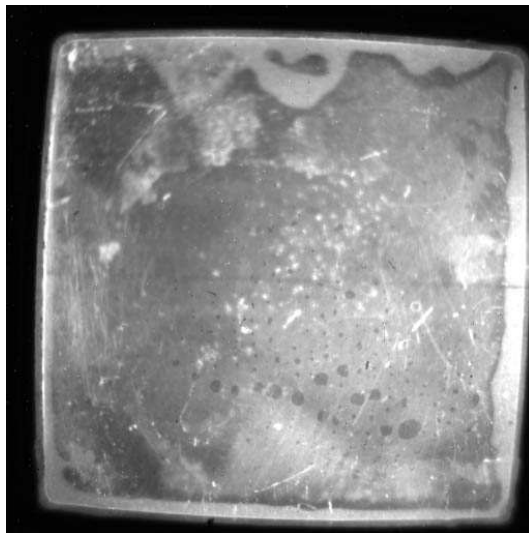
Figure 4.6: A 5 minute dark subtracted "flood" image (no collimator) of the cadaveric ^{99m}Tc-MDP mouse. The bright area on the right corresponds to the upper body of the mouse. The inhomogeneous response of the 2 mm CsI(Tl) crystal is clearly seen.
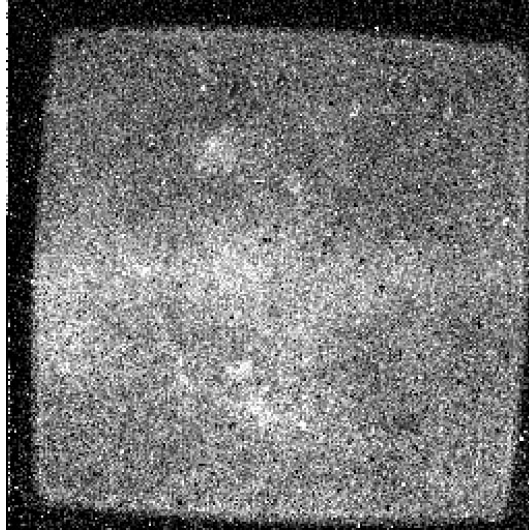
Figure 4.7: A 15 minute dark subtracted parallel-hole collimator image of the cadaveric ^{99m}Tc-MDP mouse lower body. The spine, tail, and knees can just be seen above the background crystal glow.
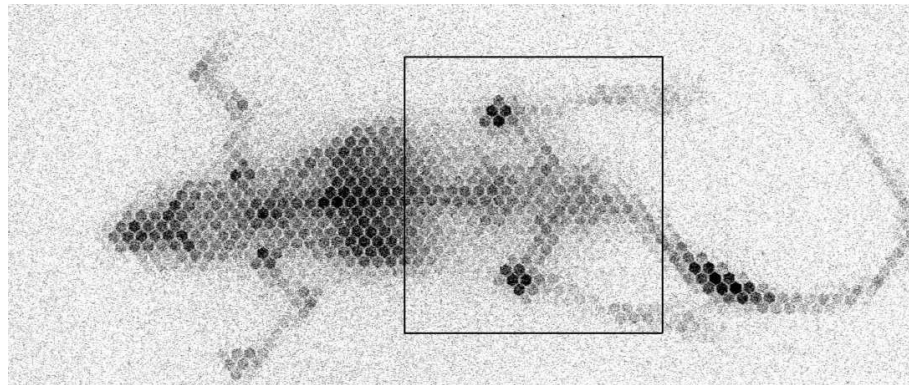
Figure 4.8: A 30 minute storage phosphor exposure of the ^{99m}Tc-MDP mouse with parallel hole collimator. The ^{99m}Tc-MDP uptake can clearly be seen with the improved signal to noise ratio. The square ROI represents the area imaged in Figure 4.7. Image courtesy of Dr. M. Lewis.

4.4 Conclusions

The experiments in this chapter essentially took the optically coupled PSPMT photodetector from the previous chapter and replaced it with a lens coupled CCD camera. It is important to note that while the PSPMT works in counting mode (measuring individual gamma ray flashes within the crystal to form an image) the CCD camera works in integration mode (integrating the gamma ray flashes over time to create an image). These initial tests showed two main problems that occur when using a lens coupled CCD camera for integration based SPECT imaging.

First, although the quantum efficiency for the SI-502A CCD is four times higher than the R2486 PSPMT, the overall sensitivity for the CCD system is much lower when comparing similar exposure times. This leads to a low signal to noise ratio as seen in Figure 4.7. One reason for the low sensitivity is that a 2 mm thick CsI(Tl) crystal will only stop about 60% of the incident 140 keV gamma rays from ^{99m}Tc. A thin crystal was chosen to reduce the light spread of scintillation events and hopefully improve the resolution of the integrated image. Another reason for the low sensitivity is that the scintillation light which leaves the crystal is inefficiently transferred to the CCD with single lens coupling. Also, although the dark noise for the CCD has been reduced by cooling to -25 °C, the dark noise signal for long exposure times is still a significant contribution to the total noise. Deeper cooling will be required to reduce the dark current to a negligible level for long exposure times. Finally, the noise floor for a regular CCD is produced by the read noise of the output amplifier (7 electrons/pixel for the SI-502A). This noise floor severely limits the signal to noise ratio obtainable at low light level imaging where there might be only few signal electrons per pixel. All of these factors contribute to the reduced sensitivity of the CCD system when compared to the PSPMT system.

The second problem observed when using a CCD camera was that due to the different index of refraction values for the CsI(Tl) and glass, some of the scintillation light will be internally reflected within the crystal and can escape at a location not related to the initial gamma ray event. This reflected light creates the background glow seen in the previous crystal images. This background obscures the true signal when performing light integration which also limits the signal to noise ratio.

In order for lens coupled CCD preclinical SPECT to become feasible, the sensitivity will have to be increased. This can be achieved by improving the optical transfer from the scintillator to the CCD and by using a more sensitive CCD photodetector. Also, for integration mode the background glow caused by internal reflections within the monolithic crystal could be reduced by blackening the crystal sides that are not viewed by the CCD. If the overall sensitivity is high enough, individual gamma ray flashes can be measured, allowing counting mode to be achieved. Counting mode experiments using highly sensitive electron-multiplying CCDs will be shown in the next two chapters.

Chapter 5

TC253 EMCCD SPECT

5.1 Overview

In order to improve the overall sensitivity of the CCD based SPECT system, several modifications were made. These modifications included switching from a regular CCD to an electron-multiplying CCD (EMCCD) for a better SNR, using a 4-stage Peltier to improve cooling, and using a FPGA (field programmable gate array) card for clocking to achieve a faster readout rate. Instead of trying to upgrade the existing CCD system, an entirely new EMCCD based system was designed and constructed. Although commercially available EMCCD camera systems existed, due to their high cost we opted to build our own. This reduced the cost per camera by an order of magnitude ($30k to $3k USD), thereby allowing us to surround the animal with multiple cameras at reasonable expense. Details of the hardware, FPGA software, EMCCD characterization, and initial SPECT line phantom images for the prototype camera are discussed in this chapter.

5.2 Hardware

A schematic of the EMCCD system is shown in Figure 5.1. The system consists of a PC with a PCI based FPGA card, an electronics box, and the EMCCD camera housing.
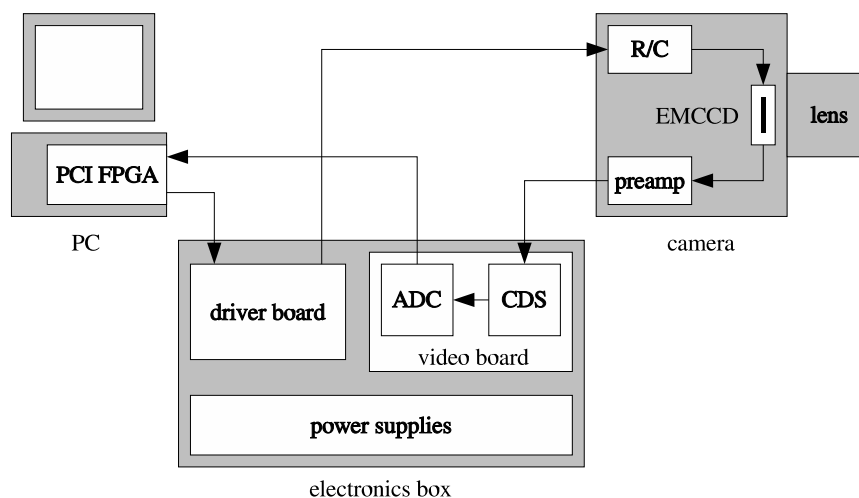
Figure 5.1: A schematic of the EMCCD setup. The three main components are the PC with FPGA card, the electronics box, and the camera housing.

The FPGA card produces the clock pulse timing for the EMCCD. These pulses are sent to the driver board inside the electronics box which converts the TTL pulses to the proper voltages needed to drive the EMCCD. The driving pulses are then sent through an R/C circuit located inside the camera housing for shaping before entering the EMCCD. The video signal from the EMCCD is first sent through a preamp and then through a video board. The video board uses correlated double sampling (CDS) of the video signal to help reduce noise before digital conversion in a 16-bit analog to digital converter (ADC). The digitized video signal is then sent back to the FPGA card which uses a DMA FIFO across the PCI bus to store the

data on the host computer which is running LabVIEW 8.0. Details of the individual hardware components follow.

5.2.1 TC253 EMCCD

The Texas Instruments Impactron$^{\text{TM}}$ TC253 EMCCD chip (TC253SPD-B0) was used for the prototype camera. This front-illuminated chip has 7.4 μm x 7.4 μm sized pixels in a 500 x 680 pixel, 1/3 inch format with 100% fill factor (340,000 pixels total). The TC253 has a read noise of 29 electrons/pixel RMS at video rate readout (12.5 MHz clock frequency). It also has low dark current generation (≈ 0.1 electron/pixel/sec at -40 °C) and a built in single-stage Peltier element capable of cooling the chip down to -10 °C. Figure 5.2 shows a close up photo and schematic of the TC253.
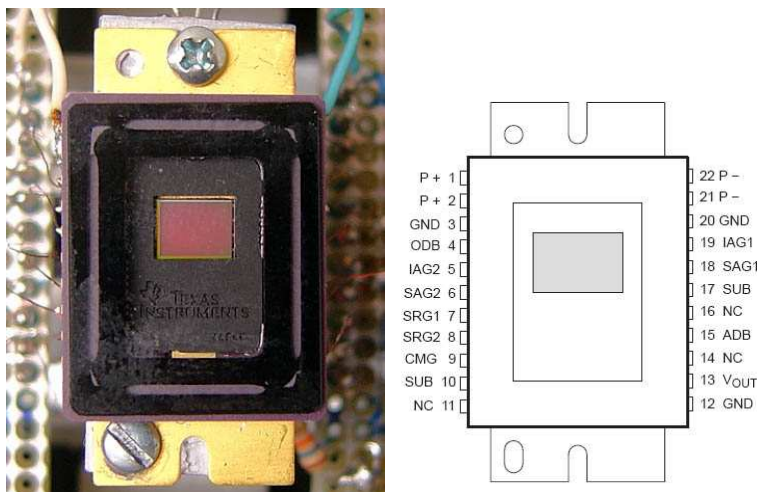
Figure 5.2: A photo and schematic showing the front face of the Texas Instruments Impactron$^{\text{TM}}$ TC253 EMCCD. The image area (500 x 680 pixels) measures 3.7 mm x 5.0 mm. Schematic courtesy of Texas Instruments.

A schematic of the TC253 architecture in Figure 5.3 shows the five main

components which are the image sensing area, image storage area, serial readout register, charge multiplier, and output amplifier. The image sensing area measures 500 x 680 pixels, or 500 lines with 680 pixels in each line. The first 24 pixels in each line of the image sensing area are masked to serve as dark reference pixels for that line. The first 4 lines of the image sensing area are also masked to serve as isolation lines between consecutive frames.

The start of the signal integration time is marked by the application of a positive Clear pulse (12.5 V, minimum width 1 μs) to the antiblooming drain (ODB, pin 4) which clears the unwanted charge from the image sensing area. As light then enters the silicon in the image sensing area, electrons are generated and collected in the potential wells of the pixels. Applying a suitable DC bias to ODB during this time (5.3 V) provides for blooming protection by draining away electrons that exceed this bias. This creates a typical full-well capacity of 44k electrons for the image sensing area pixels. After the integration cycle is completed, the entire frame of collected charge is parallel transferred to the image storage area by applying properly timed pulses (or clocks) to the image area gates (IAG1 and IAG2) and storage area gates (SAG1 and SAG2). Reducing the ODB level to 4.9 V during the parallel transfer to the image storage area prevents the creation of undesirable artifacts caused by the on-chip cross talk between the image area gate clock lines and the antiblooming drain bias lines. A single line (680 pixels) is then parallel transferred from the image storage area to the serial readout register using just the SAG1 and SAG2 gates. For a conventional CCD, the charge in the serial register would then be serially transferred directly to the charge-to-voltage output amplifier using the serial register gates (SRG1 and SRG2). For an EMCCD, the charge is first serially transferred through an extra serial register, known as the gain or

multiplication register, before being sent to the output amplifier. This process is repeated line by line until the entire image storage area has been readout. Due to the double length of the entire serial register, the first line out of the TC253 does not contain valid data and can be discarded.
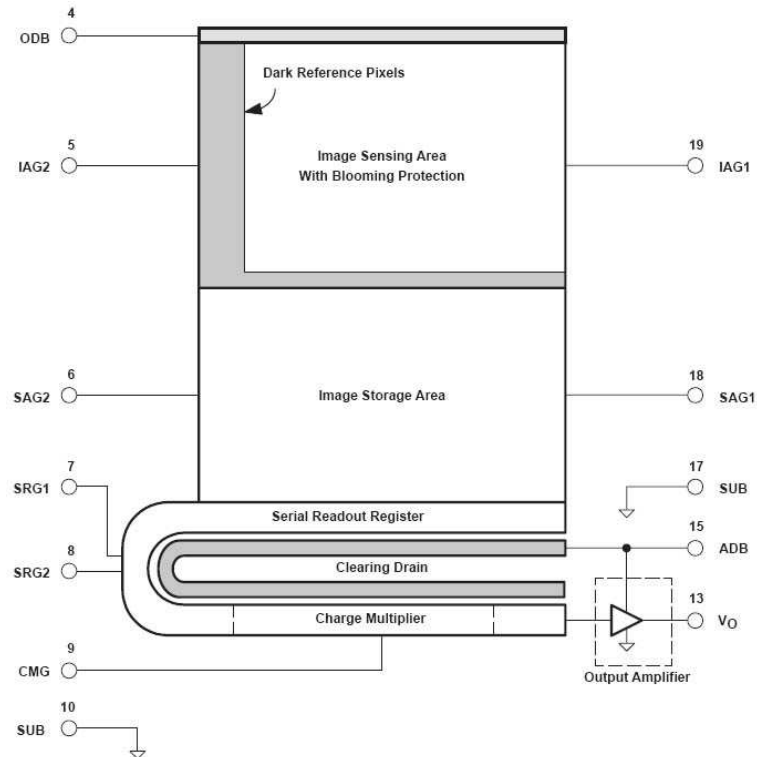
Figure 5.3: A schematic of the TC253 architecture. The five main components are the image sensing area, image storage area, serial readout register, charge multiplier, and output amplifier. Schematic courtesy of Texas Instruments.

The multiplication register differs from the normal serial register by the addition of a third gate known as the charge multiplication gate (CMG) [57]. By making the voltage of the CMG very high (up to 15 V for the TC253) the electrons undergo impact ionization as they move through the multiplication register, which amplifies the electric signal. The level of signal amplification is proportional to the

voltage applied to the multiplication gates. Although the gain per pixel step is low (1.01 to 1.018) a multiplication register of 400 pixels in length can allow gains of over 1000x to be reached [58]. Multiplication of the signal in the charge domain before charge-to-voltage conversion effectively reduces the readout noise of the output amplifier to less then 1 electron/pixel. This eliminates the noise floor found in conventional CCDs making EMCCDs sensitive to single electrons even at video rate readout ($>$ 30 frames/sec).

The charge in each pixel is then serially transferred from the multiplication register to the output amplifier. The output amplifier performs the charge-to-voltage conversion for each pixel to produce the video signal output at V_{out} (pin 13). The charge conversion gain of the TC253 output amplifier (with the electron multiplication gain turned off) is 9 μV/electron. A schematic of the video signal output is shown in Figure 5.4. The output for each pixel contains two parts: the reset level and the output signal level. When no charge is present within the pixel, the minimum voltage difference between the reset and signal levels (the zero offset signal V_{off}) is typically 90 mV. The zero offset signal remains approximately constant, is not caused by dark current, is independent of temperature, and may vary with the amplitude of the serial register gates (SRG1 and SRG2). As the number of electrons per pixel increases, the difference between the reset and signal levels increases proportionately. This voltage difference is then measured and digitized by the video board to give a 16-bit value for each pixel.

5.2.2   FPGA Card

A National Instruments PCI-7811R FPGA card was used to produce the clear, parallel, and serial clock pulse timing for the TC253 EMCCD. The 7811R was also
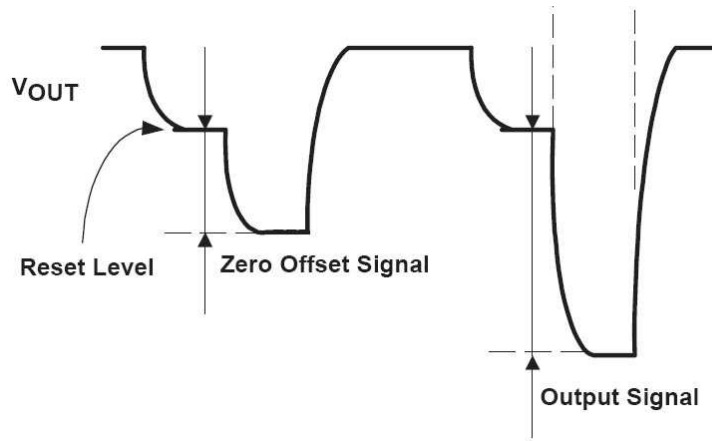
Figure 5.4: A schematic of the TC253 video signal for two pixels. The left pixel has no charge present and gives a zero offset signal, while the right pixel has some charge and gives a larger output signal. Schematic courtesy of Texas Instruments.

used to produce the pulse timing for the correlated double sampling circuit of the video board, the shutter, and to read in the 16-bit output from the ADC. The Xilinx FPGA chip used in the 7811R had one million gates, 25 ns resolution, 40 MHz loop rate, and ran independently from the host PC clock. The 7811R also had 160 digital input/output channels that were TTL compatible.

One of the four 68-pin VHDCI digital connectors on the back of the 7811R was connected via a shielded cable (SH68-C68-S) to an unshielded connector box (CB-68LP, 68-pin D-type) which had 68 screw terminals. Two color-coded flat ribbon cables were then used to connect the screw terminals to the electronics box, with one cable going to the driver board and the other to the video board via two 50-pin IDC connectors in the electronics box. Table 5.1 shows the corresponding 7811R output signals, FPGA DIO channel, connector box terminal number, and electronics box connector pin number. Table 5.2 shows the wire color, number, and signal for the ribbon connector going from the connector box to the driver board. All

even wires in the ribbon connector were grounded to improve shielding and reduce wire crosstalk.

The FPGA code was programmed using the National Instruments LabVIEW FPGA module that ran inside of LabVIEW 8.0. This FPGA module allowed graphical programming of the FPGA logic for rapid testing and development. After successful compilation on the host PC, the FPGA code was then downloaded to the 7811R target for independent execution. Details of the FPGA code are given in Section 5.3.

Signal	FPGA DIO	Box Terminal	50 Pin IDC
ODB1	15	57	22
ODB2	17	58	23
IAG1	5	31	32
IAG2	7	32	34
SAG1	1	33	36
SAG2	3	34	38
SRG1	9	60	25
SRG2	11	59	24
CMG	13	61	26
PSH	41	53	18
SSH	39	54	19
OSH	43	52	17
CON	33	51	16
Shutter	19	30	30

Table 5.1: A table showing the output signal paths from the 7811R to the electronics box.

Color	Number	Signal	Number	Signal
Black	0		10	
Brown	1	SAG1	11	SRG2
Red	2		12	
Orange	3	SAG2	13	CMG
Yellow	4		14	
Green	5	IAG1	15	ODB1
Blue	6		16	
Violet	7	IAG2	17	ODB2
Gray	8		18	
White	9	SRG1	19	Shutter

Table 5.2: A table showing the wire color, number, and signal for the ribbon cable going from the connector box to the driver board. All even numbered wires were grounded.

5.2.3 Driver Board

The clocking pulses from the 7811R are first sent to the driver board inside the electronics box. A picture of the driver board is shown in Figure 5.5. The driver board uses high speed analog switches to convert the TTL pulses from the 7811R to the proper voltage levels needed to move the charge though the TC253. This circuit is based on a schematic from the TC253 datasheet. The positive and negative voltages (or high and low rails) for the pulses are adjusted using a corresponding 10 turn potentiometer. Minimizing the clocking voltages is an important step in tuning the TC253 as will be discussed in Section 5.4.1. The nominal values for the different voltages are shown in Table 5.3. Some of the clock voltages were grouped according to the TC253 application note and are adjusted using a single potentiometer. The driver board also contains the CMG and ODB driver circuits that were also based on schematics from the TC253 datasheet.
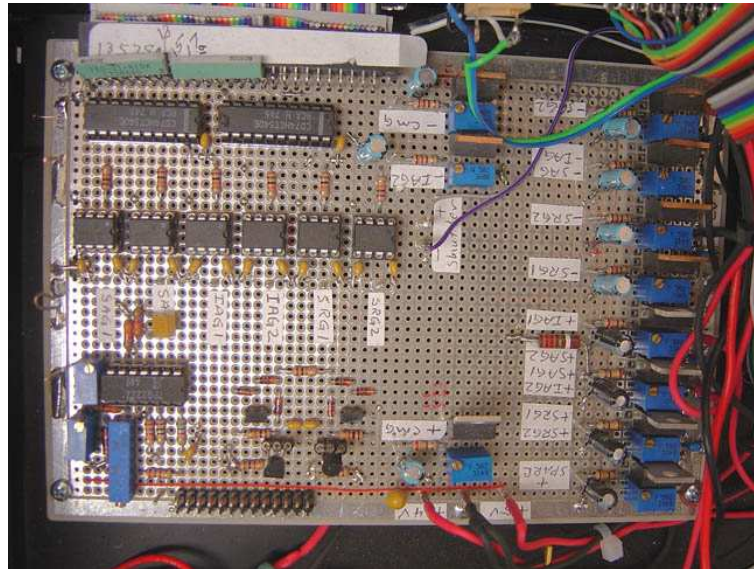
Figure 5.5: A photo of the TC253 driver board inside the electronics box. The voltage levels for the different pulses are adjusted using the 10 turn potentiometers.

	Signal	Nominal Voltage (V)
Parallel	+IAG1	5.2
	+IAG2	3.1
	+SAG1	
	+SAG2	
	-IAG1	-6.0
	-SAG1	
	-IAG2	-6.7
	-SAG2	-6.7
Blooming	Clear	12.5
	Anti-Blooming	5.3
	Transfer	4.8
Serial	+SRG1	4.9
	+SRG2	
	-SRG1	-4.3
	-SRG2	-5.5
	+CMG	7.0 (Gain 1)
	-CMG	-2.8

Table 5.3: A table showing the nominal voltages for the TC253 clocking signals.

5.2.4 Camera Housing

A photo of the camera housing is shown in Figure 5.6. The TC253 was mounted to an Aluminum cold-finger which sat on top of a 4-stage Peltier element. Heat was removed from the output surface of the Peltier using an air or liquid based heat exchanger. The air based heat exchanger was capable of cooling the TC253 to -25 °C, while the liquid based heat exchanger could cool the TC253 to -50 °C using cooled ethanol. A close up photo of the camera housing circuit board is shown in Figure 5.7. Low thermal conductivity wires connected the TC253 to the R/C and preamp circuitry. The R/C circuit was used to adjust the rise and fall times of the clocking pulses just before they entered the TC253. A rise/fall time of about

200 ns was used to help reduce spurious charge generation by allowing smoother transitions between pixels (see Section 5.4.1). The resulting video signal from the TC253 was then sent through the preamp before leaving the camera housing to the video board. The preamp was constructed from an Analog Devices AD829 integrated circuit which amplified the video signal by 5.5x gain. The circuit board also held the vacuum sensor and connectors for the temperature sensor located inside the Aluminum cold-finger. All of the camera housing components were held under a vacuum to reduce condensation. Figure 5.8 shows an exploded view of the camera assembly showing the lens, shutter, vacuum window, camera housing, and a choice of either air or liquid heat exchanger. A picture of the assembled camera is shown in Figure 5.9.
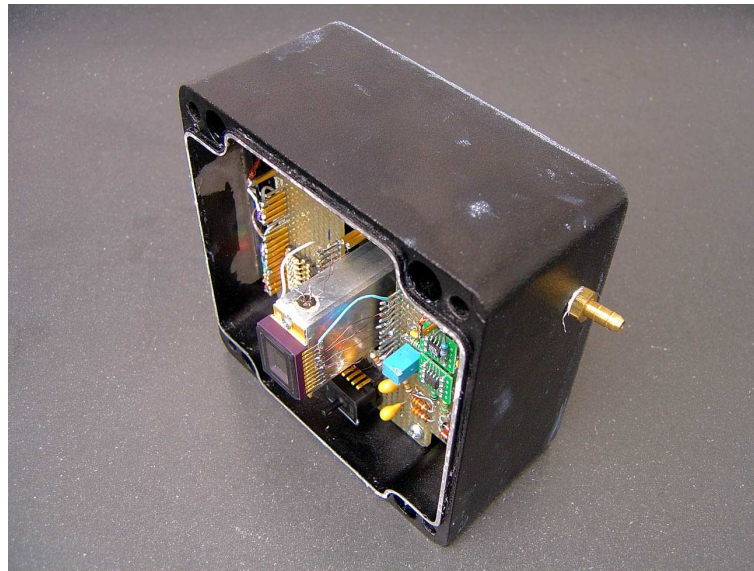
Figure 5.6: A photo of the camera housing. The TC253 can be seen mounted to the top of the Aluminum cold-figer. All components inside the housing are held under vacuum to reduce condensation.
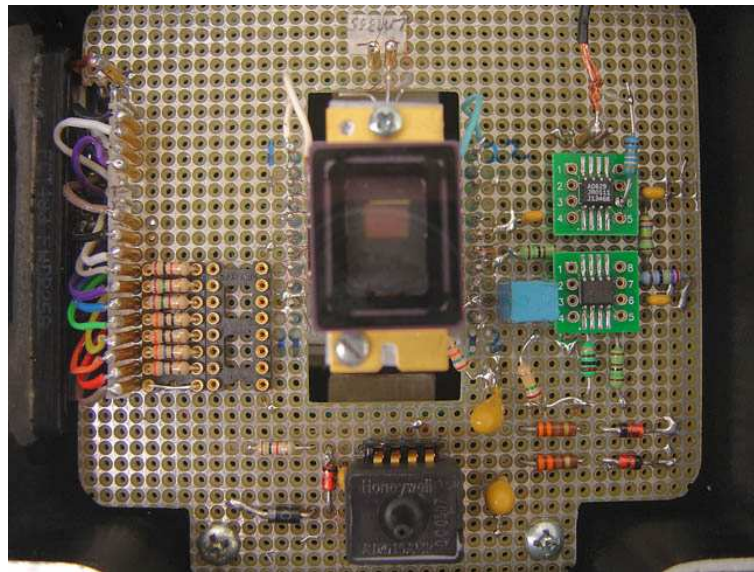
Figure 5.7: A photo of the TC253 circuit board inside the camera housing. The R/C network, preamp, vacuum and temperature sensors are connected to the circuit board.
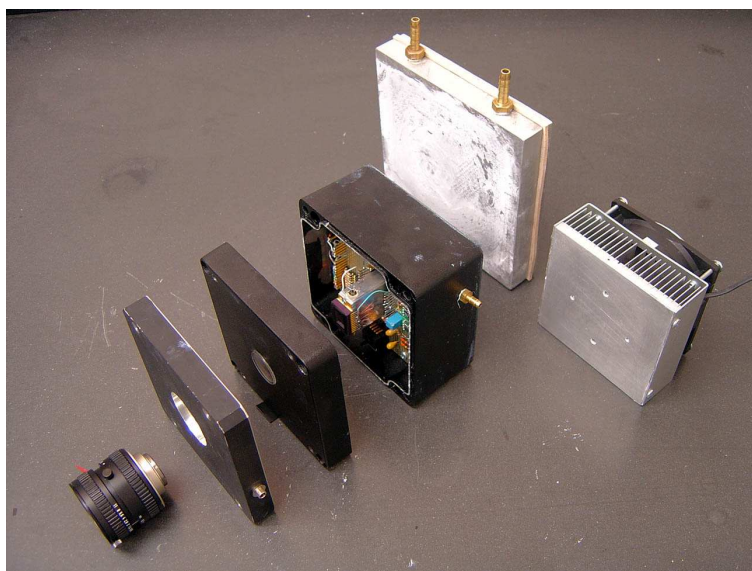
Figure 5.8: A photo showing an exploded view of the camera assembly. From left to right are the lens, shutter, vacuum window, housing, and choice of either liquid (upper) or air (lower) heat exchanger.

Figure 5.9: A photo of the assembled TC253 EMCCD camera with the air heat exchanger.

5.2.5 Video Board

The video board consists of a correlated double sampling (CDS) circuit and a 16-bit (65,535 digital units) analog-to-digital converter (ADC). A photo of the video board is shown in Figure 5.10, and a schematic of the circuit is shown in Figure 5.11. The video signal from the TC253 is first amplified by the preamp on the camera housing circuit board. This preamp multiplies the signal by a gain of 5.5x and also moves the DC level from 5 V to 0 V. The adjusted video signal then enters video board and into the CDS circuit. Details of the CDS and ADC circuits are described next.

CDS Circuit

Upon entering the video board the video signal first passes through C1 (10 μF) and R8 (variable). R8 is adjusted so that the precharge (or reset) level of the video signal is close to 0 V without becoming positive. The DC offset for the precharge level was set to -500 mV. The signal then goes through U1 where it is multiplied by a gain of 2x. Diode D1 then cuts off any signal above 0.5 V. The signal then passes though U2 which was set to a gain of 1x (no gain). U3 (also set to a gain of 1x) then inverts the video signal. From U3 the video signal then goes to integrated circuit U8.

U8 uses the precharge sample and hold (PSH) and signal sample and hold (SSH) pulses from the 7811R FPGA card to sample the precharge and signal voltage levels of the video signal. The voltages sampled during the PSH and SSH pulses are used to charge capacitors C22 and C23 respectively. The values of C22 and C23 (220 pF) and the corresponding R11 and R12 (511 Ohm) determine the RC time constant for the sampling circuit which was 112 ns. In order to completely sample the precharge and signal voltage levels the PSH and SSH pulses need to
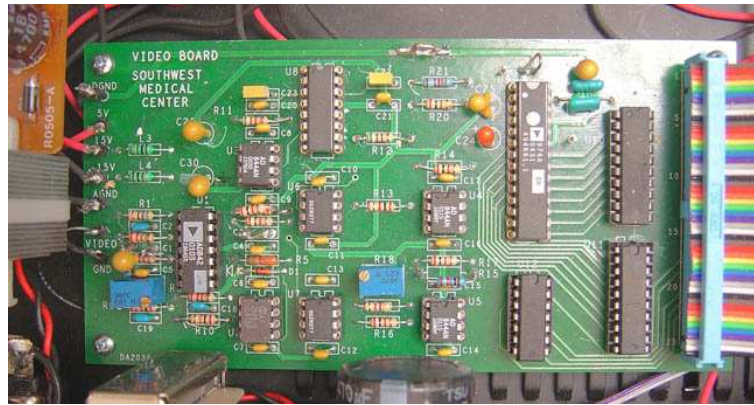
Figure 5.10: A photo of the video board inside the electronics box.

be at least five RC time constants long, or ≥ 562 ns. The sampling pulses were set to 975 ns, which is enough time to accurately sample the voltage levels of the video signal pixel. The voltage levels on C22 and C23 are then measured by U6 and U7 respectively. U6 and U7 require very low current (pA) to read the capacitors and thus do not significantly change the value. During the output sample and hold (OSH) pulse from the 7811R FPGA, the voltage difference between the outputs of U6 and U7 should correspond to the voltage difference between the precharge and signal levels for the previously sampled pixel. The PSH output of U6 is then put through U4 (gain of 1x) which inverts the signal. U5 then adds the inverted PSH signal (U4 output), the SSH signal (U7 output), and a DC shift from R18 (variable), and multiplies the output by a gain of 5.4x. The output from U5 then passes through R20 (200 Ohm) and then goes to the input of the ADC (V_{in}, pin 1). The input of the ADC varies from +10 V (0 digital units, minimum value) to -10 V (65,535 digital units, maximum value). R18 was adjusted so that the V_{in} signal was close to +10 V. The resulting bias level for a 0 second exposure (no light, minimum signal) was approximately 5000 digital units. This bias drops slightly below 5000

DU for bright exposures.
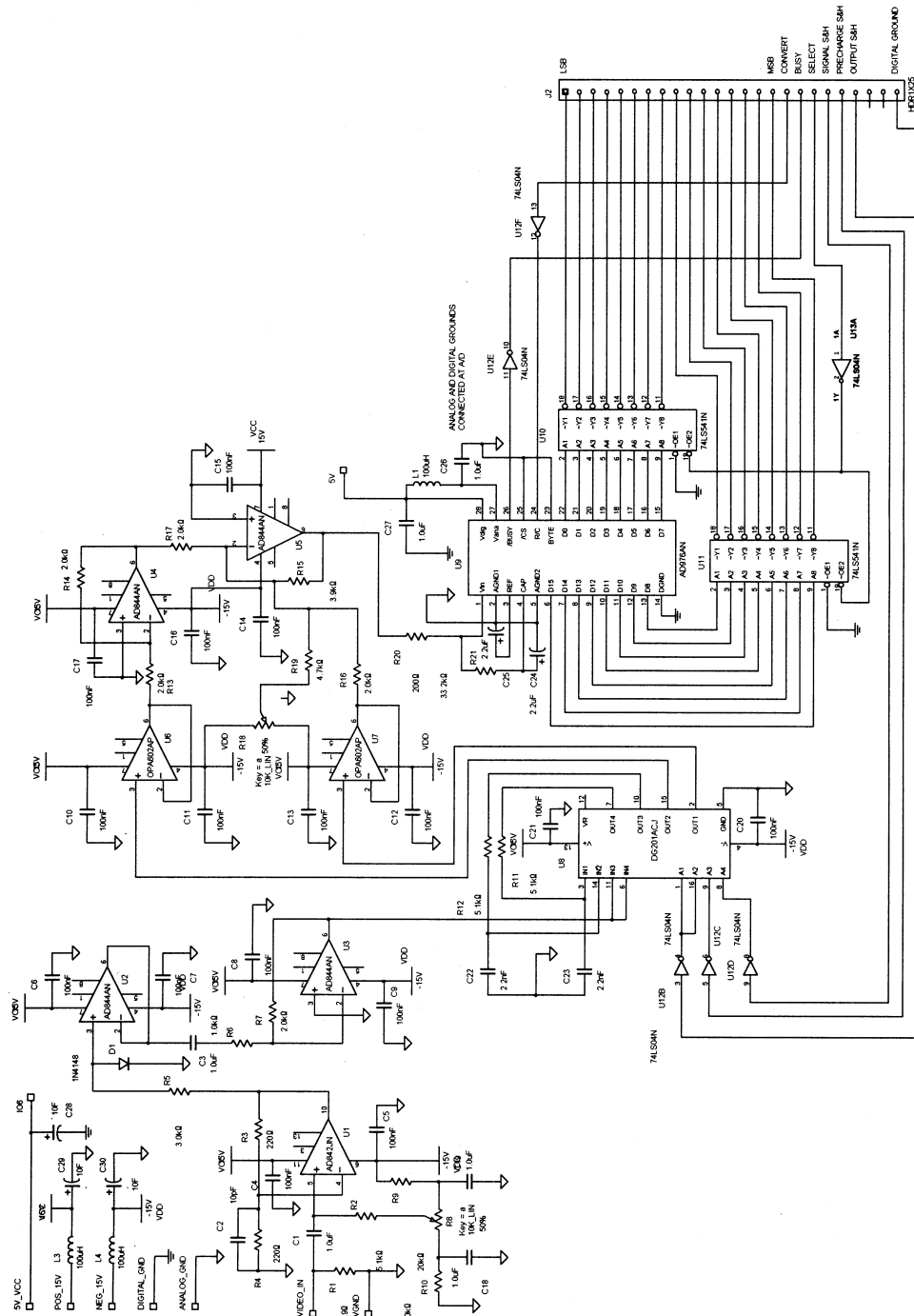
Figure 5.11: A schematic of the video board circuit, courtesy of Billy Smith.

16-bit ADC

The video board uses an Analog Devices model AD976A 16-bit ADC to digitize the voltage level from U5. The AD976A has an analog full-scale input range of ± 10 V with a maximum throughput frequency of 200 kHz. At 200 kHz the 340,000 (500 x 680) pixels of the TC253 are readout in 1.7 seconds. A schematic of the AD976A pin configuration is shown in Figure 5.12. The measured voltage corresponding to the difference between the precharge and signal levels for a single pixel is sent from the U5 output to the V_{in} input of the AD976A (pin 1). When the V_{in} voltage is ready to be digitized, the AD976A is triggered by the convert (CON) pulse originating from the FPGA card. The CON pulse is first inverted by U12 and then sent to the $R/\overline{C}$ (Read/Convert) input (pin 24) of the AD976A. When the $\overline{CS}$ (Chip Select) input (pin 25) is tied low (grounded), a falling edge on $R/\overline{C}$ puts the AD976A internal sample/hold into the hold state and starts a conversion. During conversion the $\overline{BUSY}$ output signal (pin 26) goes low for a maximum time of 4 μs. This 4 μs conversion time is what limits the throughput for the AD976A ADC to 200 kHz. When $\overline{BUSY}$ goes high (with $\overline{CS}$ tied low and $R/\overline{C}$ high) the output data for the pixel are ready on the 16 output data bits (D0 though D15) and are available until the next CON pulse. The 16-bit data for a pixel are then read by the 7811R FPGA card when the OSH pulse goes high. A schematic of the ADC pulse timing is shown in Figure 5.13. Table 5.4 shows the 16-bit signal paths from the output of the ADC, to the 50 pin IDC of the electronics box, to the terminals of the connector box, and finally to the inputs of the 7811R FPGA card. Table 5.5 shows the wire color, number, and signal for the ribbon cable going from the video bard to the connector box.
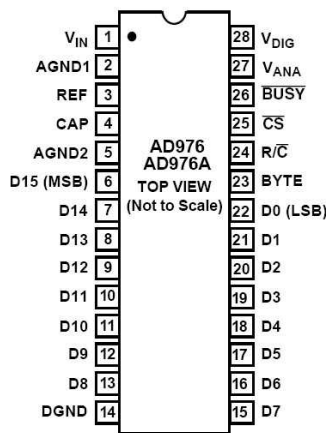
Figure 5.12: A schematic of the Analog Devices model AD976A ADC pin configuration. The 16-bit output is read from pins D0 though D15. Schematic courtesy of Analog Devices.

Total Video Gain

The total charge conversion gain (without electron multiplication) from the output amplifier of the TC253 is 9 μV/electron. The total video gain (preamp plus video board) is 59x (5.5 x 2 x 5.4) giving a total charge conversion gain of 531 μV/electron. The ADC constant is 20 V/65536 Digital Units or 305 μV/DU. This gives an electron to DU ratio of 0.57 e/DU (DU = digital units). At this setting, the maximum electron capacity of the gain register pixel well (about 46k electrons) corresponds to the maximum output of the ADC (about 60,000 DU).
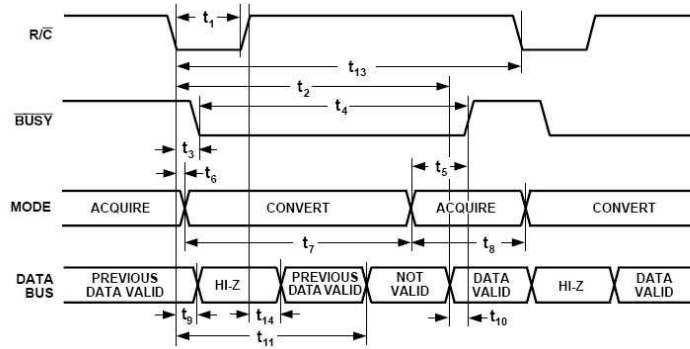
Figure 5.13: A schematic of the AD976A pulse timing. The data for a single pixel conversion, initialized by R/$\overline{\text{C}}$ going low, are available at DO through D15 when $\overline{\text{BUSY}}$ goes high. Schematic courtesy of Analog Devices.

Signal	50 Pin IDC	Box Terminal	FPGA DIO
D0	1	35	0
D1	3	36	1
D2	5	37	2
D3	7	38	3
D4	9	39	4
D5	11	40	5
D6	13	41	6
D7	15	42	7
D8	17	43	8
D9	19	44	9
D10	21	45	10
D11	23	46	11
D12	25	47	12
D13	27	48	13
D14	29	49	14
D15	31	50	15

Table 5.4: A table showing the 16-bit input signal paths from the video board to the 7811R FPGA card.

Color	#	Signal	#	Signal	#	Signal	#	Signal	#	Signal
Black	0		10		20		30		40	
Brown	1	D0	11	D5	21	D10	31	D15	41	PSH
Red	2		12		22		32		42	
Orange	3	D1	13	D6	23	D11	33	CON	43	OSH
Yellow	4		14		24		34		44	
Green	5	D2	15	D7	25	D12	35		45	
Blue	6		16		26		36		46	
Violet	7	D3	17	D8	27	D13	37		47	
Gray	8		18		28		38		48	
White	9	D4	19	D9	29	D14	39	SSH	49	

Table 5.5: A table showing the wire color, number, and signal for the ribbon cable going from the video board to the 7811R. All even and unused wires in the 50 wire ribbon were grounded.

5.3 Software

The National Instruments PCI-7811R FPGA card is programmed using the Lab-VIEW FPGA module version 8.0.0 that runs under LabVIEW version 8.0. The TC253 code consists of two parts, the *FPGA.vi* and the *Host.vi*. The DIO channels are controlled by the *FPGA.vi* which is compiled on the host PC then downloaded to the 7811R target where it ran independently of the host PC processor. The *Host.vi* then ran on the host PC and calls the *FPGA.vi*. The *Host.vi* sends the data acquisition parameters to the *FPGA.vi* then reads the data produced by the TC253 output. The data from the TC253 are stored in the host PC memory using a DMA (Direct Memory Access) FIFO (First In First Out) buffer. The first part of the FIFO resides in the 7811R, while the second part resides in the host PC memory. The two FIFO parts are bridged using a DMA link across the PCI (Peripheral Component Interconnect) bus with each FIFO element corresponding to a single 16-bit pixel value from the TC253. The FIFO length was set in the *Host.vi* to 344,187 elements which is the number of pixels readout per TC253 frame (680 x 500 pixels). If the TC253 readout speed is faster than the PCI DMA link, the 7811R FIFO will become full and cause the program to crash. This does not appear to happen for the 200 kHz readout rate of the current electronics. Since the 7811R PCI bus is 32-bit, the readout rate could potentially be doubled by first bundling two 16-bit pixels together before entering the PCI bus and then unbundling them when they reach the host PC memory. Once the data are in the host PC memory, the *Host.vi* is used to display, manipulate, and save the data. Details of the *FPGA.vi* and *Host.vi* are described in this section (5.3).

5.3.1 FPGA.vi

Installation of the FPGA module created an FGPA Input/Output (I/O) function icon in the Functions Palette of the *FPGA.vi* Block Diagram. The FPGA I/O Node function was then used to control the individual Digital I/O (DIO) channels of the 7811R. Properly timed switching of the DIO channels created the pulse sequence needed to readout the TC253 pixel data. The *FPGA.vi* code can be divided into five main sections: Initialize, Clear, Integrate, Transfer, and Readout. Each section corresponds to a step required to readout out a single frame from the TC253. These steps are implemented in the flat sequence structure of the *FPGA.vi* as shown in Figure 5.14. Details of each step are given next.
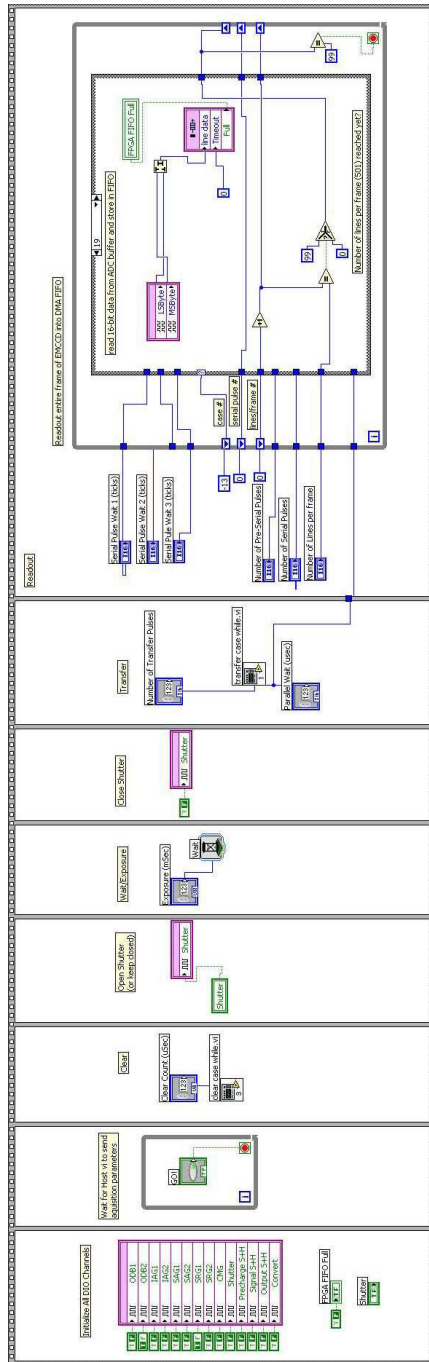
Figure 5.14: A figure showing the block diagram for the *FPGA.vi* code. The eight frames of the flat sequence structure readout one image (680 x 500 pixels) from the TC253.

Initialize

The first step in reading out the TC253 was to initialize all of the 7811R DIO channels used to their default values. This was done by placing a FPGA I/O Node in the first frame of the *FPGA.vi* flat sequence structure. Boolean constants (True or False) were then wired to each FPGA I/O item to set the default value. The initial values for the 14 items and their 7811R DIO channel numbers are given in Table 5.6. Connector 1 on the 7811R was used for all DIO channels. The boolean indicator showing if the 7811R FIFO is full, and the shutter boolean control (passed from the *Host.vi*) also appear in the first frame of the *FPGA.vi*. The second frame of *FPGA.vi* then waits for the acquisition parameters (*e.g.* exposure time and shutter open or closed) to be passed from the *Host.vi* before proceeding.

Signal	Initial Value	DIO Channel #
ODB1	F	22
ODB2	T	23
IAG1	F	32
IAG2	F	34
SAG1	F	36
SAG2	F	38
SRG1	T	25
SRG2	F	24
CMG	F	26
Shutter	F	30
PSH	F	18
SSH	F	19
OSH	F	17
CON	F	16

Table 5.6: A table showing the initial values and DIO channel numbers for the 14 digital output signals from the 7811R FPGA card.

Clear

Frame three of the *FPGA.vi* code applies the Clear pulse to the ODB drain of the TC253 by calling the *clear case while.vi*. This pulse clears all of the charge from the image sensing area of the TC253 in preparation for light integration. The *clear case while.vi* switches the ODB voltage level from Blooming Control (5.3 V) to the Clear (12.5 V), then back to Blooming Control. The three different voltage levels applied to the OBD drain (Clear, Blooming Control, and Transfer) are controlled by the 7811R DIO signals ODB1 and ODB2. The logic and voltage levels for these signals are shown in Table 5.7. The duration of the clear pulse can be adjusted from the *Host.vi* with a recommended minimum setting of 1 μs. The ODB logic circuit is based on a schematic from the TC253 data sheet and resides on the driver board inside the electronics box.

Signal	OBD1	OBD2	Volts
Clear	F	F	12.5
Blooming Control	F	T	5.3
Transfer	T	T	4.8

Table 5.7: A table showing the DIO logic and voltage levels for the three TC253 ODB drain signals.

Integrate

Frames 4, 5, and 6 of the *FPGA.vi* code open the shutter (if requested by the *Host.vi*), integrate for the given exposure time, and close the shutter respectively. The shutter is opened and closed using the Shutter DIO channel, which triggers the shutter circuit located inside the electronics box. The minimum exposure time for the shutter is 6 ms. The integrate or exposure time is created using a simple wait

function with the input (in milliseconds) being passed from the *Host.vi*.

Transfer

After integration, the next step is to transfer the charge collected in the TC243 image sensing area to the image storage area. This parallel transfer is achieved by applying appropriately timed pulses to the IAG1, IAG2, SAG1, and SAG2 gates. The pulse timing is constructed in the *transfer case while.vi*, which is called in frame seven of the *FPGA.vi* code. The *transfer case while.vi* uses a flat sequence structure with three frames as shown in Figure 5.15. The first frame switches the ODB voltage from Blooming Control (5.3 V) to Transfer (4.8 V), while the third frame sets it back to Blooming Control. The second frame of *transfer case while.vi* contains a case structure inside a while loop. Each case of the case structure has a FPGA I/O node containing the four parallel transfer gates. The boolean constants for the gates are switched in each case to form the timed pulses. A schematic showing the parallel pulse timing and case logic is shown in Figure 5.16, which represents the transfer of two lines from the image sensing area to the image storage area. Six cases are needed to form the pulse sequence with cases 3, 4, 1, and 2 being repeated for each pixel line until the total number of line transfers has been completed. The inquiry in case 3 checks to see if the requested number of line transfers (or pulses) has been reached. Upon completion, cases 5 and 6 close out the pulse sequence and the while loop is then stopped.

When compiled with an FPGA clock speed of 40 MHz (25 ns clock cycle) the minimum pulse width in *transfer case while.vi* was 450 ns. This gave a transfer frequency of 1.1 MHz. In order to reduce this transfer speed, a wait function (measured in microseconds) was placed inside each case of the case structure. These wait

123

functions increased the pulse width of the transfer pulses and reduced the transfer frequency. A slow parallel transfer frequency helps to reduce spurious charge generation as discussed in Section 5.4.1.
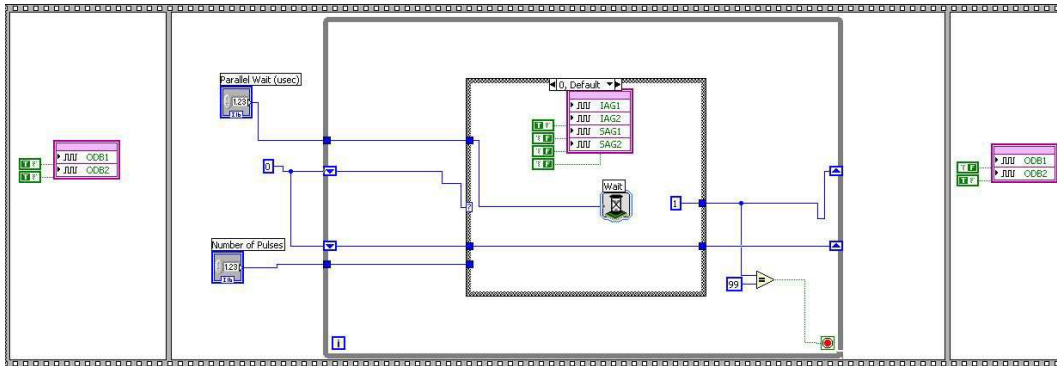
Figure 5.15: A figure showing the block diagram for the *transfer case while.vi* code. The six cases of the case structure move the pixel charge from the sensing to storage area of the TC253.

Readout

The final step in reading out an image frame from the TC253 is to transfer the pixel charge in the image storage area to the charge-to-voltage output amplifier. This is done on a line by line basis in frame eight of the *FPGA.vi* code using a case structure inside of a while loop. A schematic showing the pulse timing and case DIO logic is shown in Figure 5.17. This schematic represents the parallel transfer of one line from the image storage area to the serial register followed by a two pixel serial transfer. A single line from the image storage area is first parallel transferred to the serial register using the SAG1 and SAG2 gates (cases 0 through 3). This line is then serially transferred though the serial and multiplication registers using the SRG1, SRG2, and CMG gates (cases 4 through 19). Figure 5.17 shows that nineteen

124
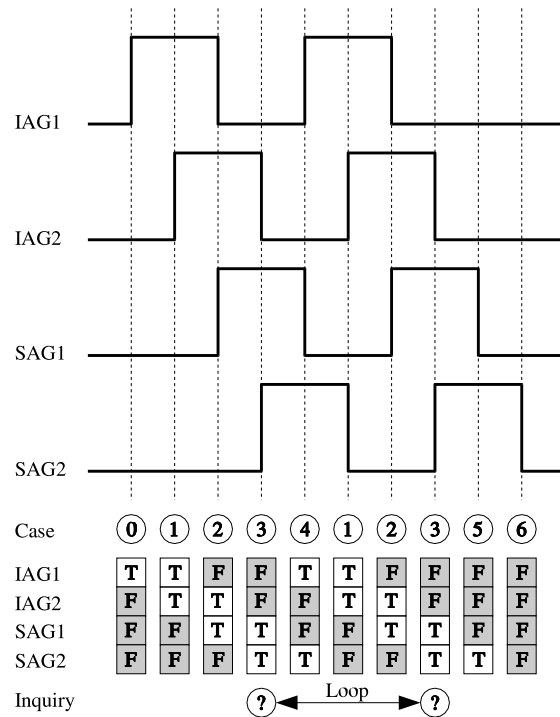
Figure 5.16: A schematic showing the parallel transfer pulse timing and case logic for the IAG1, IAG2, SAG1, and SAG2 gates.

cases are needed to form the pulse sequence for one line. Cases 4 through 15 are repeated for each serial pixel transfer until the entire line has been transferred out of the serial register. The inquiry at case 15 checks to see if the requested number of serial pixel transfers has been reached.

The combined total length of the serial and multiplication registers is 1,366 pixels. This is enough room for two 680 pixel lines with a 6 pixel isolation space between them. After the first line in the serial register has been serially transferred by 686 pixels, the case structure returns to case 0 and a second line is parallel transferred from the image storage area to the serial register. This process is repeated

125

until all 500 lines from the image storage area have been readout, as checked by the inquiry at case 19. Keeping two lines in the serial and multiplication registers greatly improves the readout speed. As a consequence, the first line readout from the TC253 does not contain valid data and can be discarded.

The timing for the four ADC pulses (PSH, SSH, OSH, and CON) are also generated during the readout step. Figure 5.17 shows the ADC pulse timing in relation to the video output signal (V_{OUT}) of the TC253. PSH and SSH sample the video reset and signal levels respectively. OSH calculates the voltage difference between PSH and SSH and presents it to the ADC. CON then triggers the ADC to digitize this voltage difference and send the result to the sixteen digital output buffers D0 though D15. The closing of the OSH signal was extended from case 15 to case 6 so that the output would be available when CON is initialized. The 16-bit output of the ADC is then read by the 7811R FPGA at case 14 (looped 686 times per line) and case 19 (the last pixel for each line). Each ADC read captures the pixel value output from the previous CON pulse. Data from the first CON pulse for each line is not valid and can be discarded.
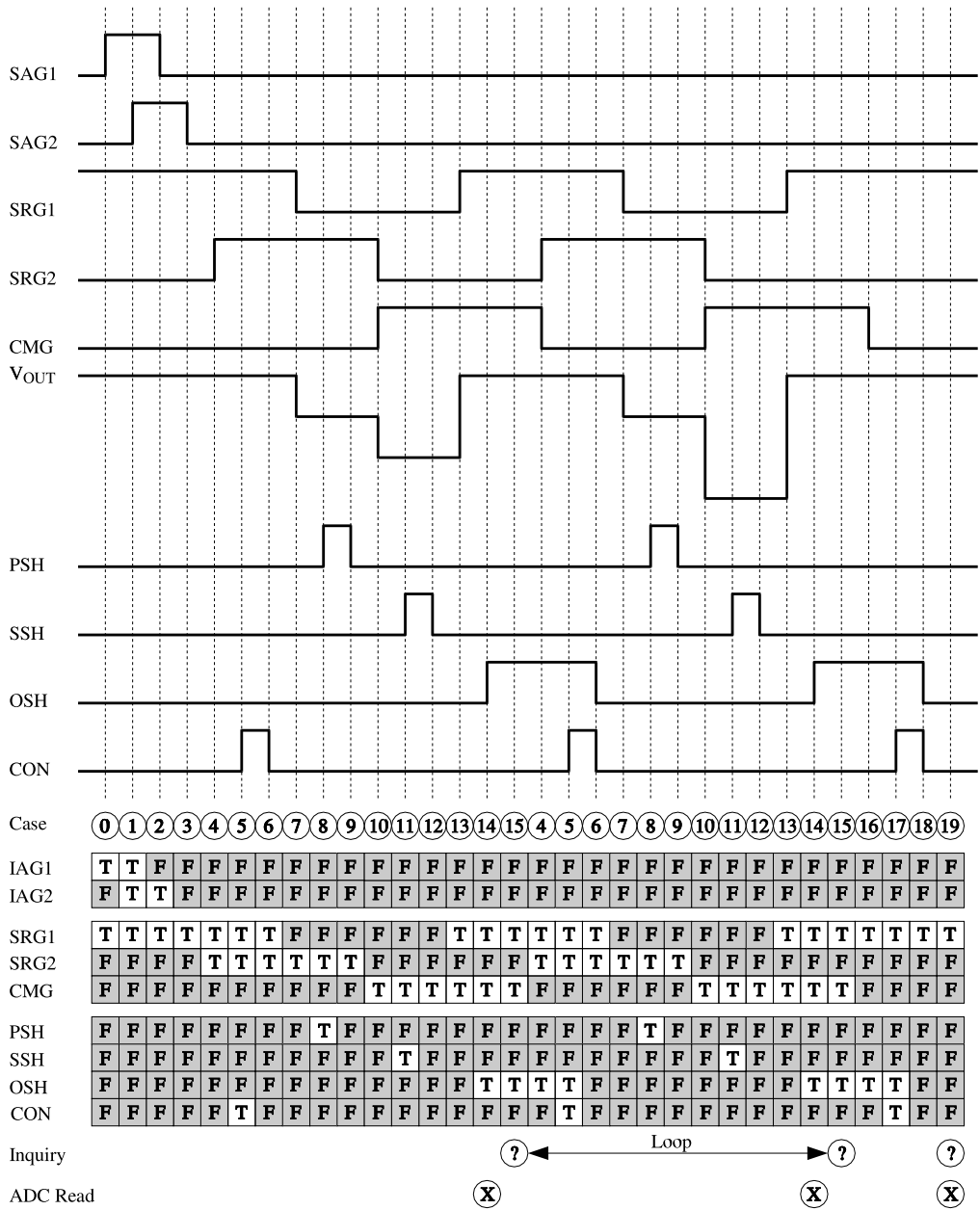
Figure 5.17: A schematic showing the pulse timing and case DIO logic for the readout stage of the TC253. The schematic represents parallel shifting one line from the image storage area to the serial register followed by a two pixel serial shift.

5.3.2   Host.vi

The *Host.vi* code is responsible for acquiring, displaying, manipulating, and saving the TC253 data readout by the *FPGA.vi*. A picture of the *Host.vi* front panel is shown in Figure 5.18. The front panel has three imaging areas or frames. The first two frames (A and B) are separate buffers that can capture independent frames from the TC253, while the third frame (C) can display B–A or A–B. For example, if frame A captures the light image (shutter open) and frame B captures the dark image (shutter closed) for a given exposure time, then frame C can be used to display the dark subtracted image (A - B). The image in each frame can be saved in either text or binary format. Each frame can also display the horizontal or vertical line profile for the current image. The acquisition parameters for frames A and B include exposure time (in milliseconds), acquisition type (single or continuous), shutter setting (open or closed), and frame averaging (off or on). The settings for frame averaging include the number of frames to aquire and whether to display the resulting pixel average or standard deviation in the frame. Once the acquisition parameters have been set and the "Start DAQ" button has been pressed, the *Host.vi* calls the *FPGA.vi* and transfers these parameters. The data for a single frame (344,187 pixels) are then readout from the DMA FIFO. Each pixel value is converted from the "binary twos complement" output of the ADC to a scale where 0 is no light and 65,535 is the maximum light. After reshaping and transposing, the 16-bit data array it is sent to either frame A or B for display. Other acquisition options in *Host.vi* include setting the length of the clear pulse, the number of pre-serial pulses, and adjusting the wait times for the parallel and serial shifts. Once these options have been properly tuned to reduce noise, they do not need to be further adjusted. The block diagram for the *Host.vi* is shown in Figure 5.19.
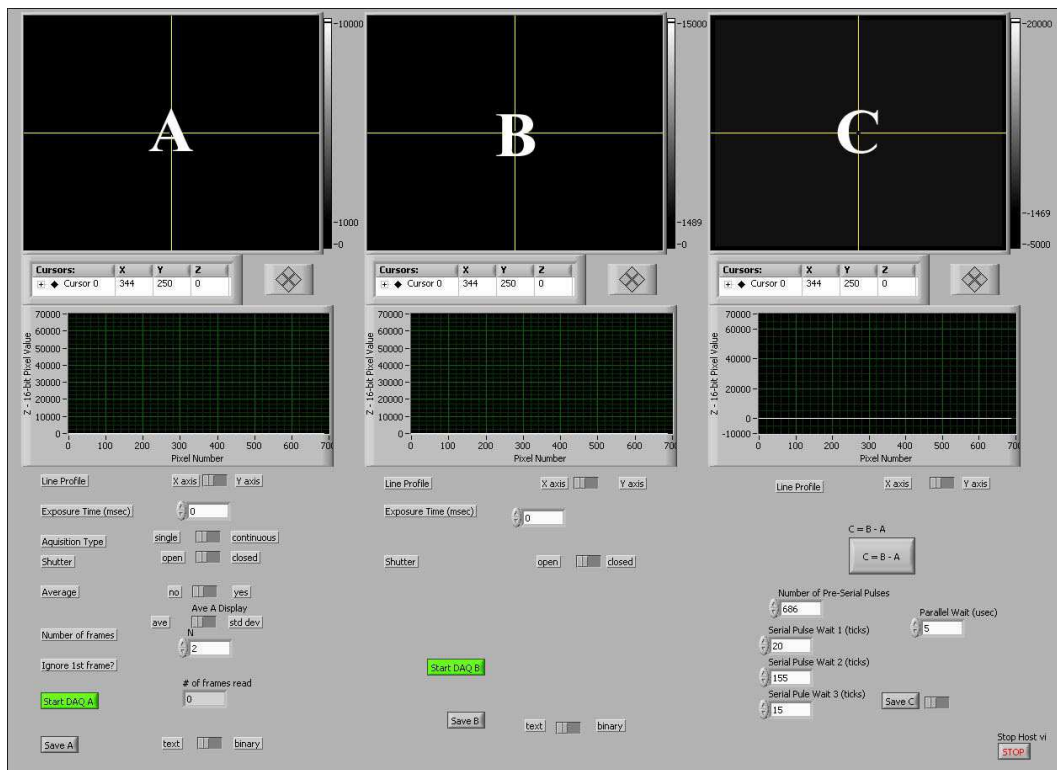
Figure 5.18: A picture showing the front panel of the Host.vi. Images from the TC253 can be stored in either frame A or B. Frame C can display either A–B or B–A.
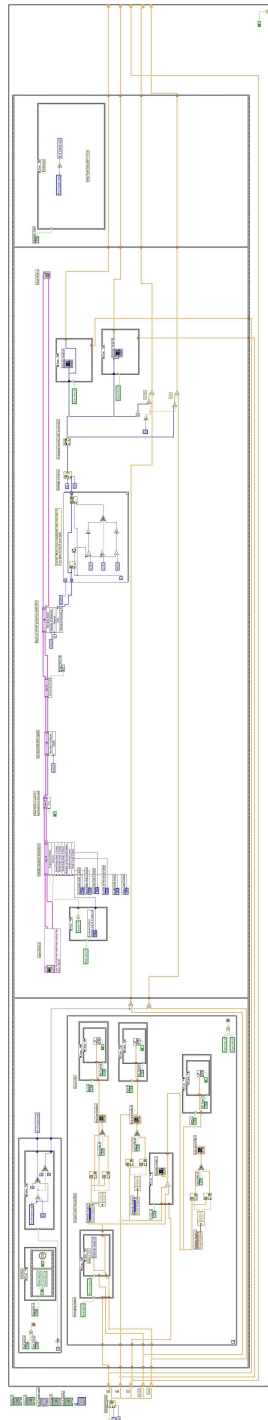
Figure 5.19: A picture showing the block diagram of Host.vi.

130

5.4 Results

5.4.1 TC253 Characterization

Once the hardware and software for the prototype EMCCD camera were completed, the TC253 was then characterized by measuring the gain, dark current accumulation rate, total read noise, and spurious charge generation to verify that they were within the specified operating ranges. Methods and results for these measurements are described here. All measurements were taken at -40 °C.

Gain

The gain versus the positive CMG voltage of the TC253 was measured using lens coupling and a controlled light source. The light source consisted of a 3 mm diameter green LED embedded in a 10 mm x 15 mm Teflon cylinder to create a small diffuse uniform source that was viewed on end (see Figure 5.20). With the TC253 gain set to 1 (+CMG = 7.0 V), the current to the LED was varied until a SNR of about 5 was achieved for an average of 1000, 33 msec exposures as shown in Figure 5.20(a). The difference between the dark reference pixels (the first 24 pixels of each line) and the peak signal was measured using a line profile of the averaged image. This measurement was repeated as the +CMG voltage was increased, with the increase between the dark and peak pixels being taken as the gain as shown in Figure 5.20(b). A plot of gain versus +CMG is shown in Figure 5.21. It can be seen that the gain starts to increase past 11 V and rises to over 1000 at 14 V. The difference between the dark pixel values in Figure 5.20(a) and 5.20(b) is due to spurious charge generation in the multiplication register at high +CMG voltages. Methods for reducing this spurious charge are discussed further in this section.
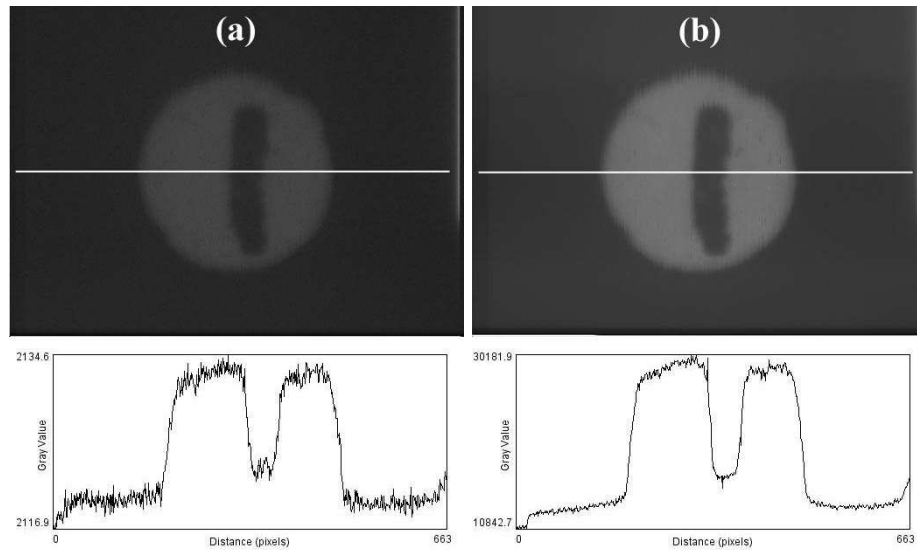
Figure 5.20: The image and line profile for the LED light source with +CMG at 7.0 V (a) and 14.0 V (b). The difference between the dark reference pixels (at the left of each line profile) and the maximum signal gives a gain of over 1000x at 14.0 V).

Dark Current

Dark current arises from the thermal generation of electrons within the silicon lattice of the EMCCD. These electrons are captured by the pixel potential wells and contribute to the non-photon related signal noise (see Equation 2.4). Dark current generation is proportional to exposure time, independent of the amount of light incident on the EMCCD, and can be significantly reduced by cooling [56]. The dark current accumulation rate for the TC253 was measured by taking N exposures at a fixed dark exposure time. The mean and standard deviation of the N exposures were then calculated for each pixel. The ensemble average of the pixel means over the active EMCCD area was taken as the dark current count (electrons/pixel), while the ensemble average of the pixel standard deviations was used to calculate the error
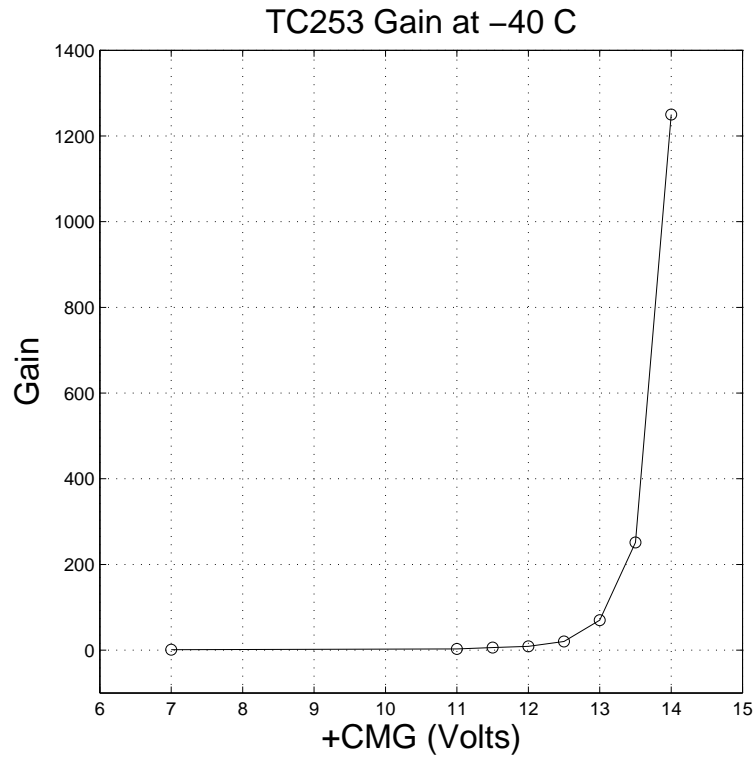
Figure 5.21: A plot of EMCCD gain versus positive charge multiplication voltage (+CMG) for the TC253. A gain of over 1000x is reached at 14 V.

$(\pm\frac{\sigma_x}{\sqrt{N}})$. This measurement was then repeated for several different dark exposure times. For these measurements, the gain was set to 1 (+CMG = 7.0 V) and the EMCCD temperature was -40 °C. A plot of exposure time versus dark current count is shown in Figure 5.22. The fitted slope gives 0.14 electrons/pixel/second which agrees with the dark current rate given in the TC253 datasheet.

Read Noise

The main source of read noise in the system arises from the charge-to-voltage conversion in the TC253 output amplifier. Assuming that the spurious charge has been
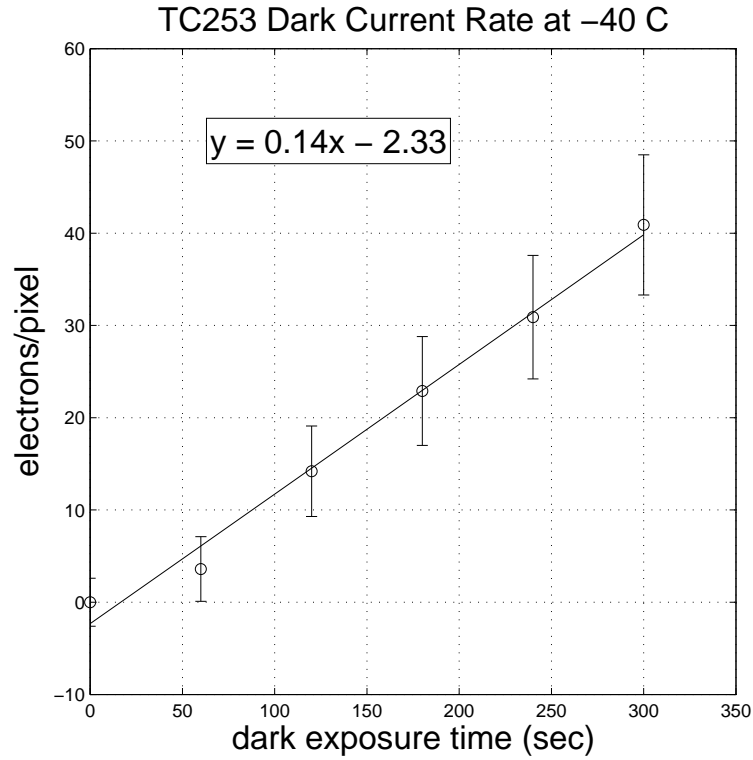
Figure 5.22: A plot of dark current count (electrons/pixel) versus dark exposure time. The fitted slope gives the dark current accumulation rate for the EMCCD at -40 °C.

reduced to a negligible level, then for a zero second dark exposure $(P = D = 0)$ at a gain of 1, Equation 2.4 reduces to:

$$\sigma_t = \sqrt{\sigma_r^2} = \sigma_r \tag{5.1}$$

so that the total noise is equal to the total read noise. The read noise of the system was measured by taking 1000 zero second exposures at a gain of 1 and calculating the standard deviation for each pixel. The ensemble average of the pixel standard deviations over the active EMCCD area was then multiplied by the system video

134

gain (0.57 electrons/ADU) to give a read noise of 18.2 electrons/pixel RMS. This measured read noise was lower than the read noise stated in the TC253 datasheet (29 electrons/pixel RMS) due to the 200 kHz maximum readout rate of the current ADC. Although fine for initial testing, a faster ADC will be needed to achieve video rate readout (12.5 MHz). This will undoubtedly increase the readout noise which is proportional to the readout speed.

Spurious Charge Generation

Along with dark current, non-photon related electrons known as spurious charge (or clock induced charge) can be generated during the readout of the EMCCD. Spurious charge arises from the rapid inversion of the clocking potentials and tends to increase with faster readout speeds and lower temperatures [56, 65]. Methods to reduce spurious charge include 1) using a slow parallel-transfer from the image area to the storage area, 2) setting the rise and fall times of the clocking pulses to about 200 ns, and 3) using the minimum clocking potentials necessary for efficient charge transfer [47, 60]. Of these three methods, the greatest observed reduction in spurious charge for the TC253 was seen by minimizing the clocking potentials [66]. The nominal and minimum clock potentials are shown in Table 5.8.

Spurious charge generation as a function of +CMG was measured for the TC253 by taking 100 zero second dark exposures for a fixed +CMG voltage. The ensemble average of the standard deviations for each pixel was then calculated and taken as the total noise (σ_t). For a zero second dark exposure ($P = D = 0$) Equation 2.4 can be rewritten as:

$$S = \frac{\sigma_t^2 + \sigma_r^2}{F^2 G^2} \tag{5.2}$$

By using σ_t from above, σ_r and G from the previous read noise and gain measure-

	Signal	Nominal Voltage (V)	Minimum Voltage (V)
Parallel	+IAG1	5.2	2.8
	+IAG2		
	+SAG1	3.1	2.1
	+SAG2		
	-IAG1	-6.0	-1.5
	-SAG1		
	-IAG2	-6.7	-5.5
	-SAG2	-6.7	-5.5
Blooming	Clear	12.5	12.4
	Anti-Blooming	5.3	5.3
	Transfer	4.8	4.8
Serial	+SRG1	4.9	3.0
	+SRG2		
	-SRG1	-4.3	-3.8
	-SRG2	-5.5	-5.5
	+CMG	7.0 (Gain 1)	7.0
	-CMG	-2.8	-2.5

Table 5.8: A table showing the nominal and minimum voltages for the TC253 clocking signals. The minimum settings greatly reduce the spurious charge generation.

ments, and knowing that $F \rightarrow \sqrt{2}$ at high gain, the spurious charge generation was calculated to be 3 to 4 electrons/pixel at gains from 500x to 1000x. This spurious charge generation could not be further reduced by the minimizing methods listed above and appears to be an inherent property of the TC253, largely caused by the use of virtual-phase electrode technology [45]. This spurious charge generation is therefore the true noise floor for the TC253 chip making it incapable of single photoelectron sensitivity. Consequences of this measurement are further discussed in Section 5.5. As a comparison, this same measurement was done with a high-quality commercially available EMCCD camera (Princeton Instruments/Acton PhotonMAX 512B with the e2v CCD97 EMCCD) which yielded a spurious charge generation of less than 0.01 electrons/pixel.

5.4.2   Intrinsic Resolution

A schematic of the lens-coupled SPECT setup is shown in Figure 5.23. Two 1-inch format lenses (Schneider Xenon 0.95/25) were coupled front-to-front in order to improve the optical transfer to the EMCCD. Both lenses had an f-stop of 0.95 with the front lens focus set to infinity and the rear lens focus being adjustable. A 3 mm thick monolithic CsI(Tl) crystal was then placed 5 to 10 mm in front of the lenses so that the shallow focal plane (less than 1 mm deep) could be moved through the crystal. The two coupled lenses image a field of view (FOV) on the crystal that is approximately the same size as the image area of the EMCCD ($\approx$ 5 mm x 5 mm). When compared to a single lens imaging the same FOV, we found the optical transfer when using two lenses to be improved by a factor of two.

Figure 5.23: A schematic of the EMCCD SPECT setup. Two lenses are used to improve the optical transfer of the scintillation light to the EMCCD. The lens focal plane can be moved through the crystal.

The intrinsic resolution (R_i) for the above setup was measured using a 30 μm slit Tungsten collimator and a ^{99m}Tc source. The slit was placed on top of the

crystal with the source was placed on top of the slit. The activity viewed by the slit was approximately 50 μCi (1.9 MBq). The line spread function for a 5 minute exposure with the gain set to 200x was acquired. The acquired image and 1 mm wide line profile (taken perpendicular to the slit) are shown in Figure 5.24. Fitting the line spread function profile with a Gaussian distribution gave a FWHM of 110 μm which was taken as the intrinsic resolution. This intrinsic resolution is two to three times better than results from EMCCD systems using fiber optic coupling and light integration [46, 67].
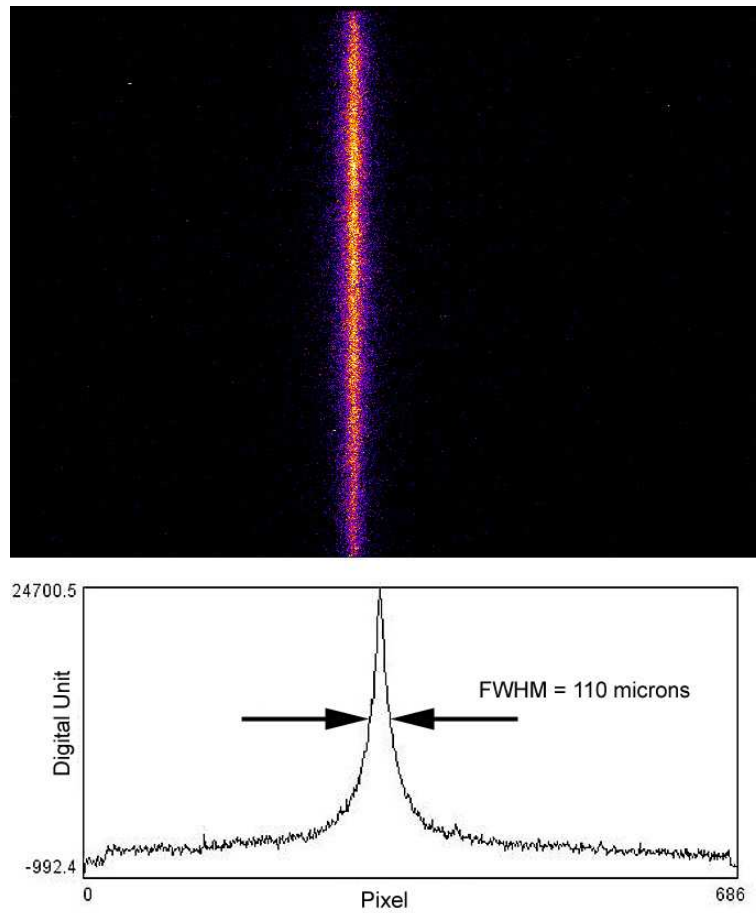
Figure 5.24: The image and line profile produced by a 30 μm slit collimator and ^{99m}Tc source. The exposure time was 5 minutes with a gain of 200x.

5.4.3 ^{99m}Tc Line Phantom SPECT using Light Integration

For SPECT imaging, the Tungsten slit collimator was replaced with a single pinhole Lead collimator. The pinhole diameter was 0.5 mm with an aperture angle of 90 degrees. A small glass capillary tube was filled with aqueous ^{99m}Tc solution, mounted to a step motor, and placed in front of the pinhole. The 3 cm long capillary had an outer diameter of 1.5 mm, an inner diameter of 0.8 mm, and a linear activity of 10 μCi/mm (0.37 MBq/mm). Projection data were then taken as the phantom was rotated (20 projections, 18° step) with a 3 minute exposure time for each projection. The EMCCD gain was set to 1000x at a temperature of -50 °C. Figure 5.25 shows a sample projection of the line source, with the subject FOV measuring 6.0 mm x 4.5 mm.

Image reconstruction was based on the Maximum Likelihood method (MLEM) [68], which was improved with the listmode high resolution algorithm for system matrix modeling (MLSM) [69, 70]. A convolution procedure based on the discrete Fast Fourier Transform (FFT) was used for resolution modeling. If photon scattering is neglected, the blurring component of the matrices which account for the finite resolution effects can be represented as a set of shift-invariant kernels (details given in [70, 71]). Figure 5.26(a) shows a transverse slice of the MLSM reconstruction for the line phantom. The total FOV (20 mm^3) was subdivided into 0.25 mm^3 voxels. Approximately 300,000 events were reconstructed into the voxel array. A Gaussian function (0.4 mm kernel) was used to model the resolution during the 10 iterations. The FWHM of the Gaussian fitted line profile in Figure 5.26(b) measures 0.96 mm. The slight increase in the reconstructed diameter is due to the total resolution of the setup being limited by the geometric resolution (R_g) which was $\approx$ 1 mm.
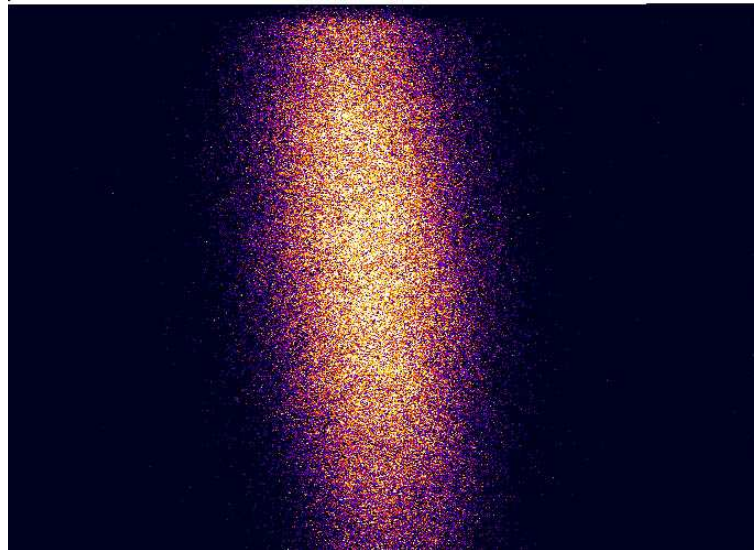
Figure 5.25: A pinhole projection image of a ^{99m}Tc filled line phantom. The source FOV measures 6.0 mm x 4.5 mm with an exposure time of 3 minutes.
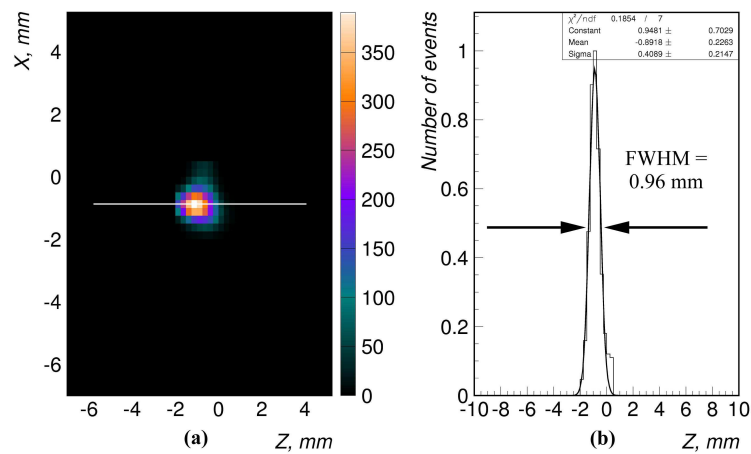
Figure 5.26: SPECT reconstruction of the line source (a) with Gaussian fitted line profile (b). Images courtesy of Dr. N. Slavine.

5.4.4 TC253 Photon Counting

Monolithic CsI(Tl) and Dual Lens Coupling

The ability of the TC253 EMCCD to perform photon counting was first tested with a 3 mm thick monolithic CsI(Tl) crystal and dual lens coupling. For photon counting, the exposure time is reduced until single photoelectric events are observed in the crystal. These events appear as small bright flashes that are above the background noise. Provided there is a minimum degree of overlap, the flashes can be analyzed with image processing to give the position and energy for each event. Photon counting collects list-mode data similar to that produced by PMT based Anger cameras.

Single photoelectric events produced by either ^{125}I (≈ 27 keV) or ^{57}Co (122 keV) could not observed within the crystal using dual lens coupling, even at high EMCCD gain (1000x). Single events were observed using a higher energy ^{137}Cs (662 keV) source. Figure 5.27 shows images produced by the ^{137}Cs source for three different exposure times ((a) 1000 msec, (b) 100 msec, and (c) 33 msec). In Figure 5.27(c) the exposure time has been reduced to a point where single events are observed (33 msec). The image processing results based on Figure 5.27(c) are shown in Figure 5.27(d) where four events have been counted. Details of the image processing algorithm are given in the next Chapter. An explanation of why the TC253 EMCCD was unable to perform photon counting for low energy isotopes is given in the Conclusion section of this Chapter.
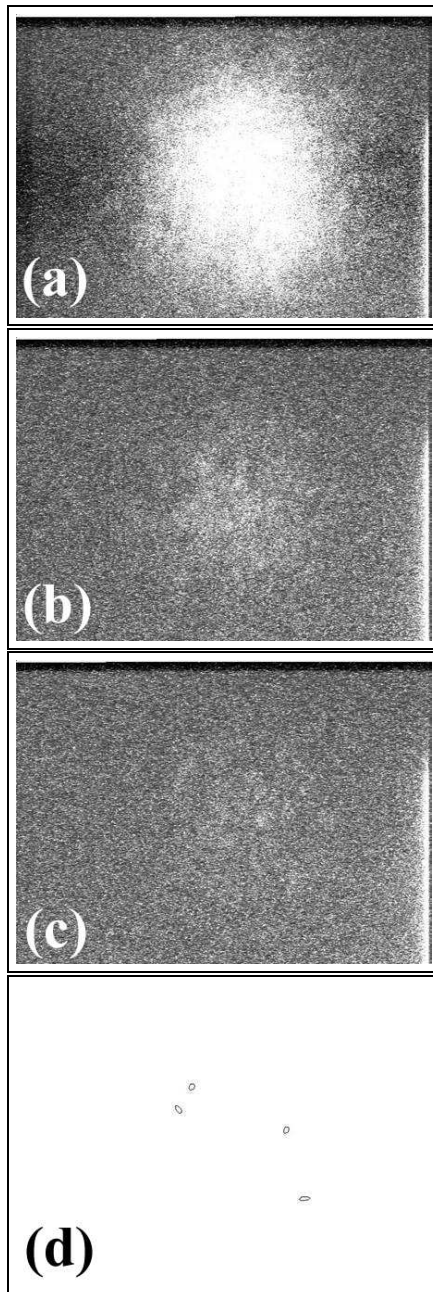
Figure 5.27: Images from the TC253 gamma camera produced by a ^{137}Cs point source for exposure times of 1000 msec (a), 100 msec (b), and 33 msec (c). The analyzed events from (c) are shown in (d).

Micro-columnar CsI(Tl) and Fiber Optic Coupling

In order to improve the optical transfer from the crystal to the TC253 image area surface, the lens coupling was replaced with fiber optic coupling. The hermetically sealed glass window of the TC253 was first removed using a diamond tipped saw. A 5.0 mm long Hamamatsu fiber optic plate (FOP) having a 3.7 mm x 5.0 mm face was then placed in direct contact with the TC253 image area. A Hamamatsu fiber optic scintillator (FOS) was then placed on top of the FOP. A ^{57}Co point source ($\approx$ 10 μCi) was then placed on top of the FOS. All optical components were physically touching with no optical grease between them. The FOS (J6675-01) has a 150 μm thick micro-columnar CsI(Tl) crystal that is grown on top of a 18 mm x 18 mm area, 3 mm thick FOP. Figure 5.28 shows photos of the opened TC253 (a) with the stacked FOP (b) and FOS and ^{57}Co point source (c). The image from a 100 msec exposure at -30 °C and 200x gain is shown in Figure 5.29. It can be seen that single photoelectric flashes within the crystal can easily be observed. This experiment showed that the optical coupling efficiency of fiber optic plates is much larger than that of lenses. Figure 5.29 also shows the damage to the EMCCD surface resulting from removing the glass window.
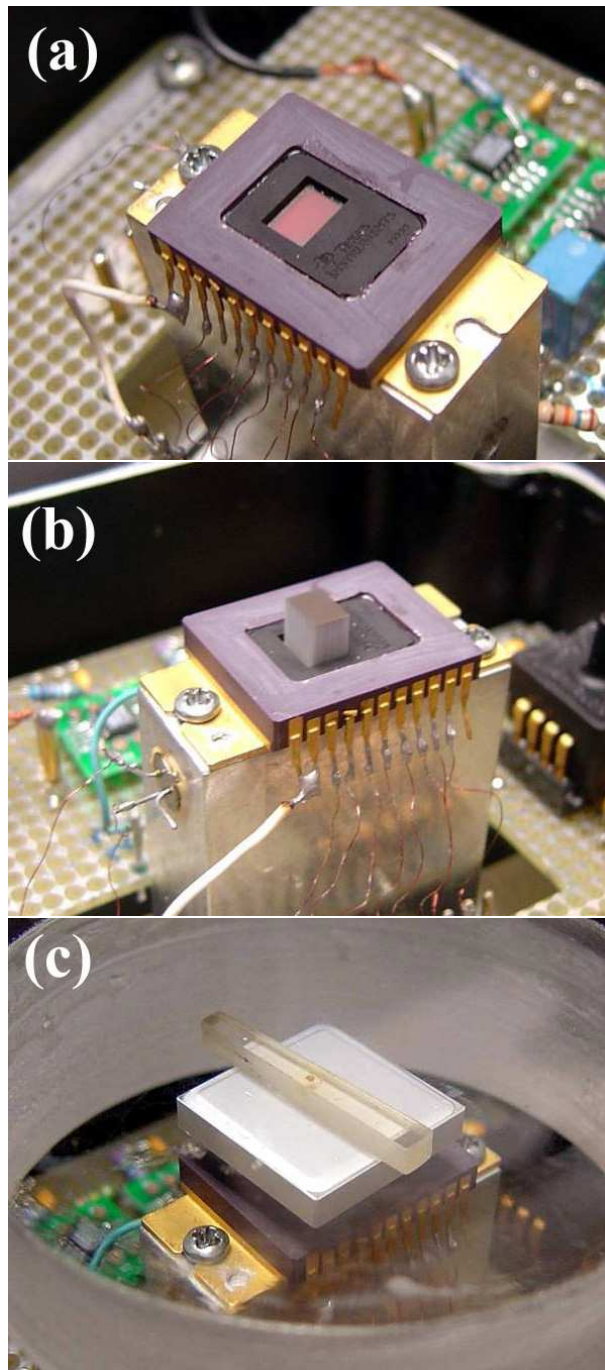
Figure 5.28: Photos showing the TC253 EMCCD with the glass cover removed (a), the stacked FOP (b), and FOS with ^{57}Co point source and acrylic vacuum enclosure (c).
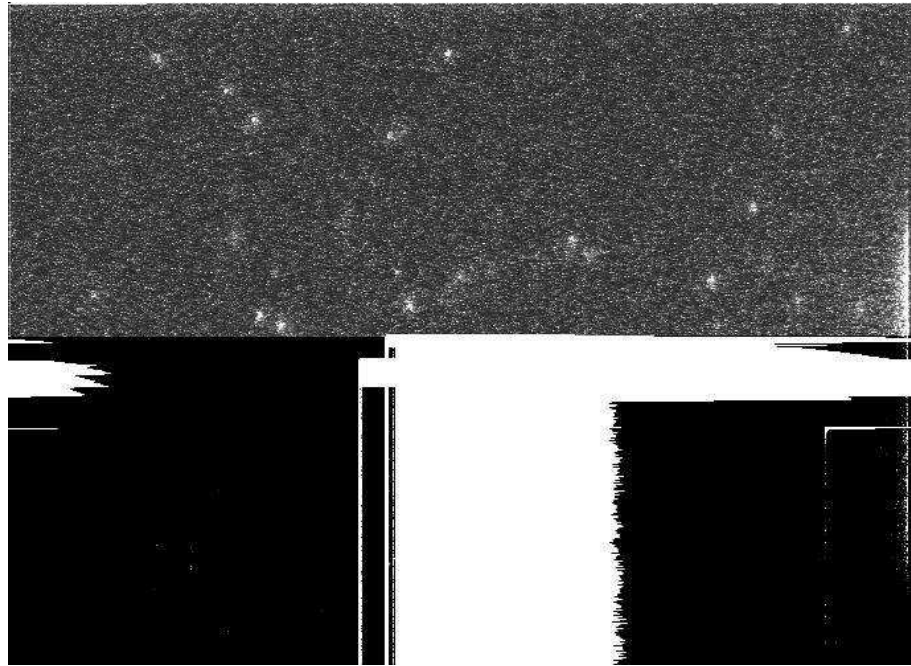
Figure 5.29: An image from the fiber coupled TC253 gamma camera produced by a ^{57}Co point source for exposure times of 100 msec. The single photoelectric event flashes can clearly be seen in the upper (undamaged) half of the EMCCD. The excessive blooming in the lower half of the EMCCD is due do damage from removing the protective glass cover.

5.5 Conclusions

The sensitivity of the CCD camera from Chapter 4 was improved in this Chapter by using an EMCCD with dual lens coupling. Although the quantum efficiency of the front-illuminated TC253 EMCCD (35% at 560 nm) was less then half that of the back-illuminated SI-502A CCD (80% at 560 nm), the gain achieved in the multiplication register of the TC253 gave it an improved SNR for low light level imaging. However, despite the low cost of the TC253 ($500 USD), which makes it an attractive candidate for a multiple camera system, the low quantum efficiency and inherent spurious charge generation (3 to 4 electrons/pixel at high gain) make the TC253 incapable of singe photoelectron sensitivity. With dual lens coupling, the optical coupling efficiency was improved by a factor of two. This improvement comes at a cost of imaging a reduced field of view at the crystal. The reduced field of view is approximately the same size as the image area of the EMCCD (1:1 object to image ratio). Also, due to lens coupling the response over the field of view is more sensitive at the center and drops off at the edges.

Although the prototype EMCCD gamma camera was capable of SPECT imaging using light integration, it was unable to perform photon counting for ^{99m}Tc (140 keV) and ^{125}I ($\approx$ 27 keV) with dual lens coupling. This can be explained by estimating the number of electrons produced in the TC253 per CsI(Tl) scintillation event. The luminosity of CsI(Tl) is 54 photons/keV with a peak wavelength of 560 nm. Approximately 10% of these scintillation photons will escape the crystal via the non-internally reflected light cone [50]. Upper limits for dual lens optical coupling efficiency (with an object to image ratio of 1:1) have been estimated to be $\approx$ 5% [72, 73], and the quantum efficiency of the TC253 is 35% at 560 nm. This gives (140 x 54 x 0.1 x 0.05 x 0.35) = 13 electrons/event for ^{99m}Tc

and (27 x 54 x 0.1 x 0.05 x 0.35) = 3 electrons/event for ^{125}I. When these signals are spread over a 3 x 3 pixel area they are easily lost within the 3 to 4 electrons/pixel spurious charge noise of the TC253. Single photoelectric events were observed with dual lens coupling using a higher energy ^{137}Cs (662 keV) source, where the increased number of scintillation photons results is more than 3 to 4 electrons/pixel/event. Also, photon counting with the TC253 was demonstrated using fiber optic coupling and micro-columnar CsI(Tl) for ^{99m}Tc, showing that fiber coupling is much more efficient than lens coupling.

When the monolithic CsI(Tl) crystal and dual lens setup were used with the PhotonMAX 512B camera (e2v CCD97 EMCCD), single photoelectric events were easily observed for both ^{99m}Tc and ^{125}I sources. This is mainly due to the high quantum efficiency of the back-illuminated CCD97 (95% at 560 nm) and the low spurious charge generation (0.01 electrons/pixel). These results are presented in the next Chapter.

Chapter 6

CCD97 EMCCD SPECT

6.1 Overview

In order to better investigate photon counting using a lens coupled EMCCD, the TC253 based camera from the previous chapter was replaced with the commercially available PhotonMAX 512B camera from Princeton Instruments [74]. Although the current cost of the PhotonMAX 512B ($\approx$ \$30k USD) makes it impractical for a multiple camera system, it was used to obtain results from a high quality EMCCD. The PhotonMAX 512B uses the e2v CCD97 EMCCD [75], which has a much higher quantum efficiency and much lower spurious charge generation than the TC253, and can be cooled to -70 °C. Both the 3 mm thick monolithic and 150 μm thick micro-columnar CsI(Tl) crystals were used with the CCD97 camera to investigate photon counting using lens coupling. Results from the two crystal types are compared in this chapter, along with a detailed description of the photon counting software algorithm. Intrinsic resolution results and initial SPECT images are also presented.

6.2 Hardware

6.2.1 PhotonMAX 512B EMCCD Camera

The Princeton Instruments PhotonMAX 512B uses the L3Vision CCD97 EMCCD by e2v Technologies. The back-illuminated CCD97 has 95% quantum efficiency at 560 nm, 16 μm^2 area pixels in a 512 by 512 array with a 100% fill factor, a maximum EM gain of 1000x, and a read noise of 37.70 electrons/pixel RMS at a 5 MHz clock rate. The patented cooling technology of the PhotonMAX uses a Peltier and air based heat exchanger to cool the EMCCD down to -70 °C, at which point the dark current generation is only 0.044 electrons/pixel/second. The CCD97 has a full-well capacity of 800k electrons in the multiplication register, which is four times larger than the full-well capacity of the image area pixels (207k electrons). This can be compared to the TC253 which had a multiplication register full-well capacity that was only 25% larger than the image area pixels. Also, the included acquisition software (WinView) performs 16-bit digitization of the EMCCD signal at true video rate readout (5 or 10 MHz clock rate) with three different video gain settings per clock speed (for example 12.72, 6.69, or 3.29 e/ADU at 5 MHz).

Another significant difference between the TC253 and CCD97 is the spurious charge generation. The spurious charge for the TC253 was measured to be 3 to 4 electrons/pixel while the CCD97 measured only 0.01 electrons/pixel. High spurious charge generation has negative effects for low light level imaging. This can be observed by comparing line profiles from sample TC253 and CCD97 frames as shown in Figure 6.1. The zero second frames were taken at high gain and similar temperatures. It can be seen in the CCD97 line profile (a) that most of the pixels are empty and only vary with the reduced read noise, while some pixels containing one or two electrons appear as sharp spikes on top of the read noise background.

The frequency of these spikes can be reduced with cooling [65], which suggests that they are thermal dark current electrons. For the TC253 (b) each pixel contains (on average) 3 to 4 electrons, therefore empty pixels are not frequently seen and the low read noise background is not observed. Rather, the TC253 line profile is a collection of sharp spikes of 3 to 4 electrons each. Further cooling of the TC253 did not reduce this noise, suggesting it was due to spurious charge generation. The large spurious charge generation of the TC253 can easily mask low light level signals (< 3 to 4 electrons/pixel) as shown in the previous chapter.
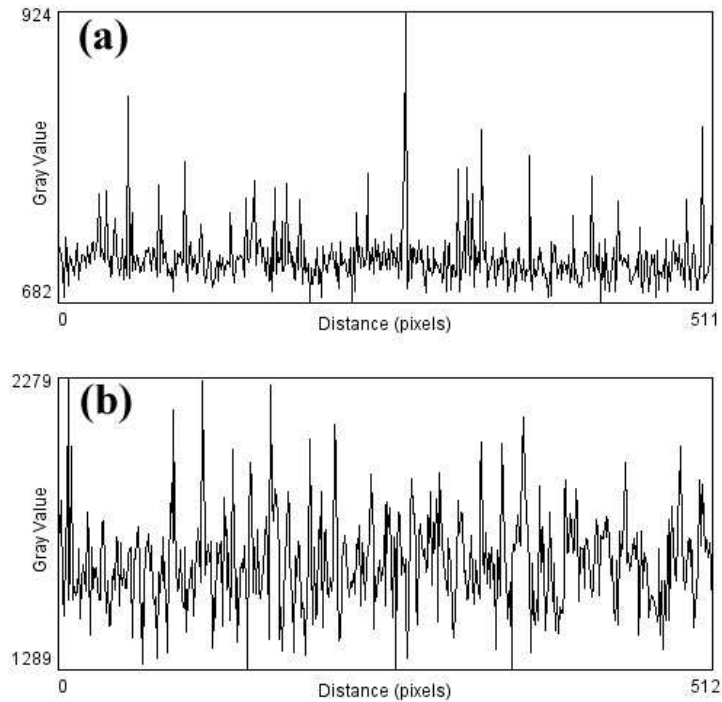
Figure 6.1: Graphs showing zero second line profiles for the CCD97 (a) and TC253 (b) EMCCDs. The high spurious charge generation of the TC253 creates a much noisier line profile.

6.2.2 Dual Lens Coupling

A schematic of the CCD97 setup is shown in Figure 6.2. The two coupled Schneider lenses (f/0.95) were attached into the C-Mount of the PhotonMAX 512B camera. Both lenses had an f-stop setting of 0.95 (open full) with the far lens focus set to infinity and the near lens focus being variable. The crystal was then placed 5 to 10 mm in front of the far lens giving an object to image ratio of $\approx$ 1:1 and an optical transfer efficiency of $\approx$ 5%. For the monolithic crystal the shallow focal plane (less than 1 mm) was moved through the crystal until the number of events in focus was maximized. For the micro-columnar crystal the focal plane was at the exit surface of the fiber optic plate (FOP).
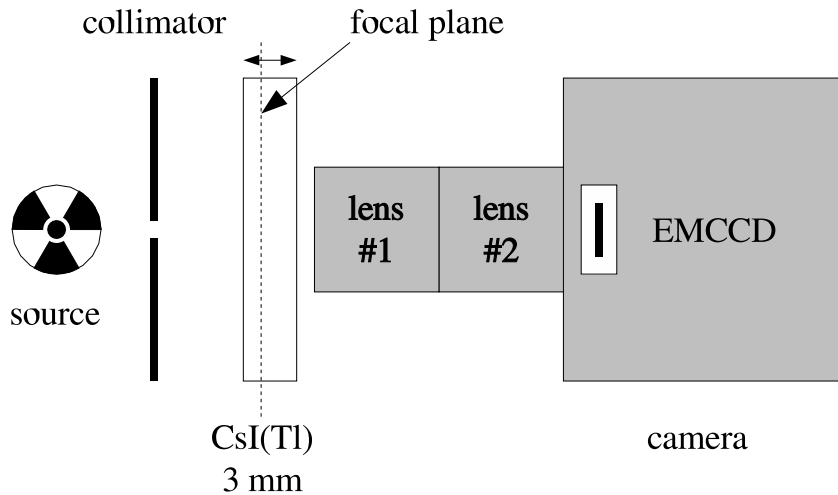
Figure 6.2: A schematic of the EMCCD setup. The focal plane can be moved through the crystal.

6.2.3   Monolithic and Micro-columnar CsI(Tl)

Both monolithic and micro-columnar CsI(Tl) scintillating crystals were used for the CCD97 experiments. Micro-columnar CsI(Tl) consists of small crystal needles (< 10 μm in diameter) grown in a close packed structure on top of a substrate. A picture of the needle structure is shown in Figure 6.3. When a photoelectric event occurs within a needle, the resulting scintillation light travels along the needle length like a fiber optic before exiting at the crystal surface. Although there is some cross-talk between the needles, the emerging scintillation light is much more focused at the crystal surface when compared to monolithic CsI(Tl). Crystal needles approaching 3 mm thick have been grown, which would be thick enough to stop $\approx 75\%$ of ^{99m}Tc gamma rays [49, 67]. For these experiments we used the Hamamatsu fiber optic scintillator (FOS) J6675-01 which has a 150 μm thick micro-columnar CsI(Tl) crystal with a 18 mm x 18 mm area. The crystal is grown on top of a 3 mm thick fiber optic plate (FOP) that has 6 μm diameter fibers as shown in Figure 6.3. The 150 μm thick crystal will stop $\approx 85\%$ of incident ^{125}I radiation (≈ 27 keV) and $\approx 5\%$ of incident ^{99m}Tc radiation (140 keV). Although the J6675-01 FOS stopping power for ^{99m}Tc is too low for a realistic gamma camera, it is adequate for initial testing.

6.3   Software

There are two different methods for acquiring SPECT projection data when using an EMCCD. The first is to simply integrate the scintillation light emerging from the crystal for a given exposure time. Although this method maximizes the light signal received by the EMCCD, the energy information from each photoelectric interaction within the crystal is lost, and discriminating events based on energy is not possible. Energy discrimination is required to reject the low energy scattered and high energy

153
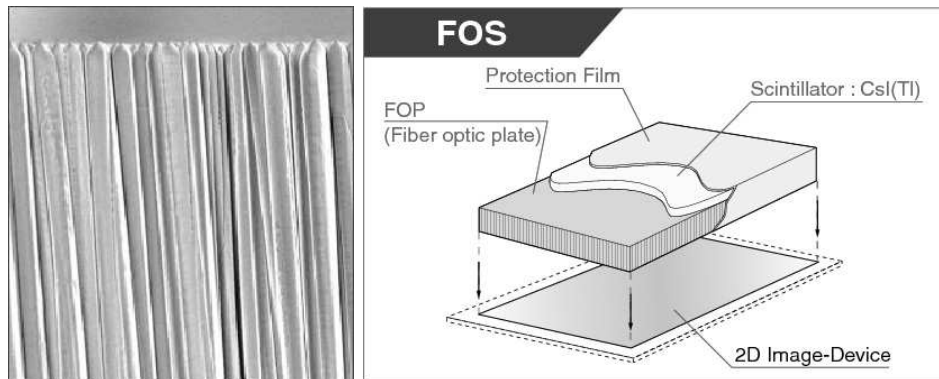
Figure 6.3: (Left) A photo showing the needle structure of micro-columnar CsI(Tl). Each crystal needle is $< 10~\mu$m in diameter. (Right) A schematic of the Hamamatsu fiber optic scintillator (FOS). Images courtesy of Hamamatsu.

background radiation, as well as direct hits to the EMCCD surface. Rejecting events based on energy can improve the SPECT reconstruction considerably. The second method is to use photon counting [46, 47]. In photon counting the exposure time is reduced until the individual scintillation flashes within the crystal can be observed. Provided there is not a high degree on overlap, the position and energy of each photoelectric interaction can be measured. If video frame rates are used ($\geq$ 30 frames/second) then real-time data acquisition is possible. In this way an EMCCD can give list-mode data, where the position and energy for each interaction is recorded, just like a PMT based Anger camera or PSPMT. The photon counting method not only provides for energy based discrimination of events but it also offers a higher intrinsic resolution when compared to light integration [46, 67].

Two different software packages were used to perform photon counting analysis with the PhotonMAX 512B EMCCD camera and lens coupled CsI(Tl) crystal. Details of the algorithm used and list-mode position and energy results are presented next.

6.3.1 Off-Line Analysis with ImageJ

The Java based image processing and analysis software ImageJ (version 1.37v) was used for initial off-line photon counting analysis. ImageJ is freely available from the National Institutes of Health (NIH) [76]. The WinView acquisition software, included with the PhotonMAX 512B camera, was first used to acquire a stack of 16-bit tiff images. In order to achieve adequate statistics, these stacks were several thousands of images thick, with each image containing tens of individual scintillation events. In order to reduce the overall size of the tiff image stack, only the center 265 x 256 pixels from the 512 x 512 CCD97 image were saved. This resulted in a stack of 1000 16-bit images being 256 MB in size. A detailed description of the algorithm used to perform off-line photon counting analysis of the image stack is given next. The ImageJ menu pathways for each command are given in parenthesis.

Background Subtraction

The saved image stack of scintillation events was first opened with the ImageJ software. A similarly sized stack of background images (equal exposure time with no source) was also opened. The average of the entire background stack was then calculated (Image/Stacks/Z Project/Average Intensity) and subtracted (Process/Image Calculator) from each frame of the events stack. A sample 33 msec exposure background subtracted 256 x 256 pixel frame containing several events is shown in Figure 6.4. An 50 x 50 pixel ROI surface plot (Analyze/Surface Plot) for the two events indicated by the arrow is also shown in Figure 6.4.
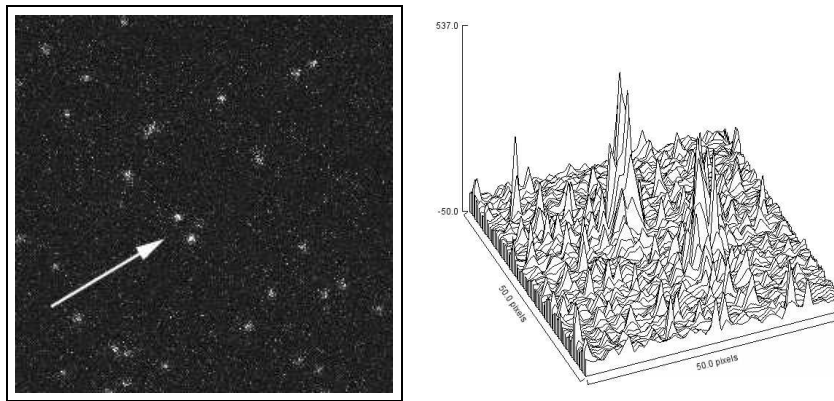
Figure 6.4: (Left) A background subtracted image of the individual scintillation events within the CsI(Tl) crystal. (Right) A surface plot for the two events indicated by the arrow.

Image Filtering

Each background subtracted image in the stack was then filtered by convolution with a Gaussian kernel (Process/Filters/Gaussian Blur). The radius of the Gaussian kernel was set to 2 pixels. Filtering helps to smooth out the response of the EMCCD at a cost of slightly lowering the dynamic range. An image of the filtered frame and ROI surface plot from Figure 6.4 are shown in Figure 6.5. It can be seen that the peaks from the scintillation events are now much more defined.

Image Threshold

A threshold was then applied to the filtered image stack (Image/Adjust/Threshold). This crated a region of interest (ROI) mask for each scintillation event. The upper limit was set to the maximum pixel value in the frame, while the lower was set so that some of the smaller noise peaks were included while retaining separation between the primary and K shell x-ray (or satellite) scintillation events. A threshold image of Figure 6.5 is shown in Figure 6.6. The upper and lower threshold limits for this
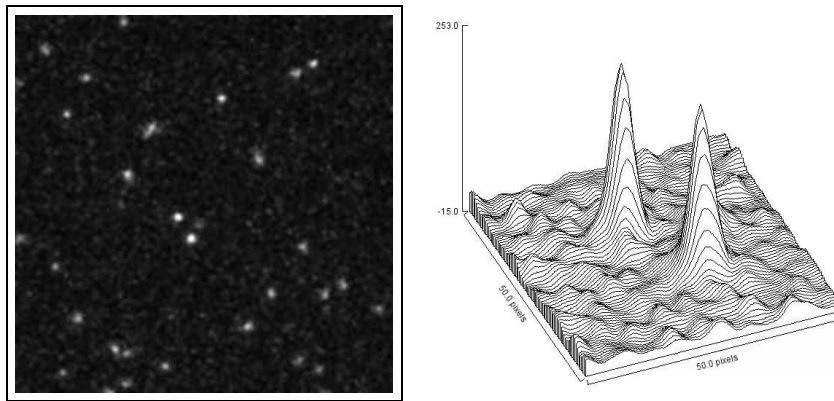
Figure 6.5: (Left) A Gaussian filtered image (r = 2) of the individual scintillation events within the CsI(Tl) crystal. (Right) A surface plot of two events as indicated by the arrow in Figure 6.4.

frame were set to 253 and 36 digital units respectively. In order to retain the pixel values from the filtered image and not switch to binary values, the threshold was not applied to the image stack but rather was used to create a mask for particle analysis.
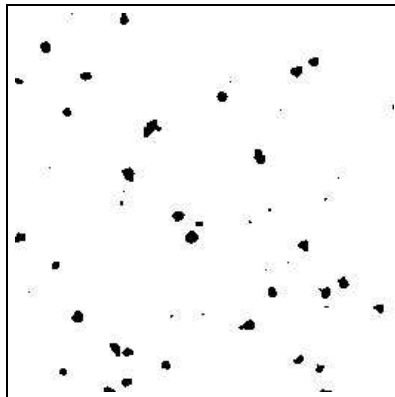
Figure 6.6: A threshold image of the scintillation events from Figure 6.5. Each scintillation light flash is defined by an ROI mask.

Analyze Particles

The threshold mask was then used to analyze the individual scintillation events within the frame (Analyze/Analyze Particles). The pixel size was set from zero to infinity and the circularity from zero to one. Particles touching the edges were excluded and any possible holes in the particles were included in the analysis since the maximum threshold might be different for each frame. The measured parameters (Analyze/Set Measurements) for each ROI included Area, Min & Max Grey Value, Center of Mass, and Integrated Density. A sample of the Analyze Particles results is shown in Figure 6.7. The particles have been identified and numbered with the list-mode data for the first ten particles being shown. A total of 42 particles were counted for this frame, with less than 1/3 being background events. A single text file containing the list-mode data for all events was then created by analyzing each frame in the image stack. While the initial tiff image stack was several hundreds of megabytes in size, the final list-mode text file is only a few hundreds of kilobytes in size.

	Area	Min	Max	XM	YM	IntDen
1	44	38	99	21	23	2805
2	34	45	175	202	33	3119
3	46	36	131	190	39	3428
4	35	37	135	48	43	2476
5	1	38	38	146	47	38
6	39	38	185	140	57	3473
7	27	37	153	35	67	2153
8	2	36	37	179	66	73
9	81	38	146	92	78	5954
10	57	37	126	165	97	3860
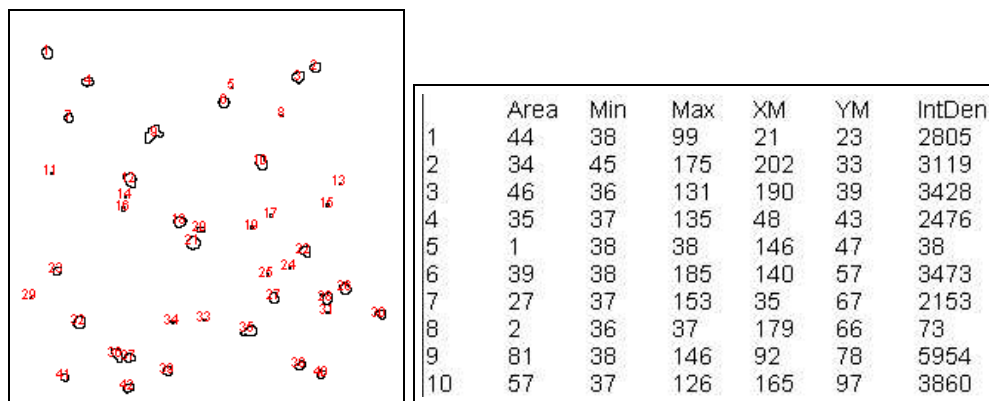
Figure 6.7: An image of the analyzed particles for the initial image in Figure 6.4 and list-mode data for the first 10 particles.

Energy Spectra

While the position for each scintillation events is given by the Center of Mass measurement (XM and YM), the energy spectrum for the isotope is given by creating a histogram of the Area, Max Grey Value (Max), or Integrated Density (IntDen). Previous examples of photon counting with EMCCDs have used either the local maximum pixel value [46, 47] or the integrated density [67, 48] to create energy histograms. Figure 6.8 shows the histograms (Analyze/Distribution) for Area, Max, and IntDen for both the signal (^{57}Co point source) and background files. It can be seen that Area data appear go give the best energy resolution for the current analysis algorithm. The energy resolution of the Area histogram is $\approx 50\%$. Although a low resolution peak for ^{57}Co (122 keV) can be identified, a peak for ^{125}I (≈ 27 keV) could not be identified. This is because the low optical coupling efficiency of the dual lens coupling ($\approx 5\%$) causes a low signal to noise ratio for the ^{125}I events, making them appear just above the noise level.
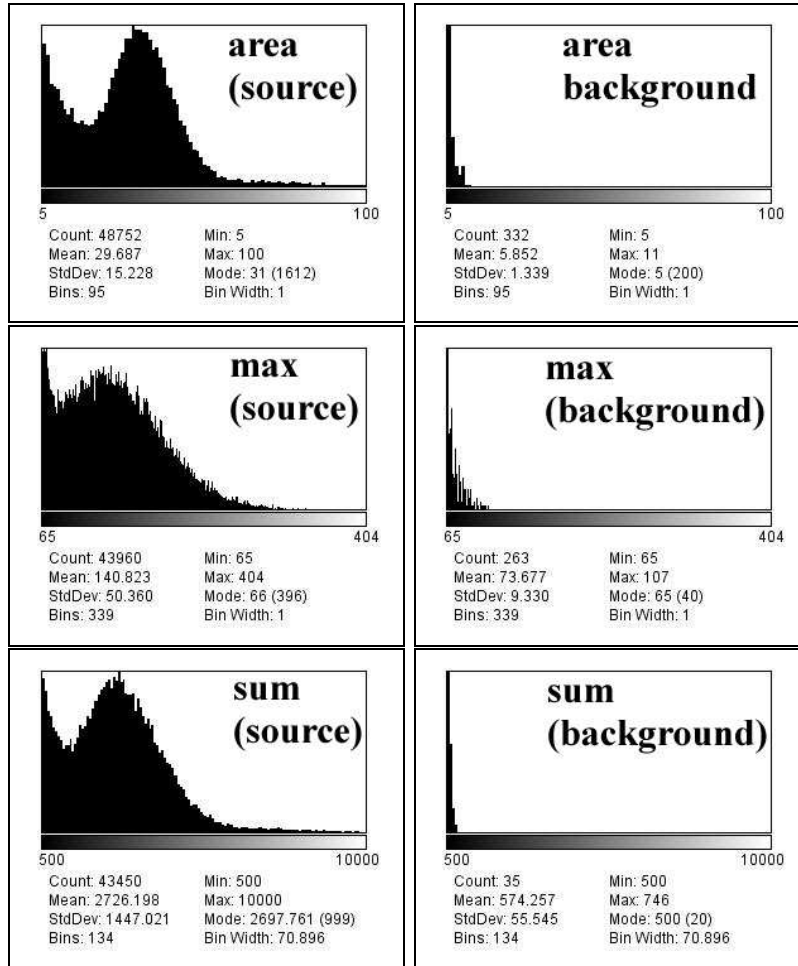
Figure 6.8: Histograms of the list-mode data Area (top), Max Grey Value (middle), and Integrated Density (bottom) for a ^{57}Co point source (left column) and background (right column).

6.3.2 Real Time Photon Counting with LabVIEW

Although off-line analysis with the ImageJ software proved that photon counting could be achieved with a lens coupled EMCCD, it required saving tiff image stacks that were hundreds of megabytes in size. These image files would be cumbersome for SPECT where large statistics are needed per projection, and several projections are required for three-dimensional image reconstruction. In order to solve this problem, a real-time list-mode analysis code was developed using the LabVIEW software (version 7.1.1) and the PhotonMAX EMCCD camrea.

The LabVIEW code uses the Scientific Imaging ToolKit software (SITK version 1.3.6, purchased with the PhotonMAX 512B camera) to communicate with the EMCCD camera. The SITK .vi library is used to set the data acquisition parameters such as temperature, exposure time, and gain, as well as read the data from the camera, just as the WinView software does. After a single 512 x 512 pixel frame is read from the EMCCD camera, the IMAQ Vision measurement library is then used to filter, threshold, analyze particles, and write the list-mode data to a file just as the ImageJ software did. This process is then repeated frame by frame until adequate statistics have been reached. One advantage of the LabVIEW code is that only the list-mode data are saved, creating much smaller data files. Another advantage is that the LabVIEW code performs near real-time analysis of the frames. The prototype code can analyze approximately ten 33 mec frames in one second. Therefore, it takes 3 lab seconds to acquire 1 real second of data. This rate could be increased to true real-time by code modification and simplification.

A picture of the LabVIEW code front panel is shown in Figure 6.9. The only adjustable settings for the camera are the temperature, EMCCD gain, and exposure time. All other camera setting were either hard-wired (such as ADC gain)

or at their default values as set by *CameraInitialize.vi*. Real-time IMAQ graphs showing the Initial, Filtered, and Threshold images are displayed at the bottom of the front panel. The upper and lower threshold can be adjusted using the slider bars above the Threshold image display. The analysis of each threshold frame is performed using the *IMAQ Particle Analysis.vi*, which measures the center of mass and area for each ROI in the threshold mask. As the list-mode data are acquired, they are saved in a file and also used to display real-tine position and energy graphs shown at the right of the front panel. The position graph can be saved separately from the list-mode data. While every measured event that falls within the threshold is written to the data file, the displayed data can be cut using the area energy spectrum. In this way, background events can be removed from the position graph in real time.
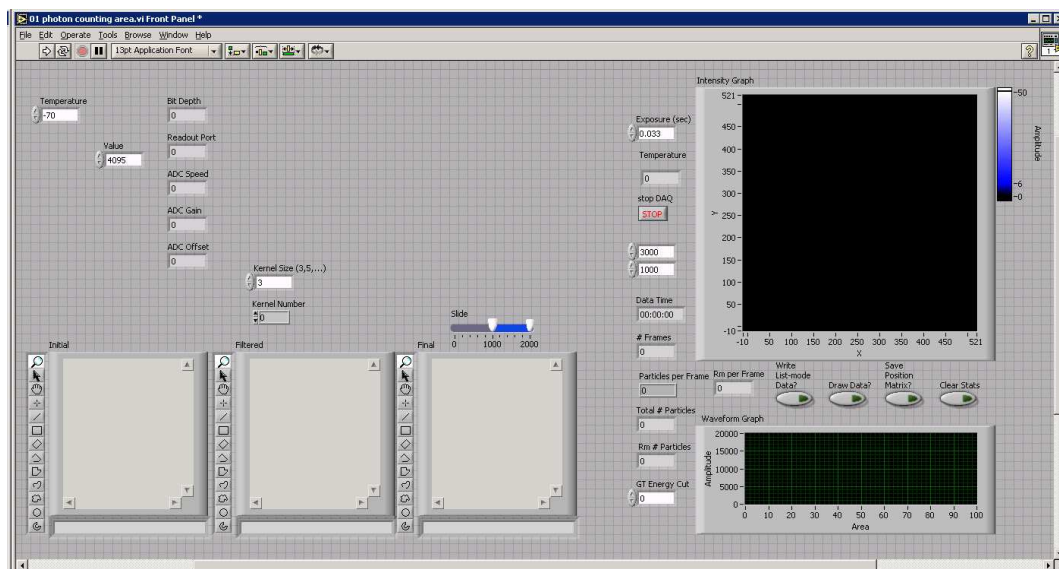
Figure 6.9: An image showing the front panel of the LabVIEW based photon counting software. The code can currently analyze about ten 33 msec frames per second.

6.4 Results

6.4.1 Light Integration using Single Lens Coupling

One of the first experiments performed with the PhotonMAX CCD97 EMCCD camera was to test if light integration based projection images could be used for SPECT reconstruction. The experimental setup consisted of a single 0.8 mm diameter pinhole collimator and a 3 mm thick monolithic CsI(Tl) crystal. The crystal was coupled to the EMCCD camera using a single lens (Computar TV Lens 1.3). The single lens imaged a FOV that measured approximately 75 mm x 75 mm at the crystal, with the focal plane being set to within the first 0.5 mm of the crystal. The EMCCD camera was operated at -70 °C, with an EM gain of 1000x, an ADC gain of 3.29 e/ADU, and a readout speed of 5 MHz. A mouse injected with 10 mCi of ^{99m}Tc-MDP was sacrificed after 3 hours uptake using CO_2. The cadaveric mouse was then placed in front of the pinhole such that the entire skull was imaged. The mouse was then rotated and 20 equiangular projections (18° step) with an exposure time of 3 minutes per projection were taken. Two 3 minute dark images (no source) were also taken, averaged, and subtracted from the projection images. The WinView software was used to acquire the light integration images.

Figure 6.10 (top left) shows a sample projection of the ^{99m}Tc-MDP uptake within the mouse skull. A photo of a mouse skull is shown in Figure 6.10 (top right) for clarity. Although an image of the mouse skull can be recognized, the SNR is fairly low as shown in the line profile (Y = 256) in Figure 6.10 (bottom). The low SNR is primarily due to the crystal glowing at areas outside of the mouse skull region, creating a large background signal. This background is due to the internally reflected scintillation light bouncing around inside of the crystal and emerging at a location far from the initial photoelectric interaction. The low SNR is also due to

the poor optical coupling efficiency from using a single lens with a large object to image ratio ($\approx$ 9:1 in this case) [50]. The low spatial resolution of the image can be attributed to the light spread as the non-internally reflected scintillation light cone moves through the 3 mm thick monolithic crystal. Also, pixel blooming due to direct interaction of the ^{99m}Tc-MDP gamma rays with the EMCCD surface can be seen in the integration image.
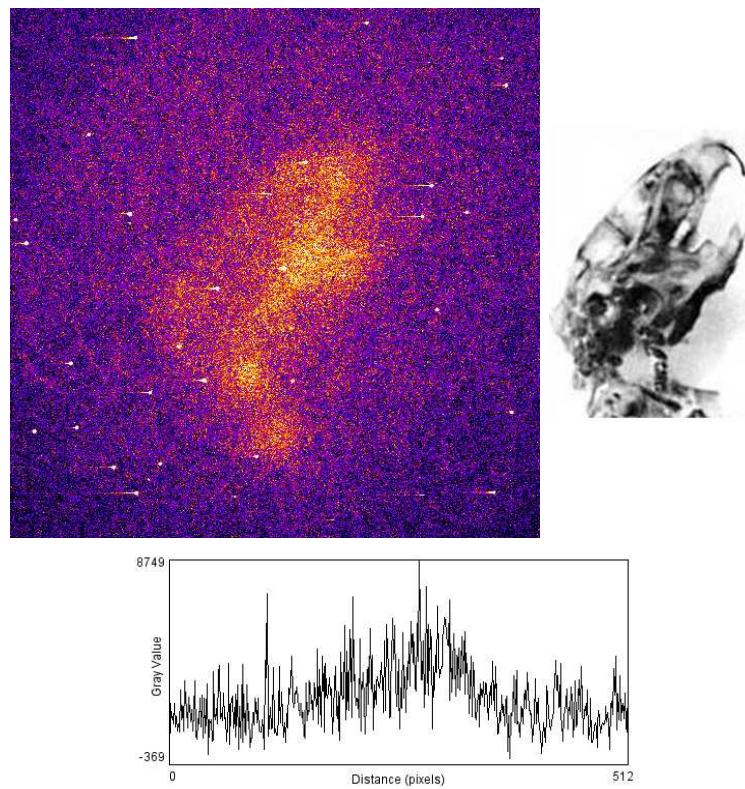
Figure 6.10: A 3 minute light integration pinhole projection image of a mouse skull with ^{99m}Tc-MDP uptake (top left). A photo of a mouse skull (top right). A line profile of the pinhole projection at Y = 256 showing the low SNR (bottom).

This experiment showed the many obstacles that must be overcome when using light integration based projection images, mainly background glow and direct

164

hits to the EMCCD. When this same setup was used to try to observe single photoelectric events within the crystal (photon counting), nothing could be seen above the background noise. This was due to the low optical coupling efficiency of the single lens setup. By using dual lens coupling with a 1:1 object to image ratio, the optical coupling efficiency was increased to a point where photon counting could be achieved, as described in the next section.

6.4.2 Photon Counting with Monolithic and Micro-columnar CsI(Tl)

The optical coupling efficiency from the previous setup can be improved by placing two lenses together front to front. Improvement by a factor of two was measured when imaging the same FOV. The improved coupling efficiency comes at a cost of viewing a reduced FOV due to the object focal plane being very close to the lens. The maximum object to image ratio with dual lens coupling is $\approx$ 1:1. This ratio is similar to those in experiments from other research groups using fiber optic based coupling with EMCCDs [46, 47, 67]. These research groups also use micro-columnar rather than monolithic CsI(Tl) crystals.

To test which crystal would work better with dual lens coupling, photon counting images taken using both monolithic and micro-columnar CsI(Tl) crystals were compared. Although the monolithic crystal used was 3 mm thick and the micro-columnar crystal was only 150 μm thick, the comparison is valid assuming the light spread and attenuation in a thicker micro-columnar crystal would be minimal. A schematic of the setup used is shown in Figure 6.2

Figure 6.11 shows a comparison between the monolithic and micro-columnar CsI(Tl) photon counting images for ^{137}Cs (662 keV), ^{57}Co (122 keV), and ^{125}I ($\approx$ 27 keV). It can be seen that for the monolithic images, some events are in focus

while others are not due to the shallow focal plane and varying depth on interaction within the crystal. Yet for the micro-columnar CsI(Tl), the events appear brighter and more homogeneous in size due to the columnar nature of the light transfer to the crystal surface. Based on these results, the micro-columnar CsI(Tl) crystal (Hamamatsu J6675-01 FOS) was used for all further photon counting experiments.
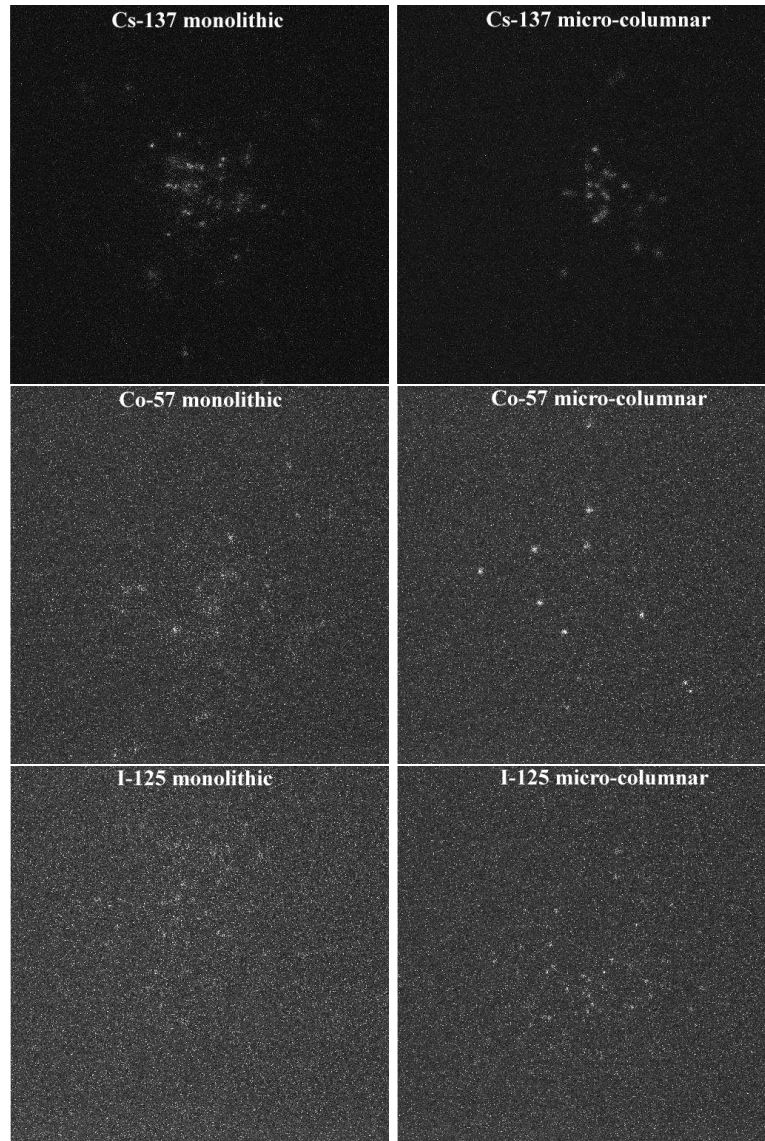
Figure 6.11: A comparison of dual lens coupled photon counting images taken using monolithic (left column) and micro-columnar (right column) CsI(Tl) crystals. The isotopes imaged are ^{137}Cs (first row), ^{57}Co (second row), and ^{125}I (third row).

6.4.3 Intrinsic Resolution

The intrinsic resolution for the lens coupled EMCCD based gamma camera was measured using the micro-columnar CsI(Tl) crystal (FOS) and a 25 μm Tungsten slit collimator. The slit collimator was placed directly on top of the FOS with the source being placed on top of the collimator. An image of the slit obtained using an ^{125}I source is shown in Figure 6.12 (top). The data were acquired using the LabVIEW photon counting software. A corresponding line average profile (taken perpendicular to the slit) is also shown in Figure 6.12 (bottom). The full width at half max (FWHM) of the profile measured 3 pixels which corresponds to an intrinsic resolution of 56 μm (18.5 μm/pixel).
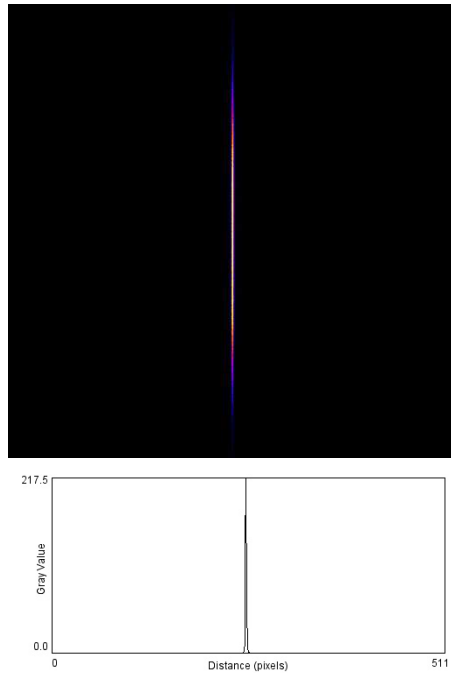
Figure 6.12: An image of the 25 μm slit using an ^{125}I source and photon counting (top). A line average profile of the above image (bottom).

As a comparison, a light integration image of the same setup was taken using the WinView software. The dark subtracted image and corresponding line average profile for a 10 second exposure are shown in Figure 6.13. The FWHM of the profile measured 110 um, showing that photon counting can improve the intrinsic resolution by a factor of two.
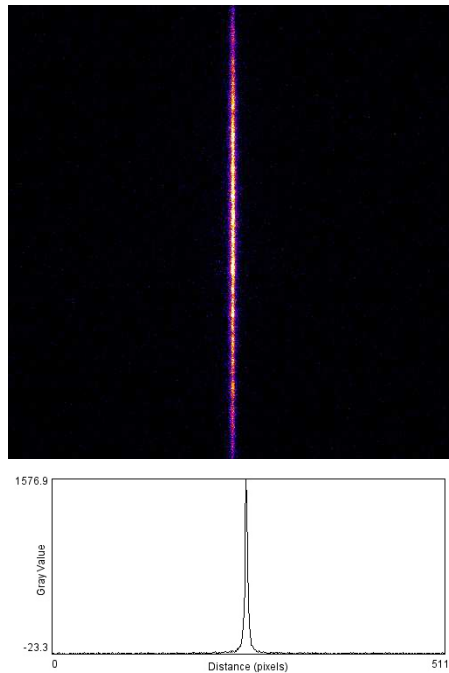
Figure 6.13: An image of the 25 μm slit using an ^{125}I source and light integration (top). A line average profile of the above image (bottom).

6.4.4 ^{125}I Phantom Images

An ^{125}I phantom was used to take initial images with the CCD97 photon counting setup (dual lens coupling and micro-columnar CsI(Tl) crystal). Both pinhole and parallel-hole collimators were used for the images. The phantom consisted of a small vial that contained $\approx$ 1 mCi of activity. The vial was approximately 3 mm

in diameter and was tapered at the bottom. Figure 6.14 shows the image (a) and corresponding line profile (b) produced using an 0.8 mm diameter pinhole with a 12 minute exposure time. It can be seen that the SNR is much improved compared to integration based images, and that the resolution is good enough to image both the tapering and meniscus of the liquid source. Figure 6.14 also shows the image (c) and corresponding line profile (d) produced using a hexagonal parallel-hole collimator. The parallel-hole collimator (1 mm holes, 20 mm length) was placed on top of the micro-columnar crystal while the ^{125}I phantom was placed on top of the collimator. The 10 minue exposure gave a good SNR with the collimator septum (0.2 mm thick) being easily resolved.
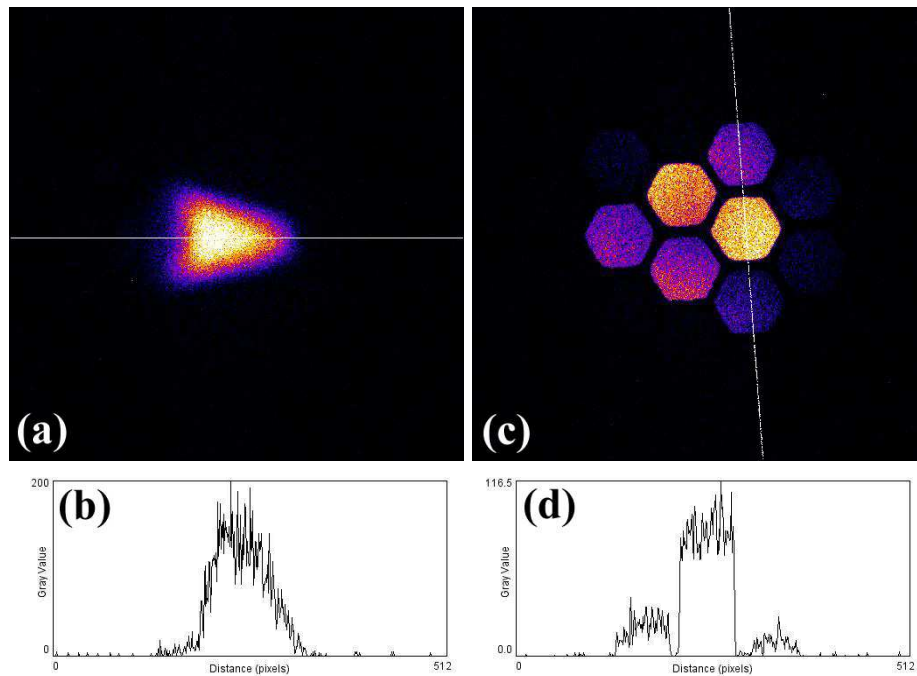
Figure 6.14: A photon counting image (a) and line profile (b) of the ^{125}I phantom using pinhole collimation. A photon counting image (c) and line profile (d) of the ^{125}I phantom using parallel-hole collimation.

6.4.5 Cadaveric ^{99m}Tc-MDP Mouse Images

Biological data were taken with the CCD97 photon counting setup using a single 0.8 mm diameter pinhole collimator and a nude type mouse. The mouse was injected with $\approx$ 13 mCi of ^{99m}Tc-MDP and was sacrificed two hours later using CO_2. The cadaveric mouse was then placed in front of the pinhole collimator such that the entire skull could be imaged. Figure 6.15 first shows the image (a) and corresponding line profile (b) previously taken using single lens coupling, 3 mm thick monolithic CsI(Tl) crystal, and light integration with a 3 minute long exposure (see Section 6.4.1). The integration image shows a poor SNR due to the background glow of the monolithic crystal, pixel blooming from direct gamma ray interactions with the EMCCD, and low optical coupling efficiency of the single lens. Figure 6.15 then shows the projection image (c) and line profile (d) produced using dual lens coupling, 150 μm thick micro-columnar CsI(Tl) crystal, and photon counting with a 1 hour long total exposure. It can be seen that the photon counting system has eliminated both the crystal background and pixel blooming noises. The elimination of these noise sources plus the increased optical coupling efficiency of the dual lenses have greatly improved the SNR as shown in the line profile. The list-mode photon counting data also has the advantage of energy windowing to reduce the number of scattered events in the final image.

A drawback of the current photon counting setup is that due to the dual lens coupling, the active detector area is only $\approx$ 8 mm x 8 mm. Therefore, in order to image the entire mouse skull ($\approx$ 25 mm x 25 mm), a reduced image was projected onto the crystal surface. This pinhole image reduction ($\frac{b}{a} = 3$) gave a geometric resolution (R_g) of $\approx$ 3 mm. The low geometric resolution is why the image in Figure 6.15(c) appears out of focus. The geometric resolution could be improved by

using tapered fiber optic coupling to increase the active area of the detector, or by imaging smaller source objects that could be placed closer to the pinhole aperture (*e.g.* the mouse thyroid).

Another drawback of the photon counting system is that the micro-columnar CsI(Tl) crystal is currently only 150 μm thick. Although this thickness will stop 85% of ^{125}I radiation ($\approx$ 27 keV), it stops $< 5\%$ of ^{99m}Tc radiation (140 keV). This explains why longer exposure times were used for ^{99m}Tc sources than for ^{125}I sources (Section 6.4.4). In order to make the CCD97 photon counting system practical for *in vivo* SPECT imaging, the thickness of the micro-columnar crystal will have to be increased to reduce the acquisition time to 3 to 5 minutes per projection.
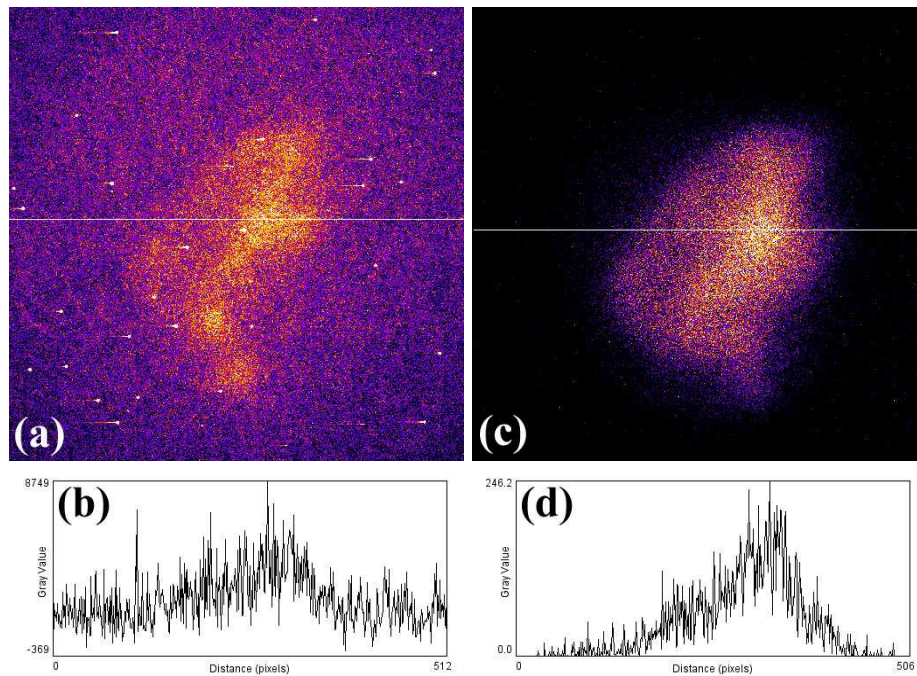
Figure 6.15: An image (a) and line profile (b) of a previous ^{99m}Tc-MDP mouse using light integration. An image (c) and line profile (d) of a new ^{99m}Tc-MDP mouse using photon counting showing an improved SNR. The poor resolution in (c) is due to the geometric resolution of the pinhole being $\approx$ 3 mm.

6.5 Conclusions

Using the commercial PhotonMAX 512B EMCCD camera as the photodetector improved upon the results from Chapters 4 and 5 in two main ways. First, the high quantum efficiency (95% at 560 nm) and low spurious charge generation (0.01 e/p) of the back-illuminated CCD97 made it sensitive to single photoelectrons at high gain. The resulting signal to noise ratio made it capable of photon counting for both ^{99m}Tc and ^{125}I sources using dual lens coupling. Although the energy peak for ^{57}Co (122 keV) was resolved with $\approx 50\%$ resolution, the energy peak for ^{125}I could not be resolved. Second, the deep cooling of the PhotonMAX (-70 °C) reduced the dark current generation to a negligible level, even for long exposure times. Yet, even with low dark current generation, integration based images still had a low signal to noise ratio due to internal light reflection within the 3 mm thick monolithic crystal and the low optical coupling efficiency of the lens. Also scattered, background, and direct hit events could not be removed from the integration based images.

The LabVIEW based photon counting software code allowed for near real-time photon counting data to be recorded in list-mode. It also allowed for energy based discrimination to filter out the scattered, background, and direct hit events. The intrinsic resolution of 56 μm is comparable to that measured from fiber optic coupled EMCCD systems with similar object to image ratios [46, 47, 67, 48, 77]. Drawbacks of the PhotonMAX EMCCD camera include its high cost ($30k USD) and it is currently not available with fiber optic coupling, which would improve the optical coupling efficiency by an order of magnitude and greatly improve the energy resolution capabilities compared to lens coupling [50].

Chapter 7

Conclusions

7.1 Experiment Summaries

7.1.1 R2486 PSPMT

A functional preclinical SPECT device was developed using a single Hamamatsu R2486 PSPMT. The effective area of the R2486 bialkali photocathode measured 50 mm in diameter and had a quantum efficiency of 20% at 410 nm (the λ_{max} of NaI(Tl)). Single 0.8 mm diameter pinhole was used to project an image of the source object onto a 6 mm thick, 60 mm diameter monolithic NaI(Tl) crystal that was directly coupled to the R2486 using optical grease. The pinhole collimator magnification was 1.4x ($\frac{b}{a} = 0.72$), while the intrinsic resolution of the crystal and R2486 was 1.5 mm. This gave a total resolution of $\approx$ 2 mm for the imaging system. The data acquisition system used standard high energy physics NIM and CAMAC components to trigger and digitize the anode wire signals from the R2486. These data were then collected and stored on a PC running LabVIEW software. The LabVIEW code was updated and rewritten to achieve a faster data readout rate. Code for off-

line analysis of the list-mode data was written using the PAW software. *In vivo* images for SPECT reconstruction were taken of a mouse injected with ^{99m}Tc-MDP. The non-submillimeter spatial resolution, hardware intensive data acquisition system, and time consuming off-line analysis made the R2486 PSPMT gamma camera an unattractive candidate for a multiple camera preclinical SPECT system.

7.1.2 SI-502A CCD

The potential for using a lens coupled CCD as the photodetector in a SPECT system was first investigated using the SITe model SI-502A CCD. The 1/2 inch format, back-illuminated SI-502A had 24 μm^2 pixels in a 512 x 512 array and a quantum efficiency of 80% at 560 nm (the λ_{max} of CsI(Tl)). The existing homemade camera system cooled the SI-502A under vacuum to -25 °C using a 2-stage Peltier and liquid-based heat exchanger to help reduce dark current noise. The data were collected, stored, and analyzed on a PC running IGOR software. The SPECT setup used a single 0.8 mm diameter pinhole, a 2 mm x 50 mm x 50 mm CsI(Tl) crystal, and a single f/1.3 lens. A phantom was constructed from a 3 mm diameter green LED and 1/2 inch diameter Teflon sphere diffuser in order to investigate the low light level imaging capabilities of the system. The low light level signal to noise ratio was greatly improved after eliminating the noise caused by a switching power supply in the electronics box. Even with the improved SNR, integration based pinhole projection images of a mouse injected with ^{99m}Tc-MDP did not produce any signal above the noise. By using a parallel-hole collimator (1 mm hexagonal holes, 25 mm in length) the uptake within the knees, spine, and tail could just been seen above the noise after a 15 minute exposure. Although the SI-502A had readout noise of only 7 electrons/pixel, the dark current generation at -25 °C was still significant for

long exposure times. Also, the high quantum efficiency of the SI-502A could not overcome the low optical coupling efficiency of the single lens ($\approx 1\%$). The SNR is also reduced by the internally reflected scintillation light emerging from the crystal at a place unrelated to the initial gamma ray interaction site, creating the observed background crystal glow.

7.1.3 TC253 EMCCD

The sensitivity of the previous CCD system was improved by replacing the SITe SI-502A with the Texas Instruments TC253 EMCCD. A cost effective prototype EMCCD based gamma camera was developed and evaluated for use in preclinical SPECT imaging. A four stage Peltier and liquid heat exchanger was used to cool the EMCCD down to -50 °C. Dual $f/0.95$ lens coupling was used to image the scintillation light from a 3 mm thick monolithic CsI(Tl) crystal. A gain of over 1000x was measured for the TC253 EMCCD. The dark current accumulation rate and read noise were within the specified operating range for a temperature of -40 °C and readout rate of 200 kHz. A spurious charge generation of 3 to 4 electrons/pixel was measured at high gain values. This intrinsic spurious charge could not be further reduced using established minimizing techniques and represents the noise floor for the TC253. A light integration based intrinsic resolution of 110 μm FWHM was measured using a 30 μm slit collimator and ^{99m}Tc source. Single pinhole collimation was used to take SPECT images of a small ^{99m}Tc line phantom. The MLEM reconstructed source size was slightly larger than the true source size due to the geometric resolution of the setup. Although the TC253 system could achieve integration based SPECT imaging, it was unable to do photon counting for ^{99m}Tc and ^{125}I sources using lens coupling. Photon counting with the TC253 and dual

lens coupling could only be achieved with high energy sources like ^{137}Cs. Photon counting using a ^{57}Co source was demonstrated with the TC253 by replacing the lens coupled monolithic crystal with a fiber optic coupled micro-columnar crystal. The drawbacks of the front-illuminated TC253 are mainly due to the low quantum efficiency (35% at 560 nm) and large spurious charge generation at high gain (3 to 4 electrons/pixel).

7.1.4   CCD97 EMCCD

The PhotonMAX 512B commercial EMCCD camera from Princeton Instruments was used to investigate the potential of using both integration and photon counting based images for preclinical SPECT. The PhotonMAX used the highly sensitive e2v CCD97 EMCCD. The back-illuminated CCD97 had 16 μm^2 pixels in a 512 x 512 array with a quantum efficiency of 95% at 560 nm. The low spurious charge generation (0.01 electrons/pixel) and high gain (1000x) of the CCD97 make it sensitive to single photoelectrons. Also, the PhotonMAX can cool the CCD97 down to -70 °C to significantly reduce the dark current noise even for long exposure times.

The light integration setup used a 0.8 mm diameter pinhole, 3 mm thick monolithic CsI(Tl) crystal, and single $f/1.3$ lens coupling. Projection images of a mouse injected with ^{99m}Tc-MDP showed that the SNR was still very low. The low SNR was mainly due to the background glow of the monolithic crystal (from the internally reflected scintillation light), and the poor optical coupling efficiency of the single lens ($\approx 1\%$). Also, blooming due to direct gamma ray interaction with the EMCCD imaging area was observed in the images.

By using dual lens coupling the optical coupling efficiency was increased to a point where single photoelectric flashes within the scintillating crystal could be

observed ($\approx 5\%$). The improved coupling came at a cost of imaging a smaller field of view at the crystal. The field of view was proportional to the EMCCD area (1:1 object to image ratio). Lens coupled photon counting using both monolithic and micro-columnar CsI(Tl) were compared, with micro-columnar CsI(Tl) giving better event uniformity for the several different isotopes tested. Photon counting data analysis was first preformed off-line using the ImageJ software, then in real-time using the LabVIEW software. The LabVIEW software had the advantage of only saving the list-mode data, thereby greatly reducing the data file size. Using a 150 μm thick micro-columnar CsI(Tl) crystal and ^{125}I source, an intrinsic resolution of 56 μm was measured with photon counting, while an intrinsic resolution of 110 μm was measured using light integration.

7.2 Experiment Conclusions

7.2.1 Integration versus Photon Counting with an EMCCD

An EMCCD can be operated in either integration or photon counting mode when used as a SPECT gamma camera photodetector. For integration mode, the optical light emerging from the scintillation crystal is simply summed over a given exposure time. The length of the exposure is chosen to get an adequate SNR and is usually on the order of minutes long. For photon counting, the exposure time is reduced until individual gamma ray scintillation flashes are observed within the crystal. This results in exposure times corresponding to video frame rates (tens of milliseconds long). If the level of event overlap is low, then digital image processing can be used to calculate the position and energy for each event. Photon counting mode allows for fast, real-time data acquisition resulting in list-mode data similar to that from PMT systems.

The long exposure times used in integration mode mean that fast EMCCD readout is not a priority. For example, a readout time of 30 seconds would not add much time onto a 5 minute long exposure. Slow readout speeds would not only lead to a low readout noise, but would also save costs by using slower electronics. In photon counting mode the exposure time is tens of milliseconds long. For example, to acquire video rate data at 30 frames/second would require a 33 mec exposure time. Therefore, if real-time acquisition is desired with photon counting then fast electronics must be used.

Since the exposure time in integration mode is minutes long, the dark current accumulation must be reduced to negligible levels by using deep cooling. It was shown that even at -40 °C the dark current noise can still significantly reduce the SNR for long exposure times. Only by deep cooling to -70 °C or below was the dark current noise greatly reduced for long exposure times. Cooling to such temperatures requires elaborate engineering to isolate the cooled components from the rest of the camera, and costly parts such as multiple-stage Peltiers and liquid-based heat exchangers. The short exposure times used in photon counting mode mean that the EMCCD only has to be cooled moderately in order to reduce the dark current noise to an insignificant level [77]. Moderate cooling would both simplify the engineering and reduce cost.

For integration mode the acquired image is simply read from the EMCCD with the only image processing being background subtraction. In photon counting mode each EMCCD frame is analyzed using digital image processing. This includes background subtraction, Gaussian filtering, thresholding, and analyzing the particles to produce the position and energy list-mode data. The photon counting analysis must also be performed at real-time video rate speeds. This requires the use of fast

electronics hardware or software to achieve. The extra photon counting electronics add both complexity and cost to the system.

It was shown that for both single and dual lens coupling the background glow from internally reflected scintillation light within the monolithic crystal significantly reduced in the SNR for integration mode. This background glow was not observed for photon counting mode. It was also shown that for the exact same setup, photon counting mode gave an intrinsic resolution that was twice as good as integration mode (56 μm versus 110 μm).

The most significant difference between integration and photon counting mode is energy discrimination. For integration mode the energy information for each event is lost as the scintillation light is summed over the exposure time. Therefore, energy based event windowing cannot be used to remove scattered, background, or direct hit events. SPECT reconstructed images can be greatly enhanced by removing these unwanted data. In integration mode the energy for each is event is estimated by measuring the pixel area, local max, or integrated sum for each event. It was shown that even with the low optical coupling efficiency from dual lens coupling ($\approx$ 5%) the energy resolution for ^{57}Co (50%) was adequate to reject background and higher energy events. Although the energy peak for ^{125}I appeared as a shoulder off of the pedestal in the energy spectrum, energy discrimination was still used to eliminate most background events.

The advantages of improved spatial resolution, energy discrimination, and improved SNR of photon counting mode greatly outweigh the overhead of fast electronics, real-time digital image processing, and moderate cooling.

7.2.2 PSPMT versus EMCCD Photodetector

One advantage of PSPMT photodetectors is that they can be directly coupled to the scintillating crystal, which helps maximize the optical coupling efficiency. Although EMCCD photodetectors could be directly coupled to a crystal, the resulting active detector area would not be very useful for preclinical SPECT. Plus, direct thermal contact with the cooled EMCCD could potentially damage the crystal. By using fiber optic bundles to transfer the scintillation light to the EMCCD, a high enough optical coupling efficiency can be achieved to allow for photon counting [50]. The active detector area can then be increased by using tapered fiber optic bundles at a cost of slightly reducing the optical coupling efficiency.

Although the photocathode of a PSPMT has a low quantum efficiency (20% at 410 nm), it has a large electron gain ($\approx 10^6$). The PSPMT gain boosts the signal well above the electronic noise to create a large SNR. The large SNR of a PSPMT allows for fast counting of the scintillation flashes within the crystal. Although an EMCCD has a quantum efficiency that is almost 5 times larger than a PSPMT (95% at 560 nm), the electron gain is much lower ($\approx 10^3$). Yet, the EMCCD gain is adequate to allow for fast counting of the scintillation flashes also. This is because the EMCCD gain only needs to overcome the read noise of the charge-to-voltage output amplifier. This read noise is typically only a few tens of electrons/pixel. Therefore, an EMCCD does not need as high a gain as a PSPMT for counting mode.

The low intrinsic resolution of PSPMT systems (on the order of millimeters) requires the use of image magnification to reach a sub-millimeter total resolution. This leads to large detector surface areas and volumes since PSPMTs require both magnetic and radiation shielding. The high intrinsic resolution of EMCCD based

systems (< 1 mm) allows sub-millimeter total resolutions to be reached even without image magnification (1:1 object to image ratio). This greatly reduces the size of the detector surface area and volume. Also, even though an EMCCD must be cooled to reduce dark current noise, the resulting detector size is still much smaller compared to PSPMT detectors.

The small form factor of EMCCD based gamma ray detectors makes them well suited for preclinical SPECT imaging where several detectors are placed together in a small volume (*e.g.* a ring formation) in order to increase the overall sensitivity.

7.2.3 Monolithic versus Micro-columnar CsI(Tl)

The photoelectric absorption of a gamma ray by a scintillating crystal produces an isotropic burst of optical wavelength photons. In monolithic crystal, some of these optical photons will leave the crystal at the exit surface, while others will be internally reflected. The angle of the resulting non-internally reflected light cone depends on the indexes of refraction of crystal and surrounding material. The internally reflected photons are what create the background glow seen when using monolithic crystal for integration based images. For micro-columnar crystal, the optical photons confined within a single micro-crystal are internally reflected along the crystal length until reaching the exit surface. Although there is some micro-crystal cross-talk and attenuation, the emerging optical photons are much more focused than in monolithic crystal.

In order to improve the sensitivity of the detector, thick scintillating crystals must be used to increase the gamma ray stopping power. For example, a 0.5 mm thick CsI(Tl) crystal will stop $\approx 20\%$ of ^{99m}Tc gamma rays (140 keV), while a 3 mm

thick CsI(Tl) crystal will stop $\approx 75\%$. For thick monolithic crystals the size of the light cone at the exit surface is dependant on the depth on interaction (DOI) within the crystal. Photoelectric events that occur far from the crystal exit surface will have larger light cone diameters than events which occur close to the exit surface. For micro-columnar crystal there is a slight DOI dependence of the spot size and brightness at the exit surface but it is much less pronounced. This results in a near-homogeneous response even for thick micro-columnar crystals.

Dual lens coupling creates a shallow focal plane that is less than 1 mm thick. For monolithic crystal the focal plane is scanned through the crystal until the number of photoelectric flashes in focus is maximized. This occurs close to the gamma ray entrance surface, where the absorption curve is the steepest. Events that occur deeper into the crystal are out of focus. This creates a very inhomogeneous response when trying to use lens coupling for photon counting. The depth of the focal plane can be increased by reducing the f-stop of the lens, but this reduces the optical coupling efficiency to where single photoelectric events can no longer be seen. For micro-columnar crystal the focal plane is simply placed at the crystal exit surface. Even though the output from a micro-columnar crystal is much more uniform than a monolithic crystal, there is still a slight dependence on DOI. Efforts have been made by some groups to correct for this using MLEM based algorithms [78].

Micro-columnar CsI(Tl) up to 3 mm thick have been grown [49] and thicker crystals are anticipated in the future. When combined with DOI correction algorithms, the performance of micro-columnar crystals will be better suited than monolithic crystals for photon counting with an EMCCD.

7.2.4 Dual Lens Coupling versus Fiber Optic Coupling

With lens coupling, the EMCCD can be sealed behind a transparent optical window and physical contact with the imaging area is not required. With fiber optic coupling, the fiber bundle must be placed in very close proximity to, or even touching, the image area of the EMCCD. This creates additional engineering complications if the EMCCD is to be placed under vacuum and cooled.

Currently, the maximum object to image ratio for dual lens coupling is 1:1, which severely limits the active area of the detector. What makes things worse is that the response over the FOV is not uniform with dual lens coupling. The optical coupling efficiency is much higher at the center of the FOV that at the edges. As a result, photoelectric events at the edge of the FOV can not be observed above the background noise. An attempt was made to improve the FOV uniformity by moving the lens closer to the EMCCD, but this simply reduced the FOV. A flat field correction algorithm was also used to improve the FOV uniformity, but since the SNR at the edges was so poor, the correction did not add any new information. It is possible that a MLEM based correction mentioned previously could be used to improve the uniformity of lens based coupling, but implementing a MELM algorithm in real-time would be cumbersome. For fiber optic coupling, the entire FOV has a uniform response. Also, by using tapered fiber bundles, the object to image ratio can be increased to 2:1 or even 3:1 and still have a higher optical coupling efficiency than dual lens coupling.

The most significant difference between lens and fiber coupling is the optical coupling efficiency. Upper estimates for dual lens coupling give an efficiency of $\approx 5\%$ for a 1:1 object to image ratio, while the efficiency for fiber coupling with the same ratio is more than an order of magnitude larger ($\approx 75\%$) [50]. A high quality

EMCCD such as the e2v CCD97 must be used with dual lens coupling in order to achieve photon counting. Even with the CCD97 at 1000x gain the SNR is fairly poor resulting in a low energy resolution for ^{57}Co and an unresolved energy for ^{125}I. By improving the optical coupling efficiency with fiber optics, the SNR is greatly improved allowing for improved spatial and energy resolutions [77]. The benefits of fiber optic coupling greatly outweigh the added engineering complications.

7.2.5   Overall Conclusions

In order to build an effective preclinical SPECT device, the EMCCD would need a high quantum efficiency and low spurious charge generation (like the CCD97). It must also use micro-columnar crystal, fiber optic coupling, and photon counting mode.

7.3   Discussion

7.3.1   Object Image Reduction with an EMCCD Photodetector

The crux of using an EMCCD for the photodetector in a gamma-camera is that the image area is rather small ($\approx$ 10 mm x 10 mm) compared to the object area. Although a 1:1 object to image ratio could be used, it would be quite ineffective, even for a preclinical device studying small animals such as mice. A more effective detector could be made by maximizing the object to image ratio while minimizing performance loss. With an object to image ratio > 1, a reduced object image must somehow be transferred to the EMCCD image area.

Image reduction can be achieved in the gamma ray phase by simply placing a pinhole collimator between the radiation source and EMCCD such that the object to image ratio is > 1. A micro-columnar crystal could then be placed on top of the EMCCD imaging area to convert the gamma-rays into optical photons. The area of the crystal would only need to be as big as the imaging area of the EMCCD. A schematic of this setup is shown in Figure 7.1(a). However, further inspection of this pinhole configuration would reveal that it limits the total resolution by using $\frac{b}{a} > 1$. For example, with $d_e = 0.5$ mm and $R_i = 0.1$ mm, when $\frac{b}{a} = 3$ ($\approx$ 30 mm x 30 mm object area) the total resolution is only $\approx$ 2 mm. The resolution could be improved by using a smaller pinhole diameter, but this would severely reduce the geometric efficiency.

An improved total resolution can be achieved by performing image reduction in the optical photon phase. This setup is shown in Figure 7.1(b). The imaging area of the EMCCD is increased by using a fiber optic taper, with a 3:1 ratio being shown in Figure X. A pinhole collimator can then be used to project an image of the source onto the crystal. The area of the crystal now matches the increased area

186

of the fiber taper ($\approx$ 30 mm x 30 mm). This method is currently used by Beekman *et al* [46, 47, 77] and Nagarkar *et al* [49, 67], and allows for a smaller $\frac{b}{a}$ ratio to be used for the same object area. For example, using the same values for d_e and R_i as before, a total resolution of 1 mm can now be achieved with $\frac{b}{a} = 1$.

Image reduction can also be achieved in the electron phase by using an image intensifier. This setup is shown in Figure 7.1(c). The gamma rays from the source are first converted into optical photos by the scintillating crystal. The optical photons are then converted to electrons by the photocathode of the image intensifier. The image intensifier (Generation 1) uses electrostatic potentials to project a reduced image onto the output phosphor, which converts the electrons back into optical photons. The optical photons from the output phosphor are then transferred to the EMCCD using a fiber optic bundle. This method is currently in use by Meng *et al* [48, 79] and allows for photon counting with high resolution over a large object area ($\approx$ 50 mm x 50 mm), although the resulting detector volume for the Intensifier/EMCCD system is much larger compared to an EMCCD alone.

7.3.2 Other Sources of Signal Gain

Compared to a conventional CCD, the EMCCD photodetector is able to achieve an improved SNR for low light level imaging due to its internal electron gain (10^3). As shown in the previous section, the object image reduction can occur at different places (and phases) within the signal chain to the photodetector. Likewise, the electron gain can also occur at different places within the signal chain. A much larger electron gain can be achieved by replacing the Generation 1 image intensifier in Figure 7.1(c) with a Generation 3 image intensifier. Generation 3 intensifiers use a highly sensitive GaAsP or GaAs photocathode (50% or 25% quantum efficiency

(a)

b=a
b=2a
b=3a

pinhole   CsI(Tl)   EMCCD

(b)

b=a/3
b=2a/3
b=a

3:1 fiber taper

(c)

b=a/3
b=2a/3
b=a

fiber window

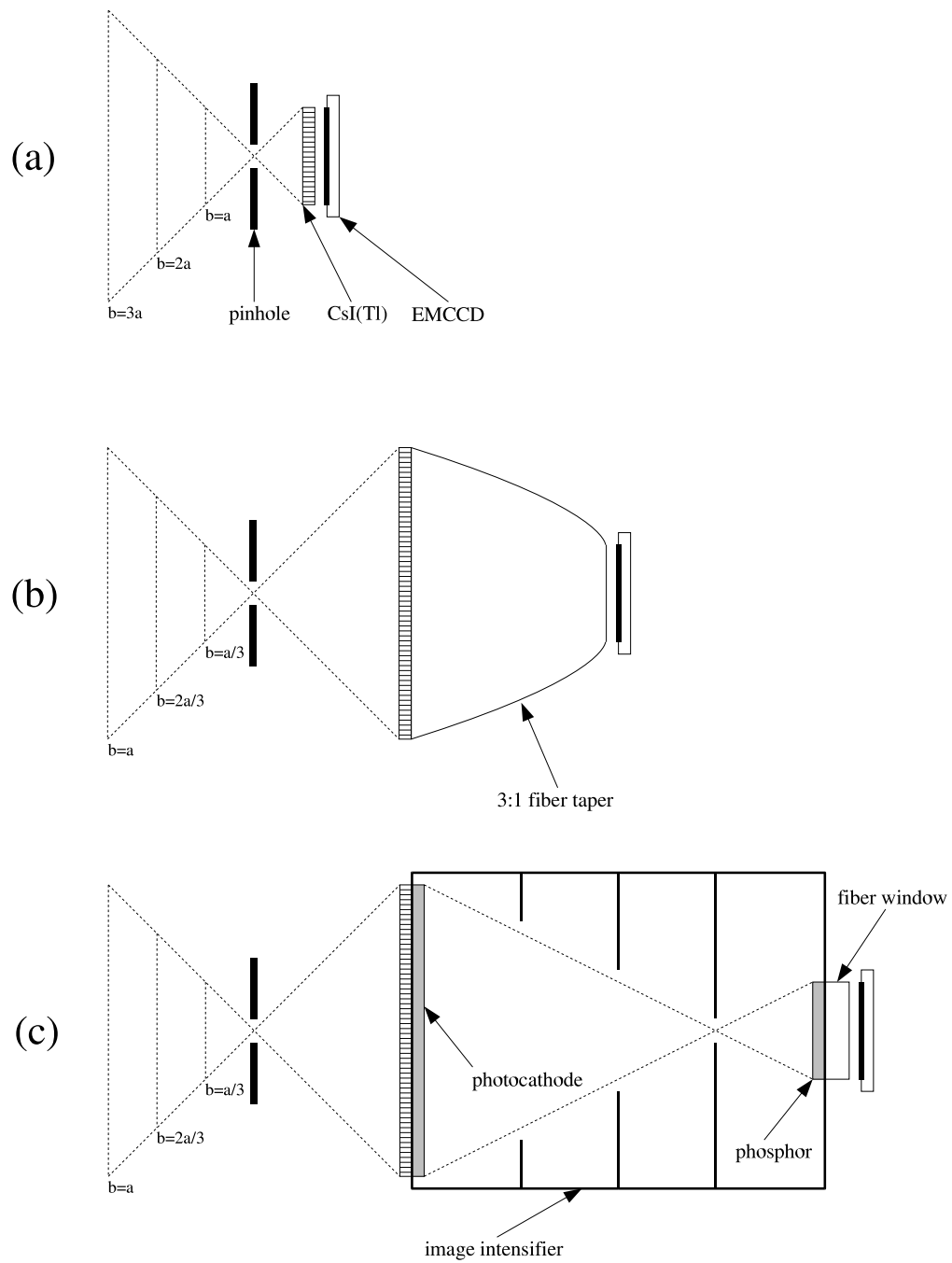photocathode

phosphor

image intensifier

Figure 7.1: A schematic showing EMCCD object image reduction in the gamma ray phase using a pinhole collimator (a), the optical photon phase using a tapered fiber optic bundle (b), and the electron phase using an image intensifier (c).

at 560 nm respectively) to convert the optical photons into photoelectrons. The photoelectrons are then sent though a micro-channel plate (MCP) which consists of an array of millions of very thin (6 μm to 10 μm diameter) parallel glass channels. When an electron strikes the inside wall of the MCP channel it produces secondary electrons. This process is then repeated several times along the length of the MCP to create a gain of 10^4. By using up to three MCP stages, electron gains of 10^7 can be reached. The amplified and highly focused electric signal then strikes a phosphor screen output window (*e.g.* P-24) where they are converted back into optical photons for imaging.

Initial tests performed by the dissertation author with a Generation 3 image intensifier (X-Ray and Specialty Instruments, Inc.), micro-columnar CsI(Tl) crystal, and ^{125}I source produced bright event flashes that were high above the background noise, similar to those seen with the CCD97 EMCCD. The image intensifier had an 18 mm diameter GaAs photocathode, single MCP (10 μm diameter holes), and P-22 phosphor. Further testing showed that the majority of bright events were not coming from the scintillating crystal or GaAs photocathode, but rather from direct gamma ray interaction with the MCP itself. This was possibly due to the thin micro-columnar CsI(Tl) crystal used (150 μm thick). Another group has reported measuring ^{99m}Tc scintillation flashes using a 500 μm thick micro-columnar CsI(Tl) crystal, Generation 2 image intensifier (S-25 photocathode), and dual lens coupling with CCD readout [80].

Using an MCP based image intensifier would allow for a large object area ($\approx$ 50 mm diameter) to be measured with high resolution (< 1 mm). Also, having the electronic gain occur in the image intensifier allows the use of a conventional CCD to capture the event flashes at video rate speeds, which both simplifies the

system and saves cost.

7.3.3 The Effects of High Intrinsic Resolution in SPECT Imaging

EMCCD images formed by counting individual photoelectric events within the scintillation crystal have improved intrinsic resolutions when compared to light integration images [46]. Although resolutions of less than 100 μm have been measured, it is not yet understood how to take full advantage of this metric in preclinical SPECT imaging. For example, when using a 0.5 mm pinhole collimator with an intrinsic resolution of 100 μm, the total spatial resolution is still limited by the geometric resolution of the pinhole. The total resolution can be improved by reducing the pinhole diameter, but this has negative effects on the sensitivity as previously shown. Figure 7.2 shows a resolution plot for $R_i = d_e = 100$ μm. It can been seen that for $\frac{b}{a} = 1$ (no image magnification) a total resolution of about 225 μm is achieved. It can also be seen that a total resolution of less than 1 mm is still reached with $\frac{b}{a} = 5$, where the projected image on the crystal surface is *smaller* than the subject object. This means that for a subject FOV of 10 mm x 10 mm, only 2 mm x 2 mm is needed on the crystal surface. Therefore, one hundred 0.1 mm diameter pinholes could be multiplexed onto a 20 mm x 20 mm collimator with no image overlap on the crystal surface. Yet the combined sensitivity of these one hundred pinholes would be equivalent to a single 1.0 mm diameter pinhole. It is possible that microchannel parallel hole [81, 82] or multiple slit [83] collimators might better use the high intrinsic resolution of an EMCCD based gamma camera to find a good balance between sensitivity and resolution in preclinical SPECT imaging.
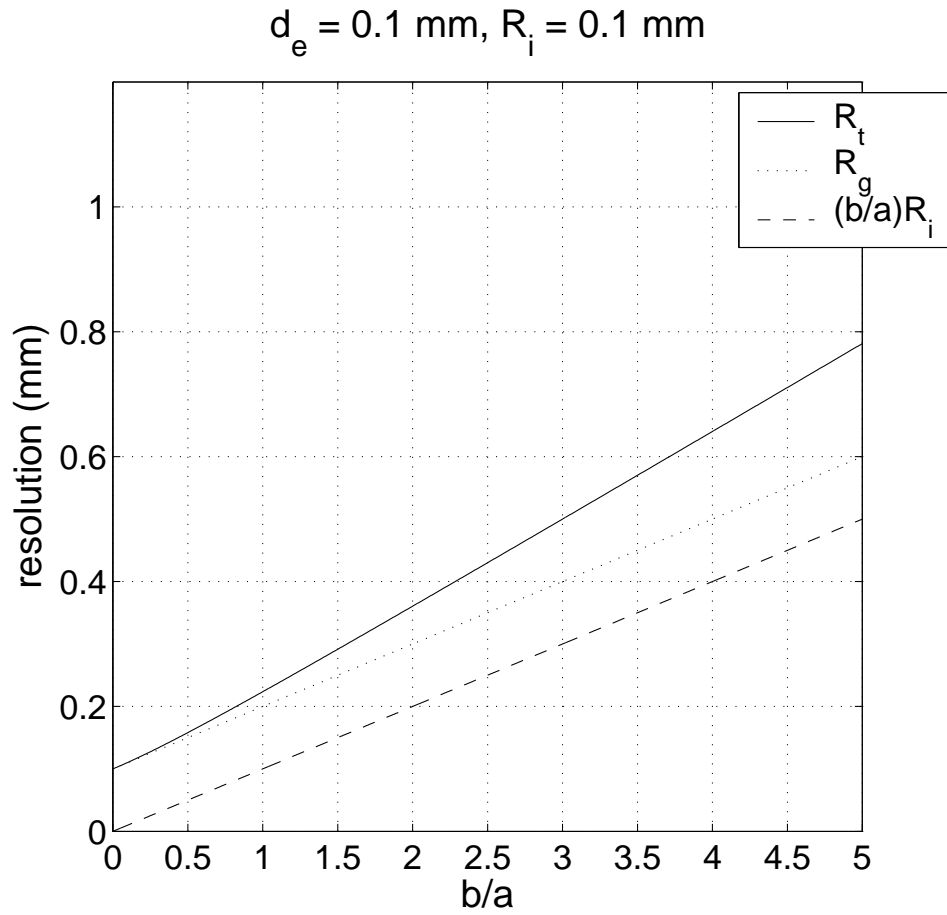
190

Figure 7.2: A plot of R_t, R_g, and $\frac{b}{a}R_i$ versus $\frac{b}{a}$ for $d_e = 0.1$ mm and $R_i = 0.1$ mm. It can be seen that a total resolution of less than 1.0 mm is still achieved at $\frac{b}{a} = 5$.

7.4 Further Work

7.4.1 TC253 EMCCD

One possible solution to allow photon counting with the TC253 is to improve the optical transfer of the scintillation photons to the EMCCD by using a micro-columnar CsI(Tl) crystal with a fiber optic bundle instead of monolithic crystal with lens coupling. Fiber optic coupling offers an order of magnitude improvement in the coupling efficiency ($> 50\%$ with a 1:1 image to object ratio) compared to lens coupling [50]. This method of photon counting has been previously established [46, 47, 49] and would allow for energy windowing, a higher intrinsic resolution, and a larger crystal FOV to be observed. Another solution could be to change from the Texas Instruments TC253 to the TC247 EMCCD. The TC247 has a higher quantum efficiency than the TC253 (50% versus 35% at 560 nm) and does not appear to be noise limited by inherent spurious charge generation [84]. Although the TC247 has a larger pixel size than the TC253 (10 μm x 10 μm versus 7.4 μm x 7.4 μm) it does not have a 100% fill factor which could effect the sensitivity. These two options should be explored with the goal of making the TC253 EMCCD gamma camera capable of both photon counting and energy discrimination for ^{99m}Tc and ^{125}I sources.

7.4.2 CCD97 EMCCD

Although the PhotonMAX 512B is able to cool the EMCCD down to -70 $^\circ$C without the use of a liquid heat exchanger, the e2v CCD97 chip is hermetically sealed under vacuum behind an optical window. Therefore, only lens coupling can be used with the PhotonMAX camera. As shown previously, a more effective EMCCD based gamma camera system can be made by using fiber optic coupling to increase the optical coupling efficiency. Also, only moderate cooling ($\approx$ -30 $^\circ$C) is needed to min-

imize the dark current when using photon counting mode. When combined with cost, the above reasons make the PhotonMAX 512B an unattractive candidate for a multiple EMCCD preclinical SPECT system. Although there are commercially available EMCCD cameras that have built in fiber optic windows (*e.g.* Andor Technology) they are still quite expensive and rather large. It would be less expensive to design a custom made, multiple camera system around the CCD97 EMCCD.

While the LabVIEW code written for the PhotonMAX was able to acquire photon counting data in near real-time, it currently cannot run at true video rate speeds. Although faster video rates could be achieved through code modification and simplification, the IMAQ software used for digital image processing is expensive. Plus, the LabVIEW system might not properly support the multiple cameras needed for a preclinical SPECT device. It is possible that dedicated digital signal processing kits (*e.g.* the Texas Instruments DSK6416 used by Beekman *et al* [47]) would be more useful for a compact multiple camera system

7.4.3   Potential Applications of Preclinical SPECT at UTSW

This section briefly discusses two possible applications of a high-resolution and high-sensitivity small animal SPECT system for research taking place at UT Southwestern.

In Vivo Imaging of Alzheimers Disease Amyloid Plaques

Alzheimer's Disease (AD) is a form of dementia and is a member of a group of brain disorders that cause memory loss and a decline in mental function over time. AD is the most common form of dementia and affects about 4.5 million people in the United States alone.

AD pathogenesis is associated with the formation of neuritic plaques and neurofibrillary tangles within the neocortex of the brain [85, 86]. The plaques contain insoluble aggregates of amyliod-β peptides (namely Aβ_{1-40} and Aβ_{1-42}), while the tangles are composed of the hyperphosphorylated, microtubule-associated protein tau [87]. Currently, the only definite diagnosis for AD is *in vitro* postmortem histopathological examination of brain tissue. The ability to detect and quantify amyliod-β plaque density *in vivo* would allow for the early diagnosis of AD and the ability asses prognosis during treatment.

Difficulties associated with imaging amyliod-β plaques *in vivo* include developing a biological agent that will effectively bind to the aggregated amyliod-β, the ability for this agent to cross the blood brain barrier (BBB), and having enough agent present in the amyloid plaque for imaging. This research is now being performed in the preclinical setting due to the development of transgenic mice that express both mutant human amyloid precursor protein (APP) and presenilin 1 (PS1) protein which are associated with familial AD in humans [88]. These mice (created by mating two strains of hemizygous transgenic mice, each expressing a single mutant human protein) exhibit abundant neuritic-type amyloid deposits and behavioral deficits in as little as 12 weeks, providing a suitable murine model for human AD.

Imaging the pathological structures associated with AD has been attempted using several modalities including Positron Emission Tomography (PET) [89], Magnetic Resonance (MR) [90], multiphoton microscopy [91], and near-infrared fluorescence imaging (NIRF) [87]. Although ^{125}I radiolabeled agents that bind to amyloid plaques have been developed, there has not yet been any direct *in vivo* imaging using SPECT in either clinical or preclinical settings [85, 92].

194

Research groups at UT Southwestern have completed initial tests on the potential use of ^{125}I radiolabeled Clioquinol (^{125}I-CQ) as an agent that binds to the amyliod-β plaques associated with AD. The ability of ^{125}I-CQ to readily bind to metal-ion sites on the amyloid-β aggregates was demonstrated *in vitro* using postmortem brain tissue samples from an AD patient and autoradiography. The AD tissue sections showed an increased uptake of ^{125}I-CQ when compared with normal, leukodystophic, post-cerebral infarct, and pre-cerebral infarct brain tissue sections prepared in the same manner. The ability of ^{125}I-CQ to effectively cross the BBB was measured *ex vivo* using normal Swiss-Webster male mice. Animals were sacrificed at intervals from 2 minutes to 24 hours after injection with ^{125}I-CQ. Both gamma counting and whole organ autoradiography were then performed on the excised brains. The initial activity (%ID/g) in the brain was 3.03 at 2 minutes, decreasing to 0.55 at 15 minutes, with no activity detectable at 24 hours. This showed that both the uptake and clearance of ^{125}I-CQ were rapid for normal mouse brain tissue, which is a required characteristic for SPECT imaging.

The next step is to repeat the latter experiment with transgenic mice, specifically PDAPP mice that express both the APP and PS1 mutant human proteins. If the activity within the brains of the transgenic mice lasts much longer than that of the normal mouse brains, this will show that ^{125}I-CQ is capable of binding to amyloid-β aggregates *in vivo*. The next step will then be to image the bound ^{125}I-CQ *in vivo* with the new SPECT system. The need for the new SPECT system to have both high-resolution and high-sensitivity is shown given the volume of a mouse brain (< 1 cm^3) and the possibility of trace activity being bound to the plaques, which are themselves small deposits of protein aggregates (< 100 μm in diameter).

In Vivo Imaging of Tumor Blood Volume

Post-avascular establishment and progressive expansion of malignant neoplasms is possible only through the formation of an adequate vascular supply [93]. This vascular supply can consist of both preexisting host vessels which are incorporated into the tumor tissue and microvessels arising from neovascularization due to the influence of tumor angiogenesis factors [94]. Both tumor vascular morphology and blood flow rate govern the movement of molecules through the vasculature [95] and thus the perfusion of blood-borne diagnostic and therapeutic agents. Tumor vascular extent, expressed by the tumor blood volume (TBV), can also be used to infer tumor physiological characteristics such as aggressiveness, growth rate, and response to antiangiogenic therapy.

Most techniques used to measure TBV in preclinical studies using small animals involve the administration of a radiopharmaceutical (^{125}I-albumin) followed by the postmortem excision of the tumor. The tumor activity is then measured using methods such as gamma counting or autoradiography. Major drawbacks of these *in vitro* methods are that each animal can only be measured once leading to several animals being used for a study, the dynamic response in the physiological characteristics within a single tumor cannot be observed, and that the methods are non-quantitative and susceptible to procedural error. Using a small animal SPECT device to measure tumor blood volume *in vivo* could overcome all of these drawbacks.

One advantage of using small animal SPECT to noninvasively investigate TBV is that the agents currently used for *in vitro* analysis can be immediately applied for *in vivo* measurements. By using pedicle tumors on rats, and since orthotopic tumors in mice are no deeper that 1 cm of tissue, the relatively low energy gamma rays (≈ 27 keV) emitted from ^{125}I-albumin can be used without concern

of inelastic (Compton) photon scattering reducing the position and energy resolutions. With *in vivo* TBV measurements, multiple measurements on the same animal and tumor can be made throughout the study, with each animal acting as its own control. This will allow the dynamic observation of tumor physiological response to such therapeutic vascular targeting agents like Combretastatin A-4-phosphate (CA4P; Oxigene Inc., Lund, Sweden).

Appendix A

Derivation of the True On-Axis Geometric Efficiency

The on-axis geometric efficiency (g) of a pinhole collimator is defined as the ratio of the number of gamma rays that pass through the pinhole over the total number of gamma rays emitted from a isotropic point source. This is illustrated in Figure A.1 where b is the distance from the point source to the pinhole and d_e is the effective diameter of the pinhole. For an isotropic point source, g is given by the ratio of the spherical cap area subtended by d_e over the total spherical area defined by the radius b.

The formula for the spherical cap area is given by:

$$A_{spherical\ cap} = 2\pi Rh \tag{A.1}$$

where R is the radius of the sphere and h is the height of the spherical cap as shown in Figure A.1. Using $R = b$, the true expression for g becomes:

198
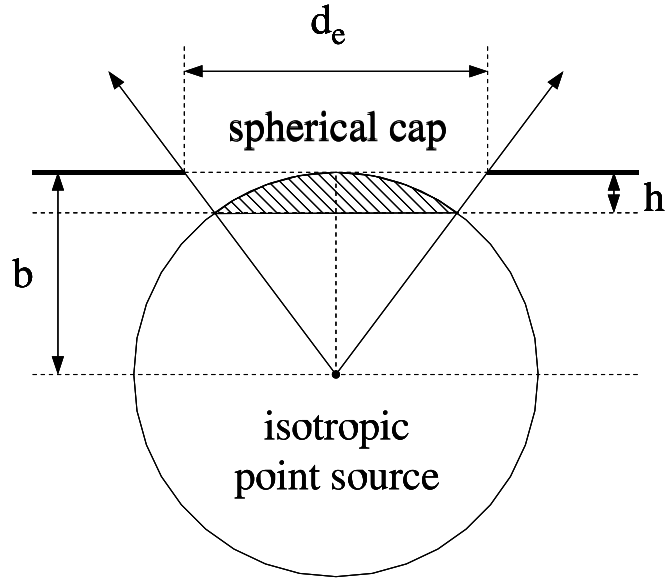
Figure A.1: A schematic showing the calculation of the on-axis geometric efficiency (g). The hatched area represents the spherical cap.

$$g_{true} = \frac{2\pi bh}{4\pi b^2} = \frac{h}{2b} \tag{A.2}$$

Therefore, an expression for h must be found. Using the principle of similar triangles gives:

$$\frac{b-h}{b} = \frac{b}{x} \tag{A.3}$$

where x is equal to the distance from the point source to one of the pinhole edges. Equation A.3 can be rewritten as:

$$h = b\left(1 - \frac{b}{x}\right) \tag{A.4}$$

Pythagoras' theorem can then be used to find an expression for x:

$$x = \sqrt{b^2 + \left(\frac{d_e}{2}\right)^2} \tag{A.5}$$

Inserting Equation A.5 into Equation A.4 gives:

$$h = b\left(1 - \frac{b}{\sqrt{b^2 + \left(\frac{d_e}{2}\right)^2}}\right) \tag{A.6}$$

which can be rewritten as:

$$h = b\left(1 - \frac{1}{\sqrt{1 + \left(\frac{d_e}{2b}\right)^2}}\right) \tag{A.7}$$

Substituting Equation A.7 (the expression for h) into Equation A.2 then gives:

$$g_{true} = \frac{h}{2b} = \frac{b\left(1 - \frac{1}{\sqrt{1 + \left(\frac{d_e}{2b}\right)^2}}\right)}{2b} \tag{A.8}$$

which can be rewritten as:

$$g_{true} = \frac{1}{2}\left(1 - \frac{1}{\sqrt{1 + \left(\frac{d_e}{2b}\right)^2}}\right) \tag{A.9}$$

which is the true expression for the on-axis geometric efficiency. It can be seen that as b goes to zero, Equation A.9 goes to $\frac{1}{2}$ (or 50% geometric efficiency).

Appendix B

IEEE Transactions on Nuclear Science Publication (accepted June 2007)

Development and Evaluation of an EMCCD based Gamma Camera for Preclinical SPECT Imaging

Todd C. Soesbe, *Student Member, IEEE*, Matthew A. Lewis, *Member, IEEE,* Edmond Richer, Nikolai V. Slavine,
Peter P. Antich, *Senior Member, IEEE*

Abstract— The electron-multiplying charge-coupled device (EMCCD) offers improved quantum efficiencies (40 to 95%) over a broader range of wavelengths (400 to 900 nm) and a higher intrinsic resolution ($<$ 100 μm using photon counting) when compared to photomultiplier tubes. The electron gain achieved in the multiplication register of an EMCCD effectively reduces the readout noise to less than 1 electron/pixel, making them sensitive to single photoelectrons. Our prototype camera uses the Texas Instruments Impactron$^{\text{TM}}$ EMCCD model TC253SPD-B0 (7.4 μm square pixels) which is cooled under vacuum to -50 $^\circ$C using a four stage Peltier and liquid heat exchanger. Shuttered lens-coupling is used to image the optical light from a 3 mm thick monolithic CsI(Tl) crystal. Precise clocking for the EMCCD is provided by a National Instruments FPGA controller (PCI-7811R) and LabVIEW FPGA module (version 8.0). A custom built electronics box contains the clock driver circuitry and 16-bit video board for digital conversion of the video signal. Our optical coupling method differs from other EMCCD SPECT systems by using lenses rather than fiber optic bundles for transfer. TC253 characterization tests measured a maximum gain just over 1000$\times$, dark current rate of 0.14 e/p/s, read noise of 18.2 e/s, and spurious charge generation of 4 e/p. A light integration intrinsic resolution of 110 μm FWHM was measured. Light integration images of a line phantom using a single pinhole collimator were used for SPECT reconstruction. We found the relative high spurious charge generation and low quantum efficiency of the TC253 made it incapable of photon counting for low energy sources using lens coupling.

Index Terms— SPECT, preclinical, small animal, EMCCD, gamma camera, pinhole collimator, high-resolution, high-sensitivity.

I. INTRODUCTION

OVER the past decade the demand for high-resolution preclinical (small animal) SPECT imaging has greatly increased. This increase is due to the development of new radiolabeled antibodies, receptor ligands, and other radiopharmaceuticals for both imaging and therapy [1]. The availability of genetically modified mice and *in vivo* molecular imaging for studying gene expression and regulation in human disease has also increased the demand for high-resolution SPECT [2]–[5]. One drawback of previous small animal radiopharmaceutical imaging methods, such as autoradiography, was that several

animals had to be sacrificed in order to achieve significant statistics since each animal could only be measured once [5]. With the development of high-resolution preclinical SPECT, an animal can be measured several times throughout a study, thereby allowing each animal to act as its own control. This leads to fewer animals needed per study, which helps to reduce the overall cost of the experiment.

The small field of view needed to image animals such as mice and rats ($\approx$ 10 cm $\times$ 10 cm) allows for the use of pinhole collimation to achieve sub-millimeter resolution ($<$ 1 mm FWHM). Yet the pinhole diameter required for this resolution severely limits the sensitivity of the device. Several methods for increasing the sensitivity of preclinical SPECT systems are currently being pursued. These methods include using multiple single pinhole detectors [6]–[10], multiplexing several pinholes onto a single detector with either minimal [11], [12] or extensive [13], [14] image overlap on the crystal surface, and even using coded apertures commonly found in gamma-ray astronomy [15], [16]. Existing clinical SPECT systems can be modified with pinhole collimators to achieve adequate resolutions for small animal imaging [6], [13], [17], [18], but compact dedicated preclinical SPECT systems can offer higher resolutions and are small enough to fit on a desktop [7].

Another method to improve sensitivity is to use a charge-coupled device (CCD) for the gamma camera photodetector. The application of CCDs to preclinical SPECT imaging has been previously shown by our group [19]. This research has been greatly accelerated by the recent availability of the electron-multiplied CCD (EMCCD) which was first technically described in 1992 [20] and made commercially available in 2001 [21], [22]. EMCCDs combine the positive aspects of photomultiplier tubes (high-gain leading to a high signal-to-noise ratio, photon counting, and energy discrimination) with the positive aspects of CCDs (high quantum efficiencies over a broad spectral range, high intrinsic resolution, and small form factor) making them well suited for preclinical SPECT applications.

Our goal is the development and evaluation of an EMCCD based small animal SPECT device for murine model studies of human disease. Previous applications of EMCCDs to preclinical SPECT imaging mainly use fiber optic bundles to transfer the light from a micro-columnar CsI(Tl) crystal to the imaging area of the EMCCD [25]–[27], [42]. This requires the bundle to be placed very close to, if not touching, the EMCCD surface which creates mechanical, cooling, and vacuum
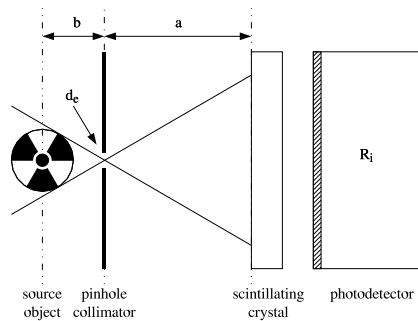
Fig. 1. A schematic showing the geometry of a gamma camera with a single pinhole collimator. When $\frac{b}{a}$ is less than 1, a magnified image of the source object is projected onto the crystal surface.

complications. Our method differs by using monolithic CsI(Tl) crystal and lens coupling for light transfer. With lens coupling, physical contact with the EMCCD is eliminated, although the transfer efficiency is lower compared to fiber coupling. Our approach also differs by using the very low cost Texas Instruments TC253 EMCCD in our custom designed camera. This paper describes the construction of the camera and electronics, EMCCD noise characterization, gamma camera intrinsic resolution, and SPECT reconstruction based on light integration and lens coupling.

II. MATERIALS AND METHODS

A. Spatial Resolution

"Pinhole collimators provide the best combination of sensitivity and resolution for small subjects that are positioned a short distance from the aperture."

Hal O. Anger, 1967

As seen in the above quote, the advantages of using pinhole collimators to image small source objects that are placed close to the aperture have been known for some 40 years [23]. In fact, the very first gamma camera used pinhole collimation to image the uptake of ^{131}I (364 keV gamma rays) in the human thyroid gland [24]. The setup for a single pinhole gamma camera is shown in Figure 1 where d_e is the effective diameter of the pinhole aperture, b is the distance from the source to the pinhole, a is the distance from the pinhole to the scintillating crystal, and R_i is the intrinsic spatial resolution of the photodetector and scintillation crystal. The total resolution of the system is given by:

$$R_t = \sqrt{\left(d_e\left(1+\frac{b}{a}\right)\right)^2 + \left(\frac{b}{a}R_i\right)^2} \qquad (1)$$

where the first quadratic term under the square root is the geometric resolution (R_g) and the second quadratic term is the effective intrinsic resolution [23]. When $\frac{b}{a}$ is less than 1, a magnified image of the source object is projected onto the crystal surface. This makes the effective intrinsic resolution lower than the intrinsic resolution, which helps to improve the

total resolution. Figure 2(a) shows a plot of R_t, R_g, and $\frac{b}{a}R_i$ versus $\frac{b}{a}$ for $d_e = 1.0$ mm and $R_i = 5.0$ mm, which correspond to the typical pinhole size used in small animal imaging and the typical intrinsic resolution of a clinical SPECT gamma camera respectively. For these conditions, it can be seen that the $\frac{b}{a}R_i$ term quickly becomes the limiting term for the total resolution as $\frac{b}{a}$ increases. As mentioned previously, clinical SPECT gamma cameras can be used for small animal imaging but require large magnification factors to adequately image mice and rats. From Figure 2(a) it can be seen that in order to achieve a total resolution of 1.5 mm with a clinical system, a magnification of $5\times$ ($\frac{b}{a} = 0.2$) must be used. This leads to large detector surface areas and volumes. In Figure 2(b) d_e is again 1.0 mm but R_i has been reduced by an order of magnitude to 0.5 mm. It can be seen that the geometric resolution is now the limiting term for the total resolution, and that a magnification of only $2\times$ ($\frac{b}{a} = 0.5$) is needed to achieve a total resolution of 1.5 mm. This greatly reduces the detector surface area leading to a smaller detector volume, which is more suitable for small animal imaging.

B. Pinhole Sensitivity

With a very low intrinsic resolution as in Figure 2(b), the total resolution of the system can be further improved by reducing d_e. Figure 2(c) shows a resolution plot for $d_e = 0.5$ mm and $R_i = 0.5$ mm. It can be seen that R_g is still the limiting term for the total resolution, but now a magnification of $2\times$ ($\frac{b}{a} = 0.5$) gives a total resolution of less than 1 mm. Although having sub-millimeter resolution is attractive, reducing d_e from 1.0 to 0.5 mm severely reduces the sensitivity (counts/second per source activity) of the system. The on-axis geometric efficiency for a pinhole is given by:

$$g = \frac{1}{2}\left(1 - \frac{1}{\sqrt{1 - \left(\frac{d_e}{2b}\right)^2}}\right) \qquad (2)$$

and represents the fraction of emitted photons that pass through d_e from an isotropic point source located a distance b from the pinhole. For $b \gg d_e$ the square root term in Equation 2 can be binomially expanded to give the approximation:

$$g \approx \frac{d_e{}^2}{16b^2} \qquad (3)$$

which is the expression more commonly seen in the literature [7], [17], [23]. When reducing d_e from 1.0 to 0.5 mm, g goes from 0.1% to 0.02% respectively (for $b = 10$ mm). Therefore simply reducing d_e by a factor of two reduces g, and thus the sensitivity, by a factor of five.

One method to increase the sensitivity of pinhole collimation is to simply surround the source object with multiple pinholes. The four main configurations for multiple pinholes are shown schematically in Figure 3, where the first row is the number of pinholes per collimator, the second row is the pinhole configuration, and the third row represents the projected image onto the crystal surface when imaging a uniform planar source. These options include surrounding the source object with multiple single pinhole detectors (a), multiplexing several pinholes onto one photodetector such
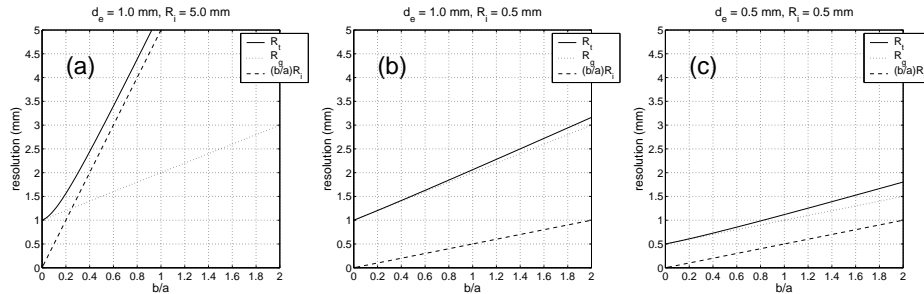
Fig. 2.   A plot of R_t, R_g, and $\frac{b}{a}R_i$ versus $\frac{b}{a}$ for (a) $d_e = 1.0$ mm and $R_i = 5.0$ mm, (b) $d_e = 1.0$ mm and $R_i = 0.5$ mm, and (c) $d_e = 0.5$ mm and $R_i = 0.5$ mm. $\frac{b}{a}R_i$ is the limiting term for (a), while R_g is the limiting term for (b) and (c).
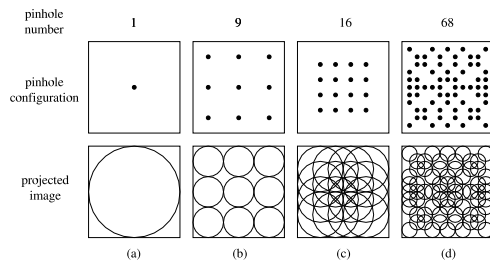

Fig. 3.   A schematic showing the four main configurations for multiple pinhole collimation. The sensitivity per collimator increases when moving from left to right.

that there is no image overlap on the crystal surface (b), multiplexing with image overlap on the crystal surface (c), and using a coded aperture which has severe image overlap (d). Although the sensitivity increases when moving from left to right in Figure 3, it is not fully understood how the resolution changes as the image overlap increases and the tomographic reconstruction becomes more complicated. For this project we intend to improve the sensitivity by multiplexing 9 pinholes onto a single EMCCD gamma camera in a non-overlapping manner and surrounding the source with a ring of up to 12 cameras for a total of over 100 pinholes.

C. EMCCD Sensitivity

The sensitivity of a gamma camera system can be further improved by using an EMCCD to detect the optical photons emerging from the scintillation crystal. EMCCDs have higher quantum efficiencies (up to 95% with back-illumination) and broader spectral responses (400 to 900 nm) when compared to PMTs. Also, intrinsic resolutions less than 100 μm have been shown for EMCCD based gamma cameras [25], [26]. The most important characteristic of an EMCCD is the improved low light level signal-to-noise ratio (SNR) when compared to conventional CCDs. This is achieved by the addition of a second serial register, known as the gain or multiplication register, to the CCD architecture as shown in Figure 4.

Electrons are first captured within the pixel potential wells of the image area, then the entire frame (for example 680×500 pixels) is parallel-transferred to the storage area. A single pixel row is then parallel-transferred from the storage area to the serial register. The pixel row in the serial register is then serial-transferred through the multiplication register to the charge-to-voltage output amplifier of the EMCCD. This is done for each row until the entire storage area has been read. The multiplication register differs from the normal serial register by the addition of a third gate known as the charge multiplication gate (CMG) [28]. By making the voltage of the CMG very high (up to 15 VDC) the electrons undergo impact ionization as they move through the multiplication register, which amplifies the electric signal. Although the gain per pixel step is very low (1.01 to 1.018) a multiplication register of 400 pixels in length can allow gains of over $1000\times$ to be reached [29]. Multiplication of the signal in the charge domain before charge-to-voltage conversion effectively reduces the readout noise of the output amplifier to less than 1 electron/pixel. This eliminates the noise floor found in conventional CCDs making EMCCDs sensitive to single electrons.

The total signal noise of an EMCCD is given by:

$$\sigma_t = \sqrt{G^2 F^2 (P + D + S) + \sigma_r^2} \qquad (4)$$

where G is the gain, F is the excess noise (Fano) factor due to the gain process in the multiplication register, and P, D, S, and σ_r are the mean signals (electron/pixel) due to the photon (shot), dark current, spurious charge, and read noises respectively [29], [30]. The dark current noise (D) and the spurious charge noise (S) can be reduced to negligible levels with cooling and proper clocking respectively [31]. Also, for a gain greater than $\approx 10\times$, F approaches $\sqrt{2}$ [32]. Under these conditions the SNR for a EMCCD reduces to:

$$SNR_{EMCCD} = \frac{GP}{\sigma_t} = \sqrt{\frac{P}{2}} \qquad (5)$$

when $G \gg \sigma_r$. This can be compared to the SNR of a conventional CCD under similar condition given by:

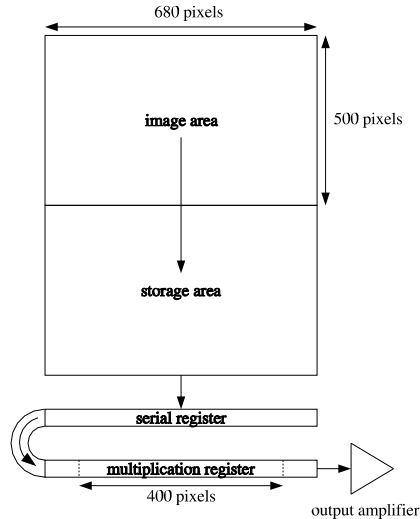$$SNR_{CCD} = \frac{P}{\sqrt{P + \sigma_r^2}} \qquad (6)$$

204

Fig. 4. A schematic showing the architecture of an EMCCD. The electrons are multiplied by impact ionization as they move through the multiplication register before charge-to-voltage conversion in the output amplifier.
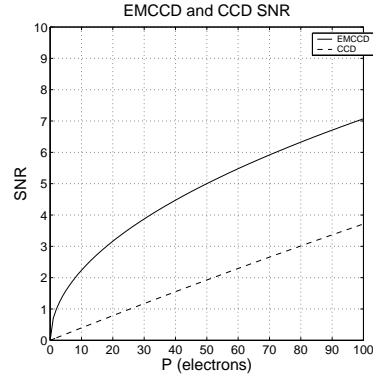

Fig. 5. A plot showing the EMCCD and CCD SNR as a function of electrons/pixel. The EMCCD SNR is much higher for low light level imaging.
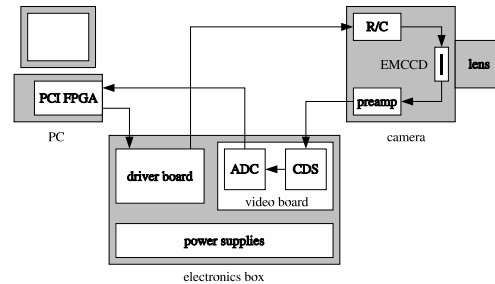

Fig. 6. A schematic showing the setup for the prototype EMCCD camera.

A plot of SNR_{EMCCD} and SNR_{CCD} versus P is shown in Figure 5 for a typical read noise ($\sigma_r = 25$ electrons/pixel). It can be seen that while the CCD has a SNR of 1 at 25 electrons/pixel, the EMCCD has a SNR that is 3.5 times higher.

D. Camera Prototype

A schematic of the prototype system is shown in Figure 6. The system consists of a PC with a FPGA card, an external electronics box, and the EMCCD camera assembly. The National Instruments PCI-7811R (Xilinx FPGA, 1 million gates, 40 MHz digital rate, 25 ns resolution) produces the clock pulse timing for the EMCCD. These pulses are sent to the driver board inside the external electronics box which converts the TTL pulses to the proper voltages needed to drive the EMCCD. The driving pulses are then sent through an R/C circuit located inside the camera housing for shaping before entering the EMCCD. The video signal from the EMCCD is first sent through a preamp and then through a video board. The video board uses correlated double sampling (CDS) of the video signal to help reduce noise before digital conversion in a 16-bit ADC (Analog Devices AD976A, 200 kHz max rate). The digitized video signal is then sent back to the FPGA which uses a DMA FIFO across the PCI bus to store the data on the host computer which is running LabVIEW 8.0.

For the prototype camera we used the Texas Instruments Impactron^{TM} TC253 EMCCD chip (TC253SPD-B0). This front-illuminated chip (35% quantum efficiency at 560 nm) has 7.4 μm square pixels (100% fill factor) in a 680×500, 1/3 inch format. The TC253 has a nominal read noise of

29 electrons/pixel RMS at video rate readout (12.5 MHz clock frequency). It also has low dark current generation (≈ 0.1 electron/pixel/sec at -40 °C) and a built in single stage Peltier element capable of cooling the chip down to -10 °C. Figure 7(a) shows a close up photo of the TC253. The TC253 is mounted onto an Aluminum cold-finger which sits on top of a four-stage Peltier element. Low thermal conductivity wires connect the TC253 to the R/C and preamp circuitry with all camera electronics being contained in the vacuum housing. Figure 7(b) shows an exploded view of the camera assembly showing the lens, shutter, vacuum window, EMCCD housing, and a choice of either air or liquid heat exchanger. A picture of the assembled camera is shown in Figure 7(c).

III. RESULTS

High quantum efficiency back-illuminated EMCCDs such as the e2v CCD97 currently cost between 6k to 7k USD. Off-the-shelf camera systems containing these EMCCDs such as the PhotonMAX 512B cost around 30k USD. To increase the sensitivity of our preclinical SPECT system, we would like to surround the animal with a ring of multiple cameras. Therefore, in order to reduce the cost per camera to a reasonable level, we have opted to design and build our own. By using
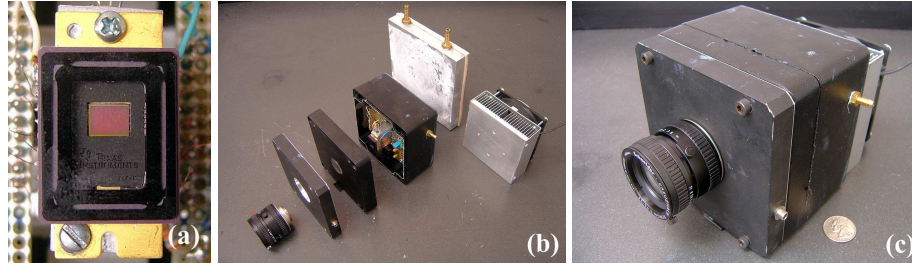
Fig. 7.   (a) A photo showing the front face of the Texas Instruments Impactron[TM] TC253 EMCCD mounted to the Aluminum cold finger. The image area (680 $\times$ 500 pixels) measures 5.0 mm $\times$ 3.7 mm. (b) An exploded photo of the camera assembly. (c) The assembled camera with air heat exchanger.

the low-cost front-illuminated TC253 EMCCD (500 USD), the PCI-7811R FPGA card with LabVIEW module (2k USD), and custom built electronics (500 USD), the cost per camera is reduced by an order of magnitude to 3k USD. Details of the camera system, followed by TC253 noise characterization, and initial light integration imaging results are presented next. Although the system has a gain of over 1000$\times$, low read and dark noises, and good intrinsic resolution, the relative high spurious charge generation and low quantum efficiency of the TC253 make it incapable of photon counting for both ^{99m}Tc and ^{125}I using monolithic CsI(Tl) crystals with lens coupling.

A. EMCCD Characterization

Upon completing the prototype camera, we first characterized the EMCCD by measuring the gain, dark current accumulation rate, total read noise, and spurious charge generation to verify that they were within the specified operating range of the TC253. Methods and results for the measurements are described here. All measurements were taken at -40 °C.

1) Gain: The gain versus positive charge multiplication gate voltage (+CMG) of the TC253 was measured using lens coupling to image a controlled light source. The light source consisted of a 3 mm green LED embedded in a 10 mm $\times$ 15 mm Teflon cylinder to create a small diffuse uniform source that was viewed on end. With the EMCCD gain set to 1 (+CMG = 7.0 V), the current to the LED was varied until a SNR of about 5 was achieved for an average of 1000, 33 msec exposures. The difference between the dark reference pixels and peak signal was measured using a line profile of the averaged image. This measurement was repeated as the +CMG voltage was increased, with the increase between the dark and peak pixels being taken as the gain. A plot of gain versus +CMG is shown in Figure 8. It can be seen that the gain starts to increase past 11 V and rises to over 1000 at 14 V.

2) Dark Current: Dark current arises from thermal generation of electrons within the silicon lattice of the EMCCD. These electrons are captured by the pixel potential wells and contribute to the non-photon related signal noise (see Equation 4). Dark current generation is proportional to exposure time, independent of the amount of light incident on the EM-CCD, and can be significantly reduced by cooling [33]. The dark current accumulation rate for the TC253 was measured
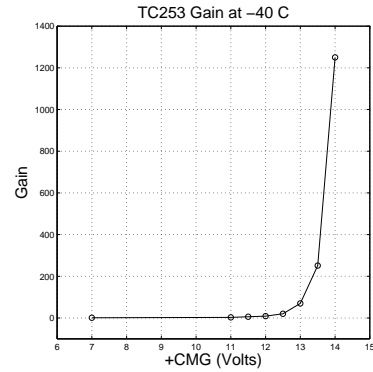

Fig. 8.   A plot of EMCCD gain versus positive charge multiplication voltage (+CMG) for the TC253. A gain of over 1000$\times$ is reached at 14 V.

by taking N exposures at a fixed dark exposure time. The mean and standard deviation of the N exposures were then calculated for each pixel. The ensemble average of the pixel means over the active EMCCD area was taken as the dark current count (electrons/pixel), while the ensemble average of the pixel standard deviations was used to calculate the error ($\pm \frac{\sigma_x}{\sqrt{N}}$). This measurement was then repeated for several different dark exposure times. For these measurements, the gain was set to 1 and the EMCCD temperature was -40 °C. A plot of exposure time versus dark current count is shown in Figure 9. The fitted slope gives 0.14 electrons/pixel/second which agrees with the dark current rate given in the TC253 datasheet.

3) Read Noise: The main source of read noise in the system arises from the charge-to-voltage conversion in the EMCCD output amplifier. Assuming that the spurious charge has been reduced to a negligible level, then for a zero second dark exposure ($P = D = 0$) at a gain of 1, Equation 4 reduces to:

$$\sigma_t = \sqrt{\sigma_r^2} = \sigma_r \qquad (7)$$

so that the total noise is equal to the total read noise. The read noise of the system was measured by taking 1000 zero second exposures at a gain of 1 and calculating the standard deviation
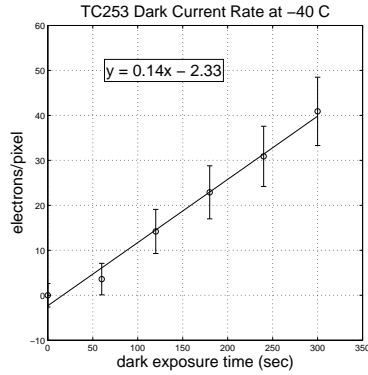
Fig. 9. A plot of dark current count (electrons/pixel) versus dark exposure time. The fitted slope gives the dark current accumulation rate for the EMCCD at -40 °C.
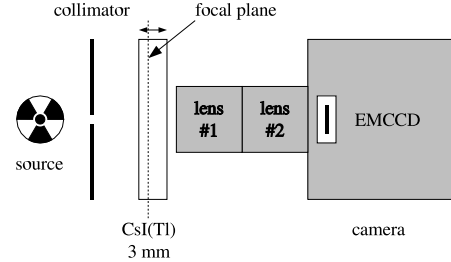

Fig. 10. A schematic of the EMCCD SPECT setup. Two lenses are used to improve the optical transfer of the scintillation light to the EMCCD. The lens focal plane can be moved through the crystal.

for each pixel. The ensemble average of the pixel standard deviations over the active EMCCD area was then multiplied by the system video gain (0.57 electrons/ADU) to give a read noise of 18.2 electrons/pixel RMS. The measured read noise was lower than the read noise stated in the TC253 datasheet (29 electrons/pixel RMS) due to the 200 kHz maximum readout rate of the current ADC. Although fine for initial testing, a faster ADC will be needed to achieve video rate readout (12.5 MHz). This will increase the readout noise which is proportional to the readout speed.

4) Spurious Charge: Along with dark current, non-photon related electrons known as spurious charge (or clock induced charge) can be generated during the readout of the EMCCD. Spurious charge arises from the rapid inversion of the clocking potentials and tends to increase with faster readout speeds and lower temperatures [33]. Methods to reduce spurious charge include using a slow parallel-transfer from the image area to the storage area, setting the rise and fall times of the clocking pulses to about 200 ns, and using the minimum clocking potentials necessary for efficient charge transfer [26], [31]. Of these three methods, the greatest observed reduction in spurious charge for the TC253 was seen by minimizing the clocking potentials [34].

Spurious charge generation as a function of +CMG was measured for the TC253 by taking 100 zero second dark exposures for a fixed +CMG voltage. The ensemble average of the standard deviations for each pixel was then calculated and taken as the total noise (σ_t). For a zero second dark exposure ($P = D = 0$) Equation 4 can be rewritten as:

$$S = \frac{\sigma_t^2 + \sigma_r^2}{F^2 G^2} \tag{8}$$

By using σ_t from above, σ_r and G from the previous read noise and gain measurements, and knowing that $F \to \sqrt{2}$ at high gain, the spurious charge generation was calculated to be 3 to 4 electrons/pixel at gains from 500× to 1000×. This spurious charge generation could not be further reduced by the minimizing methods listed above and appears to be an

inherent property of the TC253, largely caused by the use of virtual-phase electrode technology [22]. This spurious charge generation is therefore the true noise floor for the TC253 chip making it incapable of single photoelectron sensitivity. Consequences of this measurement are further discussed in Section IV. As a comparison, this same measurement was done with a high-quality commercially available EMCCD camera (Princeton Instruments/Acton PhotonMAX 512B with the e2v CCD97 EMCCD) which yielded a spurious charge generation of less than 0.01 electrons/pixel.

B. Intrinsic Resolution

A schematic of the lens-coupled SPECT setup is shown in Figure 10. Two 1-inch format lenses (Schneider Xenon 0.95/25) were coupled front-to-front in order to improve the optical transfer to the EMCCD. Both lenses had an f-stop of 0.95 with the front lens focus set to infinity and the rear lens focus being adjustable. A 3 mm thick monolithic CsI(Tl) crystal was then placed 5 to 10 mm in front of the lenses so that the shallow focal plane (less than 1 mm deep) could be moved through the crystal. The two coupled lenses image a field of view (FOV) on the crystal that is approximately the same size as the image area of the EMCCD ($\approx$ 5 mm × 5 mm). When compared to a single lens imaging the same FOV, we found the optical transfer when using two lenses to be improved by a factor of two.

The intrinsic resolution (R_i) for the above setup was measured using a 30 μm slit Tungsten collimator and a ^{99m}Tc source. The activity viewed by the slit was approximately 50 μCi (1.9 MBq). The line spread function for a 5 minute exposure with the gain set to 200× was acquired. The acquired image and 1 mm wide line profile (taken perpendicular to the slit) are shown in Figure 11. Fitting the line spread function profile with a Gaussian distribution gave a FWHM of 110 μm which was taken as the intrinsic resolution.

C. SPECT Images

For SPECT imaging, the Tungsten slit collimator was re-placed with a single pinhole Lead collimator. The pinhole diameter was 0.5 mm with an aperture angle of 90 degrees.
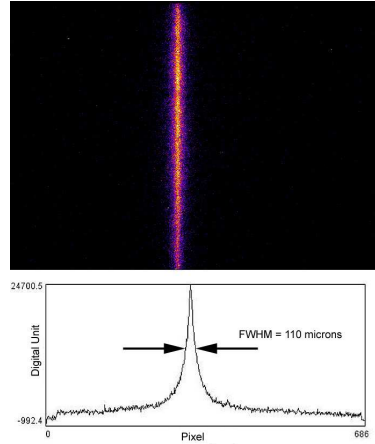
Fig. 12. A pinhole projection image of a ^{99m}Tc filled line phantom. The subject FOV measures 6.0 mm × 4.5 mm with an exposure time of 3 minutes.

Fig. 11. The image and line profile produced by a 30 μm slit collimator and ^{99m}Tc source. The exposure time was 5 minutes with a gain of 200×.

Fig. 13. SPECT reconstruction of the line source (a) with Gaussian fitted line profile (b).

A small glass capillary tube was filled with aqueous ^{99m}Tc solution, mounted to a step motor, and placed in front of the pinhole. The 3 cm long capillary had an outer diameter of 1.5 mm, an inner diameter of 0.8 mm, and a linear activity of 10 μCi/mm (0.37 MBq/mm). Projection data were then taken as the phantom was rotated (20 projections, 18° step) with a 3 minute exposure time for each projection. The EMCCD gain was set to 1000× at a temperature of -50 °C. Figure 12 shows a sample projection of the line source, with the subject FOV measuring 6.0 mm × 4.5 mm.

Image reconstruction was based on the Maximum Likelihood method (MLEM) [35] which was improved with the listmode high resolution algorithm for system matrix modeling (MLSM) [36], [37]. A convolution procedure based on the discrete Fast Fourier Transform (FFT) was used for resolution modeling. If photon scattering is neglected, the blurring component of the matrices which account for the finite resolution effects can be represented as a set of shift-invariant kernels (details given in [37], [38]). Figure 13(a) shows a transverse slice of the MLSM reconstruction for the line phantom. The total FOV (20 mm^3) was subdivided into 0.25 mm^3 voxels. Approximately 300,000 events were reconstructed into the voxel array. A Gaussian function (0.4 mm kernel) was used to model the resolution during the 10 iterations. The FWHM of the Gaussian fitted line profile in Figure 13(b) measures 0.96 mm. The slight increase in the reconstructed diameter is due to the total resolution of the setup being limited by the geometric resolution (R_g) which was $\approx$ 1 mm.

IV. CONCLUSION AND DISCUSSION

A. Summary

A cost effective prototype EMCCD based gamma camera has been developed and evaluated for use in preclinical SPECT imaging. A four stage Peltier and liquid heat exchanger was used to cool the EMCCD down to -50 °C. Dual f/0.95

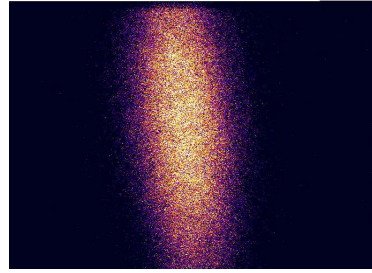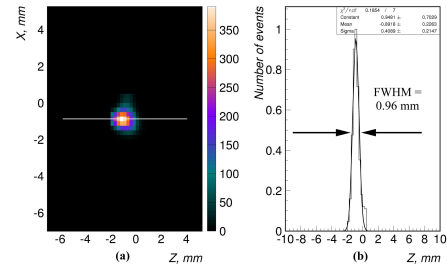lens coupling was used to image the scintillation light from a 3 mm thick monolithic CsI(Tl) crystal. A gain of over 1000× was measured for the TC253 EMCCD. The dark current accumulation rate and read noise were within the specified operating range for a temperature of -40 °C and readout rate of 200 kHz. A spurious charge generation of 3 to 4 electrons/pixel was measured at high gain values. This intrinsic spurious charge could not be further reduced using established minimizing techniques and represents the noise floor for the TC253. An intrinsic resolution of 110 μm FWHM was measured using a 30 μm slit collimator and ^{99m}Tc source. Single pinhole collimation was used to take SPECT images of a small ^{99m}Tc line phantom. The MLEM reconstructed source size was slightly larger than the true source size due to the geometric resolution of the setup.

B. Conclusions

Although the prototype EMCCD gamma camera was capable of SPECT imaging using light integration, it was unable to perform photon counting for ^{99m}Tc and ^{125}I with the current optical transfer method. This can be explained by estimating the number of electrons produced in the TC253 per CsI(Tl) scintillation event. The luminosity of CsI(Tl) is 54 photons/keV with a peak wavelength of 560 nm. Approximately 10% of these scintillation photons will escape the crystal via the non-internally reflected light cone [39]. Upper limits for dual lens optical coupling efficiency (with an object to image ratio of 1:1) have been estimated to be $\approx$ 5% [40], [41],

and the quantum efficiency of the TC253 is 35% at 560 nm. This gives $(140 \times 54 \times 0.1 \times 0.05 \times 0.35) = 13$ electrons/event for ^{99m}Tc and $(27 \times 54 \times 0.1 \times 0.05 \times 0.35) = 3$ electrons/event for ^{125}I. When these signals are spread over a 3×3 pixel area they are easily lost within the 3 to 4 electrons/pixel spurious charge noise of the TC253. Single photoelectric events were observed using a higher energy ^{137}Cs (662 keV) source where the increased number of scintillation photons results is more than 3 to 4 electrons/pixel/event. Also, when the same scintillation crystal and lens setup were used with the PhotonMAX 512B camera (e2v CCD97 EMCCD, 95% quantum efficiency at 560 nm) single photoelectric events were easily observed for both ^{99m}Tc and ^{125}I sources. These results are to be presented in a subsequent publication.

C. Further Work

One possible solution to allow photon counting with the TC253 is to improve the optical transfer of the scintillation photons to the EMCCD by using a micro-columnar CsI(Tl) crystal with a fiber-optic bundle instead of monolithic crystal with lens coupling. Fiber-optic coupling offers an order of magnitude improvement in the coupling efficiency ($> 50\%$ with a 1:1 image to object ratio) compared to lens coupling [39]. This method of photon counting has been previously established [25], [26], [42] and would allow for energy windowing, a higher intrinsic resolution, and a larger crystal FOV to be observed. Another solution could be to change from the Texas Instruments TC253 to the TC247 EMCCD. The TC247 has a higher quantum efficiency than the TC253 (50% versus 35% at 560 nm) and does not appear to be noise limited by inherent spurious charge generation [43]. Although the TC247 has a larger pixel size than the TC253 (10 μm $\times$ 10 μm versus 7.4 μm $\times$ 7.4 μm) it does not have a 100% fill factor which could effect the sensitivity. These two options will be explored with the goal of making our EMCCD gamma camera capable of both photon counting and energy discrimination for ^{99m}Tc and ^{125}I sources.

D. Discussion

EMCCD images formed by counting individual photoelectric events within the scintillation crystal have improved intrinsic resolutions when compared to light integration images [25]. Although resolutions of less than 100 μm have been measured, it is not yet understood how to take full advantage of this metric in preclinical SPECT imaging. For example, when using a 0.5 mm pinhole collimator with an intrinsic resolution of 100 μm, the total spatial resolution is still limited by the geometric resolution of the pinhole (see Equation 1). The total resolution can be improved by reducing the pinhole diameter, but this has negative effects on the sensitivity as previously shown. Figure 14 shows a resolution plot for $R_i = d_e = 100$ μm. It can been seen that for $\frac{b}{a} = 1$ (no image magnification) a total resolution of about 225 μm is achieved. It can also be seen that a total resolution of less than 1 mm is still reached with $\frac{b}{a} = 5$, where the projected image on the crystal surface is *smaller* than the subject object. This means that for a subject FOV
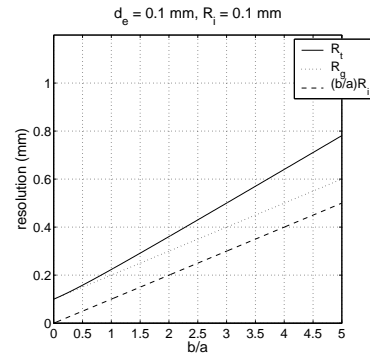

Fig. 14. A plot of R_t, R_g, and $\frac{b}{a} R_i$ versus $\frac{b}{a}$ for $d_e = 0.1$ mm and $R_i = 0.1$ mm. It can be seen that a total resolution of less than 1.0 mm is still achieved at $\frac{b}{a} = 5$.

of 10 mm $\times$ 10 mm, only 2 mm $\times$ 2 mm is needed on the crystal surface. Therefore, one hundred 0.1 mm diameter pinholes could be multiplexed onto a 20 mm $\times$ 20 mm collimator with no image overlap on the crystal surface. Yet the combined sensitivity of these one hundred pinholes would be equivalent to a single 1.0 mm diameter pinhole. It is possible that micro-channel parallel hole [44], [45] or multiple slit [46] collimators might better use the high intrinsic resolution of an EMCCD based gamma camera to find a good balance between sensitivity and resolution in preclinical SPECT imaging.

REFERENCES

[1] D. A. Weber, M. Ivanovic, D. Franceschi, S-E. Strand, K. Erlandsson, M. Franceschi, H. L. Atkins, J. A. Coderre, H. Susskind, T. Button and K. Ljunggren, "Pinhole SPECT: an approach to in vivo high resolution SPECT imaging in small laboratory animals," *J. Nucl. Med.*, vol. 35, pp. 342-348, Feb. 1994.

[2] S. R. Cherry, "In vivo molecular and genomic imaging: new challenges for imaging physics," *Phys. Med. Biol.*, vol. 49, pp. R13-R48, Jan. 2004.

[3] R. Weissleder and U. Mahmood, "Molecular imaging," *Radiology*, vol. 219, pp. 316-333, May. 2001.

[4] F. J. Beekman, D. P. McElroy, F. Berger, S. S. Gambhir, E. J. Hoffman and S. R. Cherry, "Towards in vivo nuclear microscopy: iodine-125 imaging in mice using micro-pinholes," *Eur. J. Nuc. Med.*, vol. 29, pp. 933-938, Jul. 2002.

[5] L. R. MacDonald, B. E. Patt, J. S. Iwanczyk, B. M. W. Tsui, Y. Wang, E. C. Frey, D. E. Wessell, P. D. Acton and H. F. Kung, "Pinhole SPECT of mice using the lumaGEM gamma camera," *IEEE Trans. Nuc. Sci.*, vol. 48, pp. 830-836, Jun. 2001.

[6] K. Ishizu, T. Mukai, Y. Yonekura, M. Pagani, T. Fujita, Y. Magata, S. Nishizawa, N. Tamaki, H. Shibasaki and J. Konishi, "Ultra-high resolution SPECT system using four pinhole collimators for small animal studies," *J. Nucl. Med.*, vol. 36, pp. 2282-2206, Dec. 1995.

[7] D. P. McElroy, L. R. MacDonald, F. J. Beekman, Y. Wang, B. E. Patt, J. S. Iwanczyk, B. M. W. Tsui and E. J. Hoffman, "Performance evaluation of A-SPECT: a high resolution desktop pinhole SPECT system for imaging small animals," *IEEE Trans. Nuc. Sci.*, vol. 49, pp. 2139-2147, Oct. 2002.

[8] H. Kim, L. R. Furenlid, M. J. Crawford, D. W. Wilson, H. B. Barber, T. E. Peterson, W. C. J. Hunter, Z. L. Liu, J. M. Woolfenden and H. H. Barrett, "SemiSPECT: a small-animal single-photon emission computed tomography (SPECT) imager based on eight cadmium zinc telluride (CZT) detector arrays," *Med. Phys.*, vol. 33, pp. 465-474, Feb. 2006.

[9] M. Singh and E. Mumcuoglu, "Design of a CZT based BreastSPECT system," *IEEE Trans. Nuc. Sci.*, vol. 45, pp. 1158-1165, Jun. 1998.

[10] L. R. Furenlid, D. W. Wilson, Y. C. Chen, H. Kim, P. J. Pietraski, M. J. Crawford and H. H. Barrett, "FastSPECT II: A second-generation high-resolution dynamic SPECT imager," *IEEE Trans. Nuc. Sci.*, vol. 51, pp. 631-635, Jun. 2004.

[11] F. J. Beekman, A. P. Colijn, B. Vastenhouw, V. M. Wiegant and M. A. F. M. Gerrits, "High-resolution emission tomography of small laboratory animals: physics and gamma-astronomy meet molecular biology," *Nucl. Instrum. Methods A*, vol. 509, pp. 229-234, Aug. 2003.

[12] F. J. Beekman and B. Vastenhouw, "Design and simulation of a high-resolution stationary SPECT system for small animals," *Phys. Med. Biol.*, vol. 49, pp. 4579-4592, Sep. 2004.

[13] N. U. Schramm, G. Ebel, U. Engeland, T. Schurrat, M. Béhé and T. M. Behr, "High-resolution SPECT using multipinhole collimation," *IEEE Trans. Nuc. Sci.*, vol. 50, pp. 315-320, Jun. 2003.

[14] S. Staelens, K. Vunckx, J. De Beenhouwer, F. Beekman, Y. DAsslelr, J. Nuyts and I. Lemahieu, "GATE simulations for optimization of pinhole imaging," *Nucl. Instrum. Methods A*, vol. 569, pp. 359-363, Sep. 2006.

[15] R. Accorsi, F. Gasparini and R. C. Lanza, "A coded aperture for high-resolution nuclear medicine planar imaging with a conventional Anger camera: experimental results," *IEEE Trans. Nuc. Sci.*, vol. 48, pp. 2411-2417, Dec. 2001.

[16] S. R. Meikle, P. Kench, A. G. Weisenberger, R. Wojcik, M. F. Smith, S. Majewski, S. Eberl, R. R. Fulton, A. B. Rosenfeld and M. J. Fulham, "A prototype coded aperture detector for small animal SPECT," *IEEE Trans. Nuc. Sci.*, vol. 49, pp. 2167-2171, Oct. 2002.

[17] R. J. Jaszczak, J. Li, H. Wang, M. R. Zalutsky and R. E. Coleman, "Pin-hole collimation for ultra-high-resolution, small-field-of-view SPECT," *Phys. Med. Biol.*, vol. 39, pp. 425-437, Mar. 1994.

[18] F. J. Beekman, F. van der Have, B. Vastenhouw, A. J. A. van der Linden, P. P. van Rijk, J. P. H. Burbach and M. P. Smidt, "U-SPECT-I: a novel system for submillimeter-resolution tomography with radiolabeled molecules in mice," *J. Nucl. Med.*, vol. 46, pp. 1194-1200, Jul. 2005.

[19] E. Richer, M. A. Lewis, B. Smith, X. Li, S. Seliounine, R. P. Mason and P. P. Antich, "Comparison of CsI(Tl) and scintillating plastic in a multi-pinhole/CCD-based gamma camera for small-animal low-energy SPECT," in *Small Animal SPECT Imaging*, 1st ed., M. A. Kupinski and H. H. Barrett, Ed. New York, NY: Springer, 2005, pp. 189-194.

[20] J. Hynececk, "CCM-a new low-noise charge carrier multiplier suitable for detection of charge in small pixel CCD image sensors," *IEEE Trans. Electron Devices*, vol. 39, pp. 1972-1975, Aug. 1992.

[21] J. Hynececk, "Impactron-a new solid state image intensifier," *IEEE Trans. Electron Devices*, vol. 48, pp. 2238-2241, Oct. 2001.

[22] P. Jerram, P. Pool, R. Bell, D. Burt, S. Bowring, S. Spencer, M. Hazelwood, I. Moody, N. Catlett and P. Heyes, "The L3CCD: low light imaging without the need for an intensifier," in *Proc. SPIE*, vol. 4306, 2001, pp. 178-186.

[23] H. O. Anger, "Radioisotope cameras," in *Instrumentation in Nuclear Medicine*, 1st ed., vol. 1, G. J. Hine, Ed. New York, NY: Academic Press, 1967, pp. 485-553.

[24] H. O. Anger, "Scintillation camera," *Rev. Sci. Instr.*, vol. 29, pp. 27-33, Jan. 1958.

[25] F. J. Beekman and G. A de Vree, "Photon-counting versus an integrating CCD-based gamma camera: important consequences for spatial resolution," *Phys. Med. Biol.*, vol. 50, pp. N109-N119, May 2005.

[26] G. A. de Vree, A. H. Westra, I. Moody, F. van der Have, K. M. Ligtvoet and F. J. Beekman, "Photon-counting gamma camera based on an electron-multiplying CCD," *IEEE Trans. Nuc. Sci.*, vol. 52, pp. 580-588, Jun. 2005.

[27] L. J. Meng, "An intensified EMCCD camera for low energy gamma ray imaging application," *IEEE Trans. Nuc. Sci.*, vol. 53, pp. 2376-2384, Aug. 2006.

[28] J. Hynecek and T. Nishiwaki, "Excess noise and other important characteristics of low light level imaging using charge multiplying CCDs," *IEEE Trans. Electron Devices*, vol. 50, pp. 239-245, Jan. 2003.

[29] Corporate Publication, "On-chip multiplication gain," Roper Scientific Inc., Tucson, AZ, USA, Technical Note #14, 2003.

[30] Corporate Publication, "The use of multiplication gain in L3Vision™ electron multiplying CCD sensors," e2V Technologies Limited, Essex, England, Low-Light Technical Note 2, Jul. 2003.

[31] Corporate Publication, "Dark signal and clock-induced charge in L3Vision™ CCD sensors," e2V Technologies Limited, Essex, England, Low-Light Technical Note 4, Jul. 2004.

[32] M. S. Robbins and B. J. Hadwen, "The noise performance of electron multiplying charge-coupled devices," *IEEE Trans. Electron Devices*, vol. 50, pp. 1227-1232, May 2003.

[33] J. R. Janesick, *Scientific Charge-Coupled Devices*. Bellingham, WA: SPIE, 2001, pp. 605-654.

[34] Corporate Publication, "Designer's guide for the TC253SPD/TX253SPD impactron CCD," Texas Instruments Inc., Dallas, TX, USA, Application Note, Mar. 2003.

[35] L. A. Shepp and Y. Vardi, "Maximum likelihood reconstruction for emission tomography," *IEEE Trans. Medical Imaging*, vol. 1, pp. 113-122, Oct. 1982.

[36] A. J. Reader, S. Ally, F. Bakatselos, R. Manavaki, R. J. Walledge, A. P. Jeavons, P. J. Julyan, S. Zhao, D. L. Hastings and J. Zweit, "One-pass list-mode EM algorithm for high resolution 3-D PET image reconstruction into large arrays," *IEEE Trans. Nuc. Sci.*, vol. 49, pp. 693-699, Jun. 2002.

[37] P. Antich, R. Parkey, S. Seliounine, N. Slavine, E. Tsyganov and A. Zinchenko, "Application of expectation maximization algorithms for image resolution improvement in a small animal PET system," *IEEE Trans. Nuc. Sci.*, vol. 52, pp. 684-690, Jun. 2005.

[38] E. Tsyganov, J. Anderson, G. Arbique, A. Constantinescu, M. Jennewein, P. V. Kulkarni, R. P. Mason, R. W. McColl, O. K. Oz, R. W. Parkey, E. Richer, F. Rosch, S. Y. Seliounine, N. V. Slavine, S. C. Srivastava, P. E. Thorpe, A. I. Zinchenko and P. P. Antich, "UTSW small animal positron emission imager," *IEEE Trans. Nuc. Sci.*, vol. 53, pp. 243-254, Oct. 2006.

[39] S. M. Gruner, M. W. Tate and E. F. Eikenberry, "Charge-coupled device area x-ray detectors," *Rev. Scien. Instrum.*, vol. 73, pp. 2815-2842, Aug. 2002.

[40] S. J. Taylor, H. H. Barrett and K. Zinn, "Small animal SPECT using a lens-coupled CCD camera," in *Academy of Molecular Imaging Conference*, Orlando, Florida, Mar. 2004.

[41] H. Liu, A. Karellas, L. J. Harris and C. J. D'Orsi, "Methods to calculate the lens efficiency in optically coupled CCD x-ray imaging systems," *Med. Phys.*, vol. 21, pp. 1193-1195, Jul. 1994.

[42] V. V. Nagarkar, I. Shestakova, V. Gaysinskiy, B. Singh, B. W. Miller and H. B. Barber, "Fast X-ray/γ-ray imaging using electron multiplying CCD-based detector," *Nucl. Instrum. Methods A*, vol. 563, pp. 45-48, Feb. 2006.

[43] J. Hynececk, personal correspondence, 2005.

[44] G. A. Kastis, L. R. Furenlid, D. W. Wilson, T. E. Peterson, H. B. Barber and H. H. Barrett, "Compact CT/SPECT small-animal imaging system," *IEEE Trans. Nuc. Sci.*, vol. 51, pp. 63-67, Feb. 2004.

[45] E. L. Bradley, J. Celle, S. Majewski, V. Popov, J. Qian, M. S. Saha, M. F. Smith, A. G. Weisenberger and R. E. Welsh, "A compact gamma camera for biological imaging," *IEEE Trans. Nuc. Sci.*, vol. 53, pp. 59-65, Feb. 2006.

[46] Q. Huang and G. S. L. Zeng, "An analytical algorithm for skew-slit imaging geometry with nonuniform attenuation correction," *Med. Phys.*, vol. 33, pp. 997-1004, Apr. 2006.

Bibliography

[1] J. Radon. On the determination of functions from their integrals along certain manifolds. *Mathematisch–Physische Klasse*, 69:262–277, 1917.

[2] W. V. Mayneord, R. C. Turner, S. P. Newbery, and H. J. Hodt. A method of making visible the distribution of activity in a source of ionizing radiation. *Nature*, 168:762–765, 1951.

[3] H. Geiger and M. Walther. The electron counting tube. *Physik Zeitschrift*, 29:839–841, 1928.

[4] N. Veall. Some general problems in connection with the measurement of radioactivity in patients. *British Journal of Radiology*, 23:527–534, Set. 1950.

[5] W. V. Mayneord and S. P. Newbery. An automatic method of studying the distribution of activity in a source of ionizing radiation. *British Journal of Radiology*, 25:589–596, 1952.

[6] B. Cassen. The evolution of scintillation imaging. In L. M. Freeman and P. M. Johnson, editors, *Clinical Scintillation Imaging*, chapter 1, pages 3–12. Grune & Stratton, New York–San Francisco–London, second edition, 1975.

[7] J. W. Coltman and F. H. Marshall. Some characteristics of the photomultiplier radiation detector. *Physical Review*, 72:528, 1947.

[8] H. Kallmann. Unknown title. *Natur und Technik*, Jul. 1947.

[9] B. Cassen, L. Curtis, and C. Reed. A sensitive directional gamma ray detector. *Nucleonics*, 6:78–80, Feb. 1950.

[10] W. V. Mayneord and E. H. Belcher. Some application of nuclear physics to medicine. *British Journal of Radiology*, page 259, 1950. Supplement No. 2.

[11] W. E. Goodwin, F. K. Bauer, T. F. Barrett, and B. Cassen. A method using I^{131} for the determination of abnormal thyroid morphology. *American Journal of Roentgenology*, 68:963–970, Dec. 1952.

[12] H. O. Anger. A multiple scintillation counter in vivo scanner. *American Journal of Roentgenology*, 70:605–612, 1953.

[13] B. Cassen, L. Curtis, C. Reed, and R. Libby. Instrumentation for ^{131}I use in medical studies. *Nucleonics*, 9:46–50, 1951.

[14] D. E. Copeland and E. W. Benjamin. Pinhole camera for gamma-ray sources. *Nucleonics*, 5:44–49, Aug. 1949.

[15] H. O. Anger. Use of a gamma-ray pinhole camera for in vivo studies. *Nature*, 170:200–201, 1952.

[16] H. O. Anger. Scintillation camera. *Review of Scientific Instruments*, 29:27–33, 1958.

[17] D. E. Kuhl and R. Q. Edwards. Image separation radioisotope scanning. *Radiology*, 80:653–661, 1963.

[18] D. E. Kuhl and R. Q. Edwards. Cylindrical and section radioisotope scanning of the liver and brain. *Radiology*, 83:926–935, 1964.

[19] D. E. Kuhl, J. Hale, and W. L. Eaton. Transmission scanning: a useful adjunct to conventional emission scanning for accurately keying isotope deposition to radiographic anatomy. *Radiology*, 87:278–284, Aug. 1966.

[20] D. E. Kuhl and R. Q. Edwards. The Mark III scanner: a compact device for multiple-view and section scanning of the brain. *Radiology*, 96:563–570, 1970.

[21] D. E. Kuhl, R. Q. Edwards, A. R. Ricci, and M. Reivich. Quantitative section scanning using orthogonal tangent correction. *Journal of Nuclear Medicine*, 14:196–200, 1973.

[22] D. E. Kuhl, M. Reivich, A. Alavi, and et al. Local cerebral blood volume determined by three-dimensional reconstruction of radionuclide scan data. *Circulat. Res.*, 36:610–619, May 1975.

[23] D. E. Kuhl, R. Q. Edwards, A. R. Ricci, R. J. Yacob, T. J. Mich, and A. Alavi. The Mark IV system for radionuclide computed tomography of the brain. *Radiology*, 121:405–413, 1976.

[24] D. A. Weber, M. Ivanovic, D. Franceschi, S.-E. Strand, K. Erlandsson, M. Franceschi abd H. L. Atkins, J. A. Coderre, H. Susskind, T. Button, and K. Ljunggren. Pinhole SPECT: an approach to in vivo high resolution SPECT imaging in small laboratory animals. *Journal of Nuclear Medicine*, 35:342–348, 1994.

[25] S. R. Cherry. In vivo molecular and genomic imaging: new challenges for imaging physics. *Physics in Medicine and Biology*, 49:R13–R48, Jan. 2004.

[26] R. Weissleder and U. Mahmood. Molecular imaging. *Radiology*, 219:316–333, May 2001.

[27] F. J. Beekman, D. P. McElroy, F. Berger, S. S. Gambhir, E. J. Hoffman, and S. R. Cherry. Towards in vivo nuclear microscopy: iodine-125 imaging in mice using micro-pinholes. *European Journal of Nuclear Medicine*, 29:933–938, 2002.

[28] L. R. MacDonald, B. E. Patt, J. S. Iwanczyk, B. M. W. Tsui, Y. Wang, E. C. Frey, D. E. Wessell, P. D. Acton, and H. F. Kung. Pinhole SPECT of mice using the lumaGEM gamma camera. *IEEE Transactions on Nuclear Science*, 48:830–836, 2001.

[29] K. Ishizu, T. Mukai, Y. Yonekura, M. Pagani, T. Fujita, Y. Magata, S. Nishizawa, N. Tamaki, H. Shibasaki, and J. Konishi. Ultra-high resolution SPECT system using four pinhole collimators for small animal studies. *Journal of Nuclear Medicine*, 36:2282–2287, 1995.

[30] D. P. McElroy, L. R. MacDonald, F. J. Beekman, Y. Wang, B. E. Patt, J. S. Iwanczyk, B. M. W. Tsui, and E. J. Hoffman. Performance evaluation of A-SPECT: a high resolution desktop pinhole SPECT system for imaging small animals. *IEEE Transactions on Nuclear Science*, 49:2139–2147, 2002.

[31] H. Kim, L. R. Rurenlid, M. J. Crawford, D. W. Wilson, H. B. Barber, T. E. Peterson, W. C. J. Hunter, Z. L. Liu, J. M. Woolfenden, and H. H. Barrett. SemiSPECT: a small-animal single-photon emission computed tomography (SPECT) imager based on eight cadmium zinc telluride (CZT) detector arrays. *Medical Physics*, 33:465–474, 2006.

[32] M. Singh and E. Mumcuoglu. Design of a CZT based BreastSPECT system. *IEEE Transactions on Nuclear Science*, 45:1158–1165, Jun. 1998.

[33] L. R. Furenlid, D. W. Wilson, Y. C. Chen, H. Kim, P. J. Pietraski, M. J. Crawford, and H. H. Barrett. FastSPECT II: A second-generation high-resolution dynamic SPECT imager. *IEEE Transactions on Nuclear Science*, 51:631–635, 2004.

[34] F. J. Beekman, A. P. Colijn abd B. Vastenhouw, V. M. Wiegant, and M. A. F. M. Gerrits. High-resolution emission tomography of small laboratory animals: physics and gamma-astronomy meet molecular biology. *Nuclear Instruments and Methods in Physics Research A*, 509:229–234, 2003.

[35] F. J. Beekman and B. Vastenhouw. Design and simulation of a high-resolution stationary SPECT system for small animals. *Physics in Medicine and Biology*, 49:4579–4592, 2004.

[36] N. U. Schramm, G. Ebel, U. Engeland, T. Schurrat, M. Béhé, and T. M. Behr. High-resolution SPECT using multipinhole collimation. *IEEE Transactions on Nuclear Science*, 50:315–320, 2003.

[37] S. Staelens, K. Vunckx, J. De Beenhouwer, F. Beekman, Y. D'Asslelr, J. Nuyts, and I. Lemahieu. GATE simulations for optimization of pinhole imaging. *Nuclear Instruments and Methods in Physics Research A*, 569:359–363, Sep. 2006.

[38] R. Accorsi, F. Gasparini, and R. C. Lanza. A coded aperture for high-resolution nuclear medicine planar imaging with a conventional Anger camera: experimental results. *IEEE Transactions on Nuclear Science*, 48:2411–2417, 2001.

[39] S. R. Meikle, P. Kench, M. F. Smith A. G. Weisenberger, R. Wojcik, S. Majewski, S. Eberl, R. R. Fulton, A. B. Rosenfeld, and M. J. Fulham. A prototype coded aperture detector for small animal SPECT. *IEEE Transactions on Nuclear Science*, 49:2167–2171, 2002.

[40] R. J. Jaszczak, J. Li, H. Wang, M. R. Zalutsky, and R. E. Coleman. Pinhole collimation for ultra-high-resolution, small-field-of-view SPECT. *Physics in Medicine and Biology*, 39:425–437, Mar. 1994.

[41] F. J. Beekman, F. van der Have, B. Vastenhouw, A. J. A. van der Linden, P. P. van Rijk, J. P. H. Burbach, and M. P. Smidt. U-SPECT-I: a novel system for submillimeter-resolution tomography with radiolabeled molecules in mice. *Journal of Nuclear Medicine*, 46:1194–1200, Jul. 2005.

[42] E. Richer, M. A. Lewis, B. Smith, X. Li, S. Seliounine, R. P. Mason, and P. P. Antich. Comparison of CsI(Tl) and scintillating plastic in a multi-pinhole/CCD-based gamma camera for small-animal low-energy SPECT. In M. A. Kupinski and H. H. Barrett, editors, *Small Animal SPECT Imaging*, pages 189–194. Springer, New York, first edition, 2005.

[43] J. Hynecek. CCM-a new low-noise charge carrier multiplier suitable for detection of charge in small pixel CCD image sensors. *IEEE Transactions on Electron Devices*, 39:1972–1975, Aug. 1992.

[44] J. Hynecek. Impactron-a new solid state image intensifier. *IEEE Transactions on Electron Devices*, 48:2238–2241, Oct. 2001.

[45] P. Jerram, P. Pool, R. Bell, D. Burt, S. Bowring, S. Spencer, M. Hazelwood, I. Moody, N. Catlett, and P. Heyes. The L3CCD: low light imaging without the need for an intensifier. In *Proceedings of the SPIE*, volume 4306, pages 178–186. The International Society for Optical Engineering (SPIE), 2001.

[46] F. J. Beekman and G. A de Vree. Photon-counting versus an integrating CCD-based gamma camera: important consequences for spatial resolution. *Physics in Medicine and Biology*, 50:N109–N119, May 2005.

[47] G. A. de Vree, A. H. Westra, I. Moody, F. van der Have, K. M. Ligtvoet, and F. J. Beekman. Photon-counting gamma camera based on an electron-multiplying CCD. *IEEE Transactions of Nuclear Science*, 52:580–588, Jun. 2005.

[48] L. J. Meng. An intensified emccd camera for low energy gamma ray imaging applications. *IEEE Transactions on Nuclear Science*, 53:2376–2384, Aug. 2006.

[49] V. V. Nagarkar, I. Shestakova, V. Gaysinskiy, S. V. Tipnis, B. Singh, W. Barber, B. Hasegawa, and G. Entine. A ccd-based detector for spect. *IEEE Transactions on Nuclear Science*, 53:54–58, Feb. 2006.

[50] S. M. Gruner, M. W. Tate, and E. F. Eikenberry. Charge-coupled device area x-ray detectors. *Review of Scientific Instruments*, 73:2815–2842, Aug. 2002.

[51] M. J. Berger, J. H. Hubbell, S. M. Seltzer, J. Chang, J. S. Coursey, R. Sukumar, and D. S. Zucker. National Institute of Standards and Technology. In *XCOM: Photon Cross Section Database (version 1.3)*. Gaithersburg, Maryland, http://physics.nist.gov/xcom, 2007.

[52] W.-M. Yao, C. Amsler, D. Asner, R.M. Barnett, J. Beringer, P.R. Burchat, C.D. Carone, C. Caso, O. Dahl, G. D'Ambrosio, A. DeGouvea, M. Doser, S. Eidelman, J.L. Feng, T. Gherghetta, M. Goodman, C. Grab, D.E. Groom, A. Gurtu, K. Hagiwara, K.G. Hayes, J.J. Hernández-Rey, K. Hikasa, H. Jawahery, C. Kolda, Kwon Y., M.L. Mangano, A.V. Manohar, A. Masoni, R. Miquel, K. Mönig, H. Murayama, K. Nakamura, S. Navas, K.A. Olive, L. Pape, C. Patrignani, A. Piepke, G. Punzi, G. Raffelt, J.G. Smith, M. Tanabashi, J. Terning, N.A. Törnqvist, T.G. Trippe, P. Vogel, T. Watari, C.G. Wohl, R.L. Workman, P.A. Zyla, B. Armstrong, G. Harper, V.S. Lugovsky, P. Schaffner,

M. Artuso, K.S. Babu, H.R. Band, E. Barberio, M. Battaglia, H. Bichsel, O. Biebel, P. Bloch, E. Blucher, R.N. Cahn, D. Casper, A. Cattai, A. Ceccucci, D. Chakraborty, R.S. Chivukula, G. Cowan, T. Damour, T. DeGrand, K. Desler, M.A. Dobbs, M. Drees, A. Edwards, D.A. Edwards, V.D. Elvira, J. Erler, V.V. Ezhela, W. Fetscher, B.D. Fields, B. Foster, D. Froidevaux, T.K. Gaisser, L. Garren, H.-J. Gerber, G. Gerbier, L. Gibbons, F.J. Gilman, G.F. Giudice, A.V. Gritsan, M. Grünewald, H.E. Haber, C. Hagmann, I. Hinchliffe, A. Höcker, P. Igo-Kemenes, J.D. Jackson, K.F. Johnson, D. Karlen, B. Kayser, D. Kirkby, S.R. Klein, K. Kleinknecht, I.G. Knowles, R.V. Kowalewski, P. Kreitz, B. Krusche, Yu.V. Kuyanov, O. Lahav, P. Langacker, A. Liddle, Z. Ligeti, T.M. Liss, L. Littenberg, L. Liu, K.S. Lugovsky, S.B. Lugovsky, T. Mannel, D.M. Manley, W.J. Marciano, A.D. Martin, D. Milstead, M. Narain, P. Nason, Y. Nir, J.A. Peacock, S.A. Prell, A. Quadt, S. Raby, B.N. Ratcliff, E.A. Razuvaev, B. Renk, P. Richardson, S. Roesler, G. Rolandi, M.T. Ronan, L.J. Rosenberg, C.T. Sachrajda, S. Sarkar, M. Schmitt, O. Schneider, D. Scott, T. Sjöstrand, G.F. Smoot, P. Sokolsky, S. Spanier, H. Spieler, A. Stahl, T. Stanev, R.E. Streitmatter, T. Sumiyoshi, N.P. Tkachenko, G.H. Trilling, G. Valencia, K. van Bibber, M.G. Vincter, D.R. Ward, B.R. Webber, J.D. Wells, M. Whalley, L. Wolfenstein, J. Womersley, C.L. Woody, A. Yamamoto, O.V. Zenin, J. Zhang, and R.-Y. Zhu. Review of Particle Physics. *Journal of Physics G*, 33:1+, 2006.

[53] M. M. Moses, M. J. Weber, S. E. Derenzo, D. Perry, P. Berdahl, and L. A. Boatner. Prospects for dense, infrared emitting scintillators. *IEEE Transactions on Nuclear Science*, pages 462–466, 1998.

[54] W. S. Boyle and G. E. Smith. Charge coupled semiconductor devices. *Bell*

System Technical Journal, 49:587–593, 1970.

[55] G. F. Amelio, M. F. Tompsett, and G. E. Smith. Experimental verification of the charge coupled device concept. *Bell System Technical Journal*, 49:593–600, 1970.

[56] J. R. Janesick. *Scientific Charge-Coupled Devices*, pages 605–654. SPIE, Bellingham, Washington, USA, first edition, 2001.

[57] J. Hynecek and T. Nishiwaki. Excess noise and other important characteristics of low light level imaging using charge multiplying CCDs. *IEEE Transactions of Electron Devices*, 50:239–245, Jan. 2003.

[58] Roper Scientific Inc., Tucson, Arizona, USA. *On-chip multiplication gain*, 2003. Technical Note #14.

[59] e2v Technologies Limited, Chelmsford, Essex, England. *The use of multiplication gain in L3Vision^{TM} electron multiplying CCD sensors*, Jul. 2003. Low-Light Technical Note 2.

[60] e2v Technologies Limited, Chelmsford, Essex, England. *Dark signal and clock-induced charge in L3Vision^{TM} CCD sensors*, Jul. 2004. Low-Light Technical Note 4.

[61] M. S. Robbins and B. J. Hadwen. The noise performance of electron multiplying charge-coupled devices. *IEEE Transactions of Electron Devices*, 50:1227–1232, May 2003.

[62] H. O. Anger. Radioisotope cameras. In G. J. Hine, editor, *Instrumentation in Nuclear Medicine*, volume 1, chapter 19, pages 485–553. Academic Press, New York–London, 1967.

[63] E. N. Tsyganov, P. P. Antich, P. V. Kulkarni, R. P. Mason, R. W. Parkey, S. Y. Seliuonine, J. W. Shay, T. C. Soesbe, and A. I. Zinchenko. Micro-spect combined with 3d optical imaging. In *Nuclear Science Symposium Conference Record, 2004*, volume 5, pages 3275–3279. IEEE NSS/MIC, 2004.

[64] Scientific Imaging Technologies (SITe). www.site-inc.com, 2007.

[65] ANDOR Technology, Belfast, Northern Ireland. *Darkcurrent and CIC in EM-CCDs (update from spring 2004)*, Aug. 2004. ANDOR tech note–low light imaging.

[66] Texas Instruments Inc., Dallas, Texas, USA. *Designer's guide for the TC253SPD/TX253SPD Impactron CCD*, Mar. 2003. Application Note.

[67] V. V. Nagarkar, I. Shestakova, V. Gaysinskiy, B. Singh, B. W. Miller, and H. B. Barber. Fast X-ray/γ-ray imaging using electron multiplying CCD-based detector. *Nuclear Instruments and Methods in Physics Research A*, 563:45–48, Feb. 2006.

[68] L. A. Shepp and Y. Vardi. Maximum likelihood reconstruction for emission tomography. *IEEE Transactions on Medical Imaging*, 1:113–122, 1982.

[69] A. J. Reader, S. Ally, F. Bakatselos, R. Manavaki, R. J. Walledge, A. P. Jeavons, P. J. Julyan, S. Zhao, D. L. Hastings, and J. Zweit. One-pass list-mode em algorithm for high resolution 3-d pet image reconstruction into large arrays. *IEEE Transactions on Nuclear Science*, 49:693–699, Jun. 2002.

[70] P. Antich, R. Parkey, S. Seliounine, N. Slavine, E. Tsyganov, and A. Zinchenko. Application of expectation maximization algorithms for image resolution im-

provement in a small animal PET system. *IEEE Transactions of Nuclear Science*, 52:684–690, Jun. 2005.

[71] E. Tsyganov, J. Anderson, G. Arbique, A. Constantinescu, M. Jennewein, P. V. Kulkarni, R. P. Mason, R. W. McColl, O. K. Oz, R. W. Parkey, E. Richer, S. Y. Seliounine F. Rosch and, N. V. Slavine, S. C. Srivastava, P. E. Thorpe, A. I. Zinchenko, and P. P. Antich. UTSW small animal positron emission imager. *IEEE Transactions on Nuclear Science*, 53:243–254, Oct. 2006.

[72] S. J. Taylor, H. H. Barrett, and K. Zinn. Small animal SPECT using a lens coupled CCD camera. In *Academy of Molecular Imaging Conference*. Orlando, Florida, Mar. 2004.

[73] H. Liu, A. Karellas, L. J. Harris, and C. J. D'Orsi. Methods to calculate the lens efficiency in optically coupled CCD x-ray imaging systems. *Medical Physics*, 21:1193–1195, Jul. 1994.

[74] Princeton Instruments. www.piacton.com, 2007.

[75] e2V Technologies. www.e2v.com, 2007.

[76] National Institutes of Health ImageJ Software. http://rsb.info.nih.gov/ij, 2007.

[77] J. W. T. Heemskerk, A. H. Westra, P. M. Linotte, K. M. Ligtvoet, W. Zbijewski, and F. J. Beekman. Front-illuminated versus back-illuminated photon-counting CCD-based gamma camera: important consequences for spatial resolution and energy resolution. *Physics in Medicine and Biology*, 52:N149–N162, Mar. 2007.

[78] B. W. Miller, B. H. Bradford, H. H. Barrett, I. Shestakova, B. Singh, and V. V. Nagarkar. Single-photon spatial and energy resolution enhancement of a colum-

nar CsI(Tl)/EMCCD gamma-camera using maximum-likelihood estimation. In *Proc. SPIE.* 6142, 61421T, 2006.

[79] L. J. Meng, N. H. Clinthorne, S. Skinner, R. V. Hay, and M. Gross. Design and feasibility study of a single photon emission microscope system for small animal I-125 imaging. *IEEE Transactions on Nuclear Science*, 53:1168–1178, Jun. 2006.

[80] B. W. Miller, B. H. Bradford, H. H. Barrett, D. W. Wilson, and L. Chen. A low-cost approach to high-resolution, single-photon imaging using columnar scintillators and image intensifiers. In *IEEE Nuclear Science Symposium Conference Record.* Volume 6, Pages: 3540-3545, Oct. 2006.

[81] G. A. Kastis, L. R. Furenlid, D. W. Wilson, T. E. Peterson, H. B. Barber, and H. H. Barrett. Compact CT/SPECT small-animal imaging system. *IEEE Transactions of Nuclear Science*, 51:63–67, Feb. 2004.

[82] E. L. Bradley, J. Celle, S. Majewski, V. Popov, J. Qian, M. S. Saha, M. F. Smith, A. G. Weisenberger, and R. E. Welsh. A compact gamma camera for biological imaging. *IEEE Transactions of Nuclear Science*, 53:59–65, Feb. 2006.

[83] Q. Huang and G. S. L. Zeng. An analytical algorithm for skew-slit imaging geometry with nonuniform attenuation correction. *Medical Physics*, 33:997–1004, Apr. 2006.

[84] J. Hynecek. personal correspondence, 2005.

[85] T. M. Wengenack, G. L. Curran, and J. F. Podulso. Targeting Alzheimer amyloid plaques in vivo. *Nature Biotechnology*, 18:868–872, 2000.

[86] J. Hardy and D. Selkoe. The amyloid hypothesis of Alzheimer's disease: progress and problems on the road to therapeutics. *Science*, 297:353–356, 2002.

[87] M. Hintersteiner, A. Enz, P. Frey, A.-L. Jaton, W. Kinzy, R. Kneuer, U. Neumann, M. Rudin, M. Staufenbiel, M. Stoeckli, K.-H. Wiederhold, and H.-U. Gremlich. *In vivo* detection of amyliod-β deposits by near-infrared imaging using an oxazine-derivative probe. *Nature Biotechnology*, 23:577–583, 2005.

[88] L. Holcomb, M. N. Gordon, E. McGowan, X. Yu, S. Benkovic, P. Jantzen, K. Wright, I. Saad, R. Mueller, D. Morgan, S. Sanders, C. Zehr, K. O'Campo, J. Hardy, C.-M. Prada, C. Eckman, S. Younkin, K. Hsiao, and K. Duff. Accelerated Alzheimer-type phenotype in transgenic mice carrying both mutant amyliod precursor protein and presenillin 1 transgenes. *Nature Medicine*, 43:97–100, 1998.

[89] M. Ono, A. Wilson, J. Nobrega, D. Westaway, P. Verhoeff, Z.-P. Zhuang, M.-P. Kung, and H. F. Kung. ^{11}C-labeled stilbene derivatives as Aβ-aggregate-specific PET imaging agents for Alzheimer's disease. *Nuclear Medicine and Biology*, 30:565–571, 2003.

[90] M. Higuchi, N. Iwata, Y. Matsuba, K. Sato, K. Sasamoto, and T. Saido. [19]F and ^{1}H MRI detection of amyliod β plaques. *Nature Neuroscience*, 8:527–533, 2005.

[91] W. E. Klunk, B. J. Bacskai, C. A. Mathis S. T. Kajdasz, M. E. McLellan, M. P. Frosch, M. L. Debnath, D. P. Holt, Y. Wang, and B. T. Hyman. Imaging Aβ plaques in living transgenic mice with multiphoton microscopy and methoxy-X04, a systemically administered Congo red derivative. *Journal of Neuropathology and Experimental Neurology*, 61:797–805, 2002.

[92] A. Nordberg. PET imaging of amyloid Alzheimer's disease. *Lancet Neurology*, 3:519–527, 2004.

[93] P. Vaupel, F. Kallinowski, and P. Okunieff. Blood flow, oxygen and nutrient supply, and metabolic microenvironment of human tumors: a review. *Cancer Research*, 49:6449–6465, 1989.

[94] R. K. Jain. Determinants of tumor blood flow: a review. *Cancer Research*, 48:2641–2658, 1988.

[95] R. K. Jain. Therapeutic implications of tumor physiology. *Current Opinion in Oncology*, 3:1105–1108, 1991.

Vita

Todd Christopher Soesbe was born in Temple, Texas on June 17, 1971, the son of Dr. Glenn Terry Soesbe and Carol Anne Soesbe. He received his Bachelor of Arts degree from Clark University (Worcester, Massachusetts) in May of 1993, where he majored in both Physics and Studio Art, and graduated with Honors in Physics. He received his Master of Science degree in Applied Physics from the University of Texas at Austin in May of 2000. He then worked for the Optical Networking Division of Lucent Technologies (Richardson, Texas) until resuming graduate studies in August of 2002. He received his Doctor of Philosophy degree in Radiological Sciences from the University of Texas Southwestern Medical Center at Dallas in August of 2007.

Permanent Address: 1111 Clermont ST

Dallas, Texas

75223

This dissertation was typeset with LaTeX 2_ε[1] by the author.

---

[1] LaTeX 2_ε is an extension of LaTeX. LaTeX is a collection of macros for TeX. TeX is a trademark of the American Mathematical Society. The macros used in formatting this dissertation were written by Dinesh Das, Department of Computer Sciences, The University of Texas at Austin, and extended by Bert Kay, James A. Bednar, and Ayman El-Khashab.